Università degli Studi di Modena e Reggio Emilia

Dipartimento di Ingegneria "Enzo Ferrari"

International Doctorate in
Information and Communication Technologies

XXXVII Cycle

Vehicle-to-everything (V2X) Communications for Green and Reliable Intelligent Transportation Systems – Comunicazioni veicolari per sistemi di trasporto intelligenti, verdi ed affidabili

---

Supervisor:

Prof. Giorgio Matteo Vitetta

Co-tutor:

Dott. Pasquale Di Viesti

PhD School Coordinator:

Prof. Luigi Rovati

Candidate:

Michele Mirabella

Tesi di dottorato di ricerca co-finanziata nell'ambito del Programma Operativo Nazionale Ricerca e Innovazione 2014-2020 (CCI 2014IT16M2OP005), risorse FSE REACT-EU, Azione IV.4 "Dottorati e contratti di ricerca su tematiche dell'innovazione" e Azione IV.5 "Dottorati su tematiche Green".

"Di solito siamo meglio convinti dalle ragioni che troviamo da noi stessi, che da quelle che ci provengono dagli altri."
– Blaise Pascal, *Pensieri*

Sommario

La crescente diffusione di veicoli connessi ha aperto nuove frontiere nella ricerca sulle *comunicazioni veicolari* (V2X). Questo lavoro di dottorato si concentra sull'analisi e lo sviluppo di tecnologie innovative per i sistemi di comunicazione V2X, con l'obiettivo di migliorare l'efficienza, la sicurezza e la sostenibilità dei trasporti. In particolare, la ricerca si è focalizzata sullo *strato fisico* (PHY) delle comunicazioni V2X, approfondendo lo studio dei sistemi per la comunicazione e sensing congiunti (*joint communication and sensing*, JCAS). Questi sistemi innovativi integrano le funzionalità di comunicazione e radar, consentendo ai veicoli di scambiare informazioni e allo stesso tempo generare un'immagine dell'ambiente circostante, contribuendo così a migliorare la sicurezza stradale e l'efficienza del traffico. Sono state analizzate e confrontate in dettaglio due delle principali tecniche di modulazione multiportante utilizzate nei sistemi JCAS: la modulazione OFDM (*Orthogonal Frequency Division Multiplexing*) e la modulazione OTFS (*Orthogonal Time Frequency Space*). Entrambi questi formati presentano vantaggi e svantaggi specifici, dal punto di vista della comunicazione, del sensing, della complessità computazionale e della robustezza nei confronti delle diverse condizioni del canale wireless. Da un lato, l'OFDM rappresenta un formato ampiamente adottato a livello di comunicazione, dall'altro il suo impiego nel sensing presenta ancora tanti aspetti da chiarire. Una tecnica ancora più recente è l'OTFS, che si distingue per la sua robustezza nei confronti della selettività nel tempo e in frequenza; ciò la rende una scelta promettente in scenari dinamici, come quello veicolare, i quali diventeranno sempre più critici all'aumentare delle frequenze operative dei sistemi di nuova generazione. Lo studio condotto sui sistemi JCAS si è concentrato su due problemi principali: 1) lo sviluppo di nuovi algoritmi a basso costo computazionale per la rivelazione di ostacoli multipli e stima dei loro parametri caratterizzanti (quali, distanza, velocità, coordinate spaziali ed energia) in sistemi JCAS basati su OFDM. Lo studio ha considerato sia sistemi dotati di singola antenna trasmittente e ricevente (SISO), sia dotati di schiere di antenne in trasmissione e ricezione (MIMO), analizzando l'impatto della molteplicità di antenne sulle prestazioni e la complessità del sistema. 2) L'impiego di un doppio prefisso ciclico (uno nel tempo ed uno in frequenza) nella modulazione OTFS e lo sviluppo di algoritmi innovativi per la stima del canale assistita da simboli pilota in un sistema che la utilizza (la stima di canale è utile sia per il sensing al lato trasmittente, sia per l'equalizzazione dei dati ricevuti al lato ricevente). Infine, è stato implementato un sistema di comunicazione basato su OTFS su piattaforme SDR (*Software Defined Radio*) ed è stato verificato sperimentalmente che tale sistema è in grado di operare in maniera affidabile anche in presenza di canali di comunicazione dinamici. I risultati ottenuti possono contribuire allo sviluppo della tecnologia JCAS e certamente forniscono indicazioni utili nella scelta del formato di modulazione, aprendo la strada a sistemi di comunicazione wireless più efficienti e versatili. Le soluzioni sviluppate in questo lavoro possono trovare applicazione in una vasta gamma di scenari, tra cui la guida autonoma, la gestione del traffico intelligente e la sicurezza stradale.

Abstract

The increasing number of connected vehicles has opened new frontiers in Vehicle-to-Everything (V2X) communication research. This PhD work focuses on the analysis and development of innovative technologies for vehicle-to-everything V2X communication systems that aim at enhancing transportation efficiency, safety, and sustainability. Specifically, the research concentrates on the Physical Layer (PHY) of V2X communications, with a particular focus on Joint Communication and Sensing (JCAS) systems. These cutting-edge systems integrate communication and radar functionalities, enabling vehicles to exchange information while simultaneously detecting their surroundings, thereby improving road safety and traffic efficiency. This study provides a detailed analysis and comparison of two primary multicarrier modulation techniques that are envisioned as promising candidates for JCAS systems: Orthogonal Frequency Division Multiplexing (OFDM) and Orthogonal Time Frequency Space (OTFS). Each of these modulation formats offers distinct advantages and disadvantages in terms of performance for both communication and sensing, computational complexity, and resilience under various wireless channel conditions. While OFDM is widely adopted in digital communications, its application to radio sensing presents several open challenges. On the other hand, the relatively newer OTFS technique demonstrates robustness against time and frequency selectivity, making it a promising choice for dynamic vehicular scenarios, which are expected to become more demanding as the operational frequencies of next-generation systems increase. This research addresses two primary challenges within JCAS systems: 1) The development of low-complexity algorithms for the detection of multiple obstacles (targets) and for the estimation of their key parameters (such as distance, speed, spatial coordinates, and reflected energy) in OFDM-based JCAS systems. The analysis includes both Single-Input Single-Output (SISO) and Multiple-Input Multiple-Output (MIMO) antenna systems, examining the impact of antenna cardinality on system performance and complexity. 2) The utilization of a double cyclic prefix (one in the time domain, the other one in the frequency domain) in the OTFS modulation, as well as the development of novel algorithms for pilot-aided channel estimation in OTFS-based systems. It is important to underline that channel estimation is crucial for both sensing at the transmit side and for data equalization at the receive side. Finally, an OTFS-based communication system has been implemented on Software-Defined Radio (SDR) platforms. The obtained experimental results have evidenced that this system can reliably operate in dynamic communication channels. The findings of this study contribute to the advancement of JCAS technology and provide valuable insights into the selection of modulation formats, paving the way for more efficient and versatile wireless communication systems. The solutions developed here have potential applications in a wide range of scenarios, including autonomous driving, intelligent traffic management, and road safety.

Acknowledgements

I would like to express my sincere gratitude to Prof. Giorgio Matteo Vitetta for guiding me through every aspect of my Ph.D. study with exceptional expertise and unwavering availability. His support extended beyond technical guidance, as he provided continuous advice that has shaped both my professional and personal growth. Thanks to his constant attention, I was able to make up my mind on crucial aspects of my future career.

A special thanks goes to him for appointing Dr. Pasquale Di Viesti as my co-supervisor and mentor. With Pasquale, I had the privilege of engaging in open and judgment-free discussions, which allowed me to grow both academically and personally. His patience, which I often lacked, has been an invaluable resource throughout this journey, and I will forever be grateful for it.

I am profoundly thankful to my family for their firm support. To my parents, Giovanna and Vittorio, who have always provided me with maximum encouragement and complete freedom in my life choices, I owe everything I am. Without their unconditional love and constant motivation, reaching this milestone would have been unimaginable. I also wish to thank my sister Valentina and her partner Manuel Della Rocca, who not only appreciated my efforts but gave me strength during challenging moments through their warmth and closeness. I dedicate this achievement to all my family members, whose love and support have made this journey possible.

My heartfelt thanks go to my colleagues and friends from the research lab, with whom I shared countless hours of work and discovery. The deep bond we have formed will undoubtedly endure, regardless of where our paths may lead. I wish each of them success in pursuing paths that inspire and fulfill them.

A sincere thank you goes to my friends who have always believed in me, often with a faith that exceeded my own expectations. Among them, I would like to especially mention Elia Zacchini, Fabio Sorrentino, Kaled Mathlouthi, Lorenzo Guercio, Christian Gilli, and all my teammates for their constant support and friendship.

Finally, I wish to express my gratitude to the mentors I had the privilege of working with outside of the University. I am deeply thankful to Dr. Eng. Luca Ferrari for welcoming me with kindness and enthusiasm at the R&D office of CNH Italia in Modena during my time there. I also wish to thank Prof. Christos Masouros for the opportunity to visit his research group at University College of London. Their professionalism and contagious enthusiasm for research and work have been an extraordinary source of inspiration for me.

Desidero innanzitutto esprimere la mia più sincera gratitudine al prof. Giorgio Matteo Vitetta per avermi seguito in ogni aspetto del mio percorso di dottorato, con grande competenza e disponibilità. Non solo mi ha guidato sotto il profilo tecnico, ma mi ha sempre supportato con saggi consigli, che hanno avuto un valore inestimabile, sia sul piano professionale che umano. Grazie alla sua costante attenzione, ho potuto riflettere su aspetti cruciali per la mia carriera futura, orientandomi sempre verso scelte efficaci e consapevoli.

Un ringraziamento particolare va a lui per avermi affiancato il collega e amico, Dott. Pasquale Di Viesti, come co-tutor. Con Pasquale ho avuto il privilegio di confrontarmi liberamente, senza alcun timore di giudizio, e di crescere tanto accademicamente quanto personalmente. La sua pazienza, che spesso mancava in me, è stata una risorsa fondamentale durante questo percorso e di essa sarò sempre grato.

Un ringraziamento speciale va anche alla mia famiglia, che mi ha sostenuto in ogni momento. Ai miei genitori, Giovanna e Vittorio, che mi hanno sempre dato il massimo supporto, ma anche una totale libertà nelle scelte della mia vita, devo tutto ciò che sono. Senza il loro affetto incondizionato e il loro continuo incoraggiamento, questo traguardo sarebbe stato impensabile. Un pensiero va anche a mia sorella Valentina e al suo compagno Manuel Della Rocca, che non solo hanno sempre apprezzato i miei sforzi, ma mi hanno dato forza nei momenti più difficili, con il loro calore e la loro vicinanza. Dedico questo successo a tutti i membri della mia famiglia, che con il loro amore e supporto hanno reso possibile il mio percorso.

Ringrazio di cuore anche tutti i colleghi e amici del laboratorio di ricerca, con i quali ho condiviso innumerevoli ore di lavoro e di scoperte. Il legame che si è creato è profondo e sono certo che resisterà nel tempo, indipendentemente dalle nostre strade future. Auguro a ciascuno di loro di trovare la strada che più li ispiri e li soddisfi.

Un grazie sincero va agli amici che hanno sempre creduto in me, spesso con una fiducia che ha superato ogni aspettativa. Tra questi, voglio ricordare Elia Zacchini, Fabio Sorrentino, Kaled Mathlouthi, Lorenzo Guercio, Christian Gilli e tutti i miei compagni di squadra, per il loro sostegno costante e la loro amicizia.

Infine, desidero esprimere la mia riconoscenza ai tutor delle attività svolte fuori dall'Università. Un sentito grazie al Dott. Ing. Luca Ferrari, per avermi accolto con disponibilità e interesse presso l'ufficio di R&D di CNH Italia a Modena, durante il periodo trascorso in azienda. Un ringraziamento anche al prof. Christos Masouros, che mi ha dato l'opportunità di visitare il suo gruppo di ricerca presso l'University College of London. La loro professionalità e il loro entusiasmo, quasi contagioso, nella gestione del lavoro e della ricerca, sono stati per me fonte di grande ispirazione.

Contents

List of Figures

List of Tables

Acronyms

1D	One-Dimensional
2D	Two-Dimensional
3D	Three-Dimensional
4D	Four-Dimensional
4G	Fourth-Generation
5G	Fifth-Generation
6G	Sixth-Generation
AE	Angular Estimator
AFDM	Affine Frequency Division Multiplexing
AGN	Additive Gaussian Noise
AIC	*Akaike* Information Criterion
AI	Artificial Intelligence
AoA	Angle of Arrival
APES	Amplitude and Phase Estimation
AWGN	Additive White Gaussian Noise
BER	Bit Error Rate
CFAR	Constant False Alarm Rate
CFO	Carrier Frequency Offset
CIR	Channel Impulse Response
CP	Cyclic Prefix
CPO	Cyclic Postfix
CRLB	Cramér-Rao Lower bound
CSI	Channel State Information
CS	Compressed Sensing
CSFDE	Complex Single Frequency-Delay Estimation
CSFDEC	Complex Single Frequency-Delay Estimation and Cancellation
CT	Computation Time
DCP	Double Cyclic Prefix
DD	Delay–Doppler
DFT	Discrete Fourier Transform
DRAEC	Doppler-Range-Angle Estimation with successive Compensation
DOFDM	Dual Orthogonal Frequency Division Multiplexing

DoA	Direction of Arrival
DSFT	Discrete Symplectic Fourier Transform
eMBB	Enhanced Mobile Broadband
EM	Expectation Maximization
ESPRIT	Estimation of Signal Parameters via Rotational Invariant Technique
FCT	Fourier Continuous Transform
FD	Frequency Domain
FFT	Fast Fourier Transform
FG	Full Guard
FIM	Fisher Information Matrix
FLOP	Floating Point Operation
FMCW	Frequency Modulated Continuous Wave
FS	Fourier Series
GFDM	Generalized Frequency Division Multiplexing
GPS	Global Positioning System
GQR	Gaussian Quadrature Rules
HULA	Horizontal Uniform Linear Array
IBI	Inter-Block Interference
ICI	Inter-Carrier Interference
IDI	Inter-Doppler Interference
IDFT	Inverse Discrete Fourier Transform
IDSFT	Inverse Discrete Symplectic Fourier Transform
IFFT	Inverse Fast Fourier Transform
IFCT	Inverse Fourier Continuous Transform
ISAC	Integrated Sensing and Communication
ISI	Inter-Symbol Interference
ITS	Intelligent Transportation Systems
JCAS	Joint Communication and Sensing
KLMS	Kernel Least Mean Square
LB	Lower Bound
LHS	Left-Hand Side
LO	Local Oscillator
LTE	Long-Term Evolution
MDL	Minimum Description Length
MHR	Multidimensional Harmonic Retrieval
MF	Matched Filter

MIMO	Multiple-Input Multiple-Output
ML	Maximum Likelihood
MMSE	Minimum Mean Square Error
mMTC	Massive Machine-Type Communication
MSE	Mean Square Error
MUSIC	Multiple Signal Classification
MWL	Modified Wax & Leshem
NI	National Instruments
OFDM	Orthogonal Frequency Division Multiplexing
OTFS	Orthogonal Time Frequency Space
PC	Personal Computer
PHY	Physical Layer
ppm	parts per million
PSK	Phase-Shift Keying
PSD	Power Spectral Density
QAM	Quadrature Amplitude Modulation
QPSK	Quadrature Phase-Shift Keying
RD	Range-Doppler
RDE	Range-Doppler Estimator
RF	Radio Frequency
RHS	Right-Hand Side
RPI5	Raspberry Pi 5
RMSE	Root Mean Square Error
RRC	Root of a Raised Cosine
RX	Receive
S/P	Serial-to-Parallel
SC	Suppressed Carrier
SDR	Software-Defined Radio
SE	Spectral Efficiency
SEFDM	Spectrally Efficient Frequency Division Multiplexing
SFCW	Stepped Frequency Continuous Wave
SISO	Single-Input Single-Output
SNR	Signal-to-Noise Ratio
TD	Time Domain
TF	Time-Frequency
TO	Timing Offset

TRDP	Target Range-Doppler Profile
TX	Transmit
ULA	Uniform Linear Array
URA	Uniform Rectangular Array
URLLC	Ultra-Reliable Low-Latency Communication
USB	Universal Serial Bus
USRP	Universal Software Radio Peripheral
VA	Virtual Antenna
V2I	Vehicle-to-Infrastructure
V2V	Vehicle-to-Vehicle
V2X	Vehicle-to-Everything
VRU	Vulnerable Road User
VULA	Vertical Uniform Linear Array
ZF	Zero Forcing

Introduction

This chapter starts by providing a general overview of the research area. Next, it delves into the specific objectives and finally describes the structure of the thesis.

Background

In recent years, there has been a growing awareness of road safety and the importance of sustainable transportation. A key innovation in this context is represented by *vehicular connectivity*, which enables vehicles to share real-time information with one another, with Vulnerable Road Users (VRUs), and with roadside infrastructure. The advent of Intelligent Transportation Systems (ITS) has brought about a paradigm shift in the automotive industry. Central to this transformation is Vehicle-to-Everything (V2X) communication, a technology that enables vehicles to exchange information with other vehicles, infrastructure, and pedestrians. By fostering Vehicle-to-Vehicle (V2V) and Vehicle-to-Infrastructure (V2I) communication, V2X has the potential to significantly enhance road safety, traffic efficiency, and overall mobility.

The Physical Layer (PHY), as the foundation of any communication system, plays a pivotal role in V2X. It governs the transmission and reception of data over wireless channels, encompassing aspects such as modulation, coding, and channel access. The efficacy of V2X heavily relies on the robust performance of the PHY, which must contend with various challenges, including:

1) *Channel characteristics*: The wireless channel in vehicular environments is highly dynamic and subject to fading, shadowing, and interference from other wireless devices.

2) *Reliability*: V2X communication must be highly reliable to ensure the safety of road users. Even a brief interruption in communication can have severe consequences.

3) *Latency*: Low latency is crucial for applications such as collision avoidance, where timely information exchange is essential.

4) *Security*: The security of V2X communication is paramount to protect against malicious attacks and ensure privacy.

In this context, the rapid evolution of wireless communication technologies has revolutionized the way we interact with the digital world. The Fourth-Generation (4G) Long-Term Evolution (LTE) standard, while groundbreaking in its time, is now being surpassed by the emerging Fifth-Generation (5G) technology, which promises to deliver significantly enhanced performance and capabilities. Building upon the success of its predecessors, Sixth-Generation (6G) is poised to further push the boundaries of wireless communication, offering unprecedented levels of speed, reliability, and connectivity.

6G aims to address the increasing demands of a data-driven society, where the need for high-speed, low-latency, and energy-efficient wireless communication is ever-growing. By leveraging advanced technologies such as Artificial Intelligence (AI), machine learning, and millimeter-wave and terahertz frequencies, 6G will enable a wide range of innovative applications, including Ultra-Reliable Low-Latency Communication (URLLC), Massive Machine-Type Communication (mMTC) and Enhanced Mobile Broadband (eMBB). To achieve these ambitious goals, 6G will require significant advancements in various aspects of wireless communication, including spectrum and energy efficiency, and security measures to protect sensitive data and prevent cyberattacks.

As we stand on the brink of the 6G era, the potential for transformative innovation is immense. By addressing the challenges and capitalizing on the opportunities presented by this technology, we can shape a future where wireless communication seamlessly integrates into every aspect of our lives.

Thesis Motivation

From a technical perspective, and of particular relevance to this dissertation, emerging vehicular communication scenarios will be analyzed, with a primary focus on JCAS systems.

JCAS systems primarily aim to transmit useful information to targets (i.e., pedestrians, vehicles, bicycles, walls or any other obstacle), which are thus not merely "passively" detected.

Instead, a single device handles both sensing and communication tasks, eliminating the need for separate subsystems (thus representing a paradigm shift from the communication or radar only device) and reducing cost and complexity. To address this challenge, two main approaches are commonly adopted: *radar-centric* and *communication-centric* approaches. The first involves adapting traditional radar waveforms to also carry information. Traditional radar systems, known for their effectiveness in detecting and localizing targets within the range-velocity domain, are evolving to accommodate dual functionalities, in particular in the context of millimeter-wave systems, which are known for their very high resolution. The second approach, which is also the focus of this dissertation, employs standard communication waveforms (single- or multi-carrier). In this case, communication tasks are inherently supported, while radar processing is performed through innovative methods that leverage knowledge of transmitted information (shared by both the transmitter and receiver, if *colocated*). This approach departs from conventional radar methods that rely on straightforward threshold analysis of the power reflected by the target.

Selecting an appropriate communication waveform requires balancing competing objectives. On one side, the system seeks to maximize the achievable communication rate, defined as the amount of information transmitted within a given time-frequency window. On the other side, precise radar sensing is essential to accurately localize a target in terms of range, velocity, and spatial (angular) coordinates. Traditional radar systems achieve high localization accuracy using chirp-like pulses-short single-carrier impulses with wide

bandwidth, which ensure sufficient energy delivery to the target while enabling precise localization across all dimensions. However, the information-carrying capacity of such chirp signals is strongly limited.

To enhance communication rates, multi-carrier digital waveforms can be used, where information is encoded not only in the time domain (as in single-carrier systems) but also across multiple frequency subcarriers, each carrying distinct modulation symbols. Despite this advantage, the design involves tradeoffs. The subcarrier spacing and symbol time, which are interdependent, must be carefully optimized. While multi-carrier waveforms enable higher communication rates, they present challenges in terms of radar signal processing and typically offer lower localization precision compared to single-carrier pulses. This tradeoff reflects the inherent cost of integrating communication capabilities with radar functionalities.

In conclusion, the current literature on the PHY layer of communication systems increasingly focuses on developing advanced multi-carrier schemes that aim to overcome the communication rate limitations of traditional radar waveforms. Optimizing the tradeoff between communication and sensing remains an open research problem, with no universally optimal solution yet identified. Among the most promising multi-carrier modulation techniques for joint radar and communication are OFDM and OTFS modulation.

OFDM has gained widespread adoption in recent years, forming the backbone of many modern communication standards, including 5G. Its popularity stems from its ability to simplify detection through the use of a cyclic prefix, namely a guard interval between symbols to mitigate Inter-Symbol Interference (ISI). Under moderate Doppler conditions and appropriately spaced subcarriers, OFDM effectively diagonalizes the communication channel, enabling element-wise symbol detection. This simplicity has made it a cornerstone of digital communications.

On the other hand, OTFS is an innovative Two-Dimensional (2D) modulation technique that maps data symbols into the Delay–Doppler (DD) domain, providing a fundamentally different approach to signal representation and processing. Unlike traditional One-Dimensional (1D) modulation schemes, like OFDM, OTFS leverages both time and frequency dimensions simultaneously, ensuring that each data symbol is fully expanded across the Time-Frequency (TF) domain. This enables the channel to exert a nearly uniform effect on every symbol, effectively mitigating fading and interference.

While OFDM relies on computationally intensive algorithms to manage Inter-Carrier Interference (ICI) caused by fast channel variations, OTFS approaches the problem from the perspective of interference sources. By mapping symbols into the DD domain, OTFS minimizes interference and ensures more reliable and accurate communication in rapidly changing scenarios.

As a result, OTFS is particularly advantageous for applications in highly mobile and dynamic scenarios, such as vehicular communications, where traditional modulation techniques often struggle. Furthermore, OTFS technology is expected to seamlessly integrate with existing modulation frameworks, making it a strong candidate for future wireless communication standards.

This dissertation provides a comprehensive comparative analysis of OFDM and OTFS, evaluating their strengths and weaknesses in key metrics, including the estimation of radar parameters, achievable communication rates, the estimation of channels, and other critical tasks. The aim is to offer insights that enable system designers to select the most appropriate waveform for specific applications and scenarios, balancing the needs of communication and radar functionalities in the context of JCAS systems.

Organization of the Thesis

This dissertation is structured as follows. Part 1 focuses on OFDM as a multicarrier modulation technique employed in the context of radar sensing within a *colocated* radar system. In particular, Chapter 1 introduces an approximate maximum likelihood approach to address the problem of target detection and estimation in a SISO OFDM-based radar system. A novel algorithm is developed to accurately estimate the positions and velocities of multiple targets while serially canceling their contributions from the received radar echoes. This process enhances the ability of the system to detect weaker targets while offering a significant improvement in the accuracy-complexity trade-off, especially in scenarios with closely spaced targets.

Chapter 2 offers a detailed overview of the key algorithms employed for target detection and parameter estimation in radar sensing based on *colocated* SISO OFDM radar systems. These algorithms are thoroughly described, with an emphasis on their underlying principles and computational requirements. In addition, their performance in terms of accuracy and complexity is evaluated through simulations conducted across various scenarios. The numerical results highlight the distinct trade-offs between accuracy and computational cost associated with each technique, providing useful insights for selecting the most suitable approach in practical applications.

Chapter 3 introduces a novel algorithm designed to estimate the amplitude, position, velocity, and angular coordinates (that is, azimuth and elevation angles) of multiple targets in a MIMO OFDM-based radar system. The proposed approach addresses the inherent complexity of joint maximum likelihood estimation by adopting a more computationally feasible strategy. Specifically, it separates the angle estimation problem from range-Doppler estimation, enabling the integration of well-established algorithms to solve these sub-problems. A comprehensive framework is presented, and various techniques from the technical literature are incorporated into this scheme to evaluate their performance and complexity trade-offs. Numerical simulations evidence that one of the proposed methods can achieve near-optimal performance in terms of accuracy, while maintaining a manageable computational burden across different scenarios.

Part 2 of this dissertation shifts the focus toward the communication aspects of JCAS, particularly for systems operating in high-mobility scenarios. These environments are characterized by severe degradation in communication performance caused by significant Doppler effects. While OFDM is widely used in multicarrier modulation, its performance deteriorates under such conditions due to its sensitivity to ICI, making it less suitable for high-mobility scenarios. To overcome these challenges, the recently developed OTFS

modulation is explored. Unlike OFDM, OTFS is specifically designed to operate effectively in doubly-selective channels, as it represents the transmitted symbols in the DD domain, inherently offering robustness against high Doppler shifts. In this context, this part of the dissertation proposes a novel modulation format for OTFS that incorporates a double cyclic prefix, one in Time Domain (TD), and the other in the Frequency Domain (FD). This innovative format is developed by drawing inspiration from the principles of OFDM and the duality principle between the time and frequency domains, paving the way for improved performance in JCAS applications under high mobility.

Chapter 4 focuses on the theoretical derivation and modeling of the proposed OTFS modulation format with a double cyclic prefix. The derivation takes advantage of insights from the duality principle that connects the time and frequency domains, building on the framework of OFDM and extending it to the DD domain representation. To provide the necessary context, the chapter begins with a brief overview of the traditional OFDM scheme and introduces its dual modulation, a concept that has not previously appeared in the technical literature. Following this, the chapter details the mathematical formulation of the novel OTFS format and develops an analytical model for both the transmitted and received signals. The resulting modulation format is examined under two conditions: ideal channel and doubly-selective fading channels, where both time and frequency selectivity are present. In addition, the chapter investigates the impact of pulse shaping on the structure of the waveform and power spectral density, highlighting how this affects communication performance. These results serve as a foundation for developing practical rules for pilot symbol allocation, which will be further explored in Chapter 5.

Chapter 5 builds upon the modulation framework developed in Chapter 4 by addressing the technical aspects of pilot symbol allocation and channel estimation in OTFS systems employing a double cyclic prefix. Recognizing the importance of accurate channel state information in high-mobility scenarios, the chapter proposes novel pilot-aided channel estimation and equalization algorithms tailored to the new modulation format. The obtained numerical results lead to the conclusion that the new channel estimator achieves superior accuracy with reasonable computational complexity, which makes it suitable for both channel equalization in communication tasks and sensing applications in JCAS systems.

Chapter 6 shifts the focus from theoretical analysis to practical implementation, addressing the implementation of an OTFS-based digital communication system with a double cyclic prefix on commercial SDRs. This chapter provides a detailed account of the design and implementation of the proposed OTFS system on a pair of National Instruments SDRs, leveraging the flexibility of the hardware to evaluate the real-world performance of the considered modulation scheme. Key signal processing algorithms employed at the transmitter and receiver are described, along with practical considerations for achieving robust communication in high-mobility scenarios. The experimental results demonstrate the ability of the proposed system to maintain reliable performance even under challenging channel conditions with significant Doppler effects, validating the theoretical findings and showcasing the potential of OTFS with double cyclic prefix for real-world applications. This work represents a crucial step toward bridging the gap between theory and practice, offering insights into the challenges and solutions involved in deploying advanced modulation schemes in commercial hardware environments.

In both parts, different appendices containing additional results and proofs are provided. Finally, some conclusions and suggestions for future research are given in Chapter 7.

Notation

Throughout this dissertation, the following notation has been adopted:

1) $(\cdot)^T$ denotes matrix transposition, whereas $(\cdot)^*$ and $(\cdot)^H$ denote complex conjugate and complex conjugate transpose (Hermitian operator), respectively.

2) $\Re\{x\}$ and $\Im\{x\}$ indicate the real part and imaginary part, respectively, of the complex variable x.

3) $\mathbf{0}_{D_1,D_2}$ denotes the $D_1 \times D_2$ null matrix.

4) The symbols $\otimes$, $\odot$, $\star$ and $\times$ represent the Kronecker, Hadamard, Khatri-Rao and Cartesian product operators, respectively.

5) diag($\mathbf{v}$) represents a square diagonal matrix having the elements of the vector $\mathbf{v}$ along its main diagonal.

6) $\mathbf{I}_M$ denotes the order M identity matrix;

7) $\emptyset$ represents the empty set.

8) $*$ denotes the linear convolution;

9) $R_N[\cdot]$ indicates the *modulo N operator*;

10) $\lfloor\cdot\rfloor$ and $\lceil\cdot\rceil$ denote the *floor* and *ceiling* operators, respectively;

11) $\mathbf{X} \triangleq [x_{m,n}]$ defines a matrix $\mathbf{X}$ of proper size and $x_{m,n}$ denotes the element appearing on its mth row and nth column;

12) $\mathbf{\Xi}_X$ is the unitary Discrete Fourier Transform (DFT) matrix of order X, whose element (p, q) is $\exp(-j2\pi pq/X)/\sqrt{X}$.

An Approximate Maximum Likelihood Method for the Joint Estimation of Range and Doppler of Multiple Targets in OFDM-Based Radar Systems

In this chapter, an innovative method for the detection and the estimation of multiple targets in a radar system employing orthogonal frequency division multiplexing is illustrated. The core of this method is represented by a novel algorithm for detecting multiple superimposed two-dimensional complex tones in the presence of noise and estimating their parameters. This algorithm is based on a maximum likelihood approach and combines a single tone estimator with a serial cancellation procedure. The numerical results lead to the conclusion that the developed method can achieve a substantially better accuracy-complexity trade-off than various related techniques in the presence of closely spaced targets.

1.1 Introduction

Wireless communication and radar sensing have been advancing independently for many years, even though they share various similarities in terms of both signal processing and system architecture. In the last few years, substantial research efforts have been devoted to the design of wireless systems able to perform *communication and radar* functions jointly. The interest in this class of systems, that accomplish JCAS, has been motivated by the advantages they offer in terms of device size, power consumption, cost and efficiency of radio spectrum usage with respect to traditional wireless systems in various applications [1]. Three main paradigms have emerged based on system design priorities and underlying physical layers: *communication-centric*, *radar-centric*, and *hybrid joint design and optimization*.

In *communication-centric* systems, radar sensing capabilities are added to a communication framework as a secondary function. The primary goal is to preserve communication performance, while leveraging the existing communication waveforms to extract radar information.

Radar-centric systems prioritize radar sensing while embedding communication signals within radar waveforms. This approach enables nearly optimal radar performance, as the sensing function remains the primary focus of the system. However, communication throughput is typically limited, given the constraints of radar waveform properties. Modifications to radar operations may introduce tolerable performance trade-offs, allowing for

basic communication functions. Despite its limitations in data rate, radar-centric designs offer robustness in sensing-critical applications, making them suitable for defense and certain automotive systems.

The *hybrid* approach represents a paradigm shift, involving the co-design of systems and waveforms to achieve a balance between communication and sensing. Unlike the loose integration of communication-centric or radar-centric designs, hybrid systems optimize both functions concurrently. This joint design offers tunable trade-offs, enabling flexibility in adapting performance to specific scenarios or priorities.

In this chapter we focus on a *communication-centric* JCAS approach, where the radar sensing function can be considered as an add-on to the given communication system. More specifically, we take into consideration a SISO JCAS system employing OFDM; this modulation format has been adopted in various wireless communication standards, thanks to its robustness to multipath fading and to its relatively simple synchronization [2].

In the technical literature, *direct* and *indirect sensing* methods for target detection and estimation are available for OFDM-based JCAS systems. Generally speaking, *direct sensing methods* extract target information from the received signal without compensating for the effect of the data payload it conveys [1,3] and typically exploit computationally intensive Compressed Sensing (CS) techniques. *Indirect estimation methods*, instead, require isolating and estimating the signal component related exclusively to the targets and, consequently, compensating for the contribution due to channel symbols (e.g., see [4, eq. (20)]). Indirect sensing methods can be divided in: 1) DFT-based or *correlation-based* methods (i.e., methods based on the *matched filter*, MF, concept) [5–7]; 2) subspace methods [3,8,9]; 3) Maximum Likelihood (ML) based methods [10–13].

Correlation-based and DFT-based methods for joint range-velocity estimation exploit prior knowledge of the received signal and, even if conceptually simple and computationally efficient, may generate poor radar images in the presence of closely spaced targets or strong clutter around them [14]. Such methods can be outperformed by subspace methods, like the well-known Multiple Signal Classification (MUSIC) algorithm and the Estimation of Signal Parameters via Rotational Invariant Technique (ESPRIT) at the price, however, of a significantly larger computational complexity [8]. An accuracy comparable to that of subspace methods can be achieved through various ML-based algorithms, which also require a significant computational effort. Relevant contributions to this field concern: 1) the use of the *Amplitude Weighted Linearly Constrained Minimum Variance* method for estimating the parameters of multiple targets [10]; 2) the adoption of an *alternating maximization* approach to mitigate the computational complexity of ML estimation [11]; 3) the development of an iterative non-linear Kernel Least Mean Square (KLMS) based technique for the estimation of target range [12]; 4) the derivation of a ML method, based on a kinematic model of detected targets, for estimating target speed [13].

The work illustrated in this chapter has been motivated by the interest in extending the ML-based estimator of multiple overlapped complex exponentials developed in [15] to a 2D scenario, and to investigate the application of the resulting algorithm to the detection of multiple targets and the estimation of their range and Doppler in an OFDM-based JCAS system. The contribution provided by this chapter is threefold and can be summarized as follows:

1) A novel iterative DFT-based algorithm, called Complex Single Frequency-Delay Estimation (CSFDE), is developed for the ML estimation of a single 2D complex tone. This estimator is based on the *periodogram method* for coarse frequency estimation and on a new iterative algorithm for the estimation of frequency residuals and complex amplitude. The last algorithm requires the evaluation of multiple Discrete Symplectic Fourier Transforms (DSFTs), but, unlike other estimation techniques, does not need prior knowledge of the overall number of targets. Moreover, its derivation is based on: a) a new approximate expression of the ML metric; b) the exploitation of the *alternating minimization* technique.

2) A novel recursive algorithm, called Complex Single Frequency-Delay Estimation and Cancellation (CSFDEC), for the estimation of the parameters of multiple superimposed 2D tones is derived. This algorithm, which combines the CSFDE algorithm with a serial cancellation & refinement procedure, is applied to target range and Doppler estimation in the considered JCAS system.

3) The accuracy of the CSFDEC algorithm is assessed by extensive computer simulations and compared with that achieved by various related algorithms available in the technical literature.

The obtained numerical results lead to the conclusion that the CSFDEC algorithm outperforms all the other related estimators in terms of probability of convergence, and achieves similar or better accuracy in all the considered scenarios; in particular, it is able to reliably operate in the presence of multiple closely-spaced targets in scenarios in which DFT-based methods, subspace methods and other ML-based methods fail. In addition, the computational requirements of the CSFDEC algorithm are quite limited; this is due to the fact that it exploits a DFT-based method (namely, the CSFDE algorithm) and a mathematically simple serial cancellation & refinement procedure, that, unlike ML-based and subspace methods, does not require matrix inversions and eigendecompositions. Moreover, the CSFDEC algorithm is an *off-grid* algorithm since, unlike most of the ML-based methods available in the technical literature, it does not make use of a search grid in frequency estimation; this makes its application substantially easier than *on-grid* algorithms.

The remaining part of this chapter is organized as follows. In Section 1.2, the processing accomplished in an OFDM-based radar system is summarized, and the model of the signal feeding the CSFDEC algorithm is briefly derived. Section 1.3 is devoted to the derivation of the CSFDE and CSFDEC algorithms and to the assessment of their computational complexity. The CSFDEC algorithm is then compared, in terms of accuracy and complexity, with other estimation algorithms in Section 1.4. Finally, some conclusions are offered in Section 1.5.

1.2 System and Signal Models

This section focuses on the processing accomplished at the receive side of a SISO OFDM-based JCAS system; the main objectives of this section are deriving the mathematical model of the received signal in the presence of multiple targets and illustrating some essential assumptions on which it relies. In the following, we take into consideration the transmission of a single frame, consisting of M consecutive OFDM symbols; such symbols

can convey both pilot tones (for channel estimation and synchronization) and information data to be sent to a single or multiple receivers at different locations. However, what is relevant in this study is that the considered frame is sent over a wireless channel by a transmitter which is *colocated* with the considered receiver; consequently, the receiver has full knowledge of the structure and content of the whole frame and of the transmission frequency, and exploits this information for sensing purposes only. The complex envelope of the transmitted signal conveying the mth OFDM symbol (with $m = 0, 1, ..., M-1$) of the considered frame can be expressed as (e.g., see [11, eq. (3)])

$$x_m(t) \triangleq x(t - mT_{\rm s}) = q(t - mT_{\rm s}) \sum_{n=0}^{N-1} s_m(n) \exp\big(j2\pi n \Delta_f (t - mT_{\rm s})\big), \tag{1.1}$$

where $x(t)$ denotes the OFDM baseband signal at the instant t, $q(t)$ is a windowing function, $s_m(n)$ is the channel symbol carried by the nth subcarrier of the mth OFDM symbol (with $n = 0, 1, ..., N-1$), N is the overall number of subcarriers, $\Delta_f = 1/T$ is the subcarrier spacing, T is the OFDM symbol interval, $T_{\rm s} \triangleq T + T_{\rm G}$ is the overall duration of the OFDM symbol and $T_{\rm G}$ is the Cyclic Prefix (CP) duration (also known as *guard time* [4]). Following [11], a rectangular windowing function is assumed in this chapter, so that $q(t) = 1$ for $t \in [-T_{\rm G}, T]$ and $q(t) = 0$ elsewhere.

Given the complex envelope (1.1), the Radio Frequency (RF) waveform radiated by the radar transmitter can be expressed as

$$x_{\rm RF}(t) = \Re \left\{ \exp(j2\pi f_{\rm c} t) \sum_{m=0}^{M-1} x_m(t) \right\}, \tag{1.2}$$

where $f_{\rm c}$ denotes the frequency of the Local Oscillator (LO) employed in the up-conversion at the transmit side. In order to better understand the analytical steps describing OFDM baseband processing at the receiver, we initially assume now that the last waveform is reflected by a single[1] scatterer (i.e., by a single *point target*), located at the (initial) distance R from the transmitter and moving at the radial velocity[2] v with respect to it. It is not difficult to show that, in this case, the complex envelope of the signal received by the JCAS system (i.e., by the colocated receiver) is (e.g., see [11, eq. (6)])

$$r(t) = \exp\left(-j2\pi f_{\rm c} \tau\right) \exp\big(j2\pi f_\nu t\big) \sum_{m=0}^{M-1} x\left(t - mT_{\rm s} - \tau + \frac{f_\nu}{f_{\rm c}} t\right) + w(t), \tag{1.3}$$

where $\tau \triangleq 2R/c$ is the overall propagation delay, c denotes the speed of light, $f_\nu = 2v/\lambda$ is the Doppler shift due to target motion, $\lambda = c/f_{\rm c}$ is the wavelength of the radiated signal and $w(t)$ is the complex Additive Gaussian Noise (AGN) process affecting $r(t)$.

The signal $r(t)$ (1.3) undergoes analog-to-digital conversion followed by Discrete Fourier Transform (DFT) processing. A simple mathematical model describing the sequence generated by the sampling of $r(t)$ can be derived as follows. Substituting the Right-Hand

[1] The model resulting from this initial assumption will be then generalized to multipath channel in the following.

[2] This velocity is positive (negative) if the target approaches (moves away from) the considered radar system.

Side (RHS) of (1.1) in that of (1.3) and extracting the portion associated with the mth OFDM symbol from the resulting expression yields

$$r_m(t') = A(\tau)\,\exp(j2\pi f_\nu t')\,\exp(j2\pi f_\nu m T_\mathrm{s}) \cdot \sum_{n=0}^{N-1} s_m(n)\,\gamma_n(\tau)\,\xi_n(f_\nu, t')\,\zeta_{m,n}(f_\nu)\,\exp(j2\pi n\Delta_f\, t') + w(t'), \quad (1.4)$$

where $t' \triangleq t - mT_\mathrm{s}$, $A(\tau) \triangleq \exp(-j2\pi f_\mathrm{c}\tau)$, $\gamma_n(\tau) \triangleq \exp(-j2\pi n\Delta_f\tau)$, $\xi_n(f_\nu, t') \triangleq \exp(j2\pi n\Delta_f(f_\nu/f_\mathrm{c})t')$ and $\zeta_{m,n}(f_\nu) \triangleq \exp(j2\pi n\Delta_f(f_\nu/f_\mathrm{c})\,mT_\mathrm{s})$.

Note that: 1) the phase of $A(\tau)$ depends on the target delay τ only, whereas that of $\gamma_n(\tau)$ is proportional to both τ and the subcarrier index n; 2) the factor $\xi_n(f_\nu, t')$ produces a time-dependent phase rotation influenced by both the target speed v and the subcarrier index n; 3) the factor $\zeta_{m,n}(f_\nu)$ generates a phase rotation depending on both the OFDM symbol index m and the subcarrier index n, and accounts for the so-called *inter-subcarrier Doppler effect* (e.g., see [11, Sec. II, p. 3]).

Based on (1.4), it is not difficult to show that, if $|f_\nu\,\tau| \ll 1$, sampling $r_m(t')$ (1.4) at the instant $t'_{m,l} \triangleq \tau + T(l/N)$ yields

$$r_m(l) \triangleq r_m(t'_{m,l}) = A(\tau)\,\exp\left(j2\pi\frac{l}{N}\frac{f_\nu}{\Delta_f}\right)\,\exp\big(j2\pi f_\nu m T_\mathrm{s}\big)\sum_{n=0}^{N-1} s_m(n) \cdot \gamma_n(\tau)\,\xi_{n,l}(f_\nu)\,\zeta_{m,n}(f_\nu)\,\exp\Big(j2\pi n\frac{l}{N}\Big) + w_m(l), \quad (1.5)$$

with $l = 0, 1, ..., N-1$; here, $\xi_{n,l}(f_\nu) \triangleq \xi_n(f_\nu, T\,l/N)$ and $w_m(l) \triangleq w(t'_{m,l})$ is the Gaussian noise affecting $r_m(l)$. In the following, we also assume that: 1) the sequence $\{w_m(l); l = 0, 1, ..., N-1\}$ can be modeled as Additive White Gaussian Noise (AWGN); 2) the target speed is limited, so that $|2v/c| \ll 1/(MN)$ and $|f_\nu|/\Delta_f = |f_\nu T| \ll 1$. Consequently, the factors $\exp(j2\pi(lf_\nu)/(N\Delta_f))$, $\xi_{n,l}(f_\nu)$, $\zeta_{m,n}(f_\nu)$ appearing in the RHS of (1.5) can be neglected; this leads to the simplified signal model

$$r_m(l) = A(\tau)\,\exp\big(j2\pi f_\nu m T_\mathrm{s}\big)\sum_{n=0}^{N-1} s_m(n)\,\gamma_n(\tau)\exp\Big(j2\pi n\frac{l}{N}\Big) + w_m(l), \quad (1.6)$$

that represents the reference model in the derivation of the CSFDE and CSFDEC algorithms.

The N signal samples acquired in the mth OFDM symbol interval are collected in the vector $\mathbf{r}_m \triangleq [r_m(0), r_m(1), ..., r_m(N-1)]^T$, that undergoes order N DFT processing. The nth element of the resulting DFT output vector

$$\mathbf{R}_m \triangleq [R_m(0), R_m(1), ..., R_m(N-1)]^T \quad (1.7)$$

is

$$R_m(n) \triangleq \frac{1}{N}\sum_{l=0}^{N-1} r_m(l)\exp\Big(-j2\pi\frac{l}{N}n\Big) \\ = A(\tau)\exp\big(j2\pi f_\nu m T_\mathrm{s}\big)s_m(n)\exp\big(-j2\pi n\Delta_f\tau\big) + W_m(n), \quad (1.8)$$

where $W_m(n)$ is the AWGN sample affecting the nth subcarrier of mth OFDM symbol. Since the channel symbol $s_m(n)$ is known by the JCAS receiver for any n and m, the estimate

$$\hat{H}_{m,n} \triangleq \frac{R_m(n)}{s_m(n)} = A(\tau)\, a_m(F_\nu)\, a_n^*(F_r) + \bar{W}_m(n) \quad (1.9)$$

of the channel frequency response $H_{m,n}$ at the nth subcarrier frequency in the mth OFDM symbol interval can be computed; here,

$$F_r \triangleq \Delta_f\,\tau \quad (1.10)$$

is the *normalized target delay*,

$$F_\nu \triangleq f_\nu T_\mathrm{s} \quad (1.11)$$

is the *normalized Doppler frequency*[3], $a_q(F_X) \triangleq \exp(j2\pi q F_X)$ (with $q = m$ or n and $X = \nu$ or r) and

$$\bar{W}_m(n) \triangleq \frac{W_m(n)}{s_m(n)} \quad (1.12)$$

is the noise sample affecting $\hat{H}_{m,n}$ (1.9). It is important to underline the following:

1) The parameter F_r (F_ν) satisfies the inequalities $F_{r,\min} \leqslant F_r \leqslant F_{r,\max}$, ($F_{\nu,\min} \leqslant F_\nu \leqslant F_{\nu,\max}$), with $F_{r,\min} = 0$ and $F_{r,\max} = 1$ ($F_{\nu,\min} = -1/2$ and $F_{\nu,\max} = 1/2$); in fact, only positive ranges must be taken into account, whereas Doppler can be either positive or negative.

2) In all the computer simulations, the channel symbols $\{s_m(n)\}$ belong to a $M_\mathrm{c}$ary Phase-Shift Keying (PSK) constellation; this assumption ensures that $s_m(n) \neq 0$ for every m and n, thus avoiding division by zero.

3) Based on the last assumption, the noise samples $\{\bar{W}_m(n)\}$ (see (1.12)) can be modeled as AWGN if $\{W_m(n)\}$, in (1.8), is AWGN.

4) The noise variance is denoted $\sigma^2_{\bar{W}} \triangleq \sigma^2_{\bar{W}}/\sigma^2_\mathrm{s}$, where σ^2_s denotes the power of the Transmit (TX) symbols.

5) Without any loss of generality, the factor $A(\tau)$ appearing in the RHS of (1.9) can be replaced by the complex gain $A \triangleq a\exp(j\phi)$, accounting for the phase rotation due to τ, the path loss and the gain (attenuation) introduced by the target.

[3]Note that F_r is always a positive quantity, whereas F_ν is positive (negative) if the considered target is approaching (moving away from) the radar.

The model (1.9) has been derived for a single target, but can be easily generalized to the case of K point targets. In fact, in the last case, (1.8) becomes

$$R_m(n) = s_m(n) \sum_{k=0}^{K-1} A_k \, a_m\big(F_{\nu_k}\big) \, a_n^*\big(F_{r_k}\big) + W_m(n), \tag{1.13}$$

so that $\hat{H}_{m,n}$ (1.9) can be expressed as

$$\hat{H}_{m,n} = \sum_{k=0}^{K-1} A_k \, a_m\big(F_{\nu_k}\big) \, a_n^*\big(F_{r_k}\big) + \bar{W}_m(n), \tag{1.14}$$

with $m = 0, 1, ..., M-1$ and $n = 0, 1, ..., N-1$; in the last two formulas, F_{r_k}, F_{ν_k} and A_k denote the normalized delay, the normalized Doppler frequency and the complex gain, respectively, characterizing the kth target. In the following, we assume that these complex exponentials are ordered according to a decreasing strength, so that $|A_k| \geq |A_{k+1}|$, with $k = 0, ..., K-1$.

From (1.14) it can be easily inferred that: 1) the noisy samples $\{\hat{H}_{m,n}\}$ of the 2D channel response acquired over a single frame can be modeled as the superposition of multiple 2D complex exponentials with AWGN; 2) target detection and estimation are tantamount to identifying the K complex exponentials forming the useful component of the sequence $\{\hat{H}_{m,n}\}$ and estimating their parameters. Finally, it is important to point out that the two normalized frequencies characterizing each target need to be estimated jointly; in fact, if a 1D frequency estimator is used to estimate each of them separately, a complicated pairing problem has to be solved in order to avoid any ambiguity in target detection.

1.3 Approximate Maximum Likelihood Estimation of Two-Dimensional Complex Tones

In this section, we first derive a novel algorithm for jointly estimating the parameters of a *single* 2D complex tone. Then, we show how this algorithm can be exploited to detect *multiple* superimposed tones and estimate their parameters through a procedure based on successive cancellations and refinements. Finally, we analyze the computational complexity of the developed algorithms and discuss the similarities and differences of our multiple tone estimator with other related estimation techniques.

1.3.1 Joint estimation of the parameters of a single two-dimensional complex tone

Let us focus on the problem of estimating the parameters of a single 2D complex tone affected by AWGN on the basis of the noisy observations $\{\hat{H}_{m,n}\}$, where (see (1.9) or, equivalently, (1.14) with $K = 1$)

$$\hat{H}_{m,n} = A \exp\big(j2\pi m F_\nu\big) \exp\big(-j2\pi n F_r\big) + \bar{W}_m(n), \tag{1.15}$$

with $m = 0, 1, ..., M-1$ and $n = 0, 1, ..., N-1$. It is easy to show that the ML estimates $F_{\nu,\mathrm{ML}}$, $F_{r,\mathrm{ML}}$ and A_{ML} of F_ν, F_r and A, respectively, can be evaluated as

$$\big(F_{\nu,\mathrm{ML}}, F_{r,\mathrm{ML}}, A_{\mathrm{ML}}\big) \triangleq \arg \min_{\tilde{F}_\nu, \tilde{F}_r, \tilde{A}} \varepsilon\big(\tilde{F}_\nu, \tilde{F}_r, \tilde{A}\big), \tag{1.16}$$

where $\tilde{F}_\nu$, $\tilde{F}_r$ and $\tilde{A}$ are the trial values of F_ν, F_r and A, respectively,

$$\varepsilon\big(\tilde{F}_\nu, \tilde{F}_r, \tilde{A}\big) \triangleq \frac{1}{MN} \sum_{m=0}^{M-1} \sum_{n=0}^{N-1} \varepsilon_{m,n}\big(\tilde{F}_\nu, \tilde{F}_r, \tilde{A}\big) \tag{1.17}$$

is the Mean Square Error (MSE) computed[4] over the whole set $\{\hat{H}_{m,n}\}$,

$$\varepsilon_{m,n}\big(\tilde{F}_\nu, \tilde{F}_r, \tilde{A}\big) \triangleq \left|\hat{H}_{m,n} - H_{m,n}\left(\tilde{F}_\nu, \tilde{F}_r, \tilde{A}\right)\right|^2 \tag{1.18}$$

is the *square error* between the noisy sample $\hat{H}_{m,n}$ (1.15) and its useful component

$$H_{m,n}\big(\tilde{F}_\nu, \tilde{F}_r, \tilde{A}\big) \triangleq \tilde{A} \exp\big(j2\pi m\tilde{F}_\nu\big) \exp\big(-j2\pi n\tilde{F}_r\big) \tag{1.19}$$

evaluated under the assumption that $F_\nu = \tilde{F}_\nu$, $F_r = \tilde{F}_r$ and $A = \tilde{A}$. Substituting the RHS of the last equation in that of (1.18) yields

$$\varepsilon_{m,n}\big(\tilde{F}_\nu, \tilde{F}_r, \tilde{A}\big) = \big|\hat{H}_{m,n}\big|^2 + \big|\tilde{A}\big|^2 - 2\Re\left\{\hat{H}_{m,n}\ \tilde{A}^* \exp\big(-j\left(\tilde{\varphi}_m - \tilde{\phi}_n\right)\big)\right\}, \tag{1.20}$$

where $\tilde{\varphi}_m \triangleq 2\pi m\tilde{F}_\nu$ and $\tilde{\phi}_n \triangleq 2\pi n\tilde{F}_r$. Then, substituting the RHS of (1.20) in that of (1.17) gives, after some manipulation,

$$\varepsilon\big(\tilde{F}_\nu, \tilde{F}_r, \tilde{A}\big) = \varepsilon_H + \big|\tilde{A}\big|^2 - 2\Re\left\{\tilde{A}^* \bar{Y}\left(\tilde{F}_\nu, \tilde{F}_r\right)\right\}, \tag{1.21}$$

where

$$\varepsilon_H \triangleq \frac{1}{MN} \sum_{m=0}^{M-1} \sum_{n=0}^{N-1} \left|\hat{H}_{m,n}\right|^2 \tag{1.22}$$

and

$$\bar{Y}\left(\tilde{F}_\nu, \tilde{F}_r\right) \triangleq \frac{1}{MN} \sum_{m=0}^{M-1} \sum_{n=0}^{N-1} \hat{H}_{m,n} \exp\Big(-j2\pi m\tilde{F}_\nu\Big) \exp\Big(j2\pi n\tilde{F}_r\Big). \tag{1.23}$$

It is important to note that:

1) The metric $\varepsilon(\tilde{F}_\nu, \tilde{F}_r, \tilde{A})$ is really optimal in the ML sense, if a PSK constellation is adopted for the channel symbols $\{s_m(n)\}$, so that, as already pointed out in the previous section, an AWGN model can be adopted for the noise sequence $\{\bar{W}_m(n); n = 0, 1, ..., N-1\}$ (see (1.15)). On the contrary, if a Quadrature Amplitude Modulation (QAM) constellation is selected, the samples of that sequence are not identically distributed, having, in general, different variances (e.g., see [14]); consequently, in the last case, the ML metric can still be

[4]It is not difficult to show that, if an arbitrary constellation is selected for the transmitted channel symbols, the optimal metric to be adopted in (1.16) can be still put in a form similar to (1.17), the only difference being represented by the fact that $\varepsilon_{m,n}(\tilde{F}_\nu, \tilde{F}_r, \tilde{A})$ is multiplied by $|s_m(n)|^2$.

put in a form similar to that expressed by (1.17), but its terms $\{\varepsilon_{m,n}(\tilde{F}_\nu, \tilde{F}_r, \tilde{A})\}$ cannot be uniformly weighted, being affected by different noise levels.

2) From (1.21) it is easily inferred that the optimization problem (1.16) does not admit a closed-form solution because of the nonlinear dependence of the metric $\varepsilon(\tilde{F}_\nu, \tilde{F}_r, \tilde{A})$ (1.21) on $\tilde{F}_\nu$ and $\tilde{F}_r$.

The approach we pursued in developing an approximate (but accurate) solution to (1.16) is based on:

a) Expressing the dependence of the function $\varepsilon(\tilde{F}_\nu, \tilde{F}_r, \tilde{A})$ on the variables $\tilde{F}_\nu$ and $\tilde{F}_r$ through the couples $(F_{\nu,c}\,, \tilde{\delta}_\nu)$ and $(F_{r,c}\,, \tilde{\delta}_r)$ such that

$$\tilde{F}_\nu = F_{\nu,c} + \tilde{\delta}_\nu\, \bar{F}_\nu \tag{1.24}$$

and

$$\tilde{F}_r = F_{r,c} + \tilde{\delta}_r\, \bar{F}_r. \tag{1.25}$$

Here, $F_{\nu,c}$ ($F_{r,c}$) represents a *coarse estimate* of F_ν (F_r), $\tilde{\delta}_\nu$ and $\tilde{\delta}_r$ are real variables called *residuals*[5]. Moreover, $\bar{F}_\nu \triangleq 1/M_0$ and $\bar{F}_r \triangleq 1/N_0$ are the *normalized fundamental Doppler frequency* and the *normalized fundamental delay*, respectively, characterizing the order (M_0, N_0) DSFT

$$\bar{\mathbf{Y}}_{0,0} \triangleq \left[\bar{Y}_{0,0}[l,p]\right] \tag{1.26}$$

of the zero padded version[6]

$$\hat{\mathbf{H}}_{0,0}^{(\mathrm{ZP})} \triangleq \begin{bmatrix} \hat{\mathbf{H}}_{0,0} & \mathbf{0}_{M,N_0-N} \\ \mathbf{0}_{M_0-M,\,N} & \mathbf{0}_{M_0-M,N_0-N} \end{bmatrix} \tag{1.27}$$

of the $M \times N$ matrix

$$\hat{\mathbf{H}}_{0,0} \triangleq [\hat{H}_{m,n}] \tag{1.28}$$

collecting all the elements of the sequence $\{\hat{H}_{m,n}\}$; moreover, in (1.27),

$$M_0 \triangleq L_\nu\, M \tag{1.29}$$

and

$$N_0 \triangleq L_r\, N, \tag{1.30}$$

denote the number of rows and columns, respectively, of the matrix $\hat{\mathbf{H}}_{0,0}^{(\mathrm{ZP})}$ (1.27), with L_ν and L_r being positive integers dubbed *oversampling factors*. Note that the element (l,p) of $\bar{\mathbf{Y}}_{0,0}$ (1.26) is defined as

$$\bar{Y}_{0,0}\,[l,p] \triangleq \frac{1}{M_0 N_0} \sum_{m=0}^{M-1} \sum_{n=0}^{N-1} \hat{H}_{m,n}\, \exp\Big(-j2\pi ml\bar{F}_\nu\Big)\, \exp\Big(j2\pi np\bar{F}_r\Big), \tag{1.31}$$

with $l = 0, 1, ..., M_0 - 1$ and $p = 0, 1, ..., N_0 - 1$.

[5]The decomposition of an unknown frequency into the sum of a multiple of a given *fundamental frequency* and a *frequency residual* is commonly adopted in the technical literature concerning ML frequency estimation (e.g., see [15] and references therein).

[6]Note that the following definition represents a specific case of the matrix $\hat{\mathbf{H}}_{k_1,k_2}^{(\mathrm{ZP})}$ defined right after (1.39) (in particular, its corresponds to the choice $k_1 = k_2 = 0$).

b) Assuming that the residuals $\tilde{\delta}_\nu$ and $\tilde{\delta}_r$ (appearing in the RHS of (1.24) and (1.25), respectively) are small, so that Taylor series

$$\exp\big(j\tilde{X}\big) = \sum_{k=0}^{\infty} \frac{j^k \tilde{X}^k}{k!}, \tag{1.32}$$

truncated to its first four terms (i.e., to the terms associated with $k = 0, 1, 2$ and 3) can be employed to accurately approximate the dependence of the function $\varepsilon(\tilde{F}_\nu, \tilde{F}_r, \tilde{A})$ (1.21) on these variables.

c) Exploiting an iterative method, known as *alternating minimization* (AM; e.g., see [16]) to minimize the approximate expression derived for $\varepsilon(\tilde{F}_\nu, \tilde{F}_r, \tilde{A})$; this allows us to transform the Three-Dimensional (3D) optimization (1.16) into a triplet of interconnected 1D problems, each referring to a single parameter and, consequently, much easier to solve than the original ML problem.

Let us show now how these principles can be put into practice. First of all, the exploitation of AM requires solving the following three sub-problems:

P1) minimizing $\varepsilon(\tilde{F}_\nu, \tilde{F}_r, \tilde{A})$ with respect to $\tilde{A}$, given $\tilde{F}_\nu = \hat{F}_\nu$ and $\tilde{F}_r = \hat{F}_r$;

P2) minimizing $\varepsilon(\tilde{F}_\nu, \tilde{F}_r, \tilde{A})$ with respect to $\tilde{F}_\nu$, given $\tilde{A} = \hat{A}$ and $\tilde{F}_r = \hat{F}_r$;

P3) minimizing $\varepsilon(\tilde{F}_\nu, \tilde{F}_r, \tilde{A})$ with respect to $\tilde{F}_r$, given $\tilde{A} = \hat{A}$ and $\tilde{F}_\nu = \hat{F}_\nu$.

The first sub-problem can be solved exactly thanks to the polynomial dependence of the cost function $\varepsilon(\tilde{F}_\nu, \tilde{F}_r, \tilde{A})$ (1.21) on the variable $\tilde{A}$. In fact, the function $\varepsilon(\hat{F}_\nu, \hat{F}_r, \tilde{A})$ is minimized with respect to $\tilde{A}$ if[7]

$$\tilde{A} = \hat{A} = \bar{Y}\Big(\hat{F}_\nu, \hat{F}_r\Big), \tag{1.33}$$

where $\bar{Y}(\hat{F}_\nu, \hat{F}_r)$ can be computed exactly through its expression (1.23) or, in an approximate fashion, through a computationally efficient procedure based on the fact that the matrix

$$\bar{\mathbf{Y}}_s \triangleq L_\nu \, L_r \, \bar{\mathbf{Y}}_{0,0} \tag{1.34}$$

collects $M_0 \times N_0$ uniformly spaced samples of the function $\bar{Y}(\tilde{F}_\nu, \tilde{F}_r)$, since $\bar{Y}_{0,0}[l, p] = \bar{Y}(l\bar{F}_\nu, \, p\bar{F}_r)/(L_\nu \, L_r)$ (see (1.23), (1.29)-(1.31)). For this reason, if one of the normalized frequencies $\hat{F}_\nu$ and $\hat{F}_r$ or both of them are not a multiple of $\bar{F}_\nu$ and $\bar{F}_r$, respectively, an approximate evaluation of $\bar{Y}(\hat{F}_\nu, \hat{F}_r)$ can be accomplished by *interpolating*[8] the elements of the matrix $\bar{\mathbf{Y}}_s$ (1.34). Note also that the last matrix can be efficiently computed by performing an order N_0 Inverse Fast Fourier Transform (IFFT) along the rows of $\hat{\mathbf{H}}_{0,0}^{(\mathrm{ZP})}$ (1.27), followed by an order M_0 Fast Fourier Transform (FFT) along the columns of the resulting matrix.

Let us take into consideration now **P2** and **P3**. Such sub-problems, unlike the previous one, do not admit closed form solutions. However, approximate solutions can be developed

[7] This represents a straightforward generalization of a mathematical result which is well known in 1D ML frequency estimation (e.g., see [17, Sec. IV]).

[8] See [18] for *polynomial interpolation* and [19] for *barycentric interpolation*.

by: 1) representing the parameters F_ν and F_r in the same form as $\tilde{F}_\nu$ (1.24) and $\tilde{F}_r$ (1.25), respectively, i.e., as $F_\nu = F_{\nu,c} + \delta_\nu \bar{F}_\nu$ and $F_r = F_{r,c} + \delta_r \bar{F}_r$, respectively; 2) using the 2D *periodogram method* to estimate $F_{\nu,c}$ and $F_{r,c}$; 3) devising a novel algorithm for estimating the residuals δ_ν and δ_r, i.e., for accomplishing the *fine estimation* of F_ν and F_r, respectively. The fine estimation algorithm is derived as follows. Based on the representations (1.24) and (1.25) of the trial variables $\tilde{F}_\nu$ and $\tilde{F}_r$, respectively, the variables $\tilde{\varphi}_m$ and $\tilde{\phi}_n$ defined right after (1.20) are expressed as $\tilde{\varphi}_m = 2\pi m\, F_{\nu,c} + m\tilde{\Omega}$ and $\tilde{\phi}_n = 2\pi n\, F_{r,c} + n\tilde{\Delta}$, respectively; here, $\tilde{\Omega} \triangleq 2\pi\tilde{\delta}_\nu \bar{F}_\nu$ and $\tilde{\Delta} \triangleq 2\pi\tilde{\delta}_r \bar{F}_r$. Then, the following steps are accomplished: 1) the new expressions of $\tilde{\varphi}_m$ and $\tilde{\phi}_n$ are substituted in the RHS of (1.20); 2) the resulting expression is substituted in the RHS of (1.17) and the approximation (1.32) is adopted for $\exp(jm\tilde{\Omega})$ and $\exp(jn\tilde{\Delta})$ under the assumption that both $\tilde{\Omega}$ and $\tilde{\Delta}$ are small enough[9]. This yields, after some manipulation, the approximate expression

$$\varepsilon_{\text{CSFDE}}\left(\tilde{\Omega}, \tilde{\Delta}, \hat{A}\right) \triangleq \varepsilon_H + \left|\hat{A}\right|^2 - 2\xi\left(\tilde{\Omega}, \tilde{\Delta}, \hat{A}\right) \tag{1.35}$$

for the function $\varepsilon(\tilde{F}_\nu, \tilde{F}_r, \tilde{A})$ (1.17); here,

$$\xi\left(\tilde{\Omega}, \tilde{\Delta}, \hat{A}\right) = \sum_{p=0}^{3}\sum_{q=0}^{3} (-1)^{(p+q)} \frac{\tilde{\Omega}^p\, \tilde{\Delta}^q}{p!q!} \Re\left\{ j^{(p-q)}\, \hat{A}^*\, \bar{Y}_{p,q} \right\}, \tag{1.36}$$

$$\bar{Y}_{k_1,k_2}(\rho_\nu, \rho_r) \triangleq \frac{1}{MN} \sum_{m=0}^{M-1}\sum_{n=0}^{N-1} \hat{H}_{m,n}^{(k_1,k_2)} \exp\left(j\frac{2\pi n\rho_r}{N_0}\right) \exp\left(-j\frac{2\pi m\rho_\nu}{M_0}\right), \tag{1.37}$$

$\rho_\nu \triangleq F_{\nu,c}/\bar{F}_\nu$, $\rho_r \triangleq F_{r,c}/\bar{F}_r$ and

$$\hat{H}_{m,n}^{(k_1,k_2)} \triangleq m^{k_1} n^{k_2} \hat{H}_{m,n}, \tag{1.38}$$

with $m = 0, 1, ..., M-1$ and $n = 0, 1, ..., N-1$.

It is important to point out that:

a) if both ρ_ν and ρ_r are integers, the quantity $\bar{Y}_{k_1,k_2}(\rho_\nu, \rho_r)$ (1.37) represents the (ρ_ν, ρ_r)th element of the $M_0 \times N_0$ matrix

$$\bar{\mathbf{Y}}_{k_1,k_2} \triangleq \text{DSFT}_{M_0,N_0}\left[\hat{\mathbf{H}}_{k_1,k_2}^{(\text{ZP})}\right] \tag{1.39}$$

generated by the order (M_0, N_0) DSFT of the zero padded version of the $M \times N$ matrix[10]

$$\hat{\mathbf{H}}_{k_1,k_2} \triangleq [\hat{H}_{m,n}^{(k_1,k_2)}]; \tag{1.40}$$

b) if the previous condition is not met, the quantity $\bar{Y}_{k_1,k_2}(\rho_\nu, \rho_r)$ can be evaluated exactly on the basis of (1.37) or, in an approximate fashion, by interpolating multiple adjacent elements of the matrix $L_\nu\, L_r\, \bar{\mathbf{Y}}_{k_1,k_2}$ (see (1.39)).

[9] This is equivalent to assuming that $1/M_0$ and $1/N_0$ are small enough (i.e., that M_0 and N_0 are large enough).

[10] Note that $\hat{\mathbf{H}}_{k_1,k_2}^{(\text{ZP})}$ has the same structure as $\hat{\mathbf{H}}_{0,0}^{(\text{ZP})}$ (1.27), the only difference being represented by the fact that, in its definition, $\hat{\mathbf{H}}_{0,0}$ (1.28) is replaced by $\hat{\mathbf{H}}_{k_1,k_2}$ (1.40).

Minimizing $\varepsilon_{\mathrm{CSFDE}}(\tilde{\Omega}, \tilde{\Delta}, \hat{A})$ (1.35) is equivalent to maximizing the function $\xi(\tilde{\Omega}, \tilde{\Delta}, \hat{A})$ (1.36). The last function can be easily maximized with respect to the variable $\tilde{\Omega}$ ($\tilde{\Delta}$) if $\tilde{\Delta}$ ($\tilde{\Omega}$) is known.

Therefore, given $\tilde{\Delta} = \hat{\Delta}$, the estimate $\hat{\delta}_\nu \triangleq \hat{\Omega}/(2\pi\bar{F}_\nu)$ of δ_ν can be evaluated by taking the derivative of $\xi(\tilde{\Omega}, \hat{\Delta}, \hat{A})$ with respect to $\tilde{\Omega}$ and setting it to zero. In fact, this leads to the estimate[11]

$$\hat{X} = \frac{-b_X + \sqrt{b_X^2 - 4\,a_X\,c_X}}{2\,a_X}, \tag{1.41}$$

that represents one of the two solutions of the quadratic equation

$$a_X\,\tilde{X}^2 + b_X\,\tilde{X} + c_X = 0, \tag{1.42}$$

with $X = \Omega$; here,

$$a_\Omega = -\hat{\Delta}^3\,\Re\left\{\hat{A}^*\bar{Y}_{3,3}\right\}/6 - \hat{\Delta}^2\,\Im\left\{\hat{A}^*\bar{Y}_{3,2}\right\}/2 + \hat{\Delta}\,\Re\left\{\hat{A}^*\bar{Y}_{3,1}\right\} + \Im\left\{\hat{A}^*\bar{Y}_{3,0}\right\}, \tag{1.43}$$

$$b_\Omega = \hat{\Delta}^3\,\Im\left\{\hat{A}^*\bar{Y}_{2,3}\right\}/3 - \hat{\Delta}^2\,\Re\left\{\hat{A}^*\bar{Y}_{2,2}\right\} - 2\hat{\Delta}\,\Im\left\{\hat{A}^*\bar{Y}_{2,1}\right\} + 2\Re\left\{\hat{A}^*\bar{Y}_{2,0}\right\}, \tag{1.44}$$

$$c_\Omega = \hat{\Delta}^3\,\Re\left\{\hat{A}^*\bar{Y}_{1,3}\right\}/3 + \hat{\Delta}^2\,\Im\left\{\hat{A}^*\bar{Y}_{1,2}\right\} - 2\hat{\Delta}\,\Re\left\{\hat{A}^*\bar{Y}_{1,1}\right\} - 2\Im\left\{\hat{A}^*\bar{Y}_{1,0}\right\}. \tag{1.45}$$

A simpler estimate (denoted $\hat{\Omega}'$) of Ω is obtained neglecting the contribution of the quadratic term in the Left-Hand Side (LHS) of (1.42), i.e., setting $a_\Omega = 0$. This leads to a first-degree equation, whose solution is (with $X = \Omega$)

$$\hat{X}' = -c_X/b_X. \tag{1.46}$$

Dually, given $\tilde{\Omega} = \hat{\Omega}$, an estimate $\hat{\delta}_r \triangleq \hat{\Delta}/(2\pi\bar{F}_r)$ of $\tilde{\delta}_r$ is computed by taking the derivative of $\xi(\hat{\Omega}, \tilde{\Delta}, \hat{A})$ with respect to $\tilde{\Delta}$ and setting it to zero. This leads to a quadratic equation in the variable $\tilde{\Delta}$ whose structure is still expressed by (1.42) (with $X = \Delta$); however, its coefficients are

$$a_\Delta = -\hat{\Omega}^3\,\Re\left\{\hat{A}^*\bar{Y}_{3,3}\right\}/6 + \hat{\Omega}^2\,\Im\left\{\hat{A}^*\bar{Y}_{2,3}\right\}/2 + \hat{\Omega}\,\Re\left\{\hat{A}^*\bar{Y}_{1,3}\right\} - \Im\left\{\hat{A}^*\bar{Y}_{0,3}\right\}, \tag{1.47}$$

$$b_\Delta = -\hat{\Omega}^3\,\Im\left\{\hat{A}^*\bar{Y}_{3,2}\right\}/3 - \hat{\Omega}^2\,\Re\left\{\hat{A}^*\bar{Y}_{2,2}\right\} + 2\hat{\Omega}\,\Im\left\{\hat{A}^*\bar{Y}_{1,2}\right\} + 2\Re\left\{\hat{A}^*\bar{Y}_{0,2}\right\}, \tag{1.48}$$

$$c_\Delta = \hat{\Omega}^3\,\Re\left\{\hat{A}^*\bar{Y}_{3,1}\right\}/3 - \hat{\Omega}^2\,\Im\left\{\hat{A}^*\bar{Y}_{2,1}\right\} - 2\hat{\Omega}\,\Re\left\{\hat{A}^*\bar{Y}_{1,1}\right\} + 2\Im\left\{\hat{A}^*\bar{Y}_{0,1}\right\}. \tag{1.49}$$

For this reason, the estimates $\hat{\Delta}$ and $\hat{\Delta}'$ of Δ can be computed on the basis of (1.41) and (1.46), respectively.

The previous mathematical results allow us to easily develop an AM-based procedure for estimating the parameters F_ν, F_r and A in an iterative fashion. This procedure, dubbed CSFDE, is initialized by computing:

[11] In the following equations, the dependence of the function $\bar{Y}_{k_1,k_2}(\rho_\nu, \rho_r)$ (1.37) and of the coefficients $\{a_X,\, b_X,\, c_X\}$ on (ρ_ν, ρ_r) is not explicitly specified to ease reading.

1) the set collecting the $M_0 \times N_0$ matrices[12] $\{\bar{\mathbf{Y}}_{k_1,k_2}; k_1,\, k_2 = 0,1,2,3\}$ (see (1.39));

2) the coarse estimates $\hat{F}_{\nu,c}^{(0)} = \hat{l}\,\bar{F}_\nu - 1/2$ and $\hat{F}_{r,c}^{(0)} = \hat{p}\bar{F}_r$ of F_ν and F_r, respectively, where

$$\left(\hat{l},\hat{p}\right) = \arg \max_{\tilde{l}\in\mathcal{S}_{M_0},\tilde{p}\in\mathcal{S}_{N_0}} \left|\bar{Y}_{0,0}\left[\tilde{l},\tilde{p}\right]\right|^2 \tag{1.50}$$

and $\mathcal{S}_X \triangleq \{0,1,...,X-1\}$ for any positive integer X;

3) the initial estimate $\hat{A}^{(0)}$ of $\tilde{A}$ on the basis of (1.33), with $(\hat{F}_\nu, \hat{F}_r) = (\hat{F}_{\nu,c}^{(0)}, \hat{F}_{r,c}^{(0)})$;

4) the coefficients $\{a_\Omega,\, b_\Omega,\, c_\Omega\}$ ($\{a_\Delta,\, b_\Delta,\, c_\Delta\}$) for $(\rho_\nu,\rho_r) = (\hat{l}^{(0)},\hat{p}^{(0)})$ according to (1.44)-(1.45) ((1.47)-(1.49));

5) the initial estimate $\hat{\Omega}^{(0)}(\hat{\Delta}^{(0)})$ of Ω (Δ) on the basis of (1.41) or (1.46) with $X = \Omega$ (with $X = \Delta$);

6) the initial fine estimates (see (1.24) and (1.25))

$$\hat{F}_\nu^{(0)} = \hat{F}_{\nu,c}^{(0)} + \hat{\Omega}^{(0)}/(2\pi) \tag{1.51}$$

and

$$\hat{F}_r^{(0)} = \hat{F}_{r,c}^{(0)} + \hat{\Delta}^{(0)}/(2\pi) \tag{1.52}$$

of F_ν and F_r, respectively.

Finally, we set the iteration index i to 1 and start an iterative procedure. The ith iteration is fed by the estimates $\hat{F}_\nu^{(i-1)}$, $\hat{F}_r^{(i-1)}$ and $\hat{A}^{(i-1)}$ of F_ν, F_r and A, respectively, and produces the new estimates $\hat{F}_\nu^{(i)}$, $\hat{F}_r^{(i)}$ and $\hat{A}^{(i)}$ of the same quantities (with $i = 1,2,...,N_{\rm it}$, where $N_{\rm it}$ is the overall number of iterations). The procedure adopted for the evaluation of $\hat{F}_\nu^{(i)}$, $\hat{F}_r^{(i)}$ and $\hat{A}^{(i)}$ consists of the two steps described below.

1) *Estimation of the normalized Doppler and the normalized delay* - The new estimates $\hat{\Omega}^{(i)}$ and $\hat{\Delta}^{(i)}$ of $\tilde{\Omega}$ and $\tilde{\Delta}$, respectively, are computed according to (1.41) or (1.46). In the evaluation of the coefficients of these equations, $\hat{A} = \hat{A}^{(i-1)}$,

$$\rho_\nu = \hat{\rho}_\nu^{(i-1)} = \hat{F}_\nu^{(i-1)}/\bar{F}_\nu \tag{1.53}$$

and

$$\rho_r = \hat{\rho}_r^{(i-1)} = \hat{F}_r^{(i-1)}/\bar{F}_r \tag{1.54}$$

are assumed. Then,

$$\hat{F}_\nu^{(i)} = \hat{F}_\nu^{(i-1)} + \hat{\Omega}^{(i)}/(2\pi) \tag{1.55}$$

and

$$\hat{F}_r^{(i)} = \hat{F}_r^{(i-1)} + \hat{\Delta}^{(i)}/(2\pi) \tag{1.56}$$

are computed.

[12]Note that the matrices $\{\bar{\mathbf{Y}}_{k_1,k_2}\}$ corresponding to $(k_1,k_2) = (0,3)$, $(3,0)$ and $(3,3)$ are not required if the simpler estimates $\hat{\Omega}'$ and $\hat{\Delta}'$ are evaluated.

2) *Estimation of the complex amplitude* - The new estimate $\hat{A}^{(i)}$ of $\hat{A}$ is evaluated by means of (1.33); in doing so, $\hat{F}_\nu = \hat{F}_\nu^{(i)}$ and $\hat{F}_r = \hat{F}_r^{(i)}$ are assumed.

The index i is incremented by one before starting the next iteration. At the end of the last (i.e., of the $N_{\rm it}$th) iteration, the fine estimates $\hat{F}_\nu = \hat{F}_\nu^{(N_{\rm it})}$, $\hat{F}_r = \hat{F}_r^{(N_{\rm it})}$ and $\hat{A} = \hat{A}^{(N_{\rm it})}$ of F_ν, F_r and A, respectively, become available. The CSFDE algorithm is summarized in Algorithm 1.

Algorithm 1: Complex Single Frequency-Delay Estimation (CSFDE)

Input: The matrices $\{\mathbf{Y}_{k_1,k_2}; k_1, k_2 = 0, 1, 2 \text{ and } 3\}$ (see (1.39)) and the value of the parameter $N_{\rm it}$.

1 **Initialization:**

a- Evaluate $\bar{\mathbf{Y}}_{0,0}$ (1.26), $\hat{l}$ and $\hat{p}$ (see (1.50)); then, compute the initial estimate $\hat{A}^{(0)}$ of A according to (1.33) and set $(\rho_\nu^{(0)}, \rho_r^{(0)}) = (\hat{l}, \hat{p})$ (see (1.53)-(1.54)).

b- Compute the coefficients a_Ω, b_Ω and c_Ω according to (1.43)-(1.45); then, evaluate $\hat{\Omega}^{(0)}$ according to (1.41) or (1.46).

c- Evaluate the coefficients a_Δ, b_Δ and c_Δ according to (1.47)-(1.49); then, compute $\hat{\Delta}^{(0)}$ according to (1.41) or (1.46).

d- Compute $\hat{F}_\nu^{(0)}$ and $\hat{F}_r^{(0)}$ according to (1.51) and (1.52), respectively.

2 **Refinement: for** $i = 1$ *to* $N_{\rm it}$ **do**

e- *Estimation of* A: Set $\hat{F}_\nu = \hat{F}_\nu^{(i-1)}$ and $\hat{F}_r = \hat{F}_r^{(i-1)}$; then, evaluate $\bar{Y}(\hat{F}_\nu, \hat{F}_r)$ using (1.23) or by interpolating a few adjacent elements of the matrix $\bar{\mathbf{Y}}_s$ (1.34). Finally, compute $\hat{A}^{(i)}$, $\hat{\rho}_\nu^{(i-1)}$ and $\hat{\rho}_r^{(i-1)}$ according to (1.33), (1.53) and (1.54), respectively.

f- *Estimation of* F_ν: Set $\hat{A} = \hat{A}^{(i)}$ and compute $\bar{Y}_{k_1,k_2}(\hat{\rho}_\nu^{(i-1)}, \hat{\rho}_r^{(i-1)})$ according to (1.37) or by interpolating a few adjacent elements of $\bar{\mathbf{Y}}_{k_1,k_2}$ (1.39); then, compute a_Ω, b_Ω and c_Ω according to (1.43)-(1.45) assuming $(\rho_\nu, \rho_r) = (\hat{\rho}_\nu^{(i-1)}, \hat{\rho}_r^{(i-1)})$. Finally, compute $\hat{\Omega}^{(i)}$ and $\hat{F}_\nu^{(i)}$ according to (1.41) (or (1.46)) and (1.55), respectively.

g- *Estimation of* F_r: Compute $a_{\tilde{\Delta}}$, $b_{\tilde{\Delta}}$ and $c_{\tilde{\Delta}}$ according to (1.47)-(1.49) under the assumption that $(\rho_\nu, \rho_r) = (\hat{\rho}_\nu^{(i-1)}, \hat{\rho}_r^{(i-1)})$; then, evaluate $\hat{\Delta}^{(i)}$ and $\hat{F}_r^{(i)}$ on the basis of (1.41) (or (1.46)) and (1.56), respectively.

end

Output: The estimates $\hat{F}_\nu^{(N_{\rm it})}$, $\hat{F}_r^{(N_{\rm it})}$ and $\hat{A}^{(N_{\rm it})}$ of F_ν, F_r and A, respectively.

It is worth pointing out that:

1) the initial coarse estimates $\hat{F}_{\nu,c}^{(0)}$ (1.51) and $\hat{F}_{r,c}^{(0)}$ (1.52) are computed by resorting to the 2D *periodogram method* (see (1.50));

2) unlike traditional DFT-based methods, the CSFDE algorithm requires the evaluation of multiple DSFTs and, more precisely, of 16 (13) DSFTs $\{\bar{\mathbf{Y}}_{k_1,k_2}\}$ if (1.41) ((1.46)) is employed in the evaluation of the estimates of Ω and Δ;

3) the approximate ML metric $\varepsilon_{\rm CSFDE}(\tilde{\Omega}, \tilde{\Delta}, \hat{A})$ (1.35) on which the CSFDE algorithm is based is new;

4) the estimates $\hat{\delta}_{\nu}^{(i)}$ ($\hat{\delta}_{r}^{(i)}$) of δ_{ν} (δ_r) computed by the CSFDE algorithm in its ith iteration are expected to become smaller as i increases, since $\hat{F}_{\nu}^{(i)}$ ($\hat{F}_{r}^{(i)}$) should progressively approach F_{ν} (F_r) if this algorithm converges.

1.3.2 Estimation of multiple two-dimensional tones

Let us show now how the CSFDE algorithm can be exploited to recursively estimate the multiple tones forming the useful component of the complex sequence $\{\hat{H}_{m,n}\}$, whose (m,n)th element is expressed by (1.14), where K is assumed to be greater than unity and *unknown*. The method we develop to achieve this objective is called Complex Single Frequency-Delay Estimation and Cancellation (CSFDEC) and is based on the idea of 1) separating the contribution of the first (and strongest tone) in the RHS of (1.14) from that of the remaining $(K-1)$ tones and 2) considering the latter contribution as part of the overall noise affecting the former one. Based on this representation of $\{\hat{H}_{m,n}\}$, an estimate of the parameters $(A_0, F_{\nu_0}, F_{r_0})$ can be evaluated through the CSFDE and can be employed to subtract the contribution of the first tone to $\{\hat{H}_{m,n}\}$, so generating a residual measurement. This estimation & cancellation procedure is repeated to recursively estimate the other tones on the basis of the computed residuals until the energy of the last residual falls below a given threshold; this generates, as a by-product, an estimate of K. Moreover, in the CSFDEC method, after detecting a new tone and estimating its parameters, a *re-estimation* technique is executed to improve the accuracy of both this tone and the previously estimated tones.

The CSFDEC algorithm is initialized by: 1) running the CSFDE algorithm to compute the initial estimates $\hat{F}_{\nu_0}^{(0)}$, $\hat{F}_{r_0}^{(0)}$ and $\hat{A}_0^{(0)}$ of the parameters F_{ν_0}, F_{r_0} and A_0 characterizing the first target; 2) setting the recursion index i to 1 and $\bar{\mathbf{Y}}_{0,0}^{(0)} = \bar{\mathbf{Y}}_{0,0}$ (see (1.26)). Then, a recursive procedure is started. The ith recursion of this procedure is fed by the vectors $\hat{\mathbf{F}}_{\nu}^{(i-1)} = [\hat{F}_{\nu_0}^{(i-1)}, \hat{F}_{\nu_1}^{(i-1)}, ..., \hat{F}_{\nu_{i-1}}^{(i-1)}]^T$, $\hat{\mathbf{F}}_{r}^{(i-1)} = [\hat{F}_{r_0}^{(i-1)}, \hat{F}_{r_1}^{(i-1)}, ..., \hat{F}_{r_{i-1}}^{(i-1)}]^T$ and $\hat{\mathbf{A}}^{(i-1)} = [\hat{A}_0^{(i-1)}, \hat{A}_1^{(i-1)}, ..., \hat{A}_{i-1}^{(i-1)}]^T$, collecting the estimates of the normalized Doppler frequency, normalized delay and complex amplitude, respectively, of the i tones detected and estimated in the previous recursions, and generates the new vectors $\hat{\mathbf{F}}_{\nu}^{(i)}$, $\hat{\mathbf{F}}_{r}^{(i)}$ and $\hat{\mathbf{A}}^{(i)}$ after: a) estimating the parameters $\hat{F}_{\nu_i}^{(i)}$, $\hat{F}_{r_i}^{(i)}$ and $\hat{A}_i^{(i)}$ of the new (i.e., of the ith) tone (if any); b) refining the estimates of the i tones available at the beginning of the considered recursion. The procedure employed for accomplishing all this consists of the three steps described below (the pth step is denoted CSFDE-Sp, with $p = 1$, 2 and 3)

CSFDEC-S1 (*spectral cancellation and estimation of a new tone*) - In this step, the following quantities are evaluated (see the initialization part of the CSFDE algorithm):

a) The *residual spectrum*

$$\mathbf{Y}_{0,0}^{(i)} = \left[\bar{Y}_{0,0}^{(i)}[l,p]\right] \triangleq \mathbf{Y}_{0,0}^{(i-1)} - \mathbf{C}_{0,0}^{(i)}\big(\hat{\mathbf{A}}^{(i-1)}, \hat{\mathbf{F}}_{\nu}^{(i-1)}, \hat{\mathbf{F}}_{r}^{(i-1)}\big), \tag{1.57}$$

where

$$\mathbf{C}_{0,0}^{(i)}\big(\hat{\mathbf{A}}^{(i-1)}, \hat{\mathbf{F}}_{\nu}^{(i-1)}, \hat{\mathbf{F}}_{r}^{(i-1)}\big) \triangleq \sum_{k=0}^{i-1} \bar{\mathbf{C}}_{0,0}\big(\hat{A}_k^{(i-1)}, \hat{F}_{\nu_k}^{(i-1)}, \hat{F}_{r_k}^{(i-1)}\big) \tag{1.58}$$

represents the contribution given by all the ith estimated 2D tones to $\bar{\mathbf{Y}}_{0,0}$ and $\bar{\mathbf{C}}_{0,0}(\hat{A}_k^{(i-1)}, \hat{F}_{\nu_k}^{(i-1)}, \hat{F}_{r_k}^{(i-1)})$ is the contribution provided by the kth tone (with $k = 0, 1, ..., i-1$) to the same matrix (the expression of the elements of the matrix $\bar{\mathbf{C}}_{0,0}(\cdot,\cdot,\cdot)$ is derived in Appendix A.1.1; see Eq. (A.2)). If the overall energy $\varepsilon_{0,0}[i] \triangleq \|\mathbf{Y}_{0,0}^{(i)}\|^2$ of the vector $\mathbf{Y}_{0,0}^{(i)}$ (1.57) satisfies the inequality $\varepsilon_{0,0}[i] < T_{\text{CSFDEC}}$, where T_{CSFDEC} is a proper threshold, the algorithm stops and the estimate $\hat{K} = i$ of K is generated.

b) The couple of integers $(\hat{l}^{(i)}, \hat{p}^{(i)})$ on the basis of (1.50) (where, however, $\bar{Y}_{0,0}[\tilde{l}, \tilde{p}]$ is replaced by $\bar{Y}_{0,0}^{(i)}[\tilde{l}, \tilde{p}]$) and the coarse estimates $\hat{F}_{\nu,c_i}^{(i)} = \hat{l}^{(i)}\bar{F}_\nu - 1/2$ and $\hat{F}_{r,c_i}^{(i)} = \hat{p}^{(i)}\bar{F}_r$ of $F_{\nu,c}$ and $F_{r,c}$, respectively.

c) The preliminary estimate (see (1.33))

$$\bar{A}_i^{(i)} = \bar{Y}(\hat{F}_{\nu,c_i}^{(i)}, \hat{F}_{r,c_i}^{(i)}) - \breve{Y}_{0,0}\left(\hat{F}_{\nu,c_i}^{(i)}, \hat{F}_{r,c_i}^{(i)}; \hat{\mathbf{A}}^{(i-1)}, \hat{\mathbf{F}}_\nu^{(i-1)}, \hat{\mathbf{F}}_r^{(i-1)}\right) \tag{1.59}$$

of the complex amplitude A_i; here,

$$\breve{Y}_{0,0}\left(\hat{F}_{\nu,c_i}^{(i)}, \hat{F}_{r,c_i}^{(i)}; \hat{\mathbf{A}}^{(i-1)}, \hat{\mathbf{F}}_\nu^{(i-1)}, \hat{\mathbf{F}}_r^{(i-1)}\right) \triangleq \sum_{k=0}^{i-1} \bar{Y}_{0,0}\left(\hat{F}_{\nu,c_i}^{(i)}, \hat{F}_{r,c_i}^{(i)}; \hat{A}_k^{(i-1)}, \hat{F}_{\nu_k}^{(i-1)}, \hat{F}_{r_k}^{(i-1)}\right) \tag{1.60}$$

is the contribution given to $\bar{Y}(\hat{F}_{\nu,c_i}^{(i)}, \hat{F}_{r,c_i}^{(i)})$ by the first i estimated tones for $(F_\nu, F_r) = (\hat{F}_{\nu,c_i}^{(i)}, \hat{F}_{r,c_i}^{(i)})$ and $\bar{Y}_{0,0}(\hat{F}_{\nu,c_i}^{(i)}, \hat{F}_{r,c_i}^{(i)}; \hat{A}_k^{(i-1)}, \hat{F}_{\nu_k}^{(i-1)}, \hat{F}_{r_k}^{(i-1)})$ represents the leakage due to the kth tone and affecting the ith tone. The expression of the quantity $\bar{Y}_{k_1,k_2}(\hat{F}_{\nu,c_i}^{(i)}, \hat{F}_{r,c_i}^{(i)}; \hat{A}_k^{(i-1)}, \hat{F}_{\nu_k}^{(i-1)}, \hat{F}_{r_k}^{(i-1)})$ is provided in Appendix A.1.2 (see (A.6)).

d) The spectral coefficients

$$\bar{Y}_{k_1,k_2}^{(i)}\left(\rho_\nu^{(i)}, \rho_r^{(i)}\right) = \bar{Y}_{k_1,k_2}\left(\rho_\nu^{(i)}, \rho_r^{(i)}\right) - \breve{Y}_{k_1,k_2}\left(\hat{F}_{\nu,c_i}^{(i)}, \hat{F}_{r,c_i}^{(i)}; \hat{\mathbf{A}}^{(i-1)}, \hat{\mathbf{F}}_\nu^{(i-1)}, \hat{\mathbf{F}}_r^{(i-1)}\right), \tag{1.61}$$

with $k_1, k_2 = 0, 1, 2, 3$; here, $\rho_\nu^{(i)} = \hat{F}_{\nu,c_i}^{(i)}/\bar{F}_\nu = \hat{l}^{(i)} - 1/(2\bar{F}_\nu)$ and $\rho_r^{(i)} = \hat{F}_{r,c_i}^{(i)}/\bar{F}_r = \hat{p}^{(i)}$ (see (1.53) and (1.54), respectively), whereas

$$\breve{Y}_{k_1,k_2}\left(\hat{F}_{\nu,c_i}^{(i)}, \hat{F}_{r,c_i}^{(i)}; \hat{\mathbf{A}}^{(i-1)}, \hat{\mathbf{F}}_\nu^{(i-1)}, \hat{\mathbf{F}}_r^{(i-1)}\right) \triangleq \sum_{k=0}^{i-1} \bar{Y}_{k_1,k_2}\left(\hat{F}_{\nu,c_i}^{(i)}, \hat{F}_{r,c_i}^{(i)}; \hat{A}_k^{(i-1)}, \hat{F}_{r_k}^{(i-1)}, \hat{F}_{\nu_k}^{(i-1)}\right) \tag{1.62}$$

represents the contribution given to $\bar{Y}_{k_1,k_2}^{(i)}(\rho_\nu^{(i)}, \rho_r^{(i)})$ by all the estimated tones (in particular, the term $\bar{Y}_{k_1,k_2}(\cdot,\cdot;\cdot,\cdot,\cdot)$ appearing in the RHS of (1.62) represents the leakage due to the kth estimated tone for $(F_\nu, F_r) = (\hat{F}_{\nu,c_i}^{(i)}, \hat{F}_{r,c_i}^{(i)})$).

e) The coefficients $\{a_\Omega, b_\Omega, c_\Omega\}$ ($\{a_\Delta, b_\Delta, c_\Delta\}$) on the basis of (1.43)-(1.45) ((1.47)-(1.49)) with $(\rho_\nu, \rho_r) = (\rho_\nu^{(i)}, \rho_r^{(i)})$ and the initial estimate of the residual $\hat{\Omega}_i^{(0)}(\hat{\Delta}_i^{(0)})$ of Ω (Δ) on the basis of (1.41) or (1.46) with $X = \Omega$ ($X = \Delta$).

f) The initial fine estimate of the normalized Doppler frequency $\hat{F}_{\nu_i}^{(0)} = \hat{F}_{\nu,c_i}^{(0)} + \hat{\Omega}_i^{(0)}/(2\pi)$ and that of the normalized delay $\hat{F}_{r_i}^{(0)} = \hat{F}_{r,c_i}^{(0)} + \hat{\Delta}_i^{(0)}/(2\pi)$ (see (1.24) and (1.25), respectively). The evaluation of $\hat{F}_\nu^{(0)}$ and $\hat{F}_r^{(0)}$ concludes the first step.

CSFDEC-S2 (*refinement of the last tone*) - In this step, $N_{\rm it}$ iterations are executed to refine the estimate of the parameters of the new tone detected in the previous step. The processing accomplished in this step follows closely that described in the refinement part (i.e., in the second step) of the CSFDE. For this reason, in each iteration, new estimates of the complex amplitude and of the two residuals are computed for the ith tone. This requires reusing (1.59)-(1.60) and (1.61)-(1.62) for the removal of spectral leakage. At the end of the last iteration, the estimates ($\check{F}_{\nu_i}^{(i)}$, $\check{F}_{r_i}^{(i)}$, $\check{A}_i^{(i)}$) of (F_{ν_i}, F_{r_i}, A_i) are available; these estimates represent ($\hat{F}_{\nu_i}^{(i)}$, $\hat{F}_{r_i}^{(i)}$, $\hat{A}_i^{(i)}$) if the next step is not accomplished (i.e., if tone re-estimation is avoided).

CSFDEC-S3 (*tone re-estimation*) - This step is fed by the $(i+1)$ normalized delays $\{\hat{F}_{r_0}^{(i-1)}$, $\hat{F}_{r_1}^{(i-1)}$, ...,$\hat{F}_{r_{i-1}}^{(i-1)}$, $\check{F}_{r_i}^{(i)}\}$, the normalized Doppler frequencies $\{\hat{F}_{\nu_0}^{(i-1)}$, $\hat{F}_{\nu_1}^{(i-1)}$, ...,$\hat{F}_{\nu_{i-1}}^{(i-1)}$, $\check{F}_{r_i}^{(i)}\}$ and the associated complex amplitudes $\{\hat{A}_0^{(i-1)}$, $\hat{A}_1^{(i-1)}$, ...,$\hat{A}_{i-1}^{(i-1)}$, $\check{A}_i^{(i)}\}$. It consists of repeating the previous step for each of the detected tones, starting from the first tone and ending with the last (i.e., with the $(i+1)$th) one. This means that, when re-estimating the kth tone, the leakage due to all the other $(i-1)$ tones is removed (with $k = 0, 1, ..., i$). This allows us to progressively refine the amplitude, normalized Doppler frequency and normalized delay of each tone, thus generating the final estimates. Note that, in principle, this re-estimation procedure can be repeated multiple (say, $N_{\rm REF}$) times.

1.3.3 Computational complexity of the proposed algorithms

The computational complexity, in terms of number of Floating Point Operations (FLOPs), can be assessed for both the CSFDE and the CSFDEC algorithms as follows[13]. First of all, the overall computational cost of the CSFDE is expressed as

$$\mathcal{C}_{\rm CSFDE} = \mathcal{C}_0({\rm CSFDE}) + N_{\rm it}\,\mathcal{C}_i({\rm CSFDE}), \tag{1.63}$$

where $\mathcal{C}_0$(CSFDE) ($\mathcal{C}_i$(CSFDE)) represents the computational cost of its initialization (each of its iterations). The cost $\mathcal{C}_0$(CSFDE) is evaluated by summing[14]:

1) the contribution due to the computation of the couple $(\hat{l}, \hat{p})$ on the basis of (1.50);

2) the contribution due to the computation of the matrices $\{\bar{\mathbf{Y}}_{k_1,k_2}\}$ on the basis of (1.39), including the evaluation of the spectrum $\bar{\mathbf{Y}}_{0,0}$ (1.26);

3) the contributions due to the evaluation of the estimates $\hat{\Omega}$ and $\hat{\Delta}$, respectively, on the basis of the quadratic equation (1.41).

The cost $\mathcal{C}_{i,{\rm CSFDE}}$, instead, is evaluated by summing:

1) the contribution due to the computation of $\bar{Y}(\hat{F}_\nu, \hat{F}_r)$ on the basis of (1.23) or of the interpolation of a few adjacent elements of the matrix $\bar{\mathbf{Y}}_s$ (1.34);

2) the contributions due to the evaluation of $\hat{\rho}_\nu$ ($\hat{\rho}_r$) on the basis of (1.53) ((1.54));

[13] The general criteria adopted in the evaluation of computational costs are summarized in [15, App. C].

[14] Note that the evaluation of the estimate of the tone complex amplitude is neglected, being based on (1.33), that requires a negligible computational effort.

3) the contribution due to the evaluation of $\hat{A}$ on the basis of (1.33);

4) the contribution due to the computation of the quantity $\bar{Y}_{k_1,k_2}(\hat{\rho}_\nu^{(i-1)}, \hat{\rho}_r^{(i-1)})$ (1.61) through the interpolation of a few adjacent elements of the matrix $L_\nu\, L_r\, \bar{\mathbf{Y}}_{k_1,k_2}$ (see (1.39)) for the considered values of (k_1, k_2);

5) the contributions due to the computation of $\hat{\Omega}$ and $\hat{\Delta}$ on the basis of (1.41). Based on these considerations and the mathematical results illustrated in Appendix A.1.3, it can be proved that $\mathcal{C}_{\text{CSFDE}} = \mathcal{O}(N_{\text{CSFDE}})$, where

$$N_{\text{CSFDE}} = 16\, M_0\, N_0 \log_2(M_0\, N_0) + N_{\text{it}}\, 16\, I_\nu\, I_r \tag{1.64}$$

and I_ν (I_r) is the interpolation order adopted in the Doppler (range) domain for the evaluation of $\bar{Y}_{k_1,k_2}(\hat{\rho}_\nu^{(i-1)}, \hat{\rho}_r^{(i-1)})$ (1.61). Note that, for small values of I_ν and I_r (e.g., if a 2D linear or barycentric interpolation is used; see [19]), the contribution of the second term of the RHS of the last equation can be neglected, so that the order of the whole computational cost is well approximated by its first term, i.e., by the term originating from DSFT processing.

The assessment of the complexity of the CSFDEC algorithm is based on the considerations illustrated in [15] for its 1D counterpart. Based on these, it can be proved that $\mathcal{C}_{\text{CSFDEC}} = \mathcal{O}(N_{\text{CSFDEC}})$, where

$$N_{\text{CSFDEC}} = 16\, M_0\, N_0 \log_2\,(M_0\, N_0) + K\, N_{\text{it}}\; 16\, I_\nu\, I_r, \tag{1.65}$$

so that the required computational effort depends *linearly* on K. The last result holds if *tone re-estimation* is not accomplished and all the tones are detected (i.e., $\hat{K} = K$). The first term appearing in the RHS of the last equation accounts for the initialization (and, in particular, for the computation of the matrices $\bar{\mathbf{Y}}_{0,0}$ (1.26) and $\{\bar{\mathbf{Y}}_{k_1,k_2}; (k_1, k_2) \neq (0, 0)\}$ (1.39)), whereas the second one for the fact that, in the CSFDEC algorithm, the CSFDE is executed K times. Note that the computational cost related to the estimation of the 2D-tones detected after the first one and to their frequency domain cancellation does not play an important role in this case. However, if *tone re-estimation* is executed in the CSFDEC algorithm, the parameter K appearing in the RHS of (1.65) is replaced by K^2, since this task involves all the estimated 2D-tones.

1.3.4 Comparison of CSFDEC with related techniques

The CSFDEC algorithm is conceptually related with: 1) the 2D *periodogram method* [6] (denoted 2D-FFT in the following); 2) the CLEAN algorithm [20,21]; 3) the Modified Wax & Leshem (MWL) developed in [20, 21]. The 2D-FFT, CSFDEC and CLEAN algorithms are FFT-based techniques; however, the last two algorithms are more complicated than the first one. In fact, unlike the 2D-FFT, both the CSFDEC and CLEAN algorithms perform leakage compensation, iterative cancellation of the detected targets and tone re-estimation. Note also that the CLEAN algorithm, unlike the CSFDEC algorithm, does not accomplish fine frequency estimation and employs coarse frequency estimates in its target cancellation procedure. The MWL algorithm, similarly as the CSFDEC algorithm, relies on the idea of turning a complicated 3D optimization problem (see (1.16)) into a triplet of three

simpler 1D optimization problems. However, unlike the CSFDEC algorithm, it requires the computation of orthogonal projections (and, consequently, of matrix inversions) and the definition of a search grid.

If frequency re-estimation is ignored, the following considerations can be formulated for the computational complexity of the above-mentioned algorithms:

1) The computational effort of the CLEAN algorithm is expressed by the sum of three distinct contributions, related to its initialization (which is based on the 2D-FFT), its tone cancellation and its leakage compensation; these three costs are shared with the CSFDEC algorithm, that requires the computation of another 12 (or 15) additional DSFTs (see Section 1.3.3).

2) The CLEAN and MWL algorithms perform cancellation and leakage compensation in the *time domain*, whereas the CSFDEC algorithm performs these tasks in the *frequency domain*. This explains why the computational complexity of the CSFDEC cancellation, being in the order of $M_0 \times N_0$, is $L_\nu \times L_r$ times larger than the cost of the same task for the CLEAN and MWL algorithms.

3) The computational cost of leakage removal can be neglected for the CSFDEC algorithm because of its simplicity (complex scalar subtraction), even if it has to be accomplished on multiple DSFT; on the other hand, the CLEAN and MWL algorithms execute this task in a similar fashion as cancellation, thus requiring $\mathcal{O}(MN)$ operations.

4) The computational effort of the MWL algorithm is expressed by the sum of two distinct contributions, one due to its initialization, the other one due to its iterations. The cost of the initialization task is the same as that of the *Wax and Leshem* (WL) algorithm illustrated in [20]. The cost of each iteration, instead, is given by that of the WL algorithm plus a contribution due to leakage compensation; the last cost is $\mathcal{O}(KMN)$, being equal to that required by the CLEAN algorithm for the same procedure.

To sum up, the 2D-FFT is the least demanding algorithm; moreover, its computational effort is independent of the overall number of detected targets (i.e., of K). The MWL algorithm is less computationally demanding than the CLEAN algorithm since it exploits alternating maximization. The CSFDEC algorithm has the highest initialization cost and usually is computationally heavier than all the other algorithms mentioned above. However, the dependence of its complexity on K is limited and weaker than that exhibited by the CLEAN algorithm; in addition, the CSFDEC algorithm is substantially more accurate than all the other algorithms in the presence of multiple closely spaced targets, as shown in the following section.

1.4 Numerical Results

The accuracy of the CSFDEC algorithm has been assessed in five different scenarios and compared with that achieved by the related algorithms introduced in Section 1.3.4 and four other algorithms, namely:

1) the 2D-MUSIC algorithm [8, 9], [22];

2) the approximate ML method recently proposed in [11] and dubbed *modified*[15] *alternating projection* ML (MAP-ML) algorithm;

3) an estimation algorithm based on the same 2D cost function as the MAP-ML algorithm, but not using the alternating projection method for its maximization (this algorithm is denoted *modified Zhang* ML, MZ-ML);

4) the Expectation Maximization (EM) algorithm. A detailed description of all these algorithms and an analysis of their computational complexity are provided in Chapter 2; here, we limit ourselves to pointing out that the MAP-ML and MZ-ML algorithms require a significant computational effort, since they are ML-based and do not turn, unlike the CSFDEC and MWL algorithms, a multidimensional optimization problem into significantly simpler sub-problems.

In this work, the first three scenarios (denoted **S1**, **S2** and **S3**) are characterized by a couple of targets having amplitudes $A_0 = A_1 = 1$, but differ in the assumptions we make about their ranges and speeds. In fact, we have that:

1) in **S1**, the target ranges are $R_0 = 10$ m and $R_1 = 10 + 3R_{\text{bin}}$ m, whereas the target velocities are $v_0 = 1.39$ m/s and $v_1 = 1.39 + 3v_{\text{bin}}$ m/s (here, $R_{\text{bin}} = c/(2N\Delta_f)$ and $v_{\text{bin}} = c/(2M\, f_{\text{c}}\, T_{\text{s}})$ represent the size of the range bin and velocity bin, respectively, that characterize the considered FFT processing in the absence of oversampling).

2) In **S2**, the range R_0 (velocity v_0) is uniformly distributed[16] over the interval $[R_{\min}, R_{\max}] = [3,\ 80]$ m ($[v_{\min}, v_{\max}] = [0.2778,\ 10]$ m/s), whereas $R_1 = R_0 + 1.1R_{\text{bin}}$ and $v_1 = v_0 + 1.1v_{\text{bin}}$.

3) in **S3**, the range R_0 (velocity v_0) is uniformly distributed over the interval $[R_{\min}, R_{\max}] = [3,\ 30]$ m ($[v_{\min}, v_{\max}] = [0.2778,\ 5.56]$ m/s), whereas $R_1 = R_0 + \Delta_R(d)\, R_{\text{bin}}$ ($v_1 = v_0 + \Delta_v(d)\, v_{\text{bin}}$), with $d = 0, 1, ..., 5$. In this scenario, $\Delta_R(d) = 0.8 + 0.05\, d$ ($\Delta_v(d) = 0.8 + 0.05\, d$) represents the tone spacing normalized with respect to R_{bin} (v_{bin}) and the Signal-to-Noise Ratio (SNR), which, in general, is defined as $\text{SNR} \triangleq \sum_{k=0}^{K-1} |A_k|^2/\sigma_W^2$, is equal to 0 dB.

The fourth scenario (denoted **S4**), instead, is characterized by $K \in \{2, 3, ..., 9\}$, i.e., by a varying number of targets. In addition, for any K, the amplitude, range and velocity of the kth target are given by $A_k \triangleq 10^{-k\Delta_a/10}$, $R_k \triangleq R_0 + 1.8\, k\, R_{\text{bin}}$ and $v_k \triangleq v_0 + 1.8\, k\, v_{\text{bin}}$, respectively (with $k = 0, 1, ..., K-1$), the random variables R_0 and v_0 are generated in the same way as **S3**, and the SNR is equal to 5 dB for the strongest tone.

In the last scenario (denoted **S5**), the range and velocity of the kth target are generated according to the simple mathematical laws given for **S4**, but $R_{\text{bin}} = v_{\text{bin}} = 1.1$ and $A_k = 1$ for any $k = 0, 1, ..., K-1$ (with $K \in \{3, 5, 7, 9\}$) are assumed; moreover, the SNR ranges from -15 dB to 25 dB.

It is important to point out that: 1) in **S1** the spacing of the two targets in the velocity and range domains is fixed and not small, whereas in **S2** (**S3**) the spacing in both the range and velocity domains is small and fixed (variable); 2) **S4** is characterized by a variable number of close targets; 3) **S5** is characterized by a variable number of close targets and

[15] In this work, the approximate ML-based algorithm devised in [11] has been properly modified to adapt it to the signal model (1.14) (that does not account for *inter-pulse* and *inter-subcarrier* Doppler effects).

[16] In both **S2** and **S3**, R_0 and v_0 are *independent* random variables.

by a variable SNR; 4) in all the considered scenarios, positive velocities have been selected for all the targets and the overall number of targets has been assumed to be known.

In our computer simulations, the estimation accuracy of each algorithm has been assessed by evaluating the Root Mean Square Error (RMSE) for the range (RMSE_R) and velocity (RMSE_v) of the considered targets. Moreover, the following parameters have been selected for the OFDM modulation: 1) overall number of subcarriers $N = 32$; 2) overall number of OFDM symbols/frame $M = 32$; 3) subcarrier spacing $\Delta_f = 250$ kHz; 4) CP duration $T_{\mathrm{G}} = 12.5$ µs (consequently, the OFDM symbol duration is $T_{\mathrm{s}} = 1/\Delta_f + T_{\mathrm{G}} = 16.5$ µs); 5) carrier frequency $f_{\mathrm{c}} = 78$ GHz; 6) cardinality of the PSK constellation $M_{\mathrm{c}} = 32$. Then, we have that $R_{\mathrm{bin}} = 18.75$ m and $v_{\mathrm{bin}} = 3.64$ m/s.

In **S1** the accuracy of all the considered estimation algorithms has been assessed. Moreover, the following choices have been made for these algorithms[17] selected for **S1** have been also employed in **S2** and **S3**.: 1) the oversampling factor $L_\nu = 16$ ($L_r = 16$) has been chosen for Doppler (range) estimation in both the 2D-FFT and CSFDEC algorithms (so that $M_0 = ML_\nu = 512$ and $N_0 = NL_r = 512$; see (1.29) and (1.30), respectively); 2) (1.46) has been always employed in the evaluation of the CSFDEC residuals (so that 13 DSFTs $\{\bar{\mathbf{Y}}_{k_1,k_2}\}$ have been computed in each new run); 3) the 2D-FFT method has been used to compute the initial estimates of target range and Doppler in the MZML, MAP-ML and EM algorithms; 4) $M_0 = 512$ ($N_0 = 512$) has been chosen for the refinement grid over Doppler (range) employed by the CLEAN, MWL, MZML, MAP-ML and EM algorithms; 5) in the CSFDEC algorithm $N_{\mathrm{it}} = 15$ refinement steps have been accomplished for the computation of the range and Doppler residuals, the interpolation[18] orders $I_\nu = I_r = 7$ have been selected and $N_{\mathrm{REF}} = 3$ re-estimations have been executed; 6) $N_{\mathrm{REF}} = 5$ ($N_{\mathrm{REF}} = 3$) re-estimations have been executed by the CLEAN and MWL (MZML, MAP-ML and EM) algorithms; 7) $M_0 = N_0 = 11$ ($M_0 = N_0 = 9$) have been chosen for the grid size in the CLEAN and MWL (MZML, MAP-ML and EM) algorithms during the re-estimation steps; 8) a unit value has been assigned to all the *mixing coefficients* $\{\beta_k^{(i)}\}$ of the EM algorithm (see eq. (2.65), in Chapter 2, and comment related to it); 9) the spacing between adjacent values in the search (initial search) grid for 2D-MUSIC algorithm (CLEAN and MWL algorithms) is $\Delta_R = 0.6$ m ($\Delta_v = 0.1166$ m/s). Moreover, in **S1**, $M_0 = 121$ ($N_0 = 121$) has been selected for the number of trial values of the 2D-MUSIC algorithm and for the initial trial values of the CLEAN and MWL algorithms in the Doppler (range) domain; such values are uniformly spaced in the range (velocity) interval[19] $[0, R_{\max}]$ ($[0, v_{\max}]$), with $R_{\max} = 72$ m ($v_{\max} = 13.986$ m/s).

Some numerical results referring to **S1** are given in Fig. 1.1, where the RMSE_R and RMSE_v characterizing all the considered algorithms are shown for SNR $\in [-15, 25]$ dB (in these figures and in all the following ones, simulation results are represented by labels, whereas continuous lines are drawn to ease reading). From these results, it is easily inferred that:

[17] The meaning of the parameters of the various algorithms can be found in Chapter 2, Section 2.3

[18] In all the simulations, the *barycentric interpolation* described in [19] has been always used.

[19] Note that, in the considered simulations, *positive* trial values are always considered for target velocities, without loss of generality.

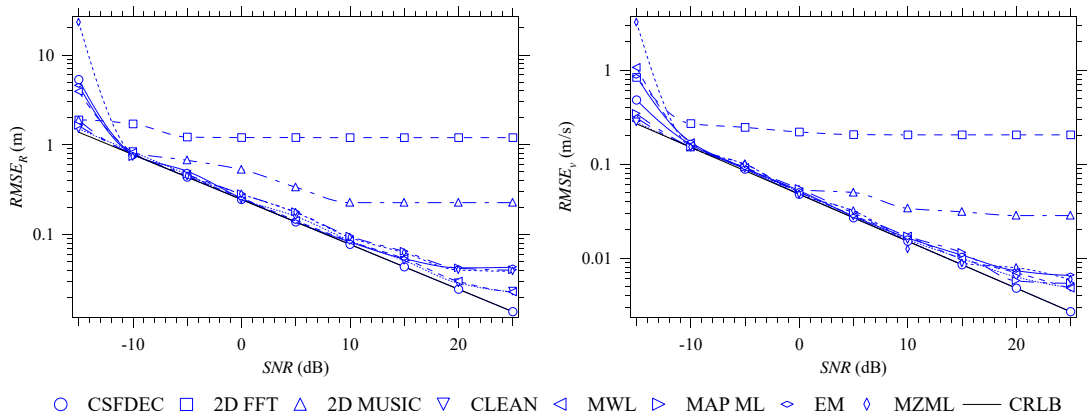

FIGURE 1.1: Root mean square error performance achieved in range and velocity estimation (first scenario).

1) The CSFDEC, CLEAN and MWL algorithms achieve good accuracy, very close to the Cramér-Rao Lower bound (CRLB)[20], thanks to their use of cancellation and refinement procedures.

2) The RMSE curves for the 2D-FFT and 2D-MUSIC algorithms exhibit a floor at high SNRs.

3) The MAP-ML and the MZML algorithms perform similarly since both aim at maximizing the same cost function.

4) The EM algorithm can be fruitfully exploited to refine the estimates generated by other methods and, in particular, if employed jointly with the 2D-FFT algorithm, achieves an estimation accuracy similar to that provided by the MAP-ML and MZML algorithms.

As far as point 2) is concerned, it is worth pointing out that:

a) The accuracy of the 2D-FFT algorithm is intrinsically limited by the adopted FFT order, whereas that of the 2D-MUSIC algorithm is limited by the discretization of its steering vector; for this reason, when the *spectral leakage* is limited (i.e., when the targets are well spaced), the RMSE achieved by these two algorithms at large SNRs is well approximated by the square root of the variance of a random variable uniformly distributed over an interval whose width is equal to the step size of the grid of the considered algorithm, i.e., to $\sqrt{(X_{\text{res}}^2/12)}$, with $X = R$ or v; here, $R_{\text{res}} = R_{\text{bin}}/N_0 = 1.171875$ m, $v_{\text{res}} = v_{\text{bin}}/M_0 = 0.2276$ m/s for the 2D-FFT, whereas $R_{\text{res}} = \Delta_R$ and $v_{\text{res}} = \Delta_v$ for the 2D-MUSIC).

b) For given values of M and N, the accuracy of the 2D-FFT algorithm improves if the associated oversampling factors increase; unfortunately, oversampling can provide a limited improvement by itself, since it does not add extra information, but simply allows to interpolate adjacent spectral samples.

c) The accuracy of the 2D-MUSIC algorithm can be improved by selecting a finer grid, at the price, however, of a higher computational complexity, as shown in Chapter 2.

[20] The evaluation of the performance bounds can be found in Appendix A.1.4

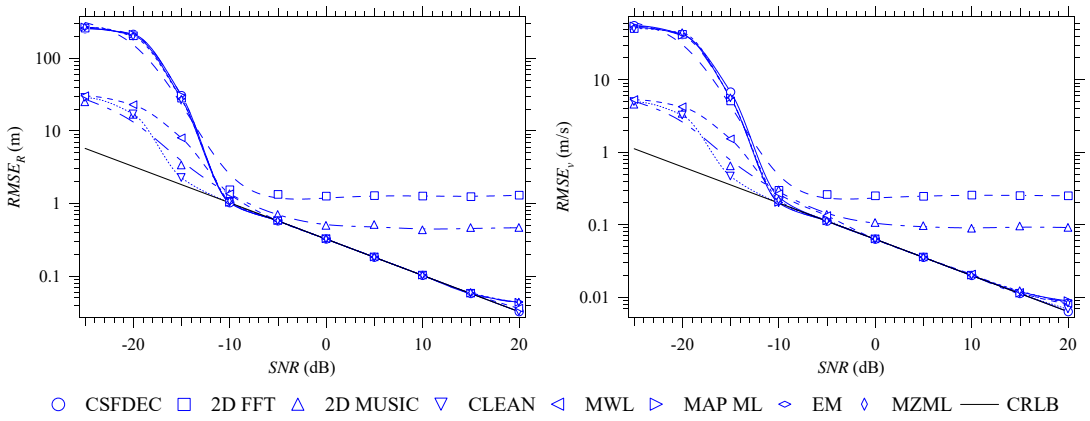

FIGURE 1.2: Root mean square error performance achieved in range and velocity estimation (second scenario).

d) Both the 2D-FFT and 2D-MUSIC algorithms do not execute refinement and/or re-estimation steps.

These considerations apply to all the following results shown for the two above mentioned algorithms. In addition, in analyzing the results shown in Fig. 1.1, readers should keep in mind that: 1) the computational complexity of the CSFDEC (CLEAN) algorithm is approximately 17 (39) times higher than that of the 2D-FFT[21], whereas that of the MWL algorithm is very close to it; 2) the complexity of the 2D-MUSIC, MAP-ML and MZML algorithms is 3481, 577 and 2593 times higher than that of the 2D-FFT algorithm, respectively; 3) the computational cost of the EM algorithm is approximately 149 (671) times smaller than that of the MAP-ML (MZML) algorithm.

Some numerical results referring to **S2** are provided in Fig. 1.2, where the RMSE_R and RMSE_v characterizing all the considered algorithms are shown for $\mathrm{SNR} \in [-25, 20]$ dB. In this case, $M_0 = 131$ ($N_0 = 181$) have been selected for the number of trial values of the 2D-MUSIC algorithm and for the initial trial values of the CLEAN and MWL algorithms in the Doppler (range) domain; such values are uniformly spaced in the range (velocity) interval $[0, R_{\max}]$ ($[0, v_{\max}]$), with $R_{\max} = 108$ m ($v_{\max} = 15.15$ m/s). These results lead to the following conclusions:

1) The CSFDEC, MWL, CLEAN, MAP-ML, MZML and EM algorithms are substantially more accurate than the 2D-FFT and 2D-MUSIC techniques. In particular, the RMSEs in range (velocity) of the 2D-FFT and 2D-MUSIC algorithms are 3.9 (4) and 1.5 (1.68) times higher, respectively, than that of the above mentioned group of algorithms at SNR = 0 dB; moreover, these performance gaps, in terms of both RMSE_R and RMSE_v, tend to increase by a factor 1.75 if the SNR is incremented by 5 dB.

2) The trend of both the RMSE_R and RMSE_v curves referring to the 2D-MUSIC and 2D-FFT algorithms does not follow that of the corresponding CRLB; for this reason, these algorithms are ignored in the following.

[21]The 2D-FFT is taken as a reference since it represents the method commonly adopted in real world systems, thanks to its computational efficiency and acceptable accuracy.

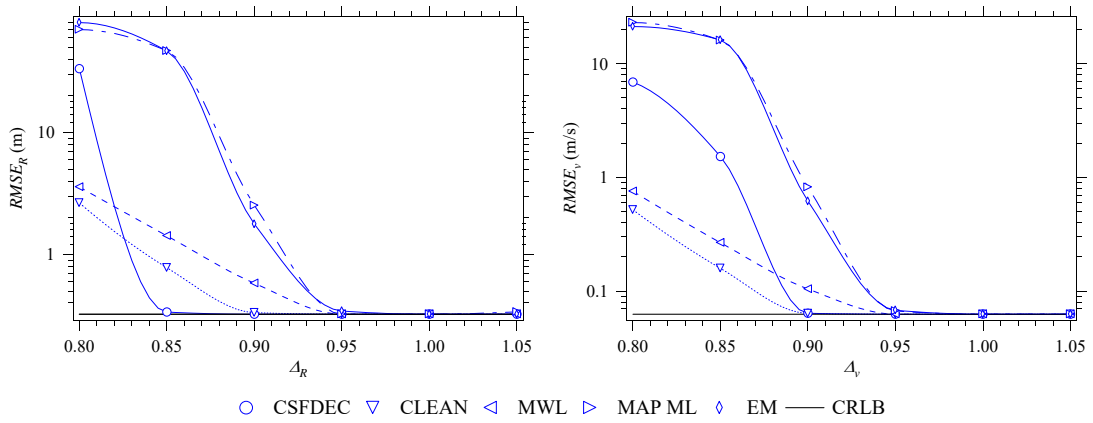

FIGURE 1.3: Root mean square error performance achieved in range and velocity estimation (third scenario) for different values of the normalized tone spacing Δ_R and Δ_v, respectively. The CSFDEC, CLEAN, MWL, MAP-ML and EM algorithms are considered.

3) The SNR threshold of the CSFDEC, CLEAN, MAP-ML and EM algorithms is about -10 dB, whereas that of the MWL algorithm is substantially higher (about -5 dB).

4) The MAP-ML algorithm performs similarly to the MZML algorithm; however, since the latter estimator requires a higher computational effort than the former one, it is ignored in the following.

It is also important to point out that the considerations illustrated about the computational complexity of the various algorithms in **S1** still hold; however, the complexities of the CLEAN, 2D-MUSIC and MWL algorithms are 64, 5497 and 1.01 times higher than that of the 2D-FFT algorithm, respectively.

In **S3**, the RMSEs have been evaluated for different values of the normalized tone spacing Δ_R and Δ_v; some numerical results referring to this scenario are illustrated in Fig. 1.3, that shows the dependence of RMSE_R and RMSE_v, respectively, on the normalized tone spacing. In this case, the number of initial trial values is $M_0 = 101$ ($N_0 = 101$) for the CLEAN and MWL algorithms in the Doppler (range) domain; such values are uniformly spaced in the range (velocity) interval $[0, R_{\max}]$ ($[0, v_{\max}]$), with $R_{\max} = 60$ m ($v_{\max} = 11.66$ m/s). These results lead to the following conclusions: 1) The lowest threshold in range estimation is achieved by the CSFDEC algorithm (more specifically, in the considered scenario, its threshold is found at the normalized spacing $\Delta_R(2) = 0.9$); 2) the lowest threshold in velocity estimation is achieved by both the CLEAN and CSFDEC algorithms. Note also that the complexity of the CLEAN is approximately 1.6 times higher than that of the CSFDEC algorithm in this case.

Based on the considerations illustrated above, in **S4** we restrict the attention to the CSFDEC, CLEAN, MWL, MAP-ML and EM algorithms. Moreover, the performance analysis does not concern estimation accuracy, but the *probability of failure* (P_f), i.e., the probability that convergence is not achieved, so that large estimation errors can be generated. In the considered computer simulations, we have observed that large estimation errors occur more frequently as K increases. To detect the frequency of occurrence of

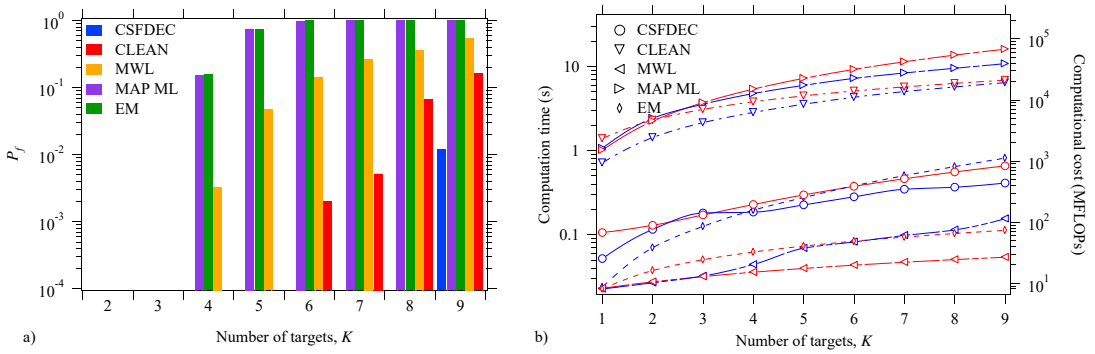

FIGURE 1.4: a) Probability of failure versus overall number of tones; b) computational complexity in terms of computation time (blue curves) and computational cost (red curves). The CSFDEC, CLEAN, MWL, MAP-ML and EM algorithms are considered (fourth scenario).

these errors, we have counted, in each simulation run, the number of *failure events* for each of the considered algorithms; in practice, an event of this type is detected whenever the absolute value of the range error and that of the velocity error (or only one of these errors) exceed the thresholds $\Delta\epsilon_r = c/(4N\Delta_f) = 9.375$ m and $\Delta\epsilon_v = c/(4Mf_cT_s) = 1.82$ m/s, respectively[22]. Moreover, in generating the results for **S4**, the following changes have been made with respect to the previous scenarios: 1) $N_{\text{REF}} = 7$ ($N_{\text{REF}} = 5$) re-estimations have been executed by the CSFDEC, CLEAN and MWL (MAP-ML and EM) algorithms; 2) $M_0 = 551$ ($N_0 = 551$) have been selected for the initial trial values of the CLEAN and MWL algorithms in the Doppler (range) domain; 3) these trial values are uniformly spaced in the range (velocity) interval $[0, R_{\max}]$ ($[0, v_{\max}]$), with $R_{\max} = 330$ m ($v_{\max} = 64$ m/s). Note that the spacing between adjacent trial values is the same as **S1-S3** in both domains.

The probability of failure estimated for $K = 2, 3, ..., 9$ is illustrated in Fig. 1.4-a). From this figure, it is easily inferred that: 1) the MAP-ML and EM (MWL) algorithms exhibit a P_f greater than 10^{-2} for $K \geq 4$ ($K \geq 5$); 2) the CSFDEC algorithm is substantially more robust than all the other algorithms since it is characterized by a P_f not exceeding 10^{-4} for $K \leq 8$; 3) the CLEAN algorithm achieves a P_f smaller than 10^{-2} for $K \leq 7$. These results evidence that the CSFDEC algorithm performs substantially better than the other estimators in the presence of multiple closely spaced targets. This feature plays a fundamental role in the estimation of extended targets, whose radar image is usually a dense point cloud.

In **S4** the computational effort required by the CSFDEC, CLEAN, MWL, MAP-ML and EM algorithms in terms of both Computation Time (CT)[23] and estimated number of *mega* FLOPs (MFLOPs) has also been evaluated. The results, illustrated in Fig. 1.4-b), evidence that: 1) the MWL (MAP-ML) algorithm requires the lowest (highest) complexity in terms of both CT and MFLOPs; 2) the complexity of the CLEAN algorithm is not far from that

[22]Note that $\Delta\epsilon_r$ ($\Delta\epsilon_v$) correspond to half the size of the range (Doppler) bin characterizing the processing of the considered algorithms.

[23]The CT has been assessed on a personal computer equipped with an i7 processor.

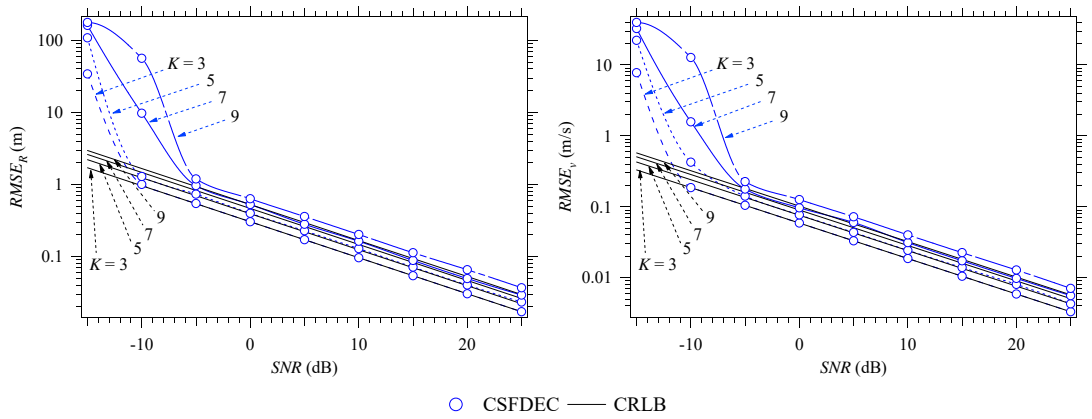

FIGURE 1.5: Root mean square error performance achieved in range and velocity estimation (fifth scenario) by the CSFDEC algorithm with a varying number of targets, i.e., $K \in [3, 5, 7, 9]$ and the SNR $\in [-15; 25]$.

of the MAP-ML algorithm; 3) the complexities of the CSFDEC and EM algorithms are comparable and placed in the middle.

The last results are shown in Fig. 1.5 and concern the RMSE_R and RMSE_v of the CSFDEC algorithm in **S5**; $N_{it} = 10$ and $N_{\text{REF}} = 3$ have been selected for this algorithm (the values of its remaining parameters are the same as **S1**).

These results show that:

1) The SNR threshold of the CSFDEC algorithm depends on K; for instance, this threshold for the range estimation is found at a SNR ≈ -9 (SNR ≈ -5) dB for $K = 3$ and 5 ($K = 7$ and 9).

2) The range and velocity estimates generated by the CSFDEC algorithm are unbiased. Note, for instance, that for both $K = 7$ and 9, the RMSE_R and RMSE_v and the corresponding CRLB curves are separated by a constant SNR gap when the SNR exceeds the above-mentioned threshold; further computer simulations have evidenced that this gap can be reduced by increasing the values of N_{REF} and, more evidently, of N_{it}, at the price, however, of a higher computational effort.

Finally, based on all the results illustrated above, we can state that, thanks to its accuracy, its limited complexity increase with respect to the 2D-FFT method and its ability to resolve multiple closely spaced point targets, the CSFDEC algorithm represents a good candidate for target detection and estimation in future OFDM-based radars.

1.5 Conclusions

In this chapter, a novel algorithm for the detection of a single 2D complex tone and the estimation of its parameters has been derived. Moreover, it has been shown how combining this algorithm, dubbed CSFDE, with a serial cancellation procedure leads to the development of a new algorithm for the detection and the estimation of multiple 2D tones. Then,

the last algorithm, called CSFDEC, has been applied to the detection of multiple targets, and to the estimation of their range and velocity in an OFDM-based SISO radar system. In addition, it has been compared, in terms of accuracy and computational complexity, with various estimation methods available in the technical literature. The proposed simulation results evidence that the CSFDEC algorithm is very accurate and outperforms all the other related estimators in the presence of multiple closely spaced targets. In the next chapter, a detailed overview of the most relevant classes of deterministic signal processing methods for the detection and the estimation of multiple targets in a JCAS system employing OFDM is conducted.

2

Deterministic Signal Processing Techniques for OFDM-based Radar Sensing: An Overview

In this chapter, we analyze the most relevant classes of deterministic signal processing methods currently available for the detection and the estimation of multiple targets in a joint communication and sensing system employing orthogonal frequency division multiplexing. The objective of this chapter is to offer a fair comparison of the available technical options in terms of required computational complexity and accuracy in both range and Doppler estimation. The proposed numerical results, obtained in various scenarios, evidence that distinct algorithms can achieve a substantially different accuracy-complexity trade-off.

2.1 Introduction

In the last few years, increasing attention has been paid to the design of wireless systems able to perform both communication and radar functions, i.e., to accomplish JCAS. Such systems make efficient use of the available spectrum and offer significant benefits in terms of size, energy consumption, and cost, since they employ a single radio device for both communication and sensing functionalities. For these reasons, they are expected to play an important role in the field of future vehicular networks [23–25].

One of the waveforms currently being considered for its adoption in JCAS systems is OFDM [2]. A huge technical literature is available about the signal processing techniques to be employed at both the TX and Receive (RX) sides of wireless communication systems exploiting this modulation format. On the contrary, limited research efforts have been devoted until now to the development of methods for target detection and estimation in OFDM-based JCAS systems. The currently available methods can be divided in *direct sensing methods* and *indirect estimation methods*. The former methods extract target information from the received signal without compensating for the effect of the data payload conveyed by its useful component [1]; moreover, they typically exploit computationally intensive compressed sensing techniques (e.g., see [3, 26–28]). The latter methods, instead, rely on the knowledge of a preliminary estimate of the communication channel. The evaluation of this estimate requires compensating for the contribution of the transmitted channel symbols to the received signal (such symbols are always known at the receive side of a *colocated* radar; e.g., see [4]). In this chapter, we focus on indirect methods only and investigate their use in a *colocated*[1] OFDM-based JCAS system equipped with a single

[1]Since the considered system is colocated (i.e., its TX and RX antennas are closely spaced), its receiver has a full knowledge of the structure and content of the transmitted frames and of the carrier frequency.

TX and a single RX antenna (i.e., of SISO type). Moreover, we take into consideration different classes of indirect methods, namely: 1) DFT-based or correlation-based methods; 2) subspace methods; 3) ML-based methods. It is worth pointing out that, even if various overviews on JCAS systems have appeared in the last three years [1, 2, 29–37], none of them provides a comparative analysis of the above mentioned methods for sensing in an OFDM-based radar system. Written with the aim of filling this gap, this chapter offers a fair comparison in terms of accuracy and computational complexity of various algorithms belonging to the aforementioned classes and highlights their peculiarities and limitations.

The remaining part of this chapter is organized as follows. In Section 2.2, the processing accomplished in an OFDM-based radar system is summarized and the model of the signal feeding target detection and estimation algorithms is illustrated. Section 2.3 is devoted to the description of various relevant estimation methods, and to the assessment of their computational complexity. The analyzed techniques are compared in terms of accuracy and complexity in Section 2.4. Finally, some conclusions are offered in Section 2.5.

2.2 System and Signal Models

In this section, the same processing accomplished in a SISO OFDM-based JCAS system described in Section 1.2 is considered. In the considered analysis, we focus on the transmission and reception of a single OFDM frame consisting of M consecutive OFDM symbols, each composed of N subcarriers. In particular, here we consider:

1) The availability of stable and accurate frequency and timing references; for this reason, the *time-frequency mismatch* at the RX side is deemed negligible [38, Sec. III-B].

2) The TX signal is sent over a wireless channel and gets reflected by K point targets before being received and processed by a *colocated* receiver.

We begin by resuming the last steps accomplished at the RX side of the considered system. In particular, by following the same steps shown in Section 1.2, it can be easily proved that the nth element of the vector (see (1.7))

$$\mathbf{R}_m \triangleq [R_{m,0}, R_{m,1}, ..., R_{m,N-1}]^T, \tag{2.1}$$

at the output of the DFT block, can be expressed as

$$R_{m,n} = s_{m,n} \sum_{k=0}^{K-1} A_k \, a_m(F_{\nu_k}) \, a_n^*(F_{\rho_k}) + W_{m,n}, \tag{2.2}$$

where A_k and F_{ν_k} (see (1.11)) denote the complex gain and the normalized Doppler frequency associated to the kth target. In (2.2)

$$a_q(F_X) \triangleq \exp(j2\pi q F_X), \tag{2.3}$$

with q being either m or n if X is either ν or r, respectively. Moreover, in (2.2), the term $W_{m,n}$ is the Gaussian noise affecting the nth subcarrier of the mth OFDM symbol and

$$F_{\rho_k} = F_{r_k} - F_{\nu_k} T/(NT_{\mathrm{s}}) \tag{2.4}$$

is a normalized frequency accounting for the target delay (through F_{r_k}, see (1.10)) and the so-called *range migration* effect due to the kth target Doppler (e.g., see [38]). In the following, we assume that N is large enough, so that the $F_{\rho_k} \approx F_{r_k}$ for any k, thus (2.2) can be simplified as

$$R_{m,n} = s_{m,n} \sum_{k=0}^{K-1} A_k \, a_m(F_{\nu_k}) \, a_n^*(F_{r_k}) + W_{m,n}. \tag{2.5}$$

Since the channel symbol $s_{m,n}$ is known at the receive side for any n and m, the estimate

$$\hat{H}_{m,n} \triangleq \frac{R_{m,n}}{s_{m,n}} = \sum_{k=0}^{K-1} A_k \, a_m(F_{\nu_k}) \, a_n^*(F_{r_k}) + \bar{W}_{m,n} \tag{2.6}$$

of the channel gain $H_{m,n}$ observed at the nth subcarrier frequency in the mth OFDM symbol interval can be computed; here,

$$\bar{W}_{m,n} \triangleq \frac{W_{m,n}}{s_{m,n}} \tag{2.7}$$

is the noise sample affecting $\hat{H}_{m,n}$, in (2.6). It is worth pointing out that:

1) The parameters F_r (1.10) and F_ν (1.11) satisfy the inequalities $F_{r,\min} \leqslant F_r \leqslant F_{r,\max}$ and $F_{\nu,\min} \leqslant F_\nu \leqslant F_{\nu,\max}$, with $F_{r,\min} = 0$, $F_{r,\max} = 1$ and $F_{\nu,\min} = -1/2$, $F_{\nu,\max} = 1/2$, respectively.

2) an AWGN model is adopted for the noise samples $\{W_{m,n}\}$ (see (2.5)) and, consequently, for the noise samples $\{\bar{W}_{m,n}\}$ (see (2.7)), since a PSK constellation is employed in the considered simulations (each element of the sequence $\{\bar{W}_{m,n}\}$ is assumed to have zero mean and variance σ_W^2).

3) Neglecting self-interference and range migration results in a signal model in which the target delay and Doppler frequency are decoupled parameters. This entails that, in principle, the values of these parameters can be evaluated separately through 1D frequency estimation techniques. However, only 2D frequency estimation techniques are considered in the following since, despite their higher computational effort than their 1D counterparts, they achieve better accuracy and do not require the use of a pairing method to associate the estimated delays and Doppler frequencies with each detected target.

4) Even if clutter plays an important role in radar sensing, its contribution to the received signal can be mitigated by resorting to various techniques available in the technical literature (e.g., see [26]). For this reason, in this work, this contribution is always neglected.

From (2.6) it can be easily inferred that: a) the noisy samples $\{\hat{H}_{m,n}\}$ of the 2D channel response acquired over a single frame can be modeled as the superposition of multiple 2D

complex exponentials with AWGN; b) target detection and estimation is tantamount to identifying the K complex exponentials forming the useful component of the 2D sequence $\{\hat{H}_{m,n}\}$ and estimating their parameters, respectively.

2.3 Detection and Estimation Algorithms

In this subsection, various algorithms for the detection and estimation of multiple targets in an OFDM-based radar system are illustrated and their computational complexity is analyzed by deriving the order of magnitude of the number of FLOPs they require to process a single OFDM frame. The general criteria adopted in estimating the computational cost of the various algorithms are the same as those illustrated in [39] and [40, App. C]. These algorithms are divided in FFT-based techniques, subspace-based methods and ML-based techniques.

2.3.1 FFT-based techniques

Correlation-based and DFT-based methods have been developed in [5–7, 41–46]. In particular, Matched Filter (MF)-based techniques for the estimation of range and Doppler in a single or multi-target scenario have been investigated in [5, 7]. Such techniques benefit from the prior knowledge of the received signal and are computationally efficient; however, the accuracy they achieve in radar imaging may be poor because of high side-lobes and leakage, especially in the presence of strong clutter around real targets. We also highlight the serial cancellation technique for improving the overall accuracy of radar images, which has been developed in Chapter 1, whereas a reduced complexity method, based on the idea of splitting a 2D estimation problem (involving target range and Doppler) into a couple of 1D simpler sub-problems, has been illustrated in [44].

In the following, we take into consideration the 2D *periodogram method* (dubbed 2D-FFT in the following) and two cancellation-based estimation algorithms, namely the CSFDEC algorithm (see Chapter 1) and the CLEAN algorithm [21, 47]. On the one hand, the first algorithm can be considered as a reference technique; on the other hand, the other two algorithms as methods able to efficiently mitigate the main problems of the first one, namely:

1) The limited accuracy, due to the discretization of the grid selected in the search for the peaks of the periodogram.

2) The need to search for multiple local maxima, which can lead to missed target detection in the presence of closely spaced targets.

3) The significant impact that spectral leakage may have in the presence of multiple targets. In fact, both the CSFDEC and the CLEAN algorithms combine the serial cancellation of the spectral contribution of each detected target with leakage compensation and re-estimation techniques. Moreover, unlike the 2D-FFT algorithm, they do not need prior

knowledge of the overall number of targets[2]. If prior knowledge of the number of targets is necessary, methods such as the generalized *Akaike* Information Criterion (AIC) [48] or the Minimum Description Length (MDL) [49] are commonly suggested for estimating this parameter. However, these approaches often come with a significant computational cost.

In the following, we provide a comprehensive description of the 2D-FFT and the CLEAN algorithms only, since the CSFDEC algorithm has been thoroughly detailed in Chapter 1.

2.3.1.1 Two-dimensional periodogram method

This method is based on the so-called Range-Doppler (RD) map [6], i.e., on the function

$$J[l,p] = \Big|S[l,p]\Big|^2, \tag{2.8}$$

with $l = 0, 1, ..., M_0 - 1$ and $p = 0, 1, ..., N_0 - 1$; here,

$$S[l,p] \triangleq \frac{1}{MN} \sum_{m=0}^{M-1} \sum_{n=0}^{N-1} \hat{H}_{m,n}\, a_m^*(F_\nu[l])\, a_n(F_r[p]), \tag{2.9}$$

is the coefficient (l,p) of the order (M_0, N_0) DSFT of the 2D sequence $\{\hat{H}_{m,n}\}$. Moreover,

$$F_\nu[l] \triangleq l/M_0 - 1/2, \tag{2.10}$$

$$F_r[p] \triangleq p/N_0, \tag{2.11}$$

$$M_0 \triangleq L_\nu M, \tag{2.12}$$

$$N_0 \triangleq L_r N; \tag{2.13}$$

and L_ν and L_r are the *oversampling factors* adopted in the Doppler and range domain, respectively. The estimates of the normalized Doppler frequency F_ν and the normalized delay F_r of a single target are evaluated as $\hat{F}_\nu = F_\nu[\hat{l}]$ and $\hat{F}_r = F_r[\hat{p}]$, respectively, where

$$\big(\hat{l}, \hat{p}\big) \triangleq \arg \max_{\tilde{l} \in \mathcal{S}_{M_0}, \tilde{p} \in \mathcal{S}_{N_0}} J[\tilde{l}, \tilde{p}] \tag{2.14}$$

and $\mathcal{S}_X$ is the set of integers $\{0, 1, ..., X-1\}$ for any positive integer X. Given $\hat{l}$ and $\hat{p}$, the target complex amplitude A is estimated as

$$\hat{A} = L_\nu\, L_r\, S\big[\hat{l}, \hat{p}\big]. \tag{2.15}$$

In a multi-target scenario, multiple (say $\hat{K}$, where $\hat{K}$ denotes a prior estimate of the number of targets K) local maxima[3] should be expected in the RD map; in this case, the parameters of the target associated with each local maximum are evaluated according to (2.10), (2.11) and (2.15).

[2]This is a relevant feature of all the detection and estimation algorithms that exploit a serial cancellation procedure for the sequential detection of multiple targets.

[3]In the simulations, the *Fast* 2D *peak finder* function available in MatlabR2022a has been exploited to locate all the relevant peaks in RD maps.

The most computationally intensive task required by this method is represented by the evaluation of the above-mentioned order (M_0, N_0) DSFT (see (2.9)). Then, the cost for the search of $\hat{K}$ local maxima in the RD map has to be added to the previous cost. For this reason, the overall computational cost of the 2D-FFT method is $\mathcal{C}_{\mathrm{2D-FFT}} = \mathcal{O}(N_{\mathrm{2D-FFT}})$, where

$$N_{\mathrm{2D-FFT}} = M_0 N_0 \log_2(M_0 N_0) + \hat{K}(M_0 N_0). \tag{2.16}$$

2.3.1.2 CLEAN algorithm

The use of the CLEAN algorithm in radar systems has been proposed in [21, 47] and [20]. On the one hand, one of the earliest implementations of the CLEAN algorithm can be found in [47], where the cancellation capability of the CLEAN algorithm is adopted to reduce side-lobe-induced artifacts affecting the images generated by microwave systems that employ antenna arrays. On the other hand, a more recent CLEAN-based algorithm has been proposed in [21] and [20], where it is employed in the context of Stepped Frequency Continuous Wave (SFCW) radar technology. In that case, the algorithm also includes a technique for the compensation of the spectral leakage due to close targets. In this subsection, we show how this algorithm can be also employed for jointly estimating the range and velocity of multiple targets in the OFDM-based radar system described in the previous section. The CLEAN algorithm is based on the same cost function as the 2D-FFT method (see (2.8)), but, unlike it, makes use of an iterative target cancellation procedure. This means that, within each of its iterations, after detecting a new target and estimating its parameters, its contribution to the aforementioned cost function is canceled; this results in a *residual* cost function, which is passed to the next iteration. More precisely, the processing executed by the CLEAN algorithm consists of an initialization step followed by an iterative procedure. In the initialization, we set the iteration index k to 0 and

$$\hat{H}_{m,n}[0] = \hat{H}_{m,n}, \tag{2.17}$$

with $m = 0, 1, ..., M-1$ and $n = 0, 1, ..., N-1$. Then, in the kth iteration (with $k = 0, 1, ..., \hat{K}-1$, where $\hat{K}$ denotes the overall number of detected targets), the four steps described below are carried out sequentially.

1) *Computation of the cost function* — The cost function

$$J_k[l, p] = \left|S_k[l, p]\right|^2 \tag{2.18}$$

is computed for $l = 0, 1, ..., M_0 - 1$ and $p = 0, 1, ..., N_0 - 1$; here, $S_k[l, p]$ is expressed by (2.9), where, however, $\hat{H}_{m,n}$ is replaced by $\hat{H}_{m,n}[k]$ (see (2.19) below).

2) *Estimation of the parameters of a new target* — A search for the global maximum over the set $\{J_k[l, p];\ l \in \mathcal{S}_{M_0},\ p \in \mathcal{S}_{N_0}\}$ (collecting $M_0\, N_0$ values) is performed to detect a new target (i.e., the kth target); the value of the couple (l, p) corresponding to the global maximum is denoted $(\hat{l}_k, \hat{p}_k)$. Then, the estimates of the normalized frequency F_{ν_k} and of the normalized delay F_{r_k} of the kth target are evaluated as $\hat{F}_{\nu_k} = F_\nu[\hat{l}_k]$ and $\hat{F}_{r_k} = F_r[\hat{p}_k]$, respectively (see (2.10) and (2.11)); whereas that of its complex amplitude $\hat{A}_k$ is evaluated according to (2.15), where $S[\hat{l}, \hat{p}]$ is replaced by $S_k[\hat{l}_k, \hat{p}_k]$.

TABLE 2.1: Description of the grid employed for the refinement step of the CLEAN algorithm.

Condition	Grid nodes	Eq.
$F_{X,\min} \leqslant \hat{F}_{X_k}^{(i-1)} < F_{X,\min} + \delta_X$	$\tilde{F}_X^{(i)}[z_X] = F_{X,\min} + (z_X/\tilde{Q}_0)\,(\delta_X/i)$	(2.23)
$F_{X,\min} + \delta_X \leqslant \hat{F}_{X_k}^{(i-1)} \leqslant F_{X,\max} - \delta_X$	$\tilde{F}_X^{(i)}[z_X] = \hat{F}_{X_k}^{(i-1)} + ((z_X/\tilde{Q}_0) - 1/2)(\delta_X/i)$	(2.24)
$F_{X,\max} - \delta_X < \hat{F}_{X_k}^{(i-1)} \leqslant F_{X,\max}$	$\tilde{F}_X^{(i)}[z_X] = F_{X,\max} + ((z_X/\tilde{Q}_0) - 1)(\delta_X/i)$	(2.25)

3) *Threshold test to identify false targets* — If $|\hat{A}_k| < \mathcal{T}_{\text{CLEAN}}$, where $\mathcal{T}_{\text{CLEAN}}$ denotes a proper (positive) threshold, a false target is identified and the execution is stopped by moving to step 5); otherwise, we proceed with the next step.

4) *Target cancellation* — The new residual frequency response

$$\hat{H}_{m,n}[k+1] \triangleq \hat{H}_{m,n}[k] - \hat{A}_k\, a_m\big(\hat{F}_{\nu_k}\big)\, a_n^*\big(\hat{F}_{r_k}\big) \tag{2.19}$$

is evaluated to cancel the contribution of the last detected target to $\hat{H}_{m,n}[k]$ (with $m = 0, 1, ..., M-1$ and $n = 0, 1, ..., N-1$). Then, the iteration index k is increased by one and a new iteration is started (i.e., we go back to step 1).

5) *End* — The final output provided by the CLEAN algorithm is represented by the set $\{(\hat{F}_{\nu_k},\, \hat{F}_{r_k},\, \hat{A}_k);\ k = 0, 1, ..., \hat{K}-1\}$, where $\hat{K}$ represents the last value taken on by the iteration index k.

The serial cancellation procedure expressed by eq. (2.19) may suffer from *error accumulation*, since the effects of errors in the estimation of target parameters accumulate over successive iterations.

This may result in: a) poor accuracy in the presence of multiple and/or closely spaced targets; b) the detection of false targets. These considerations motivate the use of a *refinement procedure* to be accomplished after the last iteration of the CLEAN algorithm. This procedure consists of N_{REF} iterations. In its ith iteration (with $i = 1, 2, ..., N_{\text{REF}}$), the refined estimates $\{(\hat{F}_{\nu_k}^{(i)},\, \hat{F}_{r_k}^{(i)},\, \hat{A}_k^{(i)});\ k = 0, 1, ..., \hat{K}-1\}$ of the parameters of the $\hat{K}$ targets detected by the CLEAN algorithm are evaluated as follows. First of all, we maximize, over a specific *rectangular grid* (consisting of $\tilde{M}_0\, \tilde{N}_0$ distinct nodes), the function

$$J_k^{(i)}\big(\tilde{F}_\nu, \tilde{F}_r\big) = \Big|S_k^{(i)}\big(\tilde{F}_\nu, \tilde{F}_r\big)\Big|^2, \tag{2.20}$$

where

$$S_k^{(i)}\big(\tilde{F}_\nu, \tilde{F}_r\big) \triangleq \frac{1}{MN} \sum_{m=0}^{M-1} \sum_{n=0}^{N-1} \hat{H}_{m,n}^{(i)}[k] a_m^*\big(\tilde{F}_D\big)\, a_n\big(\tilde{F}_r\big) \tag{2.21}$$

and

$$\hat{H}_{m,n}^{(i)}[k] = \hat{H}_{m,n}[0] - \sum_{j=0,\, j\neq k}^{\hat{K}-1} \hat{A}_j^{(i-1)} a_m\big(\hat{F}_{\nu_j}^{(i-1)}\big)\, a_n^*\big(\hat{F}_{r_j}^{(i-1)}\big), \tag{2.22}$$

with $k = 0, 1, ..., \hat{K} - 1$. The above-mentioned grid, which has a significant impact on the accuracy achieved by the CLEAN algorithm, has the following properties:

1) its center depends on both $\hat{F}_{\nu_k}^{(i-1)}$ and $\hat{F}_{r_k}^{(i-1)}$;

2) its step sizes get smaller as i increases. More precisely, its node (z_ν, z_r) (with $z_\nu = 0, 1, ..., \tilde{M}_0 - 1$ and $z_r = 0, 1, ..., \tilde{N}_0 - 1$) is associated with the frequencies $(\tilde{F}_\nu^{(i)}[z_\nu], \tilde{F}_r^{(i)}[z_r])$[4]. In Table 2.1 it is shown how the nodes of the above-mentioned grid are selected; in that Table, $\delta_X = 1/M_0$ and $\tilde{Q}_0 = \tilde{M}_0 - 1$ if $X = \nu$ ($\delta_X = 1/N_0$ and $\tilde{Q}_0 = \tilde{N}_0 - 1$ if $X = r$). The nodes are grouped in the set

$$\mathcal{I}_{\nu,r}^{(i)}\big(\tilde{M}_0, \tilde{N}_0\big) = \mathcal{I}_\nu^{(i)}\big(\tilde{M}_0\big) \times \mathcal{I}_r^{(i)}\big(\tilde{N}_0\big), \tag{2.26}$$

where $\mathcal{I}_\nu^{(i)}(\tilde{M}_0)$ and $\mathcal{I}_r^{(i)}(\tilde{N}_0)$ are the sets collecting the $\tilde{M}_0$ and $\tilde{N}_0$ frequencies $\{\tilde{F}_\nu^{(i)}[z_\nu]\}$ and $\{\tilde{F}_r^{(i)}[z_r]\}$, respectively.

Maximizing the function $S_k^{(i)}(\tilde{F}_\nu, \tilde{F}_r)$ (2.21) over $\mathcal{I}_{\nu,r}^{(i)}$ (2.26) leads to the estimates $\hat{F}_{\nu_k}^{(i)}$ and $\hat{F}_{r_k}^{(i)}$ of F_{ν_k} and F_{r_k}, respectively. Finally, the new estimate $\hat{A}_k^{(i)} = S_k^{(i)}(\hat{F}_{\nu_k}^{(i)}, \hat{F}_{r_k}^{(i)})$ of A_k is evaluated.

It is important to point out that:

1) the evaluation of $\hat{H}_{m,n}^{(i)}[k]$ according to (2.22) aims at canceling the contribution given to $\hat{H}_{m,n}[0]$ by the $(\hat{K} - 1)$ targets different from the kth one in the ith iteration;

2) at the end of the last (i.e., of the N_{REF}th) iteration, the refined estimates $\{(\hat{F}_{\nu_k}^{(N_{\text{REF}})}, \hat{F}_{r_k}^{(N_{\text{REF}})}, \hat{A}_k^{(N_{\text{REF}})}); k = 0, 1, ..., \hat{K} - 1\}$ become available;

3) the value assigned to δ_X (with $X = \nu$ and r) allows covering two adjacent bins of the evaluated DSFT.

It can be shown that the computational cost of the CLEAN algorithm with refinement is $\mathcal{O}(N_{\text{CL}})$, where (see [20, Sec. III-E, eq. (43)])

$$N_{\text{CL}} = \bar{N}_{\text{CL}}\,(M_0, N_0) + N_{\text{REF}}\,\bar{N}_{\text{CL}}\big(\tilde{M}_0, \tilde{N}_0\big). \tag{2.27}$$

Here,

$$\bar{N}_{\text{CL}}(M_0, N_0) = K[MN\,(6M_0N_0 + 15) + 2M_0N_0\,(M + N)] \tag{2.28}$$

is the contribution due to a single iteration of the algorithm; note that the parameters (M_0, N_0) and $(\tilde{M}_0, \tilde{N}_0)$ define the grid sizes for the initialization and for the refinement steps, respectively.

2.3.2 Subspace-based methods

The use of subspace methods for target range and Doppler estimation has been investigated in [3] and [8, 9, 50]. In particular, algorithms based on the MUSIC technique have

[4] In the equations listed in Table 2.1 and in (2.26), the dependence of $\tilde{F}_X^{(i)}[z_X]$ and $\mathcal{I}_{\nu,r}^{(i)}$ on the target index k is not specified to ease notation.

been analyzed in [3, 9, 22] and [8], whereas the use of the 2D-ESPRIT for the estimation of the delay and Doppler of multiple targets has been studied in [50]. Various results illustrated in the above-mentioned papers lead to the conclusion that MUSIC-based algorithms can outperform 2D FFT-based methods for joint range-velocity estimation at the price, however, of a significantly larger computational complexity [8]. A lower complexity version of the MUSIC technique, called *auto-paired method*, has been proposed in [9], whereas an iterative method for improving the robustness of the MUSIC algorithm has been developed in [3].

In the following we concentrate on the 2D-MUSIC algorithm only, since it performs similarly as the 2D-ESPRIT at a comparable computational cost [11, 51]. This algorithm is based on the search of $\hat{K}$ local maxima in the 2D-MUSIC spectrum (also known as *pseudo spectrum*), whose computation requires the identification of the so-called *noise subspace*. In practice, the algorithm needs a prior estimate (denoted $\hat{K}$) of K and consists of the following steps:

1) The $(M\,N) \times (M\,N)$ correlation matrix

$$\mathbf{R} \triangleq \frac{1}{MN} \bar{\mathbf{H}}\, \bar{\mathbf{H}}^H \tag{2.29}$$

is evaluated; here, $\bar{\mathbf{H}}$ denotes the (MN)-dimensional column vector generated by the ordered concatenation of the columns of the $M \times N$ matrix $\hat{\mathbf{H}} = [\hat{H}_{m,n}]$ (see (2.6)).

2) The *pseudo-spectrum*

$$P_{\mathrm{MUSIC}}[l,p] \triangleq \left| \mathbf{Q}_{\mathrm{n}}^H\, \bar{\mathbf{M}}[l,p] \right|^{-2} \tag{2.30}$$

is computed for $l = 0, 1, ..., M_0 - 1$ and $p = 0, 1, ..., N_0 - 1$; here, M_0 and N_0 are integer parameters defining the size of the search space for the normalized Doppler frequency and the normalized delay, respectively, $\bar{\mathbf{M}}[l,p]$ is a $(MN) \times (M_0\, N_0)$ matrix whose (m,n)th element is defined by the product $a_m(F_\nu[l])\, a_n^*(F_r[p])$ (with $F_\nu[l]$ and $F_r[p]$ expressed by (2.10) and (2.11), respectively) and $\mathbf{Q}_{\mathrm{n}}$ is $(MN) \times (MN - \hat{K})$ matrix, whose columns represent the $(MN - \hat{K})$ eigenvectors of $\mathbf{R}$ (2.29) associated with noise[5].

3) The estimates of the normalized delay and of the normalized Doppler frequency are evaluated by finding the global maximum of the pseudo-spectrum (2.30) in the case of a single target or its $\hat{K}$ highest local peaks in the case of multiple targets. Note that, in the last case, all the local maxima of the cost function can be really identified if the spacing between all the targets is greater than the grid step size; this problem can be mitigated by using a finer grid (i.e., a smaller step size) at the price, however, of a larger computational complexity.

The overall 2D-MUSIC complexity is $\mathcal{O}(N_{\mathrm{MUSIC}})$, where

$$N_{\mathrm{MUSIC}} = C_{\mathrm{R}} + C_{\mathrm{e}} + C_{\mathrm{P}}. \tag{2.31}$$

Here, we have that: a) $C_{\mathrm{R}} = 10(MN)^2 + 2MN - 2$ is the cost due to the computation of the covariance matrix $\mathbf{R}$ (2.29); b) $C_{\mathrm{e}} \approx (MN)^3$ is the contribution due to the computation of

[5]This is true in the absence of fully correlated targets, i.e., when the span of the useful signal subspace is $\hat{K}$-dimensional.

the eigenvalues of the matrix $\mathbf{R}$ (2.29); c) $C_{\mathrm{P}} = M_0\, N_0(8(M\,N)^2 + M\,N)$ is the contribution due to the evaluation of the pseudo-spectrum (see (2.30)).

2.3.3 Maximum likelihood-based techniques

Maximum likelihood-based algorithms are able to achieve an accuracy comparable to that of subspace methods at the price of an increase in computational complexity [11–13, 52]. Recent research contributions to this field concern: 1) the exploitation of *alternating maximization* approach to mitigate the computational complexity of ML estimation [11]; 2) the derivation of an iterative non-linear KLMS-based estimation technique for the estimation of target range [12]; 3) the development of an ML method, based on a kinematic model of detected targets, for estimating target speed [13].

In the following, we first take into consideration the approximate ML methods recently proposed in [11] and show how they can be adapted to the signal model [6] (2.6); the resulting algorithms are dubbed *modified Zhang* ML (MZML) and *modified alternating projection* ML (MAP-ML). Both these algorithms are iterative; however, the first one maximizes a 2D cost function, whereas the second one exploits the method of alternating projections to turn a 2D optimization problem into a couple of simpler 1D sub-problems in order to mitigate the overall computational effort. Finally, we take into consideration the Modified Wax & Leshem (MWL) algorithm developed in [21] and [20] for joint range and azimuth estimation of multiple targets in Frequency Modulated Continuous Wave (FMCW) radar systems, and the EM algorithm developed in [20] and [11]. In particular, the last algorithm is exploited as follows. It is initialized by means of the 2D-FFT technique. Then, in each of its iterations, it accomplishes leakage compensation in the same way as the MZML algorithm. The resulting algorithm is denoted *Modified Zhang* EM (MZEM) in the following.

2.3.3.1 Modified Zhang maximum likelihood algorithm

This algorithm operates in an iterative fashion; in each of its iterations, the estimates of the detected targets are refined. It is initialized by: 1) setting the iteration index i to 1; 2) selecting the initial estimate of the normalized Doppler frequency F_{ν_k} and that of the normalized delay F_{r_k} as $\hat{F}_{\nu_k}^{(0)} = F_\nu[\hat{l}_k^{(0)}]$ and $\hat{F}_{r_k}^{(0)} = F_r[\hat{p}_k^{(0)}]$, respectively (see (2.10) and (2.11)), where $(\hat{l}_k^{(0)}, \hat{p}_k^{(0)})$ is computed on the basis of (2.14) (with $k = 0, 1, ..., \hat{K}-1$, where $\hat{K}$ denotes the prior estimate of K). Then, its iterations are started. The input of the ith iteration (with $i = 1, 2, ..., N_{\mathrm{REF}}$, where N_{REF} denotes the overall number of iterations) is represented by the $\hat{K}$-dimensional vectors

$$\hat{\mathbf{F}}_\nu^{(i-1)} = \left[\hat{F}_{\nu_0}^{(i-1)}, \hat{F}_{\nu_1}^{(i-1)}, ..., \hat{F}_{\nu_{\hat{K}-1}}^{(i-1)}\right]^T \tag{2.32}$$

and

$$\hat{\mathbf{F}}_r^{(i-1)} = \left[\hat{F}_{r_0}^{(i-1)}, \hat{F}_{r_1}^{(i-1)}, ..., \hat{F}_{r_{\hat{K}-1}}^{(i-1)}\right]^T, \tag{2.33}$$

[6] Note that, in our model, unlike the one considered in [11], *inter-pulse* and *inter-subcarrier* Doppler effects are neglected.

that collect the estimates of the normalized Doppler frequency and the normalized delay, respectively, of the $\hat{K}$ tones estimated in the previous $(i-1)$ iterations, and produces the new estimates $\hat{\mathbf{F}}_{\nu}^{(i)}$ and $\hat{\mathbf{F}}_{r}^{(i)}$. Moreover, in the ith iteration, two distinct steps that are repeated sequentially for each target (i.e., for $k = 0, 1, ..., \hat{K}-1$) are executed; the description of these steps is provided below for the kth target.

1) *Computation of the cost function* — In this step, the cost function

$$J_k^{(i)}\big(\tilde{F}_{\nu_k}, \tilde{F}_{r_k}\big) \triangleq \bar{\mathbf{H}}^H \, \mathbf{P}_k^{(i)}\big(\tilde{F}_{\nu_k}, \tilde{F}_{r_k}\big)\bar{\mathbf{H}} \tag{2.34}$$

is evaluated for $(\tilde{F}_{\nu_k}, \tilde{F}_{r_k}) \in \mathcal{I}_{\nu}^{(i)}(M_0) \times \mathcal{I}_{r}^{(i)}(N_0)$; here, $\mathcal{I}_{X}^{(i)}(Y)$ denotes the set[7] of Y trial values selected for $\tilde{F}_{X_k}$ (with $X = D$ and r) in the ith iteration, $\bar{\mathbf{H}}$ is the (MN)-dimensional vector resulting from the ordered concatenation of the columns of the $M \times N$ matrix $\hat{\mathbf{H}}_{m,n} = [\hat{H}_{m,n}]$ (see (2.6)),

$$\mathbf{P}_k^{(i)}\big(\tilde{F}_{\nu_k}, \tilde{F}_{r_k}\big) \triangleq \breve{\mathbf{M}}_k^{(i)} \left(\big(\breve{\mathbf{M}}_k^{(i)}\big)^H \breve{\mathbf{M}}_k^{(i)} \right)^{-1} \big(\breve{\mathbf{M}}_k^{(i)}\big)^H \tag{2.35}$$

is the $(MN) \times (MN)$ *orthogonal projection matrix*,

$$\breve{\mathbf{M}}_k^{(i)} \triangleq \left[\mathbf{M}_0^{(i-1)}, \mathbf{M}_1^{(i-1)}, ..., \mathbf{M}_{k-1}^{(i-1)}, \mathbf{M}_{k+1}^{(i-1)}, ..., \mathbf{M}_{\hat{K}-1}^{(i-1)}, \dot{\mathbf{M}}_k^{(i)}\right] \tag{2.36}$$

is a $(MN) \times \hat{K}$ matrix[8]. The uth element of the last matrix, namely

$$\mathbf{M}_u^{(i-1)} = \mathbf{M}_u^{(i-1)}(\hat{F}_{\nu_u}^{(i-1)}, \hat{F}_{r_u}^{(i-1)}) \tag{2.37}$$

is an (MN)-dimensional column vector that results from the ordered concatenation of the columns of the $M \times N$ matrix $\hat{\mathbf{M}}_u^{(i-1)}$, whose element (m, n) is expressed by the product $a_m(\hat{F}_{\nu_u}^{(i-1)})\, a_n^*(\hat{F}_{r_u}^{(i-1)})$ for any $u \neq k$ (see (2.3)), and $\dot{\mathbf{M}}_k^{(i)}$ is an (MN)-dimensional column vector generated by the ordered concatenation of the columns of the $M \times N$ matrix $\tilde{\mathbf{M}}_k^{(i)}$, whose element (m, n) is expressed by the product $a_m(\tilde{F}_{\nu_k})\, a_n^*(\tilde{F}_{r_k})$.

It is worth pointing out that:

1) the vector $\mathbf{M}_u^{(i-1)}$ (2.37) represents the contribution of the uth target (with $u \neq k$), evaluated on the basis of its parameters estimated in the $(i-1)$th iteration, to the vector $\dot{\mathbf{M}}_k^{(i)}$ (computed for the kth target in the ith iteration);

2) evaluating the matrix $\breve{\mathbf{M}}_k^{(i)}$ on the basis of (2.36) allows compensating for the spectral *leakage* affecting the projection matrix $\mathbf{P}_k^{(i)}(\cdot, \cdot)$ (2.35);

3) the sets $\mathcal{I}_{\nu}^{(i)}(M_0)$ and $\mathcal{I}_{r}^{(i)}(N_0)$ are generated by means of the same procedure illustrated for the CLEAN algorithm [21] in Section 2.3.1.2 (see (2.23)-(2.25), in Table 2.1).

[7] Once again, the dependence of $\mathcal{I}_{X}^{(i)}(Y)$ on the target index k is omitted for simplicity. This consideration also applies to the set of trial values employed by the MZML and the MZEM algorithms.

[8] The dependence of the matrices $\breve{\mathbf{M}}_k^{(i)}$, $\tilde{\mathbf{M}}_k^{(i)}$and of the vector $\dot{\mathbf{M}}_k^{(i)}$ (see below) on the trial variables $\tilde{F}_{\nu_k}$ and $\tilde{F}_{r_k}$ is not always explicitly shown for simplicity. For the same reason, the dependence of $\hat{\mathbf{M}}_u^{(i-1)}$ (see below) on $\hat{F}_{\nu_u}^{(i-1)}$ and $\hat{F}_{r_u}^{(i-1)}$ is not indicated.

2) *Target parameter estimation* — In this step, the estimates $\hat{F}_{\nu_k}^{(i)}$ and $\hat{F}_{r_k}^{(i)}$ of F_{ν_k} and F_{r_k} are computed as

$$\left(\hat{F}_{\nu_k}^{(i)}, \hat{F}_{r_k}^{(i)}\right) = \underset{(\tilde{F}_{\nu_k}, \tilde{F}_{r_k}) \in \mathcal{I}_{\nu}^{(i)}(M_0) \times \mathcal{I}_{r}^{(i)}(N_0)}{\arg\max} \left| J_k^{(i)}\left(\tilde{F}_{\nu_k}, \tilde{F}_{r_k}\right) \right|, \tag{2.38}$$

Then, the new estimate $\hat{A}_k^{(i)}$ of the complex amplitude A_k is evaluated as

$$\hat{A}_k^{(i)} = \left(\left(\breve{\mathbf{M}}_k^{(i)}\left(\hat{F}_{\nu_k}^{(i)}, \hat{F}_{r_k}^{(i)}\right) \right)^H \breve{\mathbf{M}}_k^{(i)}\left(\hat{F}_{\nu_k}^{(i)}, \hat{F}_{r_k}^{(i)}\right) \right)^{-1} \left(\breve{\mathbf{M}}_k^{(i)}\left(\hat{F}_{\nu_k}^{(i)}, \hat{F}_{r_k}^{(i)}\right) \right)^H. \tag{2.39}$$

At the end of the last iteration, the vectors $\hat{\mathbf{F}}_{\nu}^{(N_{\mathrm{REF}})}$, $\hat{\mathbf{F}}_{r}^{(N_{\mathrm{REF}})}$ and $\hat{\mathbf{A}}^{(N_{\mathrm{REF}})}$, collecting the normalized frequencies, the normalized delays and the complex amplitudes of the $\hat{K}$ targets are available.

The overall computational cost of MZML algorithm can be expressed as

$$\mathcal{C}_{\mathrm{MZML}} \triangleq \mathcal{C}_{0,\mathrm{MZML}} + N_{\mathrm{REF}}\, \mathcal{C}_{i,\mathrm{MZML}}, \tag{2.40}$$

where $\mathcal{C}_{0,\mathrm{MZML}}$ is the cost of its initialization (i.e., the same cost as the 2D-FFT method; see (2.16)), whereas

$$\mathcal{C}_{i,\mathrm{MZML}} \triangleq \mathcal{C}_P + \mathcal{C}_J + \mathcal{C}_{\mathrm{opt}} \tag{2.41}$$

represents the cost of a single iteration; here, we have that: 1) $\mathcal{C}_P \approx 8M_0\, N_0\, \hat{K}^2 M^2 N^2$ ($\mathcal{C}_J \approx 8M_0\, N_0\, \hat{K}\, M^2 N^2$) is the cost due to the evaluation of the projection matrix $\mathbf{P}_k^{(i)}(\cdot,\cdot)$ (2.35) (of the function $J_k^{(i)}(\cdot,\cdot)$ (2.34)) for all the $M_0\, N_0$ nodes of the grid and all the $\hat{K}$ targets; 2) $\mathcal{C}_{\mathrm{opt}} = 4M_0\, N_0\, \hat{K}$ is the cost due to solving the optimization problem in (2.38). Based on these results, it can be shown that the computational cost of MZML algorithm is $\mathcal{O}(N_{\mathrm{MZML}})$, where

$$N_{\mathrm{MZML}} = N_{\mathrm{REF}}\, 8\, M_0\, N_0 \left(\hat{K}^2 + \hat{K}\right) M^2 N^2. \tag{2.42}$$

2.3.3.2 Modified alternating projection maximum likelihood algorithm

The MAP-ML algorithm is initialized exactly in the same way as the MZML algorithm (see [11]) and employs the cost function $J_k^{(i)}(\tilde{F}_{\nu_k}, \tilde{F}_{r_k})$ (2.34) in the estimation of the parameters of the kth target; however, the method of *alternating projection* is exploited for the maximization of that cost function in order to replace the 2D optimization problem (2.38) with two 1D optimization problems. In practice, in its ith iteration, the frequency estimates $\hat{F}_{\nu_k}^{(i)}$ and $\hat{F}_{r_k}^{(i)}$ appearing in the LHS of (2.38) are evaluated as

$$\hat{F}_{r_k}^{(i)} = \arg \underset{\tilde{F}_{r_k} \in \mathcal{I}_{r}^{(i)}(N_0)}{\max} \left| J_k^{(i)}\left(\hat{F}_{\nu_k}^{(i-1)}, \tilde{F}_{r_k}\right) \right| \tag{2.43}$$

and

$$\hat{F}_{\nu_k}^{(i)} = \arg \underset{\tilde{F}_{\nu_k} \in \mathcal{I}_{\nu}^{(i)}(M_0)}{\max} \left| J_k^{(i)}\left(\tilde{F}_{\nu_k}, \hat{F}_{r_k}^{(i)}\right) \right|, \tag{2.44}$$

respectively (the sets $\mathcal{I}_r^{(i)}(N_0)$ and $\mathcal{I}_\nu^{(i)}(M_0)$ have been already defined for the MZML algorithm). It is important to note that: 1) the evaluation of $J_k^{(i)}(\hat{F}_{\nu_k}^{(i-1)}, \tilde{F}_{r_k})$ and $J_k^{(i)}(\tilde{F}_{\nu_k}, \hat{F}_{r_k}^{(i)})$ in the RHSs (2.43) and (2.44) requires computing the matrices $\breve{\mathbf{M}}_k^{(i)}(\hat{F}_{\nu_k}^{(i-1)}, \tilde{F}_{r_k})$ and $\breve{\mathbf{M}}_k^{(i)}(\tilde{F}_{\nu_k}, \hat{F}_{r_k}^{(i)})$ (see (2.36)), respectively; 2) in the first iteration (i.e., for $i = 1$), $\hat{F}_{\nu_k}^{(0)}$ is computed according to (2.10), with $l = \hat{l}_k^{(0)}$, where $\hat{l}_k^{(0)}$ results from solving (2.14) (the value of p, $\hat{p}_k^{(0)}$, associated with $\hat{l}_k^{(0)}$ is discarded); 3) the estimate of the complex amplitude $\hat{A}_k^{(i)}$ is computed on the basis of (2.39).

The overall computational cost $\mathcal{C}_{\mathrm{MAP-ML}}$ of the MAP-ML algorithm can be expressed as

$$\mathcal{C}_{\mathrm{MAP-ML}} = \mathcal{C}_{0,\mathrm{MAP-ML}} + N_{\mathrm{REF}}\, \mathcal{C}_{i,\mathrm{MAP-ML}}, \tag{2.45}$$

where $\mathcal{C}_{0,\mathrm{MAP-ML}}$ is the contribution due to its initialization (equal to $\mathcal{C}_{0,\mathrm{MZML}}$; see (2.40)), whereas

$$\mathcal{C}_{i,\mathrm{MAP-ML}} = \mathcal{C}_{P_r} + \mathcal{C}_{P_\nu} + \mathcal{C}_{J_r} + \mathcal{C}_{J_\nu} + \mathcal{C}_r + \mathcal{C}_\nu \tag{2.46}$$

is the contribution due to each of its iterations. Moreover, in the last formula, we have that:

1) $\mathcal{C}_{P_r} \approx 8N_0\hat{K}^2M^2N^2$ and $\mathcal{C}_{P_\nu} \approx 8M_0\hat{K}^2M^2N^2$ are the costs due to the evaluation of the projection matrix $\mathbf{P}_k^{(i)}(\cdot,\cdot)$ (2.35) in the first and second 1D optimization, respectively;

2) $\mathcal{C}_{J_r} \approx 8N_0\hat{K}M^2N^2$ and $\mathcal{C}_{J_\nu} \approx 8M_0\hat{K}M^2N^2$ are the costs due to the evaluation of the function $J_k^{(i)}(\cdot,\cdot)$ (2.34) in the first and second 1D optimization, respectively;

3) $\mathcal{C}_r = 4N_0$ and $\mathcal{C}_\nu = 4M_0$ are the costs required by solving the 1D maximization in (2.43) and (2.44), respectively.

Based on (2.45)-(2.46), it can be shown that the computational cost of the MAP-ML algorithm is $\mathcal{O}(N_{\mathrm{MAP-ML}})$, where

$$N_{\mathrm{MAP-ML}} = N_{\mathrm{REF}}\, 8(M_0 + N_0)\,(\hat{K}^2 + \hat{K})\, M^2N^2. \tag{2.47}$$

2.3.3.3 MWL algorithm

Similarly to the CLEAN algorithm [21], the MWL algorithm operates in an iterative fashion and, in each of its iterations, estimates the parameters of a new target and performs cancellation and leakage compensation in the time domain. However, unlike the CLEAN algorithm, the MWL algorithm requires solving 1D optimization problems only. Moreover, it can achieve similar and even better accuracy than the CLEAN algorithm with a smaller computational effort [20].

The MWL algorithm is initialized by setting the iteration index k to 0 and $\hat{H}_{m,n}[0] = \hat{H}_{m,n}$ (see (2.6)), with $m = 0, 1, ..., M-1$ and $n = 0, 1, ..., N-1$. Then, its iterations are started; the processing accomplished in the kth iteration evolves through the four steps described below.

1) *Coarse estimation of the Doppler of a new target* — In this step, the *coarse estimate* $\breve{F}_{\nu_k}$ of the Doppler frequency F_{ν_k} of a new (namely, of the kth) target is computed by solving the 1D optimization problem

$$\breve{l}_k \triangleq \arg \max_{\tilde{l} \in \mathcal{S}_{M_0}} \mathbf{a}^H\big(F_\nu[\tilde{l}]\big)\mathbf{R}\,[k]\;\mathbf{a}\big(F_\nu[\tilde{l}]\big), \tag{2.48}$$

where $F_\nu[\tilde{l}]$ is defined by (2.10), $\mathbf{a}(F_\nu[\tilde{l}])$ is an M-dimensional column vector whose mth element (with $m = 0, 1, ..., M-1$) is $a_m(F_\nu[\tilde{l}])$ (see (2.3)), $\mathbf{R}[k] = [R_{m,m'}[k]]$ is an $M \times M$ autocorrelation matrix such that

$$R_{m,m'}\,[k] \triangleq \frac{1}{N}\sum_{n=0}^{N-1} \hat{H}_{m,n}\,[k]\left(\hat{H}_{m',n}[k]\right)^H, \tag{2.49}$$

where $\hat{H}_{m,n}[k]$ is evaluated on the basis of (2.19) if $k > 0$, with $m = 0, 1, ..., M-1$ and $m' = 0, 1, ..., M-1$. Given $\breve{l}_k$ (2.48), the coarse estimate of F_{ν_k} is computed as $\breve{F}_{\nu_k} = F_\nu[\breve{l}_k]$ (see (2.10)).

2) *Estimation of target delay* — In this step, an estimate $\hat{F}_{r_k}$ of the normalized delay F_{r_k} characterizing the kth target is evaluated by solving another 1D optimization problem. This requires:

a) Computing the N-dimensional column vector

$$\hat{\mathbf{v}}_k \triangleq [\hat{v}_k[0], \hat{v}_k[1], ..., \hat{v}_k[N-1]]^T, \tag{2.50}$$

where

$$\hat{v}_k[n] \triangleq \left[\mathbf{a}^H\big(\breve{F}_{\nu_k}\big)\,\mathbf{a}\big(\breve{F}_{\nu_k}\big)\right]^T\;\mathbf{a}^H\big(\breve{F}_{\nu_k}\big)\,\mathbf{H}_n\,[k], \tag{2.51}$$

with $n = 0, 1, ..., N-1$, and $\mathbf{H}_n[k] \triangleq [\hat{H}_{0,n}[k], \hat{H}_{1,n}[k], ..., \hat{H}_{M-1,n}[k]]^T$ is an M-dimensional vector.

b) Evaluating

$$\hat{p}_k = \arg \max_{\tilde{p} \in \mathcal{S}_{N_0}} \left|\mathbf{a}^H\,(-F_r\,[\tilde{p}])\;\hat{\mathbf{v}}_k\right|^2, \tag{2.52}$$

where $F_r[\tilde{p}]$ is defined by (2.11), and $\mathbf{a}(-F_r[\tilde{p}])$ is an N-dimensional column vector whose n-element (with $n = 0, 1, ..., N-1$) is $a_n(-F_r[\tilde{p}])$ (see (2.3)). Given $\hat{p}_k$ (2.52), the final estimate $\hat{F}_{r_k}$ of the target delay is evaluated according to (2.11) with $p = \hat{p}_k$.

3) *Fine estimation of target Doppler* — In this step, the *fine estimate* $\hat{F}_{\nu_k}$ of the normalized Doppler F_{ν_k} characterizing the kth target is evaluated by solving the last 1D optimization problem and, in particular, as $\hat{F}_{\nu_k} = F_\nu[\hat{l}_k]$ (see (2.10)), where

$$\hat{l}_k \triangleq \arg \max_{\tilde{l} \in \mathcal{S}_{M_0}} \left|\mathbf{a}^H\big(F_\nu[\tilde{l}]\big)\hat{\mathbf{B}}\big(\hat{F}_{r_k}\big)\right|^2, \tag{2.53}$$

$\hat{\mathbf{B}}(\hat{F}_{r_k})$ is an M-dimensional column vector, whose mth element is defined as

$$\hat{B}_m\big(\hat{F}_{r_k}\big) \triangleq \left[\sum_{n=0}^{N-1} \hat{H}_{m,n}\, a_n^*\big(-\hat{F}_{r_k}\big)\right] \hat{C}^{-1}\big(\hat{F}_{r_k}\big), \tag{2.54}$$

and

$$\hat{C}\big(\hat{F}_{r_k}\big) \triangleq \sum_{n=0}^{N-1} a_n\big(-\hat{F}_{r_k}\big) a_n^*\big(-\hat{F}_{r_k}\big). \tag{2.55}$$

4) *Estimation of target complex amplitude* — In this step, the estimate

$$\hat{A}_k = \Big\|\mathbf{a}\big(\hat{F}_{\nu_k}\big)\Big\|^{-2}\, \mathbf{a}^H\big(\hat{F}_{\nu_k}\big)\, \hat{\mathbf{B}}\big(\hat{F}_{r_k}\big), \tag{2.56}$$

of the complex amplitude A_k is evaluated. Here, $\|\cdot\|$ denotes the *vector norm* operator.

Similarly as the CLEAN algorithm [21], at the end of the last step a false target is detected if $|\hat{A}_k| < \mathcal{T}_{\mathrm{MWL}}$, where $\mathcal{T}_{\mathrm{MWL}}$ denotes a proper (positive) threshold. When this occurs, the execution is stopped; otherwise, a new iteration is started going back to step 1).

An iterative procedure can be employed to refine the target estimates generated by the MWL algorithm. Similarly to the CLEAN algorithm, this procedure is based on:

1) estimating again the parameters of each target after removing the spectral contribution of the other $(\hat{K}-1)$ targets, i.e., their *leakage*;

2) shrinking the search grid as iterations evolve (see (2.23)-(2.25), in Table 2.1). In the ith iteration of the refinement (with $i = 1, 2, ..., N_{\mathrm{REF}}$), the finer estimates $\{(\hat{F}_{\nu_k}^{(i)},\, \hat{F}_{r_k}^{(i)},\, \hat{A}_k^{(i)});\ k = 0, 1, ..., \hat{K}-1\}$ of the parameters of the $\hat{K}$ targets detected by the MWL algorithm are computed as follows. First, we compute the coarse estimate

$$\breve{F}_{\nu_k}^{(i)} \triangleq \arg \max_{\tilde{F}_{\nu_k} \in \mathcal{I}_\nu^{(i)}(\tilde{M}_0)} \Big|\mathbf{a}^H\big(\tilde{F}_{\nu_k}\big)\mathbf{R}^{(i)}\,[k]\ \mathbf{a}\big(\tilde{F}_{\nu_k}\big)\Big|^2 \tag{2.57}$$

of the normalized Doppler frequency for the kth target; here, $\mathcal{I}_\nu^{(i)}(\tilde{M}_0)$ denotes the set of $\tilde{M}_0$ trial values selected for $\tilde{F}_{\nu_k}$ in the ith iteration and $\mathbf{R}^{(i)}[k]$ is an $M \times M$ matrix whose element (m, m') is still defined by (2.49), where, however, $\hat{H}_{m,n}[k]$ is replaced by

$$\breve{H}_{m,n}^{(i)}\,[k] = \hat{H}_{m,n}[0] - \sum_{j=0,\, j\neq k}^{\hat{K}-1} \hat{A}_j^{(i-1)}\, a_m\big(\hat{F}_{\nu_j}^{(i-1)}\big)\, a_n^*\big(\hat{F}_{r_j}^{(i-1)}\big). \tag{2.58}$$

Then, we compute

$$\hat{F}_{r_k}^{(i)} = \arg \max_{\tilde{F}_{r_k} \in \mathcal{I}_r^{(i)}(\tilde{N}_0)} \Big|\mathbf{a}^H\big(-\tilde{F}_{r_k}\big)\, \hat{\mathbf{v}}_k^{(i)}\Big|^2, \tag{2.59}$$

where $\mathcal{I}_r^{(i)}(\tilde{N}_0)$ denotes the set of $\tilde{N}_0$ trial values selected for $\tilde{F}_{r_k}$ in the ith iteration, $\mathbf{a}(-\tilde{F}_{r_k})$ is an N-dimensional column vector whose nth element is $a_n(-\tilde{F}_{r_k})$ (see (2.3)),

$\hat{\mathbf{v}}_k^{(i)}$ plays the same role as $\hat{\mathbf{v}}_k$ in (2.52), but its nth element is defined as (see (2.51))

$$\hat{v}_k^{(i)}[n] \triangleq \left[\mathbf{a}^H\big(\breve{F}_{\nu_k}^{(i)}\big)\,\mathbf{a}\big(\breve{F}_{\nu_k}^{(i)}\big)\right]^T \mathbf{a}^H\big(\breve{F}_{\nu_k}^{(i)}\big)\,\mathbf{H}_n^{(i)}[k], \tag{2.60}$$

where $\mathbf{H}_n^{(i)}[k] \triangleq [\hat{H}_{0,n}^{(i)}[k],\, \hat{H}_{1,n}^{(i)}[k], ...,\, \hat{H}_{M-1,n}^{(i)}[k]]^T$. Finally, the new estimate

$$\hat{F}_{\nu_k}^{(i)} \triangleq \arg \max_{\tilde{F}_{\nu_k} \in \mathcal{I}_{\tilde{M}_0}^{(i)}} \left|\mathbf{a}^H\big(\tilde{F}_{\nu_k}\big)\hat{\mathbf{B}}\big(\hat{F}_{r_k}^{(i)}\big)\right|^2 \tag{2.61}$$

of F_{ν_k} is evaluated; here, $\hat{\mathbf{B}}(\hat{F}_{r_k}^{(i)})$ is a M-dimensional column vector, whose mth element (with $m = 0, 1, ..., M-1$) is still defined by (2.54) with $\hat{F}_{r_k}^{(i)}$ in place of $\hat{F}_{r_k}$. This concludes the ith iteration.

The estimates $\{(\hat{F}_{\nu_k}^{(N_{\mathrm{REF}})},\, \hat{F}_{r_k}^{(N_{\mathrm{REF}})}, \hat{A}_k^{(N_{\mathrm{REF}})});\ k = 0, 1, ..., \hat{K}-1\}$ available at the end of the last (i.e., of the N_{REF}th) iteration represent the output of the refinement algorithm.

It can be shown that the computational cost of the MWL algorithm is $\mathcal{O}(N_{\mathrm{MW}})$, where (see [20, Sec. III-E, eq.(44)])

$$N_{\mathrm{MW}} = \bar{N}_{\mathrm{MW}}(M_0, N_0) + K N_{\mathrm{REF}}\, \bar{N}_{\mathrm{MW}}(\tilde{M}_0, \tilde{N}_0) \tag{2.62}$$

and

$$\bar{N}_{\mathrm{MW}}(M_0, N_0) = M^2\,(6N + 8M_0) + 30MN + 8N_0\,N + 30M_0\,M \tag{2.63}$$

represents the cost due to a single iteration of the algorithm; note that the parameters (M_0, N_0) and $(\tilde{M}_0, \tilde{N}_0)$ define the grid size for the initialization and for the refinement step, respectively.

2.3.3.4 EM-based algorithm

The EM algorithm [53] can be employed jointly with each of the algorithms described above to *refine* its estimates of target parameters [11,20]. For this reason, we can assume that, in general, the EM algorithm is fed by the $\hat{K}$-dimensional vectors $\hat{\mathbf{F}}_\nu = [\hat{F}_{\nu_0}, \hat{F}_{\nu_1}, ..., \hat{F}_{\nu_{\hat{K}-1}}]$, $\hat{\mathbf{F}}_r = [\hat{F}_{r_0}, \hat{F}_{r_1}, ..., \hat{F}_{r_{\hat{K}-1}}]$ and $\hat{\mathbf{A}} = [\hat{A}_0, \hat{A}_1, ..., \hat{A}_{\hat{K}-1}]$, collecting the *initial estimates* of the normalized Doppler, normalized delay and the complex amplitude of the $\hat{K}$ detected targets.

The EM algorithm operates in an iterative fashion; in each of its iterations, it executes an *expectation step* (E-step) followed by a *maximization step* (M-step). In the description of such steps, we focus on the ith iteration (with $i = 1, ..., N_{\mathrm{REF}}$, where N_{REF} denotes the overall number of iterations) and consider the kth target (with $k = 0, 1, ..., \hat{K}-1$). At the beginning of this iteration, the estimates $(\hat{F}_{\nu_k}^{(i-1)}, \hat{F}_{r_k}^{(i-1)}, \hat{A}_k^{(i-1)})$ are available for the normalized Doppler, the normalized delay and the complex amplitude, respectively, of the considered target (if $i = 1$, $(\hat{F}_{\nu_k}^{(0)}, \hat{F}_{r_k}^{(0)}, \hat{A}_k^{(0)}) = (\hat{F}_{\nu_k}, \hat{F}_{r_k}, \hat{A}_k)$). The two steps accomplished within the considered iteration are described below.

1) *E step* — In this step, the cost function

$$J_{\mathrm{EM}_k}^{(i)}\big(\tilde{F}_{\nu_k},\tilde{F}_{r_k}\big)=\frac{1}{MN}\left|\Big(\breve{\mathbf{M}}_k^{(i)}\big(\tilde{F}_{\nu_k},\tilde{F}_{r_k}\big)\Big)^H\hat{\mathbf{H}}_k^{(i)}\right|^2, \tag{2.64}$$

where $(\tilde{F}_{\nu_k},\tilde{F}_{r_k})\in\mathcal{I}_\nu^{(i)}(M_0)\times\mathcal{I}_r^{(i)}(N_0)$; here, $\mathcal{I}_X^{(i)}(Y)$ denotes the set of Y trial values selected for $\tilde{F}_{X_k}$ (with $X=D$ and r) in the ith iteration. Moreover, the $(MN\times\hat{K})$ matrix $\breve{\mathbf{M}}_k^{(i)}(\tilde{F}_{\nu_k},\tilde{F}_{r_k})$ is defined by (2.36),

$$\hat{\mathbf{H}}_k^{(i)}=\hat{\mathbf{H}}_k^{(i-1)}+\beta_k^{(i)}\left[\bar{\mathbf{H}}-\sum_{k'=0}^{\hat{K}-1}\hat{\mathbf{H}}_{k'}^{(i-1)}\right] \tag{2.65}$$

is the reconstructed (MN)-dimensional vector of channel gains evaluated for the kth target in the ith iteration, $\bar{\mathbf{H}}$ is the (MN)-dimensional vector resulting from the ordered concatenation of the columns of the channel measurement matrix $\hat{\mathbf{H}}_{m,n}\triangleq[\hat{H}_{m,n}]$ (2.6), $\hat{\mathbf{H}}_k^{(i-1)}\triangleq\hat{A}_k^{(i-1)}\,\mathbf{M}_k^{(i-1)}$, where $\mathbf{M}_k^{(i-1)}$ is the (MN)-dimensional vector defined by (2.37) (with $u=k$). Moreover, for any i, the $\hat{K}$ parameters $\{\beta_k^{(i)};k=0,1,...,\hat{K}-1\}$ are the so-called *mixing coefficients* and satisfy the inequalities $0\leqslant\beta_k^{(i)}\leqslant 1$ for any k (e.g., see [20, Sec. III-D]).

2) *M step* — The new (and, hopefully, finer) estimates $\hat{F}_{\nu_k}^{(i)}$ and $\hat{F}_{r_k}^{(i)}$ of F_{ν_k} and F_{r_k}, respectively, are computed as

$$\big(\hat{F}_{\nu_k}^{(i)},\hat{F}_{r_k}^{(i)}\big)=\underset{(\tilde{F}_{\nu_k},\tilde{F}_{r_k})\in\mathcal{I}_\nu^{(i)}(M_0)\times\mathcal{I}_r^{(i)}(N_0)}{\arg\max}\ J_{\mathrm{EM}_k}^{(i)}\big(\tilde{F}_{\nu_k},\tilde{F}_{r_k}\big). \tag{2.66}$$

In the equation above, the term $J_{\mathrm{EM}_k}^{(i)}(\cdot,\cdot)$ evaluated through (2.64) represents the cost function computed over a specific rectangular grid, defined by the trial values $(\tilde{F}_{\nu_k},\tilde{F}_{r_k})$, whose center depends on both $\hat{F}_{\nu_k}^{(i-1)}$ and $\hat{F}_{r_k}^{(i-1)}$, and whose step sizes get smaller as i increases. The grid employed in this case is generated according to the same criteria illustrated for the refinement procedure developed for the CLEAN algorithm (see (2.23)-(2.25), in Table 2.1 and the comments related to them).

Finally, the complex amplitude $\hat{A}_k^{(i)}$ is evaluated as (e.g., see [11, Sec IV, eq. (48)]):

$$\hat{A}_k^{(i)}=\frac{1}{MN}\left(\dot{\mathbf{M}}_k^{(i)}\big(\hat{F}_{\nu_k}^{(i)},\hat{F}_{r_k}^{(i)}\big)\right)^T\hat{\mathbf{H}}_k^{(i)}, \tag{2.67}$$

where $\dot{\mathbf{M}}_k^{(i)}(\cdot,\cdot)$ is defined right after (2.36). This concludes the M step.

At the end of the last iteration (i.e., for $i=N_{\mathrm{REF}}$), the final estimates $(\hat{F}_{\nu_k}^{(N_{\mathrm{REF}})},\hat{F}_{r_k}^{(N_{\mathrm{REF}})},\hat{A}_k^{(N_{\mathrm{REF}})})$ are available, with $k=0,1,...\hat{K}-1$.

The overall computational cost of a single iteration of the EM algorithm in the presence of $\hat{K}$ targets can be expressed in a similar way as [20, App. C], i.e., as

$$N_{\mathrm{EM}}=\hat{K}\left(\mathcal{C}_H+\mathcal{C}_{\breve{M}}+\mathcal{C}_J+\mathcal{C}_{\mathrm{opt}}+\mathcal{C}_A\right), \tag{2.68}$$

TABLE 2.2: Computational complexity order of various estimation algorithms.

Algorithm	$\mathcal{O}(\cdot)$
2D-FFT	$M_0\,N_0\log_2(M_0\,N_0)+K(M_0\,N_0)$
MWL	$\bar{N}_{\mathrm{MW}}(M_0,N_0)+KN_{\mathrm{REF}}\,\bar{N}_{\mathrm{MW}}(\tilde{M}_0,\tilde{N}_0)$
CSFDEC	$13\,M_0\,N_0\log_2(M_0\,N_0)+K^2\,N_{\mathrm{REF}}\,N_{\mathrm{it}}\;13\,I_\nu\,I_r$
CLEAN	$\bar{N}_{\mathrm{CL}}(M_0,N_0)+N_{\mathrm{REF}}\,\bar{N}_{\mathrm{CL}}(\tilde{M}_0,\tilde{N}_0)$
MAP-ML	$N_{\mathrm{REF}}\,8\,(M_0+N_0)\,(K^2+K)\,M^2N^2$
EM	$N_{\mathrm{REF}}[K(14M\,N\,M_0\,N_0)+2K^2M\,N]$
2D-MUSIC	$(M\,N+M_0\,N_0)(M\,N)^2$
MZML	$N_{\mathrm{REF}}\,8M_0\,N_0(K^2+K)M^2N^2$

where: 1) $\mathcal{C}_H=2(\hat{K}+2)\,M\,N$ is the contribution due to the computation of (MN)-dimensional vectors $\{\hat{\mathbf{H}}_k^{(i)}\}$ (see (2.65)); 2) $\mathcal{C}_{\breve{M}}=6MNM_0N_0$ is the contribution due to the evaluation of the matrix $\breve{\mathbf{M}}_k^{(i)}(\cdot,\cdot)$ appearing in (2.64); 3) $\mathcal{C}_J=8MNM_0N_0$ is the cost due to the computation of $J_{\mathrm{EM}_k}^{(i)}(\cdot,\cdot)$ (2.64), whereas $\mathcal{C}_{\mathrm{opt}}=4M_0N_0$ is the cost of its optimization; 4) $\mathcal{C}_A=8MN$ is the cost due to the computation of $\hat{A}_k^{(i)}$ on the basis of (2.67). In this work, as already mentioned in Section 2.3.3, the EM algorithm has been employed to refine the estimates generated by the 2D-FFT algorithm. The overall computational complexity of the resulting algorithm, called MZEM, is $\mathcal{O}(N_{\mathrm{MZEM}})$, where $N_{\mathrm{MZEM}}=N_{\mathrm{2D-FFT}}+N_{\mathrm{EM}}$ (see (2.16) and (2.68)).

The computational complexity orders of the estimation algorithms described above and considered in the simulations are listed in Table 2.2.

2.4 Numerical Results

The estimation algorithms described in the previous section have been compared, in terms of accuracy and computational effort, in four distinct scenarios for different values of the SNR

$$\mathrm{SNR}\triangleq\sum_{k=1}^{K}|A_k|^2/\sigma_W^2, \tag{2.69}$$

where σ_W^2 represents the variance of each element of the complex noise sequence $\{\bar{W}_m(n)\}$ (see (2.7)). The *first scenario* (**S1**) is characterized by a single target (i.e., by $K=1$), whose range and velocity are uniformly distributed in the intervals [0, 10] m and [0, 2.78] m/s, respectively; the complex amplitude A_0 of its echo, instead, is set to one. The *second scenario* (**S2**) is characterized by four targets (i.e., by $K=4$). The range and velocity of the kth target (with $k=0,1,...,K-1$) are evaluated as

$$R_k=R_0+k\,\bar{R}\,R_{\mathrm{bin}} \tag{2.70}$$

and

$$v_k = v_0 + k\,\bar{v}\,v_{\text{bin}}, \tag{2.71}$$

respectively, and its amplitude A_k is set to 1 for any k; here, R_0 and v_0 are uniformly distributed in the interval [0, 10] m and [0, 2.78] m/s, respectively. Moreover, $\bar{R} = 1.65$ and $\bar{v} = 1.65$ represent the spacing of adjacent bins for normalized range and normalized velocity, whereas $R_{\text{bin}} \triangleq c/(2\,N\,\Delta_f)$ and $v_{\text{bin}} \triangleq c/(2\,M\,f_{\text{c}}\,T_{\text{s}})$ denote the size of range and velocity bins that characterize FFT processing in the absence of oversampling, respectively. In both **S1** and **S2**, the accuracy of eight different algorithms (namely, the 2D-FFT, CSFDEC, 2D-MUSIC, CLEAN, MWL, MZML, MAP-ML and MZEM algorithms) has been assessed in terms of *root mean square error*

$$\text{RMSE}_X \triangleq \frac{1}{N_{\text{mc}}} \sum_{t=0}^{N_{\text{mc}}-1} \sqrt{\frac{1}{K}\sum_{k=0}^{K-1} (\hat{X}_k[t] - X_k)^2}, \tag{2.72}$$

where $\hat{X}_k[t]$ denotes the estimate of the parameter X_k evaluated for the kth target in the tth Monte Carlo run, N_{mc} is the overall number of runs and $X = r$ ($X = v$) if target range (target velocity) is considered. Moreover, the following choices have been made:

1) in the evaluation of the RMSE_r, the vector collecting target ranges and the one collecting their estimates have been organized according to an ascending order (from minimum to maximum range).

2) In the evaluation of the RMSE_v, the vector collecting target velocities and the one collecting their estimates are sorted in the same way as the vectors referring to target ranges.

3) An SNR belonging to the interval $[-20, 20]$ dB has been considered.

4) The number of targets (K) has always been assumed to be known (so that events of missed detection are avoided). Note that the knowledge of K does not prevent all the algorithms from identifying false targets; in this work, unwanted detections contribute to the evaluation of the RMSE.

In the *third scenario* (**S3**), the range and velocity of the targets are computed according to the same strategy adopted in **S2**, but the SNR is fixed to 0 dB and the value of K ranges from 1 to 10. In this case, we focus on the *computational effort* required by all the algorithms considered in **S1** and **S2** and, in particular, we assess both their CT and the overall number of FLOPs they require[9].

The *fourth scenario* (**S4**) is characterized by the same number of targets as **S2** (i.e., $K = 4$) and by an SNR equal to 0 dB. Moreover, target ranges and speeds are computed according to (2.70) and (2.71), but smaller bin spacings (more precisely, $\bar{R} = 1$ and $\bar{v} = 1$) are assumed. For this reason, in this scenario, spectral leakage may substantially affect target estimation; this can be easily inferred from Fig. 2.1, where the range-Doppler map (or *ambiguity function*) is shown for the considered case. In that analysis of **S4**, we assess the *convergence speed* of six iterative algorithms (namely, the CSFDEC, CLEAN,

[9]All the algorithms have been executed on a desktop computer equipped with an i7 processor.

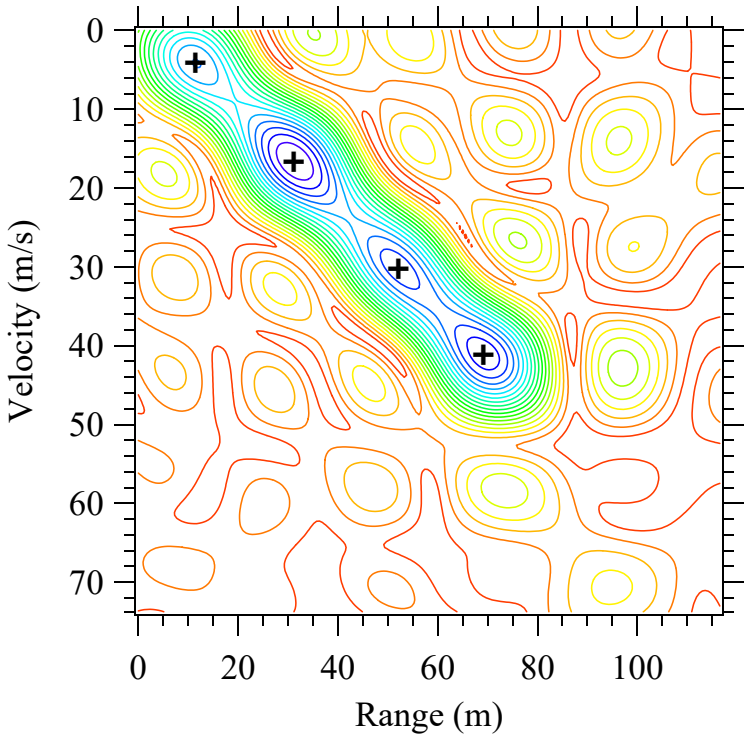

FIGURE 2.1: Range-Doppler map referring to the fourth scenario considered in the simulations. The four closely spaced targets are indicated by a black cross.

MWL, MZML, MAP-ML and MZEM algorithms) and, in particular, we analyze how their accuracy changes as the overall number of their iterations[10] ranges from 1 to 5.

The interest in the four scenarios defined above can be motivated as follows. The numerical results obtained in the first two scenarios show how the considered algorithms perform in the presence of a single tone and of multiple (but *adequately spaced*[11]) tones, respectively, whereas those obtained in the third scenario allow us to assess the trend of their computational requirements when the overall number of targets increases. Finally, the fourth scenario sheds some light on the trade-off between estimation accuracy and computational effort of the considered iterative algorithms in the presence of *closely spaced* targets.

In the simulations carried out, the following choices have been made. First of all, prior knowledge about K has been assumed and, unless differently stated, the following values have been selected for the parameters of the OFDM modulation[12]: 1) overall number of subcarriers $N = 32$; 2) overall number of OFDM symbols/frame $M = 32$; 3) subcarrier spacing $\Delta_f = 250$ kHz; 4) cyclic prefix duration $T_{\mathrm{G}} = 0.25T = 1\mu$s (consequently, the OFDM symbol duration is $T_{\mathrm{s}} = 1/\Delta_f + T_{\mathrm{G}} = 5$ µs); 5) carrier frequency $f_{\mathrm{c}} = 79$ GHz. These values entail that $R_{\mathrm{bin}} = 18.7$ m and $v_{\mathrm{bin}} = 12$ m/s.

[10] In the case of the CSFDEC algorithm, each iteration corresponds to the execution of the re-estimation procedure described in Chapter 1 Section 1.3.2.

[11] This means that the spectral leakage affecting each tone and originating from all the other tones is limited; therefore, the frequency estimation error due to this phenomenon is negligible.

[12] The choices we made for the following parameters have been dictated by the technical literature on OFDM-based JCAS systems (e.g., see [11]).

Secondly, the following values have been selected for the parameters of the considered algorithms: 1) the oversampling factor $L_\nu = 16$ and $L_r = 16$ have been chosen for Doppler and range estimation, respectively, in both the 2D-FFT and CSFDEC algorithms (so that $M_0 = ML_\nu = 512$ and $N_0 = NL_r = 512$; see (2.12) and (2.13), respectively); 2) the 2D-FFT method has been used to compute the initial estimates of the MZML, MAP-ML and MZEM algorithms; 3) in the CSFDEC algorithm, $N_{\text{it}} = 20$ refinement steps have been accomplished in the computation of the residuals and the interpolation[13] orders $I_\nu = I_r = 7$ have been selected; 4) a unit value has been assigned to the coefficient $\beta_k^{(i)}$ (with $k = 0, 1, ..., K-1$ and $i = 1, 2, ..., N_{\text{REF}}$) in the EM algorithm (see (2.65)); 5) $N_{\text{REF}} = 5$ ($N_{\text{REF}} = 3$) re-estimations have been executed by the CSFDEC, CLEAN and MWL (MZML, MAP-ML and MZEM) algorithms in the first three scenarios. Substantial attention has been paid to the selection of search grids. A brief description of the search grid adopted for the 2D-MUSIC is provided in Table 2.3, whereas that of the initial search grid employed for the CLEAN and MWL algorithms is shown in Table 2.4. In both tables, the grid chosen for a specific scenario is described by the triplet $[X_{\min}, X_{\max}, Q_0]$, where $X_{\min}$ ($X_{\max}$) denotes the minimum (maximum) trial value for the variable X, and Q_0 represents the overall number of (uniformly spaced) trial values[14] ($Q = M$ if X represents the target range R, whereas $Q = N$ if X represents target velocity v). Moreover, in our simulations, $M_0 = N_0 = 11$ ($M_0 = N_0 = 9$) have been chosen for the grid size in the CLEAN and MWL (MZML, MAP-ML and MZEM) algorithms during the re-estimation steps.

TABLE 2.3: Main parameters of the search grid selected for the 2D-MUSIC algorithm (range is expressed in m, velocity in m/s).

2D-MUSIC	$[R_{\min}, R_{\max}, N_0]$	$[v_{\min}, v_{\max}, M_0]$
S1	[0, 12, 21]	[0, 3.45, 31]
S2	[0, 120, 201]	[0, 23, 201]
S3	[0, 300, 201]	[0, 57.5, 501]

TABLE 2.4: Main parameters of the initial search grid selected for the CLEAN and MWL algorithms (range is expressed in m, velocity in m/s).

CLEAN & MWL	$[R_{\min}, R_{\max}, N_0]$	$[v_{\min}, v_{\max}, M_0]$
S1	[0, 12, 21]	[0, 3.45, 31]
S2	[0, 120, 201]	[0, 23, 201]
S3	[0, 300, 501]	[0, 57.5, 501]
S4	[0, 72, 121]	[0, 13.8, 121]

Some numerical results about the RMSE_r and RMSE_v characterizing all the considered algorithms in **S1** are illustrated in Fig. 2.2, where the CRLBs[15] for the considered estimation

[13] In all the simulations, the *barycentric interpolation* technique described in [19] has been always used.

[14] This entails that the step size between adjacent trial values selected in the interval $[X_{\min}, X_{\max}]$ is $X_{\text{step}} = (X_{\max} - X_{\min})/(Q_0 - 1)$.

[15] The expression of the CRLB for range and velocity estimation in the case of single target can be found in Appendix A.1.4. The CRLB in the case of multiple targets, instead, can be easily derived following the procedure illustrated in [54].

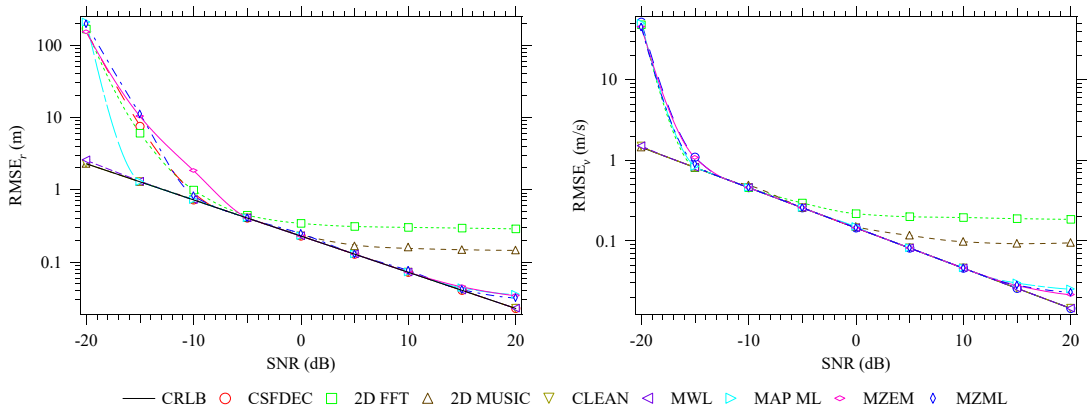

FIGURE 2.2: Root mean square error performance achieved in range and velocity estimation (first scenario). The 2D-FFT, CSFDEC, CLEAN, MWL, 2D-MUSIC, MZML, MAP-ML and MZEM algorithms are considered.

problem are also shown.

Note that: 1) most of the algorithms achieve poor estimation accuracy when the SNR drops below a threshold, which is algorithm dependent; 2) the threshold of the 2D-MUSIC, CLEAN and MWL algorithms is not visible in the considered SNR range; 3) the accuracy of each algorithm attains the CRLB above its SNR threshold, but, at high SNRs, may reach a floor. The last phenomenon, observed for the 2D-FFT and 2D-MUSIC algorithms, is due to their limited accuracy[16] (which depends on the overall number of FFT bins and on the overall number of trial points employed in the computation of the steering vectors, respectively). The other algorithms, instead, take advantage of their refinement cycles, which improve the accuracy of their final estimates.

In addition, in analyzing the results shown in Fig. 2.2, readers should keep in mind that: 1) the computational complexity of the CSFDEC, CLEAN and MZEM algorithms is approximately 13, 2.3 and 1.35 times higher, respectively, than that of the 2D-FFT, whereas that of the MWL algorithm is very close to it; 2) the complexity of the 2D-MUSIC, MAP-ML and MZML algorithms is 352, 183 and 819 times higher, respectively, than that of the 2D-FFT.

Most of the considerations illustrated above for Fig. 2.2 also apply to the results shown in Fig. 2.3 for $N = 32$ and in Fig. 2.4 for $N = 256$. In both cases **S2** is considered, but the results illustrated in Fig. 2.4 concern range estimation only and refer to a subset of the considered algorithms (2D-MUSIC, MZML and MAP-ML are ignored because of their huge memory requirements). Note that:

1) Unlike **S1**, an SNR threshold is visible in Fig. 2.3 for all the algorithms, mainly because of the presence of spectral leakage.

2) Independently of the considered algorithm, a higher number of subcarriers allows to achieve a lower RMSE_r and reduce the SNR threshold.

[16]In the case of the 2D-FFT algorithm, this phenomenon can be mitigated by interpolating its cost function to improve the accuracy in peak detection.

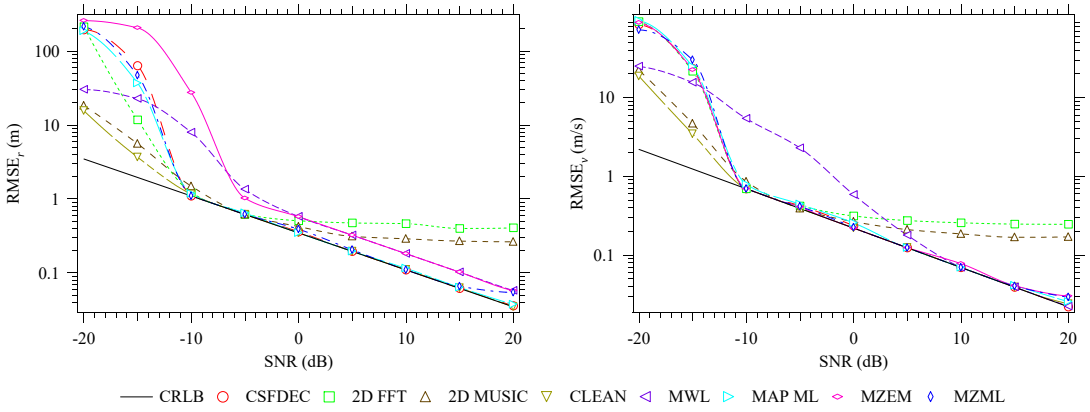

FIGURE 2.3: Root mean square error performance achieved in range and velocity estimation (second scenario). The 2D-FFT, CSFDEC, CLEAN, MWL, 2D-MUSIC, MZML, MAP-ML and MZEM algorithms are considered.

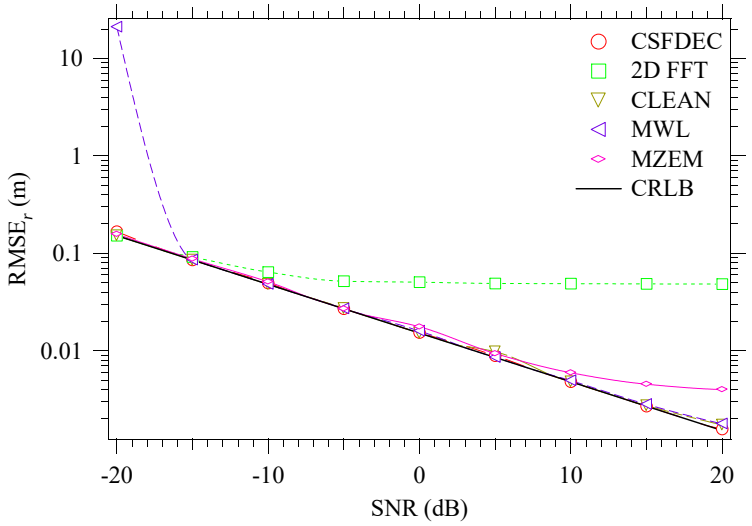

FIGURE 2.4: Root mean square error performance achieved in range estimation (second scenario) with $N = 256$ subcarriers. The 2D-FFT, CSFDEC, CLEAN, MWL and MZEM algorithms are considered.

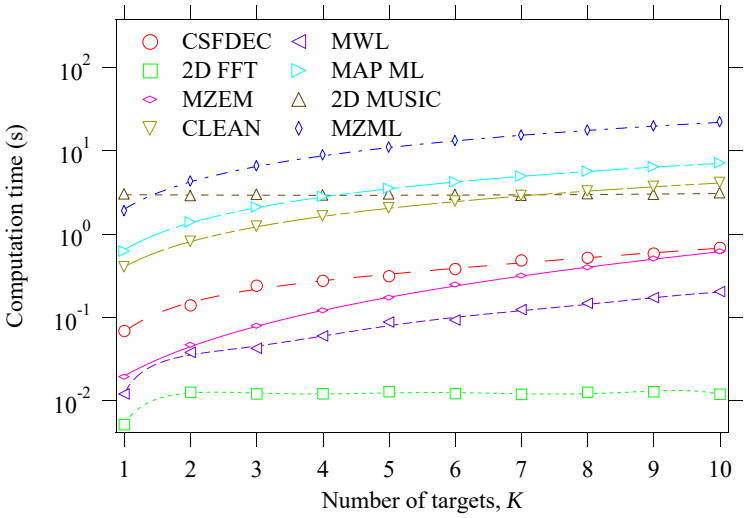

FIGURE 2.5: Computational time of the 2D-FFT, CSFDEC, CLEAN, MWL, 2D-MUSIC, MZML, MAP-ML and MZEM algorithms versus overall number of targets. The third scenario is considered.

3) In analyzing the results shown in Fig. 2.3, it should be kept into account that the computational complexity of the CSFDEC, CLEAN, MWL and MZEM algorithms is approximately 34, 177, 2.7 and 4.7 times higher, respectively, than that of the 2D-FFT. Moreover, the complexity of the 2D-MUSIC, MAP-ML and MZML algorithms is 7532, 1518 and 7070 times higher, respectively, than that of the 2D-FFT.

The CT[17] and the overall number of FLOPs assessed in **S3** are shown in Fig. 2.5 and Fig. 2.6, respectively. From these results and from those illustrated in **S1** and **S2**, it can be easily inferred that: 1) the gap, in terms of CT, between the CLEAN, MAP-ML and 2D-MUSIC algorithms is small; 2) the MAP-ML algorithm takes advantage of the *alternating projections* method to reduce the computational effort of the MZML algorithm; 3) the CT of the MWL algorithm is the closest to that of the 2D-FFT algorithm, but, as shown in Fig. 2.3, the former algorithm achieves poorer estimation accuracy than the latter one for SNR $\in [-15, 3]$ dB; 4) the CSFDEC algorithm stays in the middle between high and low complexity algorithms, but is able to achieve excellent estimation accuracy, as evidenced by the RMSE results illustrated for the previous scenarios.

Some numerical results[18] referring to **S4** are shown in Fig. 2.7 for RMSE_r and RMSE_v and in Fig. 2.8 for the CT. These results deserve the following comments: 1) the estimation accuracy of most of the considered algorithms does not improve after the first three iterations; 2) the CLEAN, MZEM and CSFDEC algorithms exhibit similar CTs if three iterations are carried out for each of them; 3) the MWL algorithm requires a lower CT, but generates poorer range and velocity estimates.

[17]The values shown for this parameter represent averages computed over one thousand runs for each algorithm.

[18]Please note that a linear scale is adopted on the ordinate axis of Fig. 2.7, since the interval which the estimated RMSEs belong to is narrow.

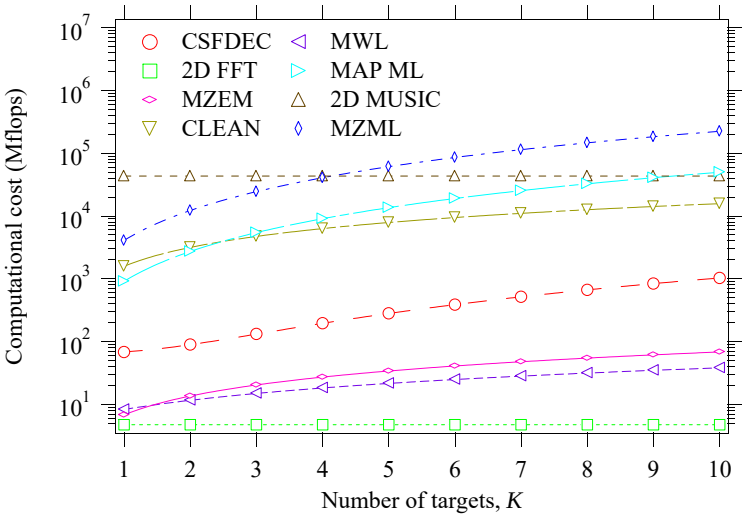

FIGURE 2.6: Estimated number of FLOPS of the 2D-FFT, CSFDEC, CLEAN, MWL, 2D-MUSIC, MZML, MAP-ML and MZEM algorithms versus overall number of targets (third scenario).

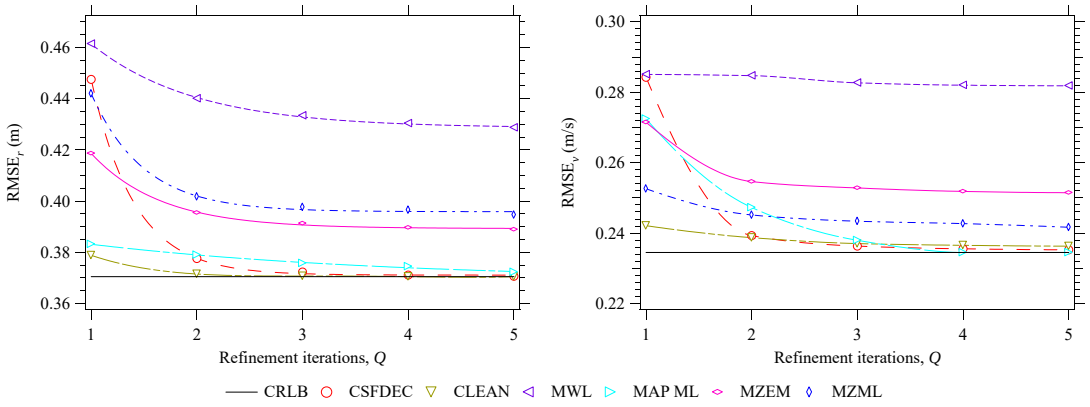

FIGURE 2.7: Root mean square error performance achieved in range and velocity estimation (fourth scenario). The CSFDEC, CLEAN, MWL, MZML, MAP-ML and MZEM algorithms are considered.

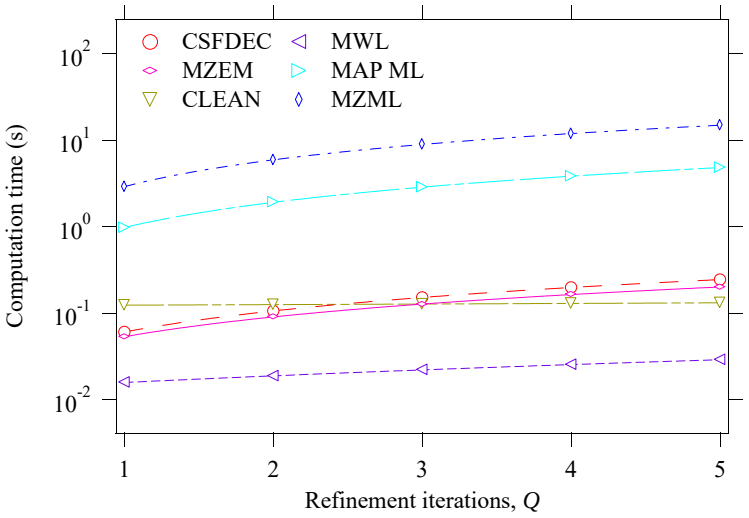

FIGURE 2.8: Computational time of the CSFDEC, CLEAN, MWL, MZML, MAP-ML and MZEM algorithms versus overall number of iterations (fourth scenario).

2.5 Conclusions

In this chapter, eight different algorithms for detecting multiple targets, and for jointly estimating their range and velocity in a SISO OFDM-based JCAS system have been described. All belong to the class of *indirect methods* and are deterministic; moreover, three of them (namely, the CLEAN, MWL and CSFDEC algorithms) exploit an iterative cancellation procedure in the estimation of target parameters. The obtained numerical results evidence that, in the presence of a single target or of multiple well-spaced targets, all the considered algorithms achieve reasonable accuracy. However, their behavior substantially changes in the presence of multiple closely spaced targets; in such conditions, the attention of this chapter has focused on how accuracy and computational effort are influenced by the overall number of a) targets and b) refinement cycles employed to improve the quality of the final estimates of target parameters. The following conclusions can be formulated in the light of the obtained simulation results: 1) the CLEAN and CSFDEC algorithms require a limited complexity and achieve excellent performance thanks to the use of a target cancellation procedure; 2) the MZML and MAP-ML algorithms achieve better accuracy than subspace-based methods (i.e., than the 2D-MUSIC algorithm) at the price of similar (and really high) computational complexities; 3) the MWL algorithm achieves a better accuracy-complexity trade-off than the MAP-ML algorithm.

Therefore, in future OFDM-based JCAS systems, the selection of a target detection and estimation algorithm requires a careful assessment of the pros and cons characterizing the various options available in the technical literature. The next chapter concerns the extension of some of the considered algorithms to MIMO OFDM-based radar systems employed for JCAS.

3

Deterministic Algorithms for Four-Dimensional Imaging in Colocated MIMO OFDM-based Radar Systems

This chapter investigates the problem of detecting multiple targets and jointly estimating their spatial coordinates (namely, the range, the Doppler and the direction of arrival of their electromagnetic echoes) in a colocated multiple-input multiple-output radar system employing orthogonal frequency division multiplexing. It is well-known that its optimal solution, namely the joint maximum likelihood estimator of an unknown number of targets, is unfeasible because of its huge computational complexity. Moreover, until now, sub-optimal solutions have not been proposed in the technical literature. Here, we introduce a novel approach to developing reduced complexity solutions. It is based on the idea of separating angle estimation from range-Doppler estimation, and of exploiting known algorithms for solving these two sub-problems. A detailed analysis of the accuracy and complexity of various detection and estimation methods based on this approach is provided. The numerical results presented in this chapter evidence that one of these methods is able to approach optimal performance in the maximum likelihood sense with a limited computational effort in different scenarios.

3.1 Introduction

Wireless communication and radar sensing have been advancing independently for many years, even though they share various similarities in terms of both signal processing and system architecture. This consideration and the problem of radio spectrum scarcity have motivated the investigation of a new class of wireless systems, able to accomplish sensing and communication jointly. Various recent research activities in this field have evidenced that JCAS systems can provide significant advantages in terms of device size, power consumption, cost, and spectral efficiency compared to traditional systems in various applications [1]. Different approaches to their development are currently being investigated [2, 4, 23, 55, 56]. In this chapter, we adopt a *communication-centric* approach; this means that radar sensing represents an add-on to the considered wireless communication system. Moreover, we assume that OFDM is employed for both communication and sensing and that the proposed system is equipped with both TX and RX arrays (i.e., it is of MIMO type).

The OFDM modulation format has been adopted in various wireless communication standards, due to its robustness to multipath fading and to its relatively simple synchronization [2]; in addition, its use in MIMO communication systems has been widely investigated (e.g., see [57, 58] and references therein). A wide technical literature on the use of OFDM

for radar sensing refers mainly to SISO systems [4–6, 8, 9, 11, 22, 59, 60]. For this class of systems, various *direct* and *indirect sensing* methods for target detection and estimation have been proposed. Generally speaking, *direct sensing methods* extract target information from the received signal without compensating for the effect of the data payload it conveys (e.g. see [1, 26, 59]) and typically exploit computationally intensive CS techniques. An example of application of CS is shown in [61], in which different multiplexing alternatives to OFDM are analyzed and the CS technique is employed to overcome the random assignment of subcarriers. *Indirect estimation methods*, instead, require estimating the communication channel and, consequently, compensating for the contribution due to channel symbols (e.g., see [4, eq. (20)]), which are known at the RX side of any colocated radar. Indirect sensing methods can be divided into: 1) DFT-based or *correlation-based* methods (i.e., methods based on the MF concept) [5, 6, 62]; 2) *subspace* methods [8, 9]; 3) ML-based methods [11–13]. Correlation-based and DFT-based algorithms are conceptually simple and computationally efficient, but can generate poor radar images in the presence of closely spaced targets and/or strong clutter [14]. Moreover, they can be outperformed by subspace methods, like the well-known MUSIC algorithm and the ESPRIT at the price, however, of a significantly larger computational complexity [8]. An estimation accuracy comparable to that of subspace methods is provided by various ML-based algorithms, which also require a significant computational effort; relevant contributions to this field can be found in [11], [13] and [12].

Indirect sensing methods for JCAS MIMO systems employing OFDM are investigated in [23, 26, 56, 63–68] and can be classified according to the same criteria as defined above for SISO systems. *Correlation*-based or DFT-based methods are developed in [23, 26, 56] and [68]. In particular, an algorithm combining matched filtering for range estimation with a 1D-MUSIC algorithm for both Doppler and azimuth (i.e., Angle of Arrival (AoA)) estimation is proposed in [56]. In [23] a Constant False Alarm Rate (CFAR) technique is employed to detect multiple targets, whereas the estimation of their range and Doppler is based on a 2D-FFT; note that in this case the estimation of AoA is ignored and the availability of antenna arrays is beneficial for communication only. In [26] a 2D-FFT technique is exploited to estimate the range of multiple targets and their azimuth, whereas in [68] multiple FFTs are combined with a clutter removal technique to estimate their range, azimuth and Doppler.

Subspace methods are investigated in [63], [64] and [65]. More specifically, in [63] a subspace-based algorithm assisted by CFAR pre-processing is developed to estimate the range, velocity, and azimuth of multiple targets on the basis of a reduced number of samples and without resorting to high-resolution spectral estimation. In [64] the estimation accuracy of the 2D-MUSIC algorithm is assessed for a varying number of available data snapshots, whereas in [65] the use of an augmented beam-space approach is proposed to make the use of 2D-MUSIC and 2D-ESPRIT possible when hybrid digital arrays are used.

Methods based on an ML approach are proposed in [66] and [67]. In particular, the strategy devised in [66] is based on: 1) a preliminary channel estimation; 2) an ML-based technique for the estimation of the range and Direction of Arrival (DoA) of multiple targets. In [67], instead, a 1D technique, based on a systematic phase correction method and leveraging the *virtual array* concept, is derived for the estimation of the azimuth of a single target. Finally, a hybrid approach, combining DFT-based and subspace methods, is illustrated

in [69]. More specifically, channel estimation is accomplished, after DFT-based processing for range estimation, by means of an Amplitude and Phase Estimation (APES)-based method; this method, that exploits the presence of ICI to produce a preliminary estimate of target Doppler, is followed by the 1D-MUSIC algorithm for angular estimation and by 1D-FFT processing to generate the final estimate of target Doppler.

It is important to point out that all the methods mentioned above for JCAS MIMO systems represent *partial solutions to the problem of jointly estimating the range, Doppler, azimuth and elevation of multiple targets*, i.e., briefly, to the Four-Dimensional (4D) imaging problem considered in this chapter. On the one hand, the authors of [23] focus on range and Doppler estimation only; moreover, they develop a correlation-based method, which is employed after channel estimation and time–frequency synchronization in the context of long-range radar processing. On the other hand, the correlation-based or subspace methods proposed in [26, 64, 65] are able to compute accurate estimates of target azimuth only, whereas the other target parameters are ignored (see [64] and [65]) or estimated with limited accuracy, without any refinement process (see [26]). Similar considerations apply to the ML-based method illustrated in [67], since it can provide accurate estimates of the azimuth of multiple targets, but coarse estimates of their range only. These limitations originate from the fact that an acceptable complexity in subspace-based and ML-based methods can be achieved by neglecting (or accepting poor accuracy in) the estimation of a portion of target parameters. These considerations have motivated the work described in this chapter, which aims at illustrating how a family of novel and computationally efficient sub-optimal methods able to generate accurate 4D radar images in an OFDM-based JCAS system equipped with TX and RX arrays can be developed; therefore, unlike previous research work, this chapter aims at providing a full solution to the above-mentioned 4D imaging problem. More specifically, the contribution provided by this chapter is threefold and can be summarized as follows:

1) A *general strategy*, called Doppler-Range-Angle Estimation with successive Compensation (DRAEC), is proposed for the detection of multiple targets and the estimation of their parameters in a MIMO OFDM-based JCAS system. This strategy is based on the idea of: a) assigning each TX antenna a subset of all subcarriers, which is disjoint from the subsets of subcarriers assigned to other TX antennas; b) decoupling the problem of range-Doppler estimation from that of azimuth-elevation estimation; c) employing an algorithm for the estimation of the parameters of 2D complex tones to solve each of these two sub-problems.

2) An *overview* of the algorithms that can be employed for the detection and the estimation of 2D complex tones, and an analysis of their computational complexity are provided. On the one hand, five of these algorithms are known DFT-based estimation techniques that have been proposed in the technical literature for related applications (namely, for harmonic retrieval [70, 71] or for radar sensing applications [72]). On the other hand, the remaining algorithm, called *extended Lee algorithm* (ELA), is new, even if it can be considered as an extended version of the ML-based 1D algorithm developed in [67]. Note that all these algorithms have been originally proposed to solve estimation problems that are formally different from the ones considered in this chapter. For this reason, in this chapter, their use for target range-Doppler estimation and azimuth-elevation estimation according to the DRAEC strategy is illustrated in detail. Moreover, a unified notation is adopted in their description to ease their implementation and the reading of this chapter.

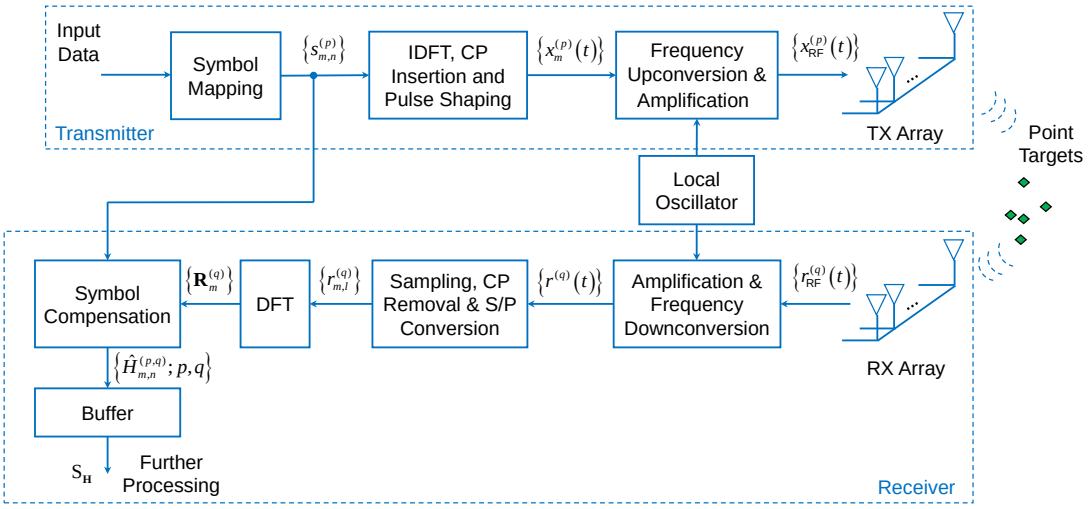

FIGURE 3.1: Architecture of the considered MIMO OFDM-based JCAS system.

3) Based on the above-mentioned estimation algorithms, *seven different embodiments* of the DRAEC strategy are proposed and compared in terms of both accuracy and computational complexity. Six of them are based on the known DFT-based estimation techniques mentioned above, whereas the remaining one relies on the CSFDEC algorithm. This allows us to assess how various state-of-the-art algorithms perform in 4D imaging and how large the computational effort they require is.

The remaining part of this chapter is organized as follows. In Section 3.2, the processing accomplished in a MIMO OFDM-based radar system is summarized, and the received signal model adopted in this work is briefly derived. The DRAEC strategy is illustrated in Section 3.3, whereas various estimators of 2D complex tones and their computational complexity are described in Section 3.4 and in Section 3.5, respectively. Different embodiments of the DRAEC strategy are proposed and compared, in terms of accuracy and complexity, in Section 3.6. Finally, some conclusions are offered in Section 3.7.

3.2 System and Signal Models

This section focuses on the architecture of the MIMO OFDM-based JCAS system considered in this chapter and on the processing accomplished at its receive side. The main objectives in this work are deriving the received signal model in the presence of multiple targets and illustrating some essential assumptions on which it relies. The architecture of the considered JCAS system is illustrated in Fig. 3.1 and has the following essential features:

1) Its transmitter is *colocated* with the receiver; consequently, the receiver has full knowledge of the structure and content of the transmitted signal and of its carrier frequency, and exploits this information for sensing purposes only.

2) It is equipped with a TX Horizontal Uniform Linear Array (HULA) and a RX Vertical Uniform Linear Array (VULA), consisting of N_{T} and N_{R} elements, respectively. All the

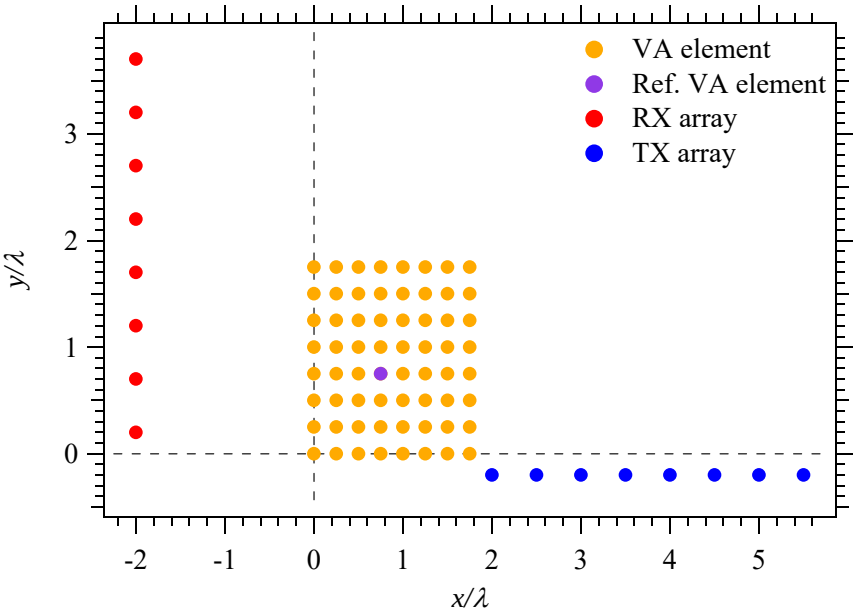

FIGURE 3.2: Representation of the physical TX and RX arrays, and of the corresponding virtual array characterizing the considered JCAS system. The reference virtual antenna element (corresponding to the couple $(p, q) = (4, 4)$ is identified by a purple circle.

antennas are placed on the same planar shield, so that a 2D reference system lying on the plane of the physical antenna array can be defined, as illustrated in Fig. 3.2 (where λ denotes the wavelength of the transmitted signal).

3) The data frames it transmits are made of M consecutive OFDM symbols, each consisting of N subcarriers. Such symbols can convey both pilot tones (for channel estimation and synchronization) and information data to be sent to a single or multiple receivers at different locations.

In the work described in this chapter, each couple of *physical* TX and RX antennas is replaced by a single Virtual Antenna (VA); the abscissa $x_{\mathrm{v}}^{(p,q)}$ and the ordinate $y_{\mathrm{v}}^{(p,q)}$ of the VA element associated with the pth TX antenna and the qth RX antenna (briefly, the (p, q) VA) are evaluated as (e.g., see [73, Eqs. (1)-(2)])

$$x_{\mathrm{v}}^{(p,q)} = (x_{\mathrm{t}}^{(p)} + x_{\mathrm{r}}^{(q)})/2 \tag{3.1}$$

and

$$y_{\mathrm{v}}^{(p,q)} = (y_{\mathrm{t}}^{(p)} + y_{\mathrm{r}}^{(q)})/2, \tag{3.2}$$

respectively, with $p = 0, 1, ..., N_{\mathrm{T}} - 1$ and $q = 0, 1, ..., N_{\mathrm{R}} - 1$; here, $(x_{\mathrm{t}}^{(p)}, y_{\mathrm{t}}^{(p)})$ and $(x_{\mathrm{r}}^{(q)}, y_{\mathrm{r}}^{(q)})$ denote the coordinates of the pth TX and qth RX antenna, respectively. It is easy to show that the set of $N_{\mathrm{VA}} = N_{\mathrm{T}} N_{\mathrm{R}}$ VAs associated with the physical arrays shown in Fig. 3.2 forms a virtual Uniform Rectangular Array (URA). Moreover, based on (3.1) and (3.2), the abscissa and ordinate of the VA (p, q) are

$$x_{\mathrm{v}}^{(p,q)} = x_{\mathrm{v}}^{(p)} = (x_{\mathrm{t}}^{(0)} + x_{\mathrm{r}}^{(0)} + p\, d_{\mathrm{t}})/2 \tag{3.3}$$

and

$$y_{\mathrm{v}}^{(p,q)} = y_{\mathrm{v}}^{(q)} = (y_{\mathrm{t}}^{(0)} + y_{\mathrm{r}}^{(0)} + q\, d_{\mathrm{r}})/2, \tag{3.4}$$

respectively; here, $(x_{\mathrm{t}}^{(0)}, y_{\mathrm{t}}^{(0)})$ $((x_{\mathrm{r}}^{(0)}, y_{\mathrm{r}}^{(0)}))$ represent the coordinates of the leftmost TX (lowermost RX) antenna and d_{t} (d_{r}) denotes the distance between adjacent antennas of the TX (RX) array (see Fig. 3.2, where it is assumed that $d_{\mathrm{t}} = d_{\mathrm{r}} = \lambda/2$).

In the following derivations, we concentrate on the transmission of a single frame. The complex envelope of the RF signal conveying the mth OFDM symbol radiated by the pth TX antenna (with $p = 0, 1, ..., N_{\mathrm{T}} - 1$) can be expressed as (e.g., see [11, Eq. (3)])

$$x_m^{(p)}(t) \triangleq q\,(t - mT_{\mathrm{s}}) \sum_{n=0}^{N-1} s_{m,n}^{(p)} \exp\left(j2\pi n \Delta_f\,(t - mT_{\mathrm{s}})\right) \tag{3.5}$$

up to a transmit delay; here, $q(t)$ is a windowing function, $s_{m,n}^{(p)}$ is the mth channel symbol conveyed by the nth subcarrier and transmitted by the pth TX antenna, $\Delta_f = 1/T$ is the subcarrier spacing, T is the OFDM symbol interval, $T_{\mathrm{s}} \triangleq T + T_{\mathrm{G}}$ is the overall duration of the OFDM symbol and T_{G} is the CP interval. Following [11], a rectangular windowing function is adopted, so that $q(t) = 1$ for $t \in [-T_{\mathrm{G}}, T]$ and $q(t) = 0$ elsewhere.

Given the complex envelope (3.5), the RF waveform radiated by the pth TX antenna in the considered frame can be expressed as

$$x_{\mathrm{RF}}^{(p)}(t) = \Re\left\{ \exp(j2\pi f_c\, t) \sum_{m=0}^{M-1} x_m^{(p)}(t) \right\}, \tag{3.6}$$

where $f_c \triangleq c/\lambda$ denotes the frequency of the LO employed in the up-conversion at the TX side and c the speed of light.

Let us assume now that $x_{\mathrm{RF}}^{(p)}(t)$ in (3.6) is reflected by K distinct point targets, and that the kth target (with $k = 0$, 1, ..., $K - 1$) is located at the (initial) distance R_k from the transmitter, moves with the radial velocity[1] v_k with respect to it and is characterized by the azimuth (elevation) angle θ_k (ϕ_k). It is not difficult to show that the complex envelope of the RF signal $r_{\mathrm{RF}}^{(q)}(t)$ (see Fig. 3.1) captured by the qth RX antenna is[2] (e.g., see [11, Eqs. (5) and (6)])

$$r^{(q)}(t) = \sum_{k=0}^{K-1} \sum_{p=0}^{N_{\mathrm{T}}-1} \alpha_k^{(p,q)} \exp\left(-j2\pi f_{\mathrm{c}} \tau_k^{(p,q)}\right) \cdot \exp\left(j2\pi f_{\nu_k} t\right) \sum_{m=0}^{M-1} x_m^{(p)}\left(t - \tau_k^{(p,q)} + \frac{f_{\nu_k}}{f_{\mathrm{c}}} t\right) + w^{(q)}(t), \tag{3.7}$$

[1] This velocity is positive (negative) if the target approaches (moves away from) the JCAS system.

[2] Note that the overall delay that characterizes the echo originating from the kth target depends on all the parameters of the target itself (namely, its range, its velocity and its angular parameters) and changes over time.

where

$$\tau_k^{(p,q)} \triangleq \frac{2}{c}\left[R_k + x_{\mathrm{v}}^{(p,q)}\sin(\theta_k)\cos(\phi_k) + y_{\mathrm{v}}^{(p,q)}\sin(\phi_k)\right] \tag{3.8}$$

and $\alpha_k^{(p,q)}$ are the overall propagation delay and the attenuation, respectively, associated with the kth point target (and observed on the VA (p,q)),

$$f_{\nu_k} \triangleq 2\frac{v_k}{\lambda} \tag{3.9}$$

is the Doppler shift due to the motion of the kth target and $w^{(q)}(t)$ is the complex AWGN process affecting $r^{(q)}(t)$.

The signal $r^{(q)}(t)$ in (3.7) undergoes analog-to-digital conversion followed by DFT processing. A simple mathematical model that describes the sequence generated by sampling $r^{(q)}(t)$ in the mth OFDM symbol interval can be derived as follows. Substituting the RHS of (3.5) in that of (3.7), extracting the portion associated with the mth OFDM symbol from the resulting expression and substituting t with $t' = t - mT_{\mathrm{s}}$ yields

$$r_m^{(q)}\left(t'\right) \triangleq \sum_{k=0}^{K-1} D\left(f_{\nu_k}, t'\right)\, \nu_m\left(f_{\nu_k}\right)\, A\left(R_k\right)\, Y_{k,m}^{(q)}(t') + w^{(q)}(t'), \tag{3.10}$$

where

$$D\left(f, t'\right) \triangleq \exp\left(j2\pi f t'\right), \tag{3.11}$$

$$\nu_m(f) \triangleq \exp(j2\pi f m T_{\mathrm{s}}), \tag{3.12}$$

$$A(R) \triangleq \exp\big(-j4\pi f_{\mathrm{c}} R/c\big), \tag{3.13}$$

$$Y_{k,m}^{(q)}(t') \triangleq \sum_{p=0}^{N_{\mathrm{T}}-1} \alpha_k^{(p,q)} B^{(p,q)}\left(\theta_k, \phi_k\right) \sum_{n=0}^{N-1} s_{m,n}^{(p)} \gamma_n(R_k) \cdot \eta_n^{(p,q)}\left(\theta_k, \phi_k\right)\, \xi_n(f_{\nu_k}, t')\, \zeta_{m,n}(f_{\nu_k})\, \exp\left(j2\pi n \Delta_f\, t'\right), \tag{3.14}$$

$$B^{(p,q)}(\theta, \phi) \triangleq \exp\left(-j4\pi(x_{\mathrm{v}}^{(p,q)}\sin(\theta)\cos(\phi) + y_{\mathrm{v}}^{(p,q)}\sin(\phi))/\lambda\right), \tag{3.15}$$

$$\gamma_n(R) \triangleq \exp(-j4\pi n \Delta_f R/c), \tag{3.16}$$

$$\eta_n^{(p,q)}(\theta, \phi) \triangleq \exp\left(-j4\pi n(\Delta_f/f_{\mathrm{c}})(x_{\mathrm{v}}^{(p,q)}\sin(\theta)\cos(\phi) + y_{\mathrm{v}}^{(p,q)}\sin(\phi))/\lambda\right), \tag{3.17}$$

$$\xi_n(f, t') \triangleq \exp(j2\pi n \Delta_f (f/f_{\mathrm{c}})\, t') \tag{3.18}$$

and

$$\zeta_{m,n}(f) \triangleq \exp(j2\pi n \Delta_f (f/f_{\mathrm{c}})\, m T_{\mathrm{s}}). \tag{3.19}$$

Note that:

1) The term $D(f, t')$, in (3.10), is responsible for the so-called *range migration effect* (see [38]) due to the kth target Doppler frequency, whereas $\nu_m(f_{\nu_k})$ is proportional to both f_{ν_k} and the OFDM symbol index m.

2) The phase of $A(R_k)$ in (3.10) depends on the range R_k only, whereas that of $\gamma_n(R_k)$ in (3.14) is proportional to both R_k and the subcarrier index n (see (3.13) and (3.16), respectively).

3) The terms in (3.15) and in (3.17) both depend on the virtual array configuration as well as the target DoA.

4) The term $\xi_n(f_{\nu_k}, t')$ in (3.14) produces a time-dependent phase rotation influenced by both the Doppler frequency f_{ν_k} and the subcarrier index n (see (3.18)).

5) The term $\zeta_{m,n}(f_{\nu_k})$ in (3.14) introduces a phase rotation depending on both the OFDM symbol index m and the subcarrier index n (see (3.19), and accounts for the so-called *intersubcarrier Doppler effect* (e.g., see [11, Sec. II, p. 3]).

It is not difficult to show that sampling $r_m^{(q)}(t')$ (3.10) at the instant $t'_l \triangleq lT/N$ (i.e., sampling $r^{(q)}(t)$ at the instant $t_l \triangleq t'_l + mT_\mathrm{s}$), with $l = 0, 1, ..., N-1$, yields[3]

$$r_{m,l}^{(q)} \triangleq r_m^{(q)}\left(t'_l\right) = \sum_{k=0}^{K-1} D_l\left(f_{\nu_k}\right) \nu_m\left(f_{\nu_k}\right) A\left(R_k\right) Y_{k,m,l}^{(q)} + w_l^{(q)}; \tag{3.20}$$

here, the term $D_l(f) \triangleq \exp(j2\pi f l T/N)$ accounts for the ICI effect due to the range migration,

$$Y_{k,m,l}^{(q)} \triangleq Y_{k,m}^{(q)}(t'_l) = \sum_{p=0}^{N_\mathrm{T}-1} \alpha_k^{(p,q)} B^{(p,q)}\left(\theta_k, \phi_k\right) \sum_{n=0}^{N-1} s_{m,n}^{(p)} \gamma_n(R_k) \cdot \eta_n^{(p,q)}\left(\theta_k, \phi_k\right) \xi_{n,l}(f_{\nu_k}) \zeta_{m,n}(f_{\nu_k}) \exp\left(j2\pi nl/N\right), \tag{3.21}$$

$\xi_{n,l}(f) \triangleq \xi_n(f, t'_l)$ and $w_l^{(q)} \triangleq w^{(q)}(t'_l)$ is the Gaussian noise affecting $r_{m,l}^{(q)}$ (an AWGN model is assumed for the sequence $\{w_l^{(q)};\, l = 0, 1, ..., N-1\}$).

If the target Doppler frequencies $\{f_{\nu_k}\}$ are sufficiently small and, more precisely, $|f_{\nu_k}/f_\mathrm{c}| \ll 1/(MN)$ for any k, the factors $\xi_{n,l}(f_{\nu_k})$ and $\zeta_{m,n}(f_{\nu_k})$ appearing in the RHS of (3.21) can be neglected; this leads to the simplified signal model

$$r_{m,l}^{(q)} = \sum_{k=0}^{K-1} D_l\left(f_{\nu_k}\right) \nu_m\left(f_{\nu_k}\right) A\left(R_k\right) \sum_{p=0}^{N_\mathrm{T}-1} \alpha_k^{(p,q)} B^{(p,q)}\left(\theta_k, \phi_k\right) \sum_{n=0}^{N-1} s_{m,n}^{(p)} \exp\left(j2\pi nl/N\right) \cdot \gamma_n(R_k)\, \eta_n^{(p,q)}\left(\theta_k, \phi_k\right) + w_l^{(q)}. \tag{3.22}$$

The N signal samples acquired in the mth OFDM symbol interval through the qth RX antenna undergo Serial-to-Parallel (S/P) conversion, as shown in Fig. 3.1; this produces the N-dimensional vector $\mathbf{r}_m^{(q)} \triangleq [r_{m,0}^{(q)}, r_{m,1}^{(q)}, ..., r_{m,N-1}^{(q)}]^T$, for which an order N DFT is computed. The nth element of the resulting DFT output vector

$$\mathbf{R}_m^{(q)} \triangleq [R_{m,0}^{(q)}, R_{m,1}^{(q)}, ..., R_{m,N-1}^{(q)}]^T \tag{3.23}$$

[3]Note that the samples associated with the CP are ignored.

can be expressed as

$$R_{m,n}^{(q)} \triangleq \frac{1}{N}\sum_{l=0}^{N-1} r_{m,l}^{(q)} \exp\left(-j2\pi nl/N\right) = \frac{1}{N}\sum_{k=0}^{K-1} D_n\left(f_{\nu_k}\right)\, \nu_m\left(f_{\nu_k}\right)\, A(R_k) \sum_{p=0}^{N_{\mathrm{T}}-1} \alpha_k^{(p,q)} \cdot B^{(p,q)}\left(\theta_k,\phi_k\right)\, s_{m,n}^{(p)}\, \gamma_n(R_k)\, \eta_n^{(p,q)}\left(\theta_k,\phi_k\right) + W_n^{(q)}, \quad (3.24)$$

where $W_n^{(q)}$ is the AWGN sample affecting the nth subcarrier.

The received signal model expressed by (3.24) is general, but quite complicated. In the work presented in this chapter, a simplified version of it can be employed since:

1) the approximation

$$\eta_n^{(p,q)}(\theta,\phi) \cong 1 \quad (3.25)$$

is made for any n, since f_{c} is assumed to be much greater than Δ_f (see (3.17));

2) it is assumed that, in the transmission of each OFDM symbol, disjoint subsets of the N available subcarriers are assigned to distinct TX antennas.

The last assumption means that the signal radiated by each TX antenna can be represented as the superposition of a set of multiple subcarriers exclusively assigned to that antenna, i.e., briefly, it consists of *private subcarriers* only[4]. Therefore, if $\mathcal{S}_m^{(p)}$ denotes the set collecting the indices of the subcarriers radiated by the pth TX antenna in the mth symbol interval, we have that

$$\mathcal{S}_m^{(p_1)} \cap \mathcal{S}_m^{(p_2)} = \emptyset \quad (3.26)$$

for any $p_1 \neq p_2$, with p_1 and $p_2 \in \{0,1,...,N_{\mathrm{T}}-1\}$, and

$$\bigcup_{p=0}^{N_{\mathrm{T}}-1} \mathcal{S}_m^{(p)} = \mathcal{J} \quad (3.27)$$

for any m, where $\mathcal{J} \triangleq \{0,1,...,N-1\}$. It is important to point out that, although the underlying assumption about the use of subcarrier frequencies is strong and entails a reduction by a factor N_{T} in the transmission rate (with respect to the case in which all the subcarriers are employed by each TX antenna), it paves the way for the development of target detection and estimation algorithms requiring a limited computational effort. In fact, under the last assumption, the sum over p appearing in the RHS of (3.24) involves a single term different from zero; consequently, (3.24) becomes

$$R_{m,n}^{(q)} = \frac{s_{m,n}^{(p_{\mathrm{a}})}}{N}\sum_{k=0}^{K-1} \alpha_k^{(p_{\mathrm{a}},q)} D_n\left(f_{\nu_k}\right)\, \nu_m\left(f_{\nu_k}\right)\, A(R_k)\, B^{(p_{\mathrm{a}},q)}\left(\theta_k,\phi_k\right)\, \gamma_n(R_k) + W_n^{(q)}, \quad (3.28)$$

which represents a sample of the 2D signal employed for channel estimation. Here, p_{a} denotes the index of the TX antenna to which the nth subcarrier has been assigned in the

[4]The use of a subset of *private subcarriers* in JCAS systems has been first proposed in [62] to improve the accuracy of target range and angle estimation through a CS technique. Although CS methods typically involve high computational complexity, the combined utilization of shared and private subcarriers enables a flexible tradeoff between communication and sensing.

mth OFDM symbol interval (the dependence of p_{a} on m and n is not explicitly shown to ease notation). Based on (3.3), (3.4), (3.11)-(3.13), (3.15) and (3.16), it is easy to show that

$$\gamma_n(R_k) D_n\left(f_{\nu_k}\right) = a_n(-F_{\rho_k}), \tag{3.29}$$

$$\nu_m\left(f_{\nu_k}\right) = a_m(F_{\nu_k}) \tag{3.30}$$

and

$$\alpha_k^{(p_{\mathrm{a}},q)} A(R_k) B^{(p_{\mathrm{a}},q)}\left(\theta_k, \phi_k\right) = \alpha_k^{(p_{\mathrm{a}},q)} \exp\left(j\omega_k\right)\, a_{p_{\mathrm{a}}}(-F_{H_k})\, a_q(-F_{V_k}), \tag{3.31}$$

where

$$a_z(F_X) \triangleq \exp(j2\pi z F_X), \tag{3.32}$$

with $z = p_{\mathrm{a}}$, q, m or n, $X = H_k$, V_k, ν_k or ρ_k,

$$F_{H_k} \triangleq d_{\mathrm{t}} \sin(\theta_k) \cos(\phi_k)/\lambda \tag{3.33}$$

and

$$F_{V_k} \triangleq d_{\mathrm{r}} \sin(\phi_k)/\lambda \tag{3.34}$$

denote the *normalized horizontal frequency* and the *normalized vertical frequency*, respectively, associated with the kth target,

$$F_{\nu_k} \triangleq f_{\nu_k} T_{\mathrm{s}} \tag{3.35}$$

is the *normalized Doppler frequency*,

$$F_{\rho_k} \triangleq F_{r_k} - F_{\nu_k} T/(N\, T_{\mathrm{s}}) \tag{3.36}$$

is a normalized frequency accounting for both the Doppler of the kth target and its range through the *normalized target delay*[5]

$$F_{r_k} \triangleq 2R_k\, \Delta_f/c \tag{3.37}$$

and

$$\omega_k \triangleq -2\pi(2R_k + (x_{\mathrm{t}}^{(0)} + x_{\mathrm{r}}^{(0)}) \sin(\theta_k) \cos(\phi_k) + (y_{\mathrm{t}}^{(0)} + y_{\mathrm{r}}^{(0)}) \sin(\phi_k))/\lambda. \tag{3.38}$$

Note that:

1) F_{ρ_k} (3.36) and F_{ν_k} (3.35) are both frequencies in the range $[-1/2,\, 1/2]$, for any k.

2) F_{V_k} and F_{H_k} satisfy the inequalities $-d_{\mathrm{r}}/\lambda \leqslant F_{V_k} \leqslant d_{\mathrm{r}}/\lambda$ and $-d_{\mathrm{r}} \cos(\phi_k)/\lambda \leqslant F_{H_k} \leqslant d_{\mathrm{r}} \cos(\phi_k)/\lambda$, respectively, for any k.

3) The range of F_{H_k} is also limited by the elevation ϕ_k of the kth target for any k (see (3.33)).

4) The ranges of F_{V_k} and F_{H_k} are maximized for $d_{\mathrm{r}} = \lambda/2$ and $d_{\mathrm{t}} = \lambda/2$, respectively.

[5]Note that, F_{r_k} is always positive, whereas F_{ν_k} is positive (negative) if the kth target is approaching (moving away from) the considered JCAS system.

Based on (3.29)-(3.31), eq. (3.28) can be rewritten as[6]

$$R_{m,n}^{(q)} = s_{m,n}^{(p_\mathrm{a})}\, \hat{H}_{m,n}^{(p_\mathrm{a},q)}, \tag{3.39}$$

where[7]

$$\hat{H}_{m,n}^{(p_\mathrm{a},q)} \triangleq \frac{1}{N} \sum_{k=0}^{K-1} A_k\, a_{p_\mathrm{a}}\left(-F_{H_k}\right)\, a_q\big(-F_{V_k}\big)\, a_m\big(F_{\nu_k}\big)\, a_n\big(-F_{\rho_k}\big) + \bar{W}_{m,n}^{(p_\mathrm{a},q)}, \tag{3.40}$$

denotes an estimate of the channel frequency response $H_{m,n}^{(p_\mathrm{a},q)}$ characterizing the nth subcarrier frequency in the mth OFDM symbol interval for the VA (p_a, q), $A_k \triangleq \alpha_k \exp(j\omega_k)$ and

$$\bar{W}_{m,n}^{(p_\mathrm{a},q)} \triangleq \frac{W_{m,n}^{(p_\mathrm{a},q)}}{s_{m,n}^{(p_\mathrm{a})}} \tag{3.41}$$

is the noise sample affecting $\hat{H}_{m,n}^{(p_\mathrm{a},q)}$. The quantity $\hat{H}_{m,n}^{(p_\mathrm{a},q)}$, in (3.40), represents the noisy measurement produced by the *symbol compensation* block for the VA (p_a, q), the nth subcarrier and the mth OFDM symbol interval (see Fig. 3.1, where this block is followed by a buffer storing the measurements acquired over each frame). Moreover, the measurements acquired over the OFDM frame and the whole virtual array are collected in the set[8]

$$\mathcal{S}_{\mathbf{H}} \triangleq \{\hat{\mathbf{H}}^{(p,q)}; p = 0, 1, ..., N_\mathrm{T} - 1, q = 0, 1, ..., N_\mathrm{R} - 1\}, \tag{3.42}$$

where $\hat{\mathbf{H}}^{(p,q)} \triangleq [\hat{H}_{m,n}^{(p,q)}]$ represents the $M \times N$ matrix formed by all the measurements acquired through the VA (p, q) over the OFDM frame. Note that this set consists of N_VA matrices, one for each of the N_VA VAs, and that it represents the output of the last block appearing in Fig. 3.1.

The measurement model (3.40) deserves the following comments:

1) The complex gain A_k appearing in its RHS accounts for the phase rotation due to the path delay, the path loss and the gain (attenuation) introduced by the kth target.

2) Since, in all the computer simulations done for this chapter, a $M_\mathrm{c}$ary PSK constellation is adopted for the channel symbols $\{s_{m,n}^{(p_\mathrm{a})}\}$, the 2D sequence of noise samples $\{\bar{W}_{m,n}^{(p_\mathrm{a},q)}\}$ (see (3.41)) affecting the measurements has the same statistical properties as $\{W_n^{(q)}\}$ (see (3.28)), i.e., it can be modeled as AWGN (the variance of each sample is denoted σ_W^2).

3) The noisy samples $\{\hat{H}_{m,n}^{(p,q)}\}$ of the 4D channel response acquired over a single OFDM frame can be modeled as the superposition of an AWGN process with K 4D complex exponentials, whose amplitude, phase and frequencies provide information about the range, the Doppler and the angular coordinates of the detectable targets. For this reason, target detection and estimation are tantamount to identifying the K complex exponentials that form the useful component of the sequence $\{\hat{H}_{m,n}^{(p,q)}\}$ and to estimating their parameters, respectively.

[6] Note that channel symbols $\{s_{m,n}^{(p_\mathrm{a})}\}$ are known to the JCAS receiver for any m, n and p_a.

[7] In the following, the dependence of $\alpha_k^{(p_\mathrm{a},q)}$ on (p_a, q) is neglected; therefore, $\alpha_k = \alpha_k^{(p_\mathrm{a},q)}$ is assumed.

[8] In the following, the antenna index p_a is replaced by p (with $p = 0, 1, ..., N_T - 1$) for simplicity.

Finally, it is important to make some considerations about the use of private subcarriers and the criteria that can be adopted in the selection of their subsets $\{\mathcal{S}_m^{(p)}\}$. From the rules illustrated above about the use of private subcarriers, it can be easily inferred that the maximum data rate achievable through the proposed transmission scheme is identical to that of a JCAS system equipped with a single TX antenna, i.e., as already mentioned above, it is N_{T} times lower than that provided by a MIMO system with *shared subcarriers* (e.g. see [62]). In addition, the TX array is not exploited for beamsteering, as suggested, for instance, in [69], where a single-stream beamforming model is assumed. Despite this, the considered JCAS system benefits from the availability of a TX array, since this results in a larger virtual array (i.e., in an increase of the overall number of VAs, N_{VA}) and, consequently, in a better angular resolution [67]. As far as the selection of the subsets $\{\mathcal{S}_m^{(p)}\}$ is concerned, in the computer simulations carried out for this chapter, a pseudo-random mechanism has been adopted in assigning the N available subcarriers to the N_{T} TX antennas in the transmission of the mth OFDM symbol of a given frame; moreover, the same pseudo-random pattern has been employed for all the transmitted frames. The choice of this strategy is motivated by the fact that randomly changing the subset of subcarriers from symbol to symbol allows the considered radar system to benefit from *transmit diversity*.

3.3 Description of the Proposed Approach to the Estimation of Multiple Targets

In this section, the problem of developing reduced complexity methods for the detection of multiple targets and for the estimation of their parameters in the MIMO OFDM-based JCAS system described in the previous section is tackled. We first describe a general strategy to devise novel solutions to this problem. Then, we provide some indications about the processing to be accomplished by each of the two main parts it consists of.

3.3.1 Description of the proposed strategy

Achieving joint ML estimation of an unknown number of targets, given the set of measurements $\mathcal{S}_{\mathbf{H}}$, in (3.42), is an overly complicated problem, since it involves a large number of parameters to be estimated (more precisely, five parameters per target plus the overall number of targets), even for small values of K. This motivates the interest in the development of sub-optimal methods based on the idea of turning a multidimensional estimation problem into a set of interconnected lower dimensional sub-problems. In the remaining part of this subsection, we illustrate a general strategy, called DRAEC, for the derivation of a new class of such methods. According to this strategy, range and Doppler estimation are decoupled from angular estimation. This explains why its structure, described by the block diagram shown in Fig. 3.3, contains two *core* blocks, called Range-Doppler Estimator (RDE) and Angular Estimator (AE): in fact, the former block accomplishes target detection and jointly estimates target range and Doppler, whereas the second one identifies multiple targets characterized by similar Doppler and ranges, and estimates their azimuth and elevation. Note also that the proposed structure includes a *fusion* block, whose task is

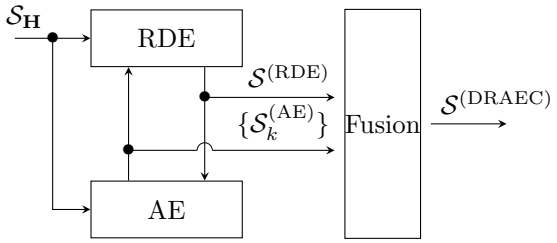

FIGURE 3.3: Block diagram describing the DRAEC strategy. Two interconnected *core* blocks, namely the RDE and the AE, and a fusion block, generating the final output, are employed.

merging the information provided by the first two blocks in order to generate a 4D radar image in the form of a point cloud. The processing accomplished by the core blocks can be summarized as follows. Based on the available measurements (i.e., on the set $\mathcal{S}_{\mathbf{H}}$, in (3.42)), the RDE generates the so-called Target Range-Doppler Profile (TRDP), namely a collection of: 1) *range-Doppler* couples at which relevant echoes are detected; 2) an estimate of the complex amplitude associated with each of these couples (the absolute value of such amplitudes allows us to rank the couples on the basis of their perceptual importance). More precisely, the TRDP is represented by the set

$$\mathcal{S}^{(\mathrm{RDE})} \triangleq \left\{ \left(\hat{F}_{\nu_k}, \hat{F}_{r_k}, \hat{A}_k \right) ; \, k = 0, 1, ..., K^{(\mathrm{RDE})} - 1 \right\}, \tag{3.43}$$

where $\hat{F}_{\nu_k}$, $\hat{F}_{r_k}$ and $\hat{A}_k$ denote the estimates of the normalized Doppler frequency, the normalized delay and the complex amplitude, respectively, associated with the kth range-Doppler bin[9] in which (at least) one target has been detected[10], and $K^{(\mathrm{RDE})}$ is the overall number of relevant range-Doppler bins identified by the RDE.

The set $\mathcal{S}^{(\mathrm{RDE})}$, in (3.43), is passed to the AE, which processes it jointly with the set $\mathcal{S}_{\mathbf{H}}$ (see (3.42)) in order to:

1) Identify all the targets associated with each of the range-Doppler-complex amplitude triplets forming the TRDP;

2) Generate the so-called *angular profile* (AP), that collects the estimates of the angular parameters and the complex amplitude of all the targets detected within each range-Doppler bin. In practice, the AP information associated with the kth element (i.e., triplet) of $\mathcal{S}^{(\mathrm{RDE})}$ is represented by the set

$$\mathcal{S}_k^{(\mathrm{AE})} \triangleq \left\{ \left(\hat{F}_{H_k}[l], \hat{F}_{V_k}[l], \hat{A}_k[l] \right); \, l = 0, 1, ..., K_k^{(\mathrm{AE})} - 1 \right\}, \tag{3.44}$$

with $k = 0, 1, ..., K^{(\mathrm{RDE})} - 1$; here, $\hat{F}_{H_k}[l]$, $\hat{F}_{V_k}[l]$ and $\hat{A}_k[l]$ denote the estimates of the normalized horizontal frequency, normalized vertical frequency and complex amplitude of the lth target detected in the kth range-Doppler bin, respectively, whereas $K_k^{(\mathrm{AE})}$ represents

[9] As shown in the next section, the 2D-FFT processing executed by the RDE leads to discretizing the range-Doppler domain and, in particular, to partitioning it into multiple range-Doppler *bins*.

[10] Note that the RDE is unable to separate multiple targets whose range and Doppler fall in the same bin.

the overall number of targets detected in that bin. The normalized frequencies $\hat{F}_{H_k}[l]$ and $\hat{F}_{V_k}[l]$ are jointly processed by the fusion block in order to generate, on the basis of (3.33) and (3.34), the estimates $\hat{\theta}_k[l]$ and $\hat{\phi}_k[l]$ of the azimuth $\theta_k[l]$ and the elevation $\phi_k[l]$, respectively, characterizing the lth target identified in the kth range-Doppler bin. Moreover, the fusion block processes the estimates $\hat{F}_{\nu_k}$ and $\hat{F}_{r_k}$ to compute the estimates $\hat{v}_k[l]$ and $\hat{R}_k[l]$ of the velocity $v_k[l]$ and range $R_k[l]$, respectively, on the basis of (3.9), (3.35) and (3.37). Then, the above-mentioned estimates are collected in the set

$$\mathcal{S}^{(\mathrm{DRAEC})} \triangleq \bigcup_{k=0}^{K^{(\mathrm{RDE})}-1} \mathcal{S}_k^{(\mathrm{DRAEC})}, \tag{3.45}$$

where

$$\mathcal{S}_k^{(\mathrm{DRAEC})} \triangleq \left\{ \left(\hat{R}_k[l], \hat{v}_k[l], \hat{\theta}_k[l], \hat{\phi}_k[l], \hat{A}_k[l] \right); \, l = 0, 1, ..., K_k^{(\mathrm{AE})} - 1 \right\}, \tag{3.46}$$

with $k = 0, 1, .., K^{(\mathrm{RDE})} - 1$. The set $\mathcal{S}^{(\mathrm{DRAEC})}$, in (3.45), represents the final output of the DRAEC strategy if the RDE is not exploited again. Alternatively, it can be passed to the RDE with the aim of re-estimating[11] the range and Doppler parameters of each of the $K_k^{(\mathrm{AE})}$ detected targets for any k; this step is expected to generate an updated version of the set $\mathcal{S}^{(\mathrm{RDE})}$ (see (3.43)). Fusing the obtained set with the overall AP produces an updated version of the set $\mathcal{S}^{(\mathrm{DRAEC})}$, that collects *finer estimates* of the parameters of all the detected targets.

3.3.2 Processing tasks accomplished by the constituent blocks

In this subsection, the essential processing tasks accomplished by the RDE and AE blocks appearing in Fig. 3.3 are sketched; in this description, it is assumed, without any loss of generality, that the considered MIMO OFDM-based JCAS system is equipped with the URA illustrated in Fig. 3.2.

The RDE extracts from the set $\mathcal{S}_{\mathbf{H}}$ (see (3.42)), collecting N_{VA} matrices, a single matrix, denoted $\hat{\mathbf{H}}^{(p_{\mathrm{R}},q_{\mathrm{R}})}$ and referring to a specific VA (called *reference* VA and associated with the choice $(p, q) = (p_{\mathrm{R}}, q_{\mathrm{R}})$; see Fig. 3.2). Then, it processes $\hat{\mathbf{H}}^{(p_{\mathrm{R}},q_{\mathrm{R}})}$ to generate the TRDP, i.e., the set $\mathcal{S}^{(\mathrm{RDE})}$, in (3.43). It is important to point out that:

1) Based on $\hat{\mathbf{H}}^{(p_{\mathrm{R}},q_{\mathrm{R}})}$, the TRDP can be generated by estimating the complex amplitudes and the frequencies of the complex exponentials that form the useful component of the 2D sequence $\{\hat{H}_{m,n}^{(p_{\mathrm{R}},q_{\mathrm{R}})}\}$.

2) The parameter $K^{(\mathrm{RDE})}$ appearing in (3.43) represents the overall number of range-Doppler bins in which at least a single target is detected. In fact, at this stage, the RDE detects multiple targets, characterized by similar ranges and Dopplers (and, in particular, such that their parameters fall inside the same range-Doppler bin[12]) as a single target. This explains why, in general, the kth range-Doppler bin selected by the RDE (with

[11] A similar approach, where the 1D angle estimates are employed for re-estimating the range estimates in [62].

[12] This condition may occur in the presence of *extended targets* [74].

$k = 0, 1, ..., K^{(\mathrm{RDE})} - 1$) may contain multiple (say, $K_k^{(\mathrm{AE})}$) targets, which are overlapped in the range-Doppler domain but have distinct angular coordinates.

3) The absolute value of the complex amplitude $\hat{A}_k$ appearing in (3.43) represents the *perceptual importance* of the kth detected range-Doppler bin (with $k = 0, 1, ..., K^{(\mathrm{RDE})}$); in the following, we assume that the elements of $\mathcal{S}^{(\mathrm{RDE})}$ are ordered according to a decreasing perceptual importance, so that $|\hat{A}_{k+1}| \geq |\hat{A}_k|$, with $k = 0, 1, ..., K^{(\mathrm{RDE})} - 1$.

4) The RDE sets a single VA as the reference for range and Doppler estimation for simplicity. However, this process can be made more robust by utilizing multiple VAs, such as those with the highest SNR values. The estimates obtained from these antennas can then be combined (for example, by averaging) to enhance the estimation accuracy.

The set $\mathcal{S}_{\mathbf{H}}$ and the TRDP (see (3.42) and (3.43), respectively) feed the AE, which sequentially accomplishes the three steps listed below.

1) It checks if the kth range-Doppler bin satisfies the inequality

$$|\hat{A}_k|^2 > \mathcal{T}^{(\mathrm{RDE})}, \tag{3.47}$$

with $k = 0, 1, ..., K^{(\mathrm{RDE})}$; here, $\mathcal{T}^{(\mathrm{RDE})}$ is a proper threshold. Any bin not meeting this condition is discarded. This leads to the reduced TRDP

$$\bar{\mathcal{S}}^{(\mathrm{RDE})} \triangleq \left\{ \left(\hat{F}_{\nu_k}, \hat{F}_{r_k}, \hat{A}_k \right) ; \, k = 0, 1, ..., \bar{K}^{(\mathrm{RDE})} - 1 \right\}, \tag{3.48}$$

with $\bar{K}^{(\mathrm{RDE})} \leq K^{(\mathrm{RDE})}$.

2) It merges the information provided by the N_{VA} matrices of the set $\mathcal{S}_{\mathbf{H}}$ (see (3.42)) in $\bar{K}^{(\mathrm{RDE})}$ $N_{\mathrm{T}} \times N_{\mathrm{R}}$ matrices, one for each of $\bar{K}^{(\mathrm{RDE})}$ range-Doppler bins selected in the previous step. The kth matrix (with $k = 0, 1, ..., \bar{K}^{(\mathrm{RDE})} - 1$) is denoted $\breve{\mathbf{H}}_k \triangleq [\breve{H}_k^{(p,q)}]$; the element appearing on its pth row and qth column is evaluated as

$$\breve{H}_k^{(p,q)} = \frac{1}{M\,N} \sum_{m=0}^{M-1} \sum_{n=0}^{N-1} \hat{H}_{m,n}^{(p,q)} \, a_m^*(\hat{F}_{\nu_k}) \, a_n^*(-\hat{F}_{\rho_k}), \tag{3.49}$$

with $p = 0, 1, ..., N_{\mathrm{T}} - 1$ and with $q = 0, 1, ..., N_{\mathrm{R}} - 1$; here, $\hat{F}_{\rho_k}$ represents the estimate of the normalized frequency in (3.36).

3) It processes the matrix $\breve{\mathbf{H}}_k$ to identify all the targets contained in the kth range-Doppler bin in order to generate the set $\mathcal{S}_k^{(\mathrm{AE})}$ in (3.44) where, however, $k = 0, 1, ..., \bar{K}^{(\mathrm{RDE})} - 1$.

The AE output, i.e., the overall AP, results from merging all the information contained in the $\bar{K}^{(\mathrm{RDE})}$ sets $\{\mathcal{S}_k^{(\mathrm{AE})}\}$ and collects the estimates of all the angular parameters referring to

$$K^{(\mathrm{AE})} \triangleq \sum_{k=0}^{\bar{K}^{(\mathrm{RDE})}-1} K_k^{(\mathrm{AE})} \tag{3.50}$$

distinct targets. This concludes the AE processing.

It is worth noting that:

1) The term $a_m^*(\hat{F}_{\nu_k})$ ($a_n^*(-\hat{F}_{\rho_k})$) appearing in the RHS of (3.49) aims at *compensating* for the factor $a_m(F_{\nu_k})$ ($a_n(-F_{\rho_k})$) which is visible on the same side of (3.40); in other words, it is expected to cancel the dependence of $\breve{H}_k^{(p,q)}$ on the Doppler and range of the kth target (leaving, however, the dependence on its *normalized horizontal* and *vertical frequencies*).

2) Similarly to step 1) of the RDE, step 3) of the AE processing requires estimating the complex amplitudes and the frequencies of the overlapped complex exponentials that form the useful component of the 2D sequence $\{\breve{H}_k^{(p,q)}\}$ (with $k = 0, 1, ..., \bar{K}^{(\mathrm{RDE})} - 1$).

If the AE output is passed to the RDE, the last block sequentially accomplishes the three steps[13] illustrated below for each of the considered $\bar{K}^{(\mathrm{RDE})}$ range-Doppler bins; in the description of such steps we refer to the kth range-Doppler bin (with $k = 0, 1, ..., \bar{K}^{(\mathrm{RDE})} - 1$).

1) The RDE generates the subset

$$\bar{\mathcal{S}}_k^{(\mathrm{AE})} \triangleq \left\{ \left(\hat{F}_{H_k}[l], \hat{F}_{V_k}[l], \hat{A}_k[l] \right);\ l = 0, 1, ..., \bar{K}_k^{(\mathrm{AE})} - 1 \right\} \tag{3.51}$$

of $\mathcal{S}_k^{(\mathrm{AE})}$, in (3.44), (here, $\bar{K}_k^{(\mathrm{AE})}$ denotes the size of $\bar{\mathcal{S}}_k^{(\mathrm{AE})}$, with $\bar{K}_k^{(\mathrm{AE})} \leq K_k^{(\mathrm{AE})}$); in doing so, it discards the lth element of $\mathcal{S}_k^{(\mathrm{AE})}$ (with $l = 0, 1, ..., K_k^{(\mathrm{AE})} - 1$) if

$$|\hat{A}_k[l]|^2 \leq \mathcal{T}^{(\mathrm{AE})}, \tag{3.52}$$

where $\mathcal{T}^{(\mathrm{AE})}$ is a proper threshold.

2) It merges the information provided by the N_{VA} antennas at the N subcarrier frequencies and over the M OFDM symbol intervals (i.e., over the whole OFDM frame) to generate a set of $\bar{K}_k^{(\mathrm{AE})}$ $M \times N$ matrices, each referring to a single element of the set $\bar{\mathcal{S}}_k^{(\mathrm{AE})}$. More specifically, the matrix associated with the lth element of $\bar{\mathcal{S}}_k^{(\mathrm{AE})}$ (with $l = 0, 1, ..., \bar{K}_k^{(\mathrm{AE})} - 1$) is denoted $\breve{\mathbf{H}}_k[l] \triangleq [\breve{H}_{m,n}[k, l]]$; moreover, the element appearing on its mth row and nth column is evaluated as

$$\breve{H}_{m,n}[k, l] \triangleq \frac{1}{N_{\mathrm{T}} N_{\mathrm{R}}} \sum_{p=0}^{N_{\mathrm{T}}-1} \sum_{q=0}^{N_{\mathrm{R}}-1} \hat{H}_{m,n}^{(p,q)}\, a_p\big(\hat{F}_{H_k}[l]\big)\, a_q\big(\hat{F}_{V_k}[l]\big), \tag{3.53}$$

with $m = 0, 1, ..., M - 1$ and $n = 0, 1, ..., N - 1$.

3) It processes the matrix $\breve{\mathbf{H}}_k[l]$ (with $l = 0, 1, ..., \bar{K}_k^{(\mathrm{AE})} - 1$) in order to estimate the range, Doppler and complex amplitude of the lth target detected in the kth range-Doppler bin. This requires estimating the parameters of a single complex exponential on the basis of the 2D sequence $\{\breve{H}_{m,n}[k, l]\}$) and leads to the *fine* estimates $(\hat{F}_{\nu_k}[l], \hat{F}_{r_k}[l], \hat{A}_k[l])$ of the normalized Doppler frequency, normalized delay and complex amplitude, respectively, of the above-mentioned target. These information are collected in the set

$$\bar{\mathcal{S}}_k^{(\mathrm{RDE})} \triangleq \left\{ \left(\hat{F}_{\nu_k}[l], \hat{F}_{r_k}[l], \hat{A}_k[l] \right);\ l = 0, 1, ..., \bar{K}_k^{(\mathrm{AE})} - 1 \right\}. \tag{3.54}$$

[13] Actually, the first step is ignored if all the targets detected in each range-Doppler bin are taken into consideration.

Note that the term $a_p(\hat{F}_{H_k}[l])$ ($a_q(\hat{F}_{V_k}[l])$) appearing in the RHS of (3.53) aims at *compensating* for the factor $a_p(-F_{H_k})$ ($a_q(-F_{V_k})$) that appears in the same side of (3.40); in other words, it is expected to cancel the dependence of $\hat{H}_{m,n}[k,l]$ on the *normalized horizontal* and *vertical frequencies* (i.e., on the angular parameters) of lth target detected in kth range-Doppler bin.

The strategy described above is called *Doppler-range-angle estimation with successive compensation*, or DRAEC, and is summarized in Algorithm 2. Its final output is represented by the set

$$\bar{\mathcal{S}}^{(\mathrm{DRAEC})} \triangleq \bigcup_{k=0}^{\bar{K}^{(\mathrm{RDE})}-1} \bar{\mathcal{S}}_k^{(\mathrm{DRAEC})}. \tag{3.55}$$

that collects the estimates referring to

$$K^{(\mathrm{DRAEC})} \triangleq \sum_{k=0}^{\bar{K}^{(\mathrm{RDE})}-1} \bar{K}_k^{(\mathrm{AE})} \tag{3.56}$$

distinct targets; here,

$$\bar{\mathcal{S}}_k^{(\mathrm{DRAEC})} \triangleq \left\{ \left(\hat{R}_k[l], \hat{v}_k[l], \hat{\theta}_k[l], \hat{\phi}_k[l], \hat{A}_k[l] \right); \, l = 0, 1, ..., \bar{K}_k^{(\mathrm{AE})} - 1 \right\}, \tag{3.57}$$

represents the contribution due to all the targets detected in the kth range-Doppler bin. Note that the set $\bar{\mathcal{S}}^{(\mathrm{DRAEC})}$, in (3.55), results from merging all the information provided by the RDE and the AE, namely the sets $\bar{\mathcal{S}}^{(\mathrm{RDE})}$ and $\{\bar{\mathcal{S}}_k^{(\mathrm{AE})}\}$. In other words, the final output is obtained by 1) converting each normalized frequency to the corresponding spatial parameter; 2) associating each target with its set of spatial parameters. These operations are carried out by the fusion block appearing in Fig. 3.3.

Finally, it is important to stress that the most important task accomplished by both the RDE and the AE is represented by the estimation of the parameters of 2D complex oscillations on the basis of a set of noisy measurements. Different algorithms can be employed for this task; the selection of a specific algorithm leads to a different instance of the DRAEC strategy, as illustrated in the following sections.

3.4 Description of Various Algorithms for the Detection and the Estimation of Two-Dimensional Complex Oscillations

In this section, we concentrate on the problem of detecting multiple overlapped 2D complex exponentials and estimating their parameters in the presence of AWGN. Various estimators, representing distinct solutions to this problem, are illustrated. In all cases, essential mathematical details are provided and a unified mathematical notation is employed. More specifically, it is assumed that: 1) $\{\hat{H}_{m,n}^{(\mathrm{X})};\ m = 0, 1, ..., M-1,\ n = 0, 1, ..., N-1\}$ (with

Algorithm 2: The DRAEC strategy.

Input: The set $\mathcal{S}_{\mathbf{H}}$, in (3.42), made of N_{VA} $M \times N$ matrices, and the indices of the reference antenna $((p_R, q_R))$.

1 **RDE-1:**

a- Generation of the TRDP: Process $\hat{\mathbf{H}}^{(p_R,q_R)}$ to generate the set $\mathcal{S}^{(\mathrm{RDE})}$ (see (3.43)), made of $K^{(\mathrm{RDE})}$ elements; one of the estimators described in Section 3.4 is employed in this step.

2 **AE:**

b- Reduction of the TRDP size: Discard some elements of the set $\mathcal{S}^{(\mathrm{RDE})}$ on the basis of their perceptual relevance (see (3.47)); the resulting set consists of $\bar{K}^{(\mathrm{RDE})}$ elements.

for $k = 0$ *to* $\bar{K}^{(\mathrm{RDE})} - 1$ **do**

c- Doppler and range compensation: Compute the $N_R \times N_T$ matrix $\breve{\mathbf{H}}_k$, whose element (p, q) is defined by (3.49).

d- Detection and angular estimation of the targets contributing to the kth range-Doppler bin: Detect all the targets contained in the kth range-Doppler bin and estimate their normalized horizontal and vertical frequencies, and their complex amplitude on the basis of the matrix $\breve{\mathbf{H}}_k$ (one of the estimators described in Section 3.4 is employed); this produces the set $\mathcal{S}_k^{(\mathrm{AE})}$, in (3.44), made of $K_k^{(\mathrm{AE})}$ elements.

3 **RDE-2:**

e- Reduction of the AP size: Discard some elements of the set $\mathcal{S}_k^{(\mathrm{AE})}$, in (3.44), on the basis of their perceptual relevance (see (3.52)); the resulting set (see (3.51)) consists of $\bar{K}_k^{(\mathrm{AE})}$ elements.

for $l = 0$ *to* $\bar{K}_k^{(\mathrm{AE})} - 1$ **do**

f- Angular compensation: Compute the $M \times N$ matrix $\breve{\mathbf{H}}_k[l]$, whose element (m, n) is defined by (3.53).

g- Fine estimation: Evaluate the fine estimates of the normalized Doppler frequency $F_{\nu_k}[l]$, the normalized delay $F_{r_k}[l]$, and the complex amplitude $A_k[l]$ of the lth target contained in the kth range-Doppler bin on the basis of the matrix $\breve{\mathbf{H}}_k[l]$; one of the estimators described in Section 3.4 is employed in this step.

end

end

Output: The set $\bar{\mathcal{S}}^{(\mathrm{DRAEC})}$, in (3.55).

X = RDE or X = AE) represents the input sequence[14] of any 2D estimator employed in the RDE or in the AE; 2) the element (m, n) of this sequence can be expressed as

$$\hat{H}^{(\mathrm{X})}_{m,n} \triangleq \sum_{k=0}^{K-1} A_k \, a_m(F_{1,k}) \, a_n(F_{2,k}) + W^{(\mathrm{X})}_{m,n}, \tag{3.58}$$

where $F_{1,k} = F_{\nu_k}$, $F_{2,k} = -F_{\rho_k}$ ($F_{1,k} = -F_{H_k}$, $F_{2,k} = -F_{V_k}$) if the estimator is employed in the RDE (AE); 3) the parameters A_k, F_{ν_k}, F_{ρ_k}, F_{H_k} and F_{V_k} have the same meaning as the corresponding parameters appearing in the RHS of (3.40) and $W^{(\mathrm{X})}_{m,n}$ is the noise sample affecting $\hat{H}^{(\mathrm{X})}_{m,n}$ (an AWGN model is adopted for the sequence $\{W^{(\mathrm{X})}_{m,n}\}$).

All the algorithms described in the following subsections make use of 2D periodograms. More specifically, *target detection* and *range & Doppler estimation* in the RDE require the computation of the $M_0 \times N_0$ matrix

$$\mathbf{Y}^{(\mathrm{RDE})} = [Y^{(\mathrm{RDE})}[l, p]] \triangleq \mathrm{DSFT}_{M_0,N_0}\left[\hat{\mathbf{H}}^{(\mathrm{RDE})}_{\mathrm{ZP}}\right] \triangleq \mathbf{F}_{M_0} \hat{\mathbf{H}}^{(\mathrm{RDE})}_{\mathrm{ZP}} \mathbf{F}^{H}_{N_0}, \tag{3.59}$$

that represents the order (M_0, N_0) DSFT of the $M_0 \times N_0$ matrix

$$\hat{\mathbf{H}}^{(\mathrm{RDE})}_{\mathrm{ZP}} \triangleq \begin{bmatrix} \hat{\mathbf{H}}^{(\mathrm{RDE})} & \mathbf{0}_{M,N_0-N} \\ \mathbf{0}_{M_0-M,N} & \mathbf{0}_{M_0-M,N_0-N} \end{bmatrix}, \tag{3.60}$$

that results from zero-padding the $M \times N$ matrix $\hat{\mathbf{H}}^{(\mathrm{RDE})} \triangleq [\hat{H}^{(\mathrm{RDE})}_{m,n}]$ (see (3.58)); here, $\mathbf{F}_N$ represents the order N Fourier matrix (its element (a, b) is equal to ω_N^{ab}/N, where $\omega_N = \exp(-j2\pi/N)$). The element (l, p) of $\mathbf{Y}^{(\mathrm{RDE})}$, in (3.59), is given by

$$Y^{(\mathrm{RDE})}[l, p] \triangleq \frac{1}{MN} \sum_{m=0}^{M-1} \sum_{n=0}^{N-1} \hat{H}^{(\mathrm{RDE})}_{m,n} \exp\left(-j2\pi m \frac{l}{M_0}\right) \exp\left(j2\pi n \frac{p}{N_0}\right), \tag{3.61}$$

where

$$M_0 \triangleq L_1^{(\mathrm{RDE})} M, \tag{3.62}$$

$$N_0 \triangleq L_2^{(\mathrm{RDE})} N, \tag{3.63}$$

and $L_1^{(\mathrm{RDE})}$ and $L_2^{(\mathrm{RDE})}$ represent the *oversampling factors* adopted in RDE processing. Note that $Y^{(\mathrm{RDE})}[l, p]$ is associated with the *normalized Doppler frequency*

$$F_\nu[l] \triangleq l \, \bar{F}_\nu - 1/2 \tag{3.64}$$

and the *normalized frequency* (accounting for both range and Doppler; see (3.36))

$$F_\rho[p] \triangleq p \, \bar{F}_\rho, \tag{3.65}$$

where

$$\bar{F}_\nu \triangleq 1/M_0 \tag{3.66}$$

[14] This 2D sequence corresponds to $\{\hat{H}^{(p_{\mathrm{R}},q_{\mathrm{R}})}_{m,n}\}$ or $\{\check{H}_{m,n}[k, l]\}$ (see (3.40) and (3.53), respectively) in the case of the RDE; it corresponds, instead, to $\{\check{H}^{(p,q)}_k\}$ (see (3.49)) in the case of the AE.

and

$$\bar{F}_\rho \triangleq 1/N_0. \tag{3.67}$$

Similarly, *angular estimation* in the AE requires the computation of the $\bar{M}_0 \times \bar{N}_0$ matrix

$$\mathbf{Y}^{(\mathrm{AE})} = [Y^{(\mathrm{AE})}[l,p]] \triangleq \mathrm{IDFT}_{\bar{M}_0,\bar{N}_0}\left[\hat{\mathbf{H}}_{\mathrm{ZP}}^{(\mathrm{AE})}\right] \triangleq \mathbf{F}_{\bar{M}_0}^H \hat{\mathbf{H}}_{\mathrm{ZP}}^{(\mathrm{AE})} \mathbf{F}_{\bar{N}_0}^H, \tag{3.68}$$

that represents the order $(\bar{M}_0, \bar{N}_0)$ 2D-Inverse Discrete Fourier Transform (IDFT) of the $\bar{M}_0 \times \bar{N}_0$ matrix $\hat{\mathbf{H}}_{\mathrm{ZP}}^{(\mathrm{AE})}$, that results from zero-padding the $N_\mathrm{T} \times N_\mathrm{R}$ matrix $\hat{\mathbf{H}}^{(\mathrm{AE})} \triangleq [\hat{H}_{m,n}^{(\mathrm{AE})}]$ (see (3.58)). In practice, the structure of the matrix $\hat{\mathbf{H}}_{\mathrm{ZP}}^{(\mathrm{AE})}$ is expressed by the RHS of (3.60) if the matrix $\hat{\mathbf{H}}^{(\mathrm{RDE})}$ and the parameters M, N, M_0 and N_0 are replaced by $\hat{\mathbf{H}}^{(\mathrm{AE})}$ and N_R, N_T, $\bar{M}_0$ and $\bar{N}_0$, respectively; moreover, the element (l,p) of $\mathbf{Y}^{(\mathrm{AE})}$ is given by

$$Y^{(\mathrm{AE})}[l,p] \triangleq \frac{1}{N_R N_T} \sum_{m=0}^{N_\mathrm{R}-1} \sum_{n=0}^{N_\mathrm{T}-1} \hat{H}_{m,n}^{(\mathrm{AE})} \exp\left(j2\pi m \frac{l}{\bar{M}_0}\right) \exp\left(j2\pi n \frac{p}{\bar{N}_0}\right), \tag{3.69}$$

where

$$\bar{M}_0 \triangleq L_1^{(\mathrm{AE})} N_\mathrm{R}, \tag{3.70}$$

$$\bar{N}_0 \triangleq L_2^{(\mathrm{AE})} N_\mathrm{T}, \tag{3.71}$$

and $L_1^{(\mathrm{AE})}$ and $L_2^{(\mathrm{AE})}$ are the *oversampling factors* adopted in AE processing. Furthermore, $Y^{(\mathrm{AE})}[l,p]$ is associated with the *normalized horizontal frequency*

$$F_H[p] \triangleq p\,\bar{F}_H - 1/2 \tag{3.72}$$

and the *normalized vertical frequency*

$$F_V[l] \triangleq l\,\bar{F}_V - 1/2, \tag{3.73}$$

where

$$\bar{F}_H \triangleq 1/\bar{N}_0 \tag{3.74}$$

and

$$\bar{F}_V \triangleq 1/\bar{M}_0. \tag{3.75}$$

In the remaining part of this section, we take into consideration six different estimation algorithms and provide a brief mathematical description of each of them. The first five algorithms are FFT-based methods and, more precisely, are the 2D periodogram method [4], the CSFDEC algorithm derived in Chapter 1, the estimation algorithm proposed by *Popović et al.* in [70], a *modified* version of the estimation algorithm devised by *Fan et al.* in [72] for solving the problem of channel estimation in a hybrid millimeter-wave massive MIMO system and the *q-shift estimator* (dubbed QSE) developed in [71]. The sixth (and last) algorithm can be considered as an extension to 2D frequency estimation of the algorithm developed by *Lee et al.* in [67]; therefore, it is dubbed *extended Lee algorithm*, or ELA. In the description of each estimation algorithm, we first describe its formulation for the RDE; then, we illustrate the changes required to make its use possible in the AE.

3.4.1 Two-dimensional periodogram method

This method is based on the idea that the frequencies of the 2D complex exponentials forming the useful component of the sequence $\{\hat{H}_{m,n}^{(\mathrm{X})}\}$ are associated with the peaks of a 2D periodogram. For this reason, if the kth target is considered (with $k = 0, 1, ..., \hat{K} - 1$, where $\hat{K}$ denotes an estimate of the overall number of targets), the estimates $\hat{F}_{\nu_k}$ and $\hat{F}_{\rho_k}$ of its normalized frequencies F_{ν_k} (3.35) and F_{ρ_k} (3.36), respectively, are evaluated as $\hat{F}_{\nu_k} = F_{\nu}[\hat{l}_k^{(\mathrm{RDE})}]$ and $F_{\rho_k} = F_{\rho}[\hat{p}_k^{(\mathrm{RDE})}]$ (see (3.64) and (3.65), respectively), where $(\hat{l}_k^{(\mathrm{RDE})}, \hat{p}_k^{(\mathrm{RDE})})$ is the value of the couple $(\tilde{l}, \tilde{p})$ associated with the kth of the $\hat{K}$ most relevant local maxima (peaks) of the 2D sequence $\{|Y^{(\mathrm{RDE})}[\tilde{l}, \tilde{p}]|^2;\ \tilde{l} \in \mathcal{S}_{M_0},\ \tilde{p} \in \mathcal{S}_{N_0}\}$, $Y^{(\mathrm{RDE})}[l, p]$ is expressed by (3.61) and

$$\mathcal{S}_U \triangleq \{0, 1, ..., U - 1\} \tag{3.76}$$

for any positive integer U.

This algorithm can be also used in the AE block to evaluate the estimates $\hat{F}_{H_k} = F_H[\hat{p}_k^{(\mathrm{AE})}]$ and $\hat{F}_{V_k} = F_V[\hat{l}_k^{(\mathrm{AE})}]$ (see (3.72) and (3.73), respectively) of the normalized frequencies F_{H_k} (3.33) and F_{V_k} (3.34); the couple of $(\hat{l}_k^{(\mathrm{AE})}, \hat{p}_k^{(\mathrm{AE})})$ is generated in a similar way as $(\hat{l}_k^{(\mathrm{RDE})}, \hat{p}_k^{(\mathrm{RDE})})$, the only difference being represented by the fact that $Y^{(\mathrm{RDE})}[l, p]$, in (3.61), is replaced by $Y^{(\mathrm{AE})}[l, p]$, in (3.69).

The estimation accuracy of this method can be improved by:

1) Extracting an $I_l \times I_p$ sub-matrix (where I_l and I_p denote the interpolation orders adopted in the Doppler and range domains, respectively), whose central element is $Y^{(\mathrm{X})}[\hat{l}_k^{(\mathrm{X})}, \hat{p}_k^{(\mathrm{X})}]$ (with $k = 0, 1, ..., \hat{K} - 1$ and X = RDE or AE) from $\mathbf{Y}^{(\mathrm{X})}$ in order to generate a more detailed representation of the analyzed spectrum through the *interpolation*[15] of the sub-matrix elements.

2) Identifying the peak of the interpolated spectrum over the considered 2D domain.

3.4.2 Complex single frequency delay estimation and cancellation algorithm

The second FFT-based method is the CSFDEC and it is described in Chapter 1. This algorithm can be exploited by the RDE block as it is, whereas some modifications are required if it is employed in the AE block. For this reason, here we limit ourselves to illustrating the changes to be made for its use in the AE.

In particular, this requires:

1) Using $\hat{H}_{m,n}^{(\mathrm{AE})}$ (see (3.58)) in place of $\hat{H}_{m,n}^{(\mathrm{RDE})}$ in the evaluation of $\hat{H}_{m,n}^{(k_1,k_2)}$ according to (1.38).

[15] In the considered computer simulations, the 'spline' interpolation (*interp2* function) of Matlab R2022b has been employed.

2) Evaluating the initial estimate of the complex amplitude of the strongest 2D tone as (see (1.33))

$$\hat{A}^{(0)} = \bar{Y}_{0,0}\left(\hat{F}_{V,c}^{(0)}, \hat{F}_{H,c}^{(0)}\right), \tag{3.77}$$

where $\hat{F}_{V,c}^{(0)} = F_V[\hat{l}_k^{(0)}]$ and $\hat{F}_{H,c}^{(0)} = F_H[\hat{p}_k^{(0)}]$ (see (3.73) and (3.72), respectively) are the coarse estimates of the normalized vertical and horizontal frequencies, respectively.

3) Replacing (1.48) and (1.49) with

$$\begin{aligned} b_\Delta(F_V, F_H) &= -\hat{\Omega}^3\, \Im\{\hat{A}^* \bar{Y}_{3,2}(F_V, F_H)\}/3 + \hat{\Omega}^2\, \Re\{\hat{A}^* \bar{Y}_{2,2}(F_V, F_H)\} \\ &\quad + 2\hat{\Omega}\, \Im\{\hat{A}^* \bar{Y}_{1,2}(F_V, F_H)\} - 2\Re\{\hat{A}^* \bar{Y}_{0,2}((F_V, F_H)\} \end{aligned} \tag{3.78}$$

and

$$\begin{aligned} c_\Delta(F_V, F_H) &= \hat{\Omega}^3\, \Re\{\hat{A}^* \bar{Y}_{3,1}(F_V, F_H)\}/3 + \hat{\Omega}^2\, \Im\{\hat{A}^* \bar{Y}_{2,1}(F_V, F_H)\} \\ &\quad - 2\hat{\Omega}\, \Re\{\hat{A}^* \bar{Y}_{1,1}(F_V, F_H)\} - 2\Im\{\hat{A}^* \bar{Y}_{0,1}(F_V, F_H)\}, \end{aligned} \tag{3.79}$$

respectively.

3.4.3 Popović algorithm

The third FFT-based method (namely, Alg-P) computes the frequency estimates through a serial refinement and cancellation procedure based on the computation of a set of shifted DFT coefficients and their subsequent parabolic fitting. If employed in the RDE, it is fed by the complex sequence $\{\hat{H}_{m,n}^{(\mathrm{RDE})}\}$ and it is initialized by setting the target index k to zero and $H_{m,n}^{(0)} = \hat{H}_{m,n}^{(\mathrm{RDE})}$ for $m = 0, 1, ..., M-1$ and $n = 0, 1, ..., N-1$. Then, it sequentially executes the three steps described below for the kth target (with $k = 0, 1, ..., \hat{K}-1$, where $\hat{K}$ is an estimate of K).

1) *2D periodogram maximization* - In this step, the coarse estimates of the normalized Doppler frequency F_{ν_k} and the normalized range frequency F_{ρ_k} are evaluated as $\hat{F}_{\nu,c}^{(k)} = F_\nu[\hat{l}_k^{(0)}]$ and $\hat{F}_{\rho,c}^{(k)} = F_\rho[\hat{p}_k^{(0)}]$, respectively (see (3.64) and (3.65), respectively); here,

$$\left(\hat{l}_k^{(0)}, \hat{p}_k^{(0)}\right) = \underset{\tilde{l} \in \mathcal{S}_{M_0}, \tilde{p} \in \mathcal{S}_{N_0}}{\arg\max} \left| Y^{(k)}[\tilde{l}, \tilde{p}] \right|^2, \tag{3.80}$$

and $Y^{(k)}[l, p]$ is defined in a similar way as $Y^{(\mathrm{RDE})}[l, p]$, in (3.61), the only difference being represented by the fact that $\hat{H}_{m,n}^{(\mathrm{RDE})}$ is replaced by $H_{m,n}^{(k)}$ (the evaluation of $H_{m,n}^{(k)}$ is illustrated below).

2) *Frequency refinement and amplitude estimation* - In this step, the fine estimates $\hat{F}_{\nu_k}$ and $\hat{F}_{\rho_k}$ of F_{ν_k} and F_{ρ_k}, respectively, are computed according to the formula (see [70, Table 1,

eqs. (10)-(11)])

$$\hat{F}_X = \frac{1}{2}\frac{\Gamma_{\mathrm{NUM}}}{\Gamma_{\mathrm{DEN}}}, \tag{3.81}$$

with $X = \nu$ or ρ; here,

$$\Gamma_{\mathrm{NUM}} = \psi_{X,3}^2 \left(P_{X,1} - P_{X,2}\right) + \psi_{X,2}^2 \left(P_{X,3} - P_{X,1}\right) + \psi_{X,1}^2 \left(P_{X,2} - P_{X,3}\right), \tag{3.82}$$

$$\Gamma_{\mathrm{DEN}} = \psi_{X,3} \left(P_{X,1} - P_{X,2}\right) + \psi_{X,2} \left(P_{X,3} - P_{X,1}\right) + \psi_{X,1} \left(P_{X,2} - P_{X,3}\right), \tag{3.83}$$

$\psi_{X,i} \triangleq \delta_{X,c} + (i-2)/(2\,Q_0)$ (with $i = 1, 2$ and 3), $Q = M$ ($Q = N$) if $X = \nu$ (if $X = \rho$),

$$\delta_{\nu,c} \triangleq \hat{F}_{\nu,c} + \frac{1}{\pi} \arctan\left(\tan\left(\pi/M_0\right) \Re\left\{\Theta_D\right\}\right), \tag{3.84}$$

$$\delta_{\rho,c} \triangleq \hat{F}_{\rho,c} + \frac{1}{\pi} \arctan\left(\tan\left(\pi/N_0\right) \Re\left\{\Theta_\rho\right\}\right), \tag{3.85}$$

$$\Theta_D \triangleq \frac{Y^{(k)}\big(\hat{l}-1,\hat{p}\big) - Y^{(k)}\big(\hat{l}+1,\hat{p}\big)}{2Y^{(k)}\big(\hat{l},\hat{p}\big) - Y^{(k)}\big(\hat{l}-1,\hat{p}\big) - Y^{(k)}\big(\hat{l}+1,\hat{p}\big)}, \tag{3.86}$$

$$\Theta_\rho \triangleq \frac{Y^{(k)}\big(\hat{l},\hat{p}-1\big) - Y^{(k)}\big(\hat{l},\hat{p}+1\big)}{2Y^{(k)}\big(\hat{l},\hat{p}\big) - Y^{(k)}\big(\hat{l},\hat{p}-1\big) - Y^{(k)}\big(\hat{l},\hat{p}+1\big)}, \tag{3.87}$$

$$P_{\nu,i} \triangleq \left| \sum_{m=0}^{M-1} \sum_{n=0}^{N-1} \hat{H}_{m,n}^{(\mathrm{RDE})} \exp\left(-j2\pi(m\,\psi_{\nu,i} - n\,\psi_{r,2})\right) \right| \tag{3.88}$$

and

$$P_{\rho,i} \triangleq \left| \sum_{m=0}^{M-1} \sum_{n=0}^{N-1} \hat{H}_{m,n}^{(\mathrm{RDE})} \exp\left(-j2\pi(m\,\psi_{\nu,2} - n\,\psi_{\rho,i})\right) \right|, \tag{3.89}$$

with $i = 1, 2$ and 3. Finally, an estimate of the complex amplitude A_k is evaluated on the basis of (1.33), where $(\hat{F}_\nu, \hat{F}_r)$ is replaced by $(\hat{F}_{\nu_k}, \hat{F}_{\rho_k})$.

3) *Target cancellation* - In this step, the contribution of the $(k+1)$ previously detected targets is subtracted from $\{\hat{H}_{m,n}^{(\mathrm{RDE})}\}$; this produces the 2D residual sequence $\{H_{m,n}^{(k+1)}\}$, where

$$H_{m,n}^{(k+1)} \triangleq \hat{H}_{m,n}^{(\mathrm{RDE})} - \sum_{i=0}^{k} \hat{A}_i\, a_m\big(\hat{F}_{\nu_i}\big) a_n\big(-\hat{F}_{\rho_i}\big), \tag{3.90}$$

with $m = 0, 1, ..., M-1$ and $n = 0, 1, ..., N-1$. Then, the residual spectrum $\mathbf{Y}^{(k+1)} \triangleq [Y^{(k+1)}[l,p]]$ is computed; the expression of the element (l,p) of this $M_0 \times N_0$ matrix is obtained from that of $Y^{(\mathrm{RDE})}[l,p]$, in (3.61), by simply replacing $\hat{H}_{m,n}^{(\mathrm{RDE})}$ with $H_{m,n}^{(k+1)}$ (additional details can be found in the description of the *sinousoid removal* step available in [70, Table 2, eq.(12)-(13)]). If the energy $\varepsilon[k+1] \triangleq \|\mathbf{Y}^{(k+1)}\|^2$ (with $\|\cdot\|$ denoting the *norm* operator) is smaller than $\mathcal{T}^{(P)}$, where $\mathcal{T}^{(P)}$ is a proper threshold, the algorithm stops and the estimate $\hat{K} = k+1$ of K is generated; otherwise, k is increased by one and the three steps described above are accomplished again.

The use of Alg-P in the AE requires the following modifications: 1) the spectral coefficient $Y^{(k)}[\tilde{l},\tilde{p}]$ appearing in the RHS of (3.80) is still expressed by (3.69), where, however, $\hat{H}_{m,n}^{(\mathrm{AE})}$

is replaced by

$$H_{m,n}^{(k+1)} \triangleq \hat{H}_{m,n}^{(\mathrm{AE})} - \sum_{i=0}^{k} \hat{A}_i \, a_m\big(-\hat{F}_{V_i}\big) a_n\big(-\hat{F}_{H_i}\big); \tag{3.91}$$

2) formula (3.81) (with $X = V$ or H) is employed to compute the estimates $\hat{F}_{H_k}$ and $\hat{F}_{V_k}$ of F_{H_k} and F_{V_k}, but the quantities

$$P_{H,i} \triangleq \Big| \sum_{m=0}^{M-1} \sum_{n=0}^{N-1} \hat{H}_{m,n}^{(\mathrm{AE})} \exp\left(j2\pi(m\,\psi_{V,2} + n\,\psi_{H,i})\right) \Big| \tag{3.92}$$

and

$$P_{V,i} \triangleq \Big| \sum_{m=0}^{M-1} \sum_{n=0}^{N-1} \hat{H}_{m,n}^{(\mathrm{AE})} \exp\left(j2\pi(m\,\psi_{V,i} + n\,\psi_{H,2})\right) \Big| \tag{3.93}$$

are used in place of $P_{\rho,i}$ (3.89) and $P_{\nu,i}$ (3.88), respectively. A schematic description of Alg-P is provided in [70, Sec. 3, Table 1 and Table 2].

3.4.4 Modified Fan algorithm

The fourth FFT-based method (namely, the MFA) results from: 1) adapting the estimation algorithm devised in [72] to the signal model expressed by (3.58); 2) including zero-padding in the initialization of the 2D periodogram method (see Section 3.4.1). The processing accomplished by the proposed algorithm evolves through the following two consecutive steps; note that, in this case, an estimate, denoted $\hat{K}$, of the overall number of targets is required.

1) 2D *periodogram maximization* - In this step, the 2D periodogram is maximized (see the description of the 2D periodogram method in Section 3.4.1) in order to evaluate the *coarse estimates* $\hat{F}_{\nu_k,c}$ and $\hat{F}_{\rho_k,c}$ of the normalized Doppler frequency F_{ν_k}, in (3.35), and the normalized range frequency F_{ρ_k}, in (3.36), respectively, with $k = 0, 1, ..., \hat{K} - 1$.

2) *Frequency refinement* - First, the *fine estimates* of normalized Doppler frequency F_{ν_k} and the normalized range frequency F_{ρ_k} are evaluated as

$$\hat{F}_{\nu_k} = \hat{F}_{\nu_k,c} - \hat{\Delta}_{\nu_k} \tag{3.94}$$

and

$$\hat{F}_{\rho_k} = \hat{F}_{\rho_k,c} + \hat{\Delta}_{\rho_k} \tag{3.95}$$

respectively, where

$$(\hat{\Delta}_{\nu_k}, \hat{\Delta}_{\rho_k}) \triangleq \underset{(\tilde{\Delta}_{\nu_k}, \tilde{\Delta}_{\rho_k}) \in \mathcal{I}_\nu(M_0) \times \mathcal{I}_\rho(N_0)}{\arg\max} J_k\big(\tilde{\Delta}_{\nu_k}, \tilde{\Delta}_{\rho_k}\big), \tag{3.96}$$

with $k = 0, 1, ..., \hat{K} - 1$, $\tilde{\Delta}_{\nu_k}$ ($\tilde{\Delta}_{\rho_k}$) represents the trial variable for the residual Δ_{ν_k} (Δ_{ρ_k}), $\mathcal{I}_\nu(M_0)$ ($\mathcal{I}_\rho(N_0)$) is the *search domain* for Δ_{ν_k} (Δ_{ρ_k}),

$$J_k\big(\tilde{\Delta}_{\nu_k}, \tilde{\Delta}_{\rho_k}\big) \triangleq \Big| \mathbf{f}_M^H\big(\hat{F}_{\nu_k,c}\big) \mathbf{\Phi}_M\big(\tilde{\Delta}_{\nu_k}\big) \hat{\mathbf{H}}^{(\mathrm{RDE})} \mathbf{\Phi}_N\big(\tilde{\Delta}_{\rho_k}\big) \mathbf{g}_N\big(\hat{F}_{\rho_k,c}\big) \Big|^2 \tag{3.97}$$

is the cost function selected for the considered estimation problem (see [72, Sec. III, eq. (31)]),

$$\mathbf{f}_M(F_\nu) \triangleq \frac{1}{M}\left[\exp(j2\pi(M/2)F_\nu), ..., 1, \exp(-j2\pi F_\nu), ..., \exp(-j2\pi(M/2-1)F_\nu)\right]^T, \tag{3.98}$$

$$\mathbf{g}_N(F_\rho) \triangleq \frac{1}{N}\left[1, \exp(j2\pi F_\rho), ..., \exp(j2\pi(N-1)F_\rho)\right]^T \tag{3.99}$$

and

$$\mathbf{\Phi}_X\Big(\Delta_{Q_k}\Big) \triangleq \mathrm{diag}\Big\{\Big[1, \exp\Big(j2\pi\Delta_{Q_k}\Big), ..., \exp\Big(j2\pi\big(X-1\big)\Delta_{Q_k}\Big)\Big]\Big\}, \tag{3.100}$$

with $Q=\nu$ ($Q=\rho$) if $X=M$ (if $X=N$). Then, the estimate

$$\hat{A}_k \triangleq \mathbf{f}_M^H\big(\hat{F}_{\nu_k}\big)\hat{\mathbf{H}}^{(\mathrm{RDE})}\mathbf{g}_N\big(\hat{F}_{\rho_k}\big) \tag{3.101}$$

of the complex amplitude characterizing the kth target is evaluated (with $k=0,1,...,\hat{K}-1$). It is important to point out that the search domain $\mathcal{I}_\nu(M_0)$ ($\mathcal{I}_\rho(N_0)$) selected in the computer simulations consists of N_{F_ν} (N_{F_ρ}) equally spaced numbers belonging to the interval $[-1/M_0,\, 1/M_0]$ ($[-1/N_0,\, 1/N_0]$); this interval covers two adjacent bins of the periodogram computed in the initialization of the algorithm.

The use of the MFA in the AE block requires the following changes:

1) The 2D periodogram method processes the spectral matrix $\mathbf{Y}^{(\mathrm{AE})}$, in (3.68), (in place of $\mathbf{Y}^{(\mathrm{RDE})}$, in (3.59)) to produce the *coarse estimates* $\hat{F}_{H_k,c}$ and $\hat{F}_{V_k,c}$ of the normalized frequencies F_{H_k} (3.33) and F_{V_k} (3.34), respectively (with $k=0,1,...,\hat{K}-1$).

2) The *fine estimates* of F_{H_k} and F_{V_k} are evaluated as $\hat{F}_{H_k}=\hat{F}_{H_k,c}+\hat{\Delta}_{H_k}$ and $\hat{F}_{V_k}=\hat{F}_{V_k,c}+\hat{\Delta}_{V_k}$, respectively. The estimates of the residuals $\hat{\Delta}_{H_k}$ and $\hat{\Delta}_{V_k}$ represent the solution of an optimization problem formally identical to (3.96), where, however, $J_k(\tilde{\Delta}_{\nu_k}, \tilde{\Delta}_{\rho_k})$ is replaced by

$$J_k\big(\tilde{\Delta}_{V_k}, \tilde{\Delta}_{H_k}\big) \triangleq \Big|\mathbf{f}_M^H\big(\hat{F}_{V_k,c}\big)\mathbf{\Phi}_M\big(\Delta_{V_k}\big)\hat{\mathbf{H}}^{(\mathrm{AE})}\mathbf{\Phi}_N\big(\Delta_{H_k}\big)\mathbf{f}_N\big(\hat{F}_{H_k,c}\big)\Big|^2, \tag{3.102}$$

where

$$\mathbf{f}_X(F_Q) \triangleq \frac{1}{X}\big[\exp\big(-j2\pi(X/2)F_Q\big), ..., 1, \exp\big(j2\pi F_Q\big), \exp\big(j2\pi(X/2-1)F_Q\big)\big]^T, \tag{3.103}$$

with $Q=V$ ($Q=H$) if $X=M$ (if $X=N$). Finally, the estimate

$$\hat{A}_k \triangleq \mathbf{f}_M^H\big(\hat{F}_{V_k}\big)\hat{\mathbf{H}}^{(\mathrm{AE})}\mathbf{f}_N\big(\hat{F}_{H_k}\big) \tag{3.104}$$

of the complex amplitude characterizing the kth target is evaluated (with $k=0,1,...,\hat{K}-1$).

The MFA is summarized in Algorithm 3.

Algorithm 3: Modified Fan algorithm (MFA)

Input: The matrix $\hat{\mathbf{H}}^{(\mathrm{RDE})}$ ($\hat{\mathbf{H}}^{(\mathrm{AE})}$) if the RDE (AE) is considered and an estimate of the overall number of targets ($\hat{K}$).

1 **Initialization:**

a- Compute the coarse estimates $\hat{F}_{\nu_k,c}$ and $\hat{F}_{\rho_k,c}$ ($\hat{F}_{V_k,c}$ and $\hat{F}_{H_k,c}$), if the RDE (AE) is considered, by resorting the 2D periodogram method.

2 **Refinement procedure:**

for $k = 0$ *to* $\hat{K} - 1$ **do**

b- Compute the *fine estimates* $\hat{F}_{\nu_k} = \hat{F}_{\nu_k,c} - \hat{\Delta}_{\nu_k}$ and $\hat{F}_{\rho_k} = \hat{F}_{\rho_k,c} + \hat{\Delta}_{\rho_k}$ ($\hat{F}_{H_k} = \hat{F}_{H_k,c} + \hat{\Delta}_{H_k}$ and $\hat{F}_{V_k} = \hat{F}_{V_k,c} + \hat{\Delta}_{V_k}$) if the RDE (AE) is considered. The quantities $(\hat{\Delta}_{\nu_k}, \hat{\Delta}_{\rho_k})$ ($(\hat{\Delta}_{H_k}, \hat{\Delta}_{V_k})$) result from solving the optimization problem (3.96) with the cost function (3.97) ((3.102)) for the RDE (AE).

c- Compute the amplitude estimate $\hat{A}_k$ through (3.101) ((3.104)) for the RDE (AE).

end

Output: The set of estimates $\{(\hat{F}_{\nu_k}, \hat{F}_{\rho_k}, \hat{A}_k); k = 0, 1, ..., \hat{K} - 1\}$ ($\{(\hat{F}_{H_k}, \hat{F}_{V_k}, \hat{A}_k); k = 0, 1, ..., \hat{K} - 1\}$) for the RDE (AE).

3.4.5 Q-shift estimator

The fifth FFT-based algorithm (namely, the QSE) has been proposed by [71] to estimate the frequency of a 2D complex tone in the presence of AWGN. Similarly to the MFA, this estimator makes use of the 2D periodogram method for coarse frequency estimation and requires prior knowledge of the overall number of targets; however, it exploits a different method for frequency refinement. In fact, the last task is accomplished by a serial procedure that requires the evaluation of the DFT coefficients located at the relevant frequency bins shifted by a quantity $q \in [-0.5, 0.5]$. In practice, the final estimates of the normalized frequencies F_{ν_k} (3.35) and F_{ρ_k} (3.36) are evaluated as

$$\hat{F}_{Q_k} = \hat{F}_{Q_k,c} + \hat{\delta}_{Q_k}/X, \tag{3.105}$$

with $Q = \nu$ ($Q = \rho$) if $X = M$ (if $X = N$); here, $\hat{F}_{Q_k,c}$ is a coarse estimate of F_{Q_k} and $\hat{\delta}_{Q_k}$ is an estimate of the associated residual. In the QSE, $\hat{F}_{\nu_k,c}$ ($\hat{F}_{\rho_k,c}$) is evaluated according to (3.64) ((3.65)) with $l = \hat{l}_k^{(\mathrm{RDE})}$ (with $p = \hat{p}_k^{(\mathrm{RDE})}$) and the couple $(\hat{l}_k^{(\mathrm{RDE})}, \hat{p}_k^{(\mathrm{RDE})})$ is provided by the 2D periodogram method for the RDE (see Section 3.4.1). The estimation of the residuals $(\hat{\delta}_{\nu_k}, \hat{\delta}_{\rho_k})$, instead, is accomplished by an iterative procedure; this is initialized by setting the initial estimates of the residuals (namely, $\hat{\delta}_{\nu_k}^{(0)}$ and $\hat{\delta}_{\rho_k}^{(0)}$) to zero and the iteration index i to 1. In the ith iteration (with $i = 1, 2, ..., N_{\mathrm{it}}$, where N_{it} is the overall number of iterations), the new estimate of the residual $\hat{\delta}_{X_k}^{(i)}$ is computed as

$$\hat{\delta}_{X_k}^{(i)} = \hat{\delta}_{X_k}^{(i-1)} + \frac{1}{c_X(q_X)} \Re \left\{ \frac{S_{+q_X}^{(i)} - S_{-q_X}^{(i)}}{S_{+q_X}^{(i)} + S_{-q_X}^{(i)}} \right\}, \tag{3.106}$$

with $X = \nu$ or ρ, and $k = 0, 1, ..., \hat{K} - 1$; here, $\hat{K}$ denotes the estimate of K,

$$S_{\pm q_\nu}^{(i)} \triangleq \sum_{m=0}^{M-1} \sum_{n=0}^{N-1} \hat{H}_{m,n}^{(\mathrm{RDE})} \exp\left(-j2\pi \left(m\Upsilon_{\pm 1,q_\nu} - n\Upsilon_{0,q_\rho}\right)\right) \tag{3.107}$$

and

$$S_{\pm q_\rho}^{(i)} \triangleq \sum_{m=0}^{M-1} \sum_{n=0}^{N-1} \hat{H}_{m,n}^{(\mathrm{RDE})} \exp\left(-j2\pi \left(m\Upsilon_{0,q_\nu} - n\Upsilon_{\pm 1,q_\rho}\right)\right) \tag{3.108}$$

are the DFT coefficients evaluated with small shifts (quantified by the real parameters q_ν and q_ρ) with respect to the periodogram peak associated with the couple $(\hat{l}_k^{(\mathrm{RDE})}, \hat{p}_k^{(\mathrm{RDE})})$. Moreover,

$$\Upsilon_{z,q_\nu} \triangleq \left(\hat{l}_k^{(\mathrm{RDE})} \bar{F}_\nu + \frac{\hat{\delta}_{\nu_k}^{(i-1)} + zq_\nu}{M}\right) \tag{3.109}$$

and

$$\Upsilon_{z,q_\rho} \triangleq \left(\hat{p}_k^{(\mathrm{RDE})} \bar{F}_\rho + \frac{\hat{\delta}_{\rho_k}^{(i-1)} + zq_\rho}{N}\right) \tag{3.110}$$

are the normalized frequencies associated with the shifts q_ν and q_ρ, respectively, z is an integer belonging to the set $\{0, \pm 1\}$, and

$$c_\nu(q_\nu) \triangleq \frac{1 - \pi q_\nu \cot(\pi q)}{q \cos^2(\pi q)} \tag{3.111}$$

and

$$c_\rho(q_\rho) \triangleq \frac{2\pi}{\sin(2\pi q_\rho)} \tag{3.112}$$

are correction factors. The final estimates of the residuals ($\hat{\delta}_{\nu_k}$ and $\hat{\delta}_{\rho_k}$) are evaluated as $\hat{\delta}_{\nu_k} = \hat{\delta}_{\nu_k}^{(N_{\mathrm{it}})}$ and $\hat{\delta}_{\rho_k} = \hat{\delta}_{\rho_k}^{(N_{\mathrm{it}})}$, respectively.

The use of the QSE in the AE requires the following modifications:

1) The final estimates of the normalized frequencies F_{H_k} and F_{Vk} are evaluated through (3.105), where $X = N$ ($X = M$) if $Q = H$ (if $Q = V$). Moreover, the coarse estimate $\hat{F}_{H_k,c}$ ($\hat{F}_{V_k,c}$) appearing in that formula is evaluated on the basis of (3.72) ((3.73)) with $p = \hat{p}_k^{(\mathrm{AE})}$ (with $l = \hat{l}_k^{(\mathrm{AE})}$); here, $(\hat{l}_k^{(\mathrm{AE})}, \hat{p}_k^{(\mathrm{AE})})$ denotes the couple of spectral indexes provided by the 2D periodogram method for the AE (see Section 3.4.1).

2) The computation of the residuals $\hat{\delta}_{H_k}$ and $\hat{\delta}_{V_k}$ is still based on (3.106) (with $X = H$ or V), but (3.108) and (3.107) are replaced by

$$S_{\pm q_H}^{(i)} \triangleq \sum_{m=0}^{M-1} \sum_{n=0}^{N-1} \hat{H}_{m,n}^{(\mathrm{AE})} \exp\left(j2\pi \left(m\Psi_{0,q_V} + n\Psi_{\pm 1,q_H}\right)\right), \tag{3.113}$$

and

$$S_{\pm q_V}^{(i)} \triangleq \sum_{m=0}^{M-1} \sum_{n=0}^{N-1} \hat{H}_{m,n}^{(\mathrm{AE})} \exp\left(j2\pi \left(m\Psi_{\pm 1,q_V} + n\Psi_{0,q_H}\right)\right), \tag{3.114}$$

respectively; here,

$$\Psi_{z,q_H} \triangleq \left(\hat{p}_k^{(\mathrm{RDE})}\,\bar{F}_H + \frac{\hat{\delta}_{H_k}^{(i-1)} + zq_H}{N}\right) \tag{3.115}$$

and

$$\Psi_{z,q_V} \triangleq \left(\hat{l}_k^{(\mathrm{RDE})}\,\bar{F}_V + \frac{\hat{\delta}_{V_k}^{(i-1)} + zq_V}{M}\right) \tag{3.116}$$

are the normalized frequencies associated with the shifts q_H and q_V, respectively, and z is an integer belonging to the set $\{0, \pm 1\}$. Moreover, the correction factors $c_X(q_X)$ (with $X = H$ or V) are both computed according to (3.112).

A schematic description of the QSE is provided in [71, Sec. IV, Algorithm 2].

3.4.6 Extended Lee algorithm

The last algorithm (namely, the ELA) has been originally proposed in [67, Sec. III] to perform azimuth estimation in a MIMO radar equipped with a Uniform Linear Array (ULA) and is based on an ML approach. However, in this work, the following modifications have been made:

1) The original algorithm, being developed to estimate the frequencies of 1D tones, has been adapted to the 2D signal model expressed by (3.58), thus making its use possible in both the RDE and the AE.

2) An iterative procedure for frequency refinement has been added. In each iteration of this procedure, the grid adopted in the search for the frequency estimate of a given target is adjusted to improve the achieved accuracy.

3) The 2D periodogram method has been employed for the initialization of the ELA; in the original algorithm, instead, the frequency estimates are initialized to zero for all the detected targets.

The ELA is fed by the 2D sequence $\{\hat{H}_{m,n}^{(\mathrm{RDE})}\}$; in its initialization, this sequence is processed by the 2D periodogram method to evaluate the initial estimates $\hat{F}_{\nu_k}^{(0)}$, $\hat{F}_{\rho_k}^{(0)}$ and $\hat{A}_k^{(0)}$ of F_{ν_k}, F_{ρ_k} and A_k, respectively, with $k = 0, 1, ..., \hat{K} - 1$ (being $\hat{K}$ a preliminary estimate of the overall number of targets K), and the iteration index i is set to one. Then, the refinement procedure is started. In its ith iteration (with $i = 1, 2, ..., N_{\mathrm{it}}$, where N_{it} is the overall number of iterations), the new estimates $\hat{F}_{\nu_k}^{(i)}$ and $\hat{F}_{\rho_k}^{(i)}$ of F_{ν_k} and F_{ρ_k}, respectively, are evaluated as

$$\left(\hat{F}_{\nu_k}^{(i)}, \hat{F}_{\rho_k}^{(i)}\right) = \underset{(\tilde{F}_{\nu_k}, \tilde{F}_{\rho_k}) \in \mathcal{I}_{F_\nu}^{(i)}(N_{F_\nu}) \times \mathcal{I}_{F_\rho}^{(i)}(N_{F_\rho})}{\arg\max} \left| J^{(i)}\big(\tilde{F}_{\nu_k}, \tilde{F}_{\rho_k}\big) \right|^2, \tag{3.117}$$

with $k = 0, 1, ..., \hat{K} - 1$; here,

$$J^{(i)}\big(\tilde{F}_{\nu_k}, \tilde{F}_{\rho_k}\big) \triangleq \frac{\mathbf{a}\big(\tilde{F}_{\nu_k}, \tilde{F}_{\rho_k}\big)^H \mathbf{R}^{-1} \bar{\mathbf{H}}}{\mathbf{a}\big(\tilde{F}_{\nu_k}, \tilde{F}_{\rho_k}\big)^H \mathbf{R}^{-1} \mathbf{a}\big(\tilde{F}_{\nu_k}, \tilde{F}_{\rho_k}\big)} \tag{3.118}$$

is the ML cost function evaluated for the trial couple $(\tilde{F}_{\nu_k}, \tilde{F}_{\rho_k})$, $\mathbf{a}(\tilde{F}_{\nu_k}, \tilde{F}_{\rho_k}) \triangleq \mathbf{a}(\tilde{F}_{\nu_k}) \otimes \mathbf{a}(-\tilde{F}_{\rho_k})$,

$$\mathbf{a}_Q(F_X) \triangleq [1, \exp(j2\pi F_X), ..., \exp(j2\pi(Q-1)F_X)]^T \tag{3.119}$$

is a *steering vector*, $\bar{\mathbf{H}} \triangleq [\mathbf{H}_0, \mathbf{H}_1, ..., \mathbf{H}_{M-1}]$ is a (MN)-dimensional row vector, $\mathbf{H}_m \triangleq [\hat{H}^{(\mathrm{RDE})}_{m,0}, \hat{H}^{(\mathrm{RDE})}_{m,1}, ..., \hat{H}^{(\mathrm{RDE})}_{m,N-1}]$ (with $m = 0, 1, ..., M-1$) and $\mathbf{R} = \sigma_H^2 \mathbf{I}_{MN}$ represents the covariance matrix of the Gaussian measurement noise, whose samples have variance σ_H^2 ($\sigma_H^2 = MN$ can be selected as the first attempt guess of the noise variance of $\bar{\mathbf{H}}$; see [67, Sec. III, eq. (21)]). Moreover, the search grid in (3.117) results from the Cartesian product of the sets[16] $\mathcal{I}^{(i)}_{F_\nu}(N_{F_\nu}) \triangleq \{\tilde{F}^{(i)}_\nu[z_\nu];\ z_\nu = 0, 1, ..., N_{F_\nu} - 1\}$ and $\mathcal{I}^{(i)}_{F_\rho}(N_{F_\rho}) \triangleq \{\tilde{F}^{(i)}_\rho[z_\rho];\ z_\rho = 0, 1, ..., N_{F_\rho} - 1\}$.

This grid has the following relevant properties: 1) its center depends on both $\hat{F}^{(i-1)}_{\nu_k}$ and $\hat{F}^{(i-1)}_{\rho_k}$; 2) its step sizes get smaller as i increases. More precisely, its node (z_ν, z_ρ) (with $z_\nu = 0, 1, ..., N_{F_\nu} - 1$ and $z_\rho = 0, 1, ..., N_{F_\rho} - 1$) is associated with the frequencies $(\tilde{F}^{(i)}_\nu[z_\nu], \tilde{F}^{(i)}_\rho[z_\rho])$, where

$$\tilde{F}^{(i)}_X[z_X] = F_{X,\min} + (z_X/(N_{F_X} - 1))(\delta_X/i), \tag{3.120}$$

if $F_{X,\min} \leqslant \hat{F}^{(i-1)}_{X_k} < F_{X,\min} + \delta_X$,

$$\tilde{F}^{(i)}_X[z_X] = \hat{F}^{(i-1)}_{X_k} + ((z_X/(N_{F_X} - 1)) - 1/2)(\delta_X/i), \tag{3.121}$$

if $F_{X,\min} + \delta_X \leqslant \hat{F}^{(i-1)}_{X_k} \leqslant F_{X,\max} - \delta_X$ and

$$\tilde{F}^{(i)}_X[z_X] = F_{X,\max} + ((z_X/(N_{F_X} - 1)) - 1)(\delta_X/i), \tag{3.122}$$

if $F_{X,\max} - \delta_X < \hat{F}^{(i-1)}_{X_k} \leqslant F_{X,\max}$, with $X = \nu$ or ρ. Moreover, $\delta_X = 1/M_0$ ($\delta_X = 1/N_0$) is selected if $X = \nu$ (if $X = \rho$), so that, when $i = 1$, two adjacent bins of the spectrum considered in coarse frequency estimation are covered.

At the end of the last (namely, the N_{it}th) iteration, an estimate of the complex amplitude of the kth target is evaluated as $\hat{A}_k = J^{(N_{\mathrm{it}})}(\hat{F}^{(N_{\mathrm{it}})}_{\nu_k}, \hat{F}^{(N_{\mathrm{it}})}_{\rho_k})$ (see (3.118)).

The ELA can also be employed in the AE; its formulation for the last block can be easily derived from that illustrated above for the RDE by simply replacing $\hat{H}^{(\mathrm{RDE})}_{m,n}$, F_ν and F_ρ with $\hat{H}^{(\mathrm{AE})}_{m,n}$, $-F_V$ and F_H, respectively.

The ELA is summarized in Algorithm 4.

[16] The dependence of $\mathcal{I}^{(i)}_{F_\nu}$, $\mathcal{I}^{(i)}_{F_\rho}$ and $\tilde{F}^{(i)}_X[z]$ on the target index k is not shown in the following three equations to ease notation.

Algorithm 4: Extended Lee algorithm (ELA)

Input: The matrix $\hat{\mathbf{H}}^{(\mathrm{RDE})}$ ($\hat{\mathbf{H}}^{(\mathrm{AE})}$) for the RDE (AE), the overall number of iterations in frequency refinement (N_{it}) and an estimate of the overall number of targets ($\hat{K}$).

Initialization: Evaluate the estimates $(\hat{F}_{\nu_k}^{(0)}, \hat{F}_{\rho_k}^{(0)}, \hat{A}_k^{(0)})$ $((\hat{F}_{H_k}^{(0)}, \hat{F}_{V_k}^{(0)}, \hat{A}_k^{(0)}))$ by finding $\hat{K}$ peaks in the spectrum (3.61) ((3.69)) for the RDE (AE).

Refinement: **for** $k = 0$ *to* $\hat{K} - 1$ **do**

  for $i = 1$ *to* N_{it} **do**

    a- Compute the estimates $(\hat{F}_{\nu_k}^{(i)}, \hat{F}_{\rho_k}^{(i)})$ $((\hat{F}_{V_k}^{(i)}, \hat{F}_{H_k}^{(i)}))$ by means of (3.117).

  end

  b- Evaluate the kth target amplitude as $\hat{A}_k = J^{(N_{\mathrm{it}})}(\hat{F}_{\nu_k}^{(N_{\mathrm{it}})}, \hat{F}_{\rho_k}^{(N_{\mathrm{it}})})$ for the RDE or $\hat{A}_k = J^{(N_{\mathrm{it}})}(\hat{F}_{V_k}^{(N_{\mathrm{it}})}, \hat{F}_{H_k}^{(N_{\mathrm{it}})})$ for the AE (see (3.118)).

end

Output: The estimates $(\hat{F}_{\nu_k}^{(N_{\mathrm{it}})}, \hat{F}_{\rho_k}^{(N_{\mathrm{it}})}, \hat{A}_k^{(i)})$ $((\hat{F}_{H_k}^{(N_{\mathrm{it}})}, \hat{F}_{V_k}^{(N_{\mathrm{it}})}, \hat{A}_k^{(N_{\mathrm{it}})}))$ for the kth target (with $k = 0, 1, ..., \hat{K} - 1$) if the RDE (AE) is considered.

3.5 Computational complexity

In this section, the computational cost of the DRAEC strategy and of the estimation algorithms exploited by it is analyzed in terms of the FLOPs to be executed when K targets are detected and estimated. In general, the complexity of the DRAEC technique is approximately of order $\mathcal{O}(N_{\mathrm{DRAEC}})$, where

$$N_{\mathrm{DRAEC}} = N_{\mathrm{RDE}} + N_{\mathrm{CAE}} + N_{\mathrm{AE}} + N_{\mathrm{CRDE}} + \bar{N}_{\mathrm{RDE}}. \tag{3.123}$$

In the last formula, the terms N_{RDE} and N_{AE} represent the number of FLOPs required by the RDE and the AE, respectively, whereas $\bar{N}_{\mathrm{RDE}}$ refers to the number of FLOPs required by the second instance of the RDE for the refinement of the range-Doppler estimates. Moreover, $N_{\mathrm{CAE}} = 4K\,M\,N\,N_{\mathrm{T}}\,N_{\mathrm{R}}$ and $N_{\mathrm{CRDE}} = 4K\,M\,N\,N_{\mathrm{T}}\,N_{\mathrm{R}}$ represent the costs due to range-Doppler and angular compensation through (3.49) and (3.53), respectively. The expressions of the terms N_{RDE}, N_{AE} and $\bar{N}_{\mathrm{RDE}}$ depend on the choice of the detection & estimation algorithm employed by the RDE and AE; the main results about the computational complexity of the algorithms described in the previous section are summarized below.

2D *periodogram method* - The computational complexity of this method is $\mathcal{O}(\mathcal{C}_{2D-FFT})$, where

$$\mathcal{C}_{2D-FFT} = M_0 N_0 \log_2(M_0 N_0) + K M_0 N_0. \tag{3.124}$$

If spectral interpolation is used, the term

$$\mathcal{C}_{int} = K(I_l I_p + N_l N_p) \tag{3.125}$$

has to be added to $\mathcal{C}_{2D-FFT}$, in (3.124); here, I_l (I_p) is the number of nodes employed along the first (second) dimension, whereas N_l (N_p) is the resulting number of points evaluated by means of interpolation for the first (second) dimension.

CSFDEC *algorithm* - The computational complexity of this method is $\mathcal{O}(N_{\mathrm{CSFDEC}})$, where N_{CSFDEC} is given by (1.65).

Alg-P - Unlike the CSFDEC algorithm, this algorithm does not operate in an iterative fashion, performs *time domain* cancellation and re-computes the spectral residual after each cancellation step in order to get ready for the detection of a new target (if any). For these reasons, its computational complexity is $\mathcal{O}(C_{\mathrm{ALG-P}})$, where

$$C_{\mathrm{ALG-P}} = K(C_{\mathrm{init}} + C_P + C_{\mathrm{canc}}). \tag{3.126}$$

In the last formula, $C_{\mathrm{init}} = M_0 N_0 \log_2(M_0 N_0) + M_0 N_0$ is the contribution due to step 1) of Alg-P (i.e., to the 2D *periodogram maximization*), $C_P = C_{P_M} + C_{P_N}$ (with $C_{P_M} = C_{P_N} = 12MN$) is the cost originating from the computation of the spectral samples for the first and second frequency of the kth target (see (3.88) and (3.89), respectively) and $C_{\mathrm{canc}} = KMN$ is the contribution due to cancellation in the time domain. Note that the initialization cost depends on the number of targets K; this is due to the fact that the residual spectrum for the coarse estimation of a new target is evaluated after each time domain cancellation (see (3.80)).

MFA - The initialization phase of this algorithm relies, similarly as both the CSFDEC algorithm and the Alg-P, on the 2D periodogram method; however, since the MFA does not include a cancellation procedure, the search for K local maxima in the periodogram is required in order to acquire K coarse frequency estimates. Moreover, the initialization is followed by a frequency refinement process, which is sequentially repeated for each target. Therefore, the computational complexity of the MFA is $\mathcal{O}(C_{\mathrm{MFA}})$, where

$$C_{\mathrm{MFA}} = C_{\mathrm{init}} + KC_{\mathrm{ref}}. \tag{3.127}$$

In the last formula, C_{init} is equal to $\mathcal{C}_{2D-FFT}$, in (3.124), (initialization cost) and $C_{\mathrm{ref}} = 16MNN_{F_\nu}N_{F_\rho}$ ($C_{\mathrm{ref}} = 16MNN_{F_V}N_{F_H}$) is the cost of the refinement step, being N_{F_ν} and N_{F_ρ} (N_{F_V} and N_{F_H}) the number of trial values characterizing the grid selected for F_ν and F_ρ (F_V and F_H) if the RDE (AE) is considered.

QSE - Similarly to the MFA and the ELA, this algorithm evaluates first the coarse estimates of K targets through the 2D periodogram method. The frequency refinement step requires evaluating (3.106) N_{it} times for each target. Therefore, the computational complexity of the QSE is $\mathcal{O}(C_{\mathrm{QSE}})$, where

$$C_{\mathrm{QSE}} = C_{\mathrm{init}} + KN_{\mathrm{it}}C_{\mathrm{ref}}. \tag{3.128}$$

In the last formula, C_{init} is the initialization cost (which is equal to that of the same step of the MFA and the ELA), N_{it} represents the overall number of iterations carried out to evaluate (3.106) and $C_{\mathrm{ref}} = 8MN$ is the complexity due to the computation of the DFT coefficients required to solve the last referred equation.

ELA - The initialization of this algorithm is based on the 2D periodogram method and is followed by the frequency refinement step, which requires solving (3.117) N_{it} times for each target. Therefore, the computational complexity of the ELA is $\mathcal{O}(C_{\text{ELA}})$, where

$$C_{\text{ELA}} = C_{\text{init}} + KN_{\text{it}}C_{\text{ref}}. \tag{3.129}$$

In the last formula, C_{init} is equal to $\mathcal{C}_{2D-FFT}$, in (3.124), (being the cost of 2D periodogram method), N_{it} is the number of iterations carried out to refine the estimates of each target and $C_{\text{ref}} = 16(M^2+N^2+MN)N_{F_\nu}N_{F_\rho}$ ($C_{\text{ref}} = 16(M^2+N^2+MN)N_{F_V}N_{F_H}$) represents the cost of each iteration of the refinement step, being N_{F_ν} and N_{F_ρ} (N_{F_V} and N_{F_H}) the sizes of the grid for the refinement of F_ν and F_ρ (F_V and F_H), respectively, if the RDE (AE) is considered.

3.6 Numerical results

In this work, seven different embodiments of the DRAEC strategy are compared in terms of computational effort and estimation accuracy achieved in various scenarios. In each embodiment, the same algorithm for the detection and estimation of 2D complex tones is employed in both the RDE and the AE, and the RDE is executed for the second time after that the AE has estimated the DoA (i.e., both the azimuth and the elevation) of all the detected targets in order to generate a finer estimate[17] of their range and velocity. For this reason, in the following, the acronyms FFT0 (FFTi), CSFDEC, Alg-P, MFA, QSE and ELA are adopted to identify the embodiments employing the 2D periodogram method *without spectral interpolation* (*with spectral interpolation*), the CSFDEC algorithm, the Alg-P, the MFA, the QSE and the ELA, respectively. It is important to point out that embedding these algorithms in the DRAEC allows us to compare state-of-the-art estimators, in terms of accuracy and complexity, in a 4D radar imaging problem and, in particular, to assess their performance in the estimation of specific parameters of multiple targets.

In the following, we also assume that:

1) The considered radar system is equipped with a TX HULA (RX VULA) consisting of $N_{\text{T}} = 8$ ($N_{\text{R}} = 8$) elements, whose spacing, as already mentioned in Section 3.2, is $d_{\text{t}} = \lambda/2$ ($d_{\text{r}} = \lambda/2$); consequently, the structure of its virtual array is described by Fig. 3.2.

2) The OFDM modulation employed by the radar system is characterized by the following parameters: a) overall number of subcarriers $N = 512$; b) overall number of OFDM symbols/frame $M = 64$; c) subcarrier spacing $\Delta_f = 250$ kHz; d) cyclic prefix duration $T_{\text{G}} = 12.5$ µs (consequently, the OFDM symbol duration is $T_{\text{s}} = 1/\Delta_f + T_{\text{G}} = 16.5$ μs); e) carrier frequency $f_{\text{c}} = 79$ GHz (consequently, the carrier wavelength is $\lambda = c/f_{\text{c}} = 3.8$ mm); f) cardinality of the PSK constellation $M_{\text{c}} = 4$.

In our simulations, four different scenarios have been considered. The first three scenarios share the following features:

[17]Note that the performance of the second instance of the RDE is affected by the estimation errors introduced by the AE.

1) They are characterized by a couple of targets (i.e., by $K = 2$), whose echoes have a unitary amplitude (so that $|A_0| = |A_1| = 1$). The range R_0, the velocity v_0, the normalized vertical frequency[18] F_{V_0} and the normalized horizontal frequency F_{H_0} of the first target are mutually independent and uniformly distributed random variables (the interval characterizing the uniform distribution of these variables is denoted $(X_{\min}, X_{\max})$ in the following, with $X = R$, v, F_V or F_H)[19]. The same parameters for the second target (namely, R_1,v_1, F_{V_1} and F_{H_1}), instead, depend on those of the first one, since they are evaluated as

$$X_1 = X_0 + X_{\text{bin}}\, X_{\text{res}}, \tag{3.130}$$

where $X = R$, v, F_V or F_H, and X_{bin} and X_{res} represent the normalized target spacing and the resolution, respectively, of the radar system along the X dimension; moreover, $R_{\text{res}} = c/(2N\Delta_f) = 1.1719$ m, $v_{\text{res}} = \lambda/(2MT_{\text{s}}) = 1.798$ m/s, $F_{V_{\text{res}}} = 1/N_{\text{R}} = 0.125$ and $F_{H_{\text{res}}} = 1/N_{\text{T}} = 0.125$ denote the resolutions in the range, velocity, normalized vertical frequency and normalized horizontal frequency domains, respectively.

2) The SNR[20]

$$\text{SNR} \triangleq \sum_{k=0}^{K-1} |A_k|^2 / \sigma_W^2, \tag{3.131}$$

at the RX side varies from -20 to 20 dB.

However, the first three scenarios differ for the values selected for the parameters $X_{\min}$, $X_{\max}$ and X_{bin}, with $X = R$, v, F_V and F_H. In fact, we have that:

1) In the first scenario (denoted **S1**), $(R_{\min}, R_{\max}) = (0,\ 10)$ m, $(v_{\min}, v_{\max}) = (0,\ 2.78)$ m/s, $(F_{V_{\min}}, F_{V_{\max}}) = (0,\ 0.1754)$, $(F_{H_{\min}}, F_{H_{\max}}) = (-0.1761,\ 0.1761)$, $R_{\text{bin}} = v_{\text{bin}} = 3$ and $F_{V_{\text{bin}}} = F_{H_{\text{bin}}} = 2$.

2) In the second scenario (denoted **S2**), the intervals $(F_{V_{\min}}, F_{V_{\max}})$ and $(F_{H_{\min}}, F_{H_{\max}})$ are the same as **S1**, but $(R_{\min}, R_{\max}) = (10,\ 20)$ m, $(v_{\min}, v_{\max}) = (2.78,\ 5.56)$ m/s, $R_{\text{bin}} = v_{\text{bin}} = 0$ and $F_{V_{\text{bin}}} = F_{H_{\text{bin}}} = 2.2$.

3) In the third scenario (denoted **S3**), the intervals $(R_{\min}, R_{\max})$ and $(v_{\min}, v_{\max})$ are the same as **S2**, but $(F_{V_{\min}}, F_{V_{\max}}) = (0,\ 0.3566)$, $(F_{H_{\min}}, F_{H_{\max}}) = (-0.3623,\ 0.3623)$, $R_{\text{bin}} = v_{\text{bin}} = 3$ and $F_{V_{\text{bin}}} = F_{H_{\text{bin}}} = 0$.

The fourth scenario (denoted **S4**), instead, has the following characteristics:

1) Its overall number of targets is varying (in particular, $K \in \{1, 2, ..., 5\}$).

2) The range R_0, the velocity v_0, the normalized vertical frequency F_{V_0} and the normalized horizontal frequency F_{H_0} of the first target are mutually independent and uniformly distributed random variables; the intervals $(R_{\min}, R_{\max})$, $(v_{\min}, v_{\max})$ and $(F_{V_{\min}}, F_{V_{\max}})$ selected for R_0, v_0 and F_{V_0}, respectively, are the same as **S2**, whereas the interval $(F_{H_{\min}}, F_{H_{\max}}) = (-0.7765,\ -0.5534)$ is chosen for F_{H_0}.

[18] Note that, given the normalized spatial frequencies F_V and F_H characterizing a given target, target elevation θ and azimuth ϕ can be easily computed on the basis of (3.33) and (3.34), respectively.

[19] In all the scenarios, target parameters have been generated by means of the function *rand* available in MatlabR2022b.

[20] Note that σ_W^2 represents the variance of the noise sample $\bar{W}_{m,n}^{(p_a,q)}$ appearing in the RHS of (3.40).

3) The amplitude of the kth target (with $k = 0, 1, ..., K-1$) is unitary.

4) The range R_k, velocity v_k, normalized vertical frequency F_{V_k} and normalized horizontal frequency F_{H_k} of the kth target (with $k = 1, 2, ..., K-1$) are evaluated as $X_k = X_0 + k\, X_{\rm bin}\, X_{\rm res}$, with $X = R$, v, F_V or F_H (the parameters $X_{\rm bin}$ and $X_{\rm res}$ have been already defined; see (3.130)); here, $R_{\rm bin} = v_{\rm bin} = 1.8$ and $F_{V_{\rm bin}} = F_{H_{\rm bin}} = 0.7$.

5) The SNR is fixed and set to 10 dB.

The selection of the four scenarios defined above can be motivated as follows. On the one hand, the first scenario allows us to compare the considered embodiments of the DRAEC strategy in the presence of two targets whose spacing in the range, velocity and angular domains is *fixed*, *but not small*. On the other hand, in the second (third) scenario, we still focus on the case of two targets, but assume that they are overlapped in range and velocity (azimuth and elevation) domains, whereas they are well spaced in the azimuth and elevation (range and velocity) domains. The fourth scenario, instead, allows us to assess the impact of a variable number of targets on the estimation accuracy; note that such targets are quite close in the azimuth and elevation domains, but are fairly spaced in the range and velocity domains.

In the considered simulations[21], the following choices have also been made:

1) The overall number of targets (i.e., K) has always been assumed to be known. This entails that none of the 2D estimators employed in the DRAEC strategy requires setting a specific threshold. Note, however, that the target configuration is unknown at the RX side; for instance, the radar receiver is unaware of the existence of targets characterized by the same parameters in some domain (e.g., by the same DoA).

2) In the first three scenarios, the estimation accuracy achieved by each embodiment of the DRAEC strategy has been assessed by evaluating the RMSE

$$\mathrm{RMSE}_X \triangleq \frac{1}{N_{\rm r}} \sum_{t=0}^{N_{\rm r}-1} \sqrt{\frac{1}{K} \sum_{k=0}^{K-1} (\hat{X}_k[t] - X_k)^2} \tag{3.132}$$

for the range ($X = R$), velocity ($X = v$), azimuth ($X = \theta$) and elevation angle ($X = \phi$) of the considered targets; here, $\hat{X}_k[t]$ denotes the estimate of the parameter X_k evaluated for the kth target in the tth Monte Carlo run and $N_{\rm r}$ is the overall number of Monte Carlo runs. Moreover, in applying the last formula, the parameters of the K targets and the estimates generated for them have been ordered on the basis of their range (in particular, according to an ascending order, i.e., from minimum to maximum range).

3) In the fourth scenario, instead, the estimation accuracy achieved by each embodiment of the DRAEC strategy has been assessed by evaluating the *normalized* RMSE

$$\mathrm{NRMSE}_X \triangleq \frac{\mathrm{RMSE}_X}{\mathrm{CRLB}_X}, \tag{3.133}$$

[21] All the simulations have been performed on Matlab R2022b, running on a personal computer equipped with an i7 processor.

with $X = R$, v, F_V and F_H; here, CRLB_X denotes the CRLB for the estimation of X (the evaluation of the CRLB for the considered scenarios is illustrated in Appendix A.2.1). Note that the adoption of NRMSE_X, in (3.133), as a performance index allows us to fairly compare the estimation accuracy of each algorithm achieved in the presence of a variable number of targets and its computation is done for each SNR value.

4) The detection thresholds adopted in the inequalities (3.47) and (3.52) have not been selected, being K known. In practice, the RDE, in its first instance, searches for $K^{(\mathrm{RDE})} = K$ targets (i.e., K range-Doppler bins). Then, the AE identifies $K^{(\mathrm{AE})} \geq K$ targets, orders them according to decreasing perceptual importance, and discards the last $(K^{(\mathrm{AE})} - K)$ of them.

5) In all the considered scenarios, the oversampling factors $L_1^{(\mathrm{RDE})} = L_2^{(\mathrm{RDE})} = 4$ ($L_1^{(\mathrm{AE})} = L_2^{(\mathrm{AE})} = 8$) have been adopted for the RDE (for the AE), independently of the employed frequency estimation algorithm; consequently, according to (3.62), (3.63), (3.70), (3.71), we have that $M_0 = 512$ ($\bar{M}_0 = 64$) and $N_0 = 2048$ ($\bar{N}_0 = 64$).

In addition, in all the considered scenarios, the following choices have been made for the parameters of the 2D complex tone estimators:

2D *periodogram method with interpolation* - Orders $I_l = I_p = 7$ have been adopted for the spectral interpolation accomplished in both the RDE and the AE, and a grid of size $N_l \times N_p = 251 \times 251$ is selected in the serial refinement of the target estimates.

CSFDEC *algorithm* - Number of iterations carried out in the evaluation of the residuals $N_{\mathrm{it}}^{(\mathrm{RDE})} = 30$ ($N_{\mathrm{it}}^{(\mathrm{AE})} = 35$), number of re-estimations $N_{\mathrm{REF}}^{(\mathrm{RDE})} = 3$ ($N_{\mathrm{REF}}^{(\mathrm{AE})} = 3$) and interpolation orders along the two dimensions of the spectral components $I_M^{(\mathrm{RDE})} = I_N^{(\mathrm{RDE})} = 7$ ($I_M^{(\mathrm{AE})} = I_N^{(\mathrm{AE})} = 7$) for the RDE (for the AE).

MFA - Number of trial values employed in (3.97) (in (3.102)) $N_{F_\nu} = N_{F_\rho} = 51$ ($N_{F_V} = N_{F_H} = 51$) for the RDE (for the AE).

QSE - Number of iterations for frequency refinement $N_{\mathrm{it}}^{(\mathrm{RDE})} = 20$ ($N_{\mathrm{it}}^{(\mathrm{AE})} = 20$) and q-shifts $q_\nu = q_\rho = 0.031$ ($q_V = q_H = 0.25$) for the RDE (for the AE).

ELA - Number of iterations accomplished to refine target estimates $N_{\mathrm{it}}^{(\mathrm{RDE})} = 7$ ($N_{\mathrm{it}}^{(\mathrm{AE})} = 7$) and number of trial values employed in (3.118) $N_{F_\nu} = N_{F_\rho} = 15$ ($N_{F_V} = N_{F_H} = 15$) for the RDE (for the AE).

Some numerical results referring to **S1** are shown in Fig. 3.4, where the performance index RMSE_X (with $X = R$, v, θ or ϕ) characterizing all the considered algorithms is shown for SNR $\in [-20, 20]$ dB (in these figures and in all the following ones, simulation results are represented by labels, whereas continuous and dotted lines are drawn to ease reading). From these results, it is easily inferred that:

1) The FFT0 is outperformed by all the other methods; note also that the floor observed in the RMSE performance of this embodiment is due to the discretization of the grid (see (3.76) employed in the RDE and in the AE (see (3.61) and (3.69), respectively).

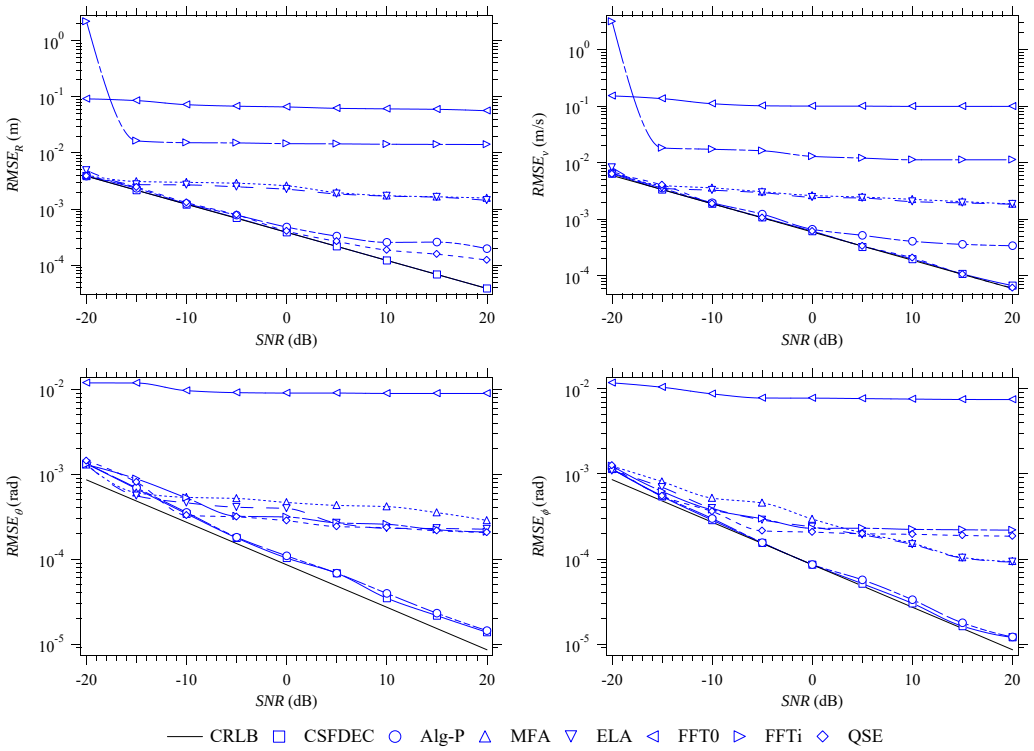

FIGURE 3.4: Root mean square error performance achieved by the considered embodiments of the DRAEC strategy. The first scenario is considered.

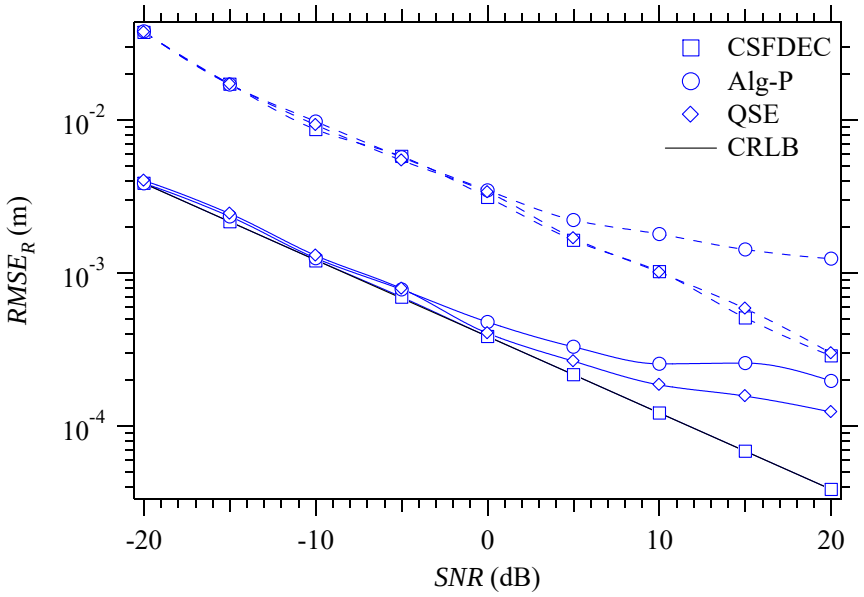

FIGURE 3.5: Root mean square error performance achieved in range estimation by the first and the second instance of the RDE. The first scenario and three different embodiments of the DRAEC strategy are considered.

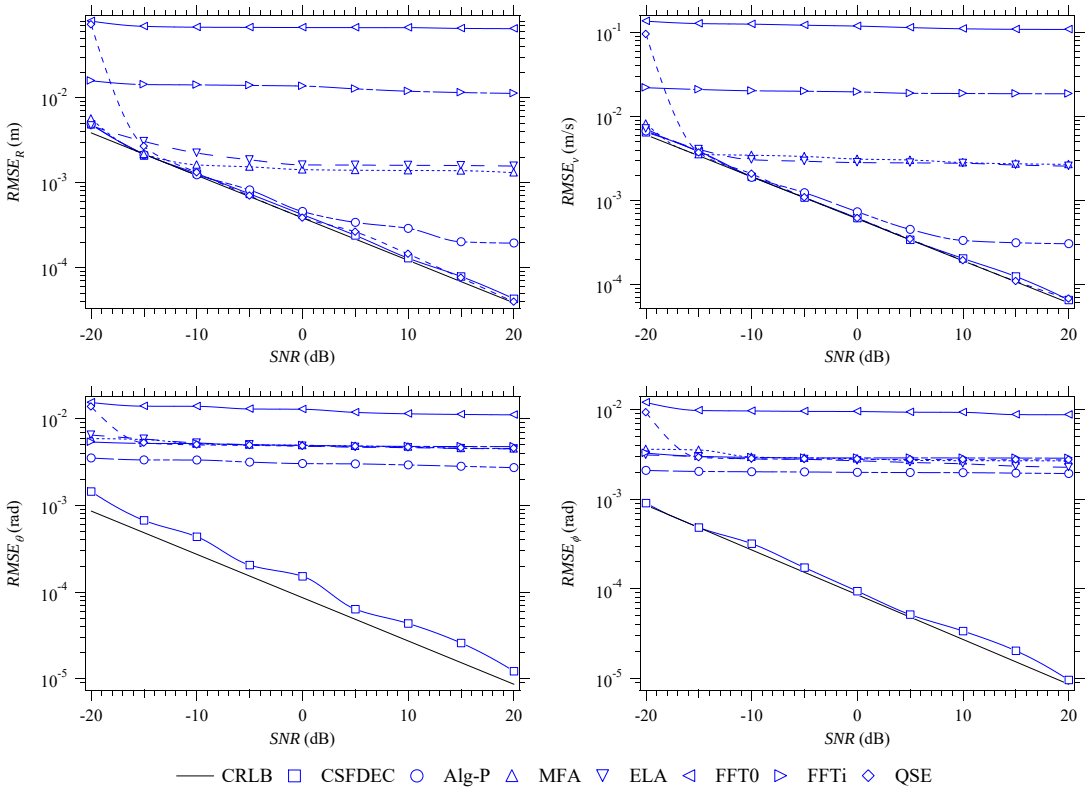

FIGURE 3.6: Root mean square error performance achieved by the considered embodiments of the DRAEC strategy. The second scenario is considered.

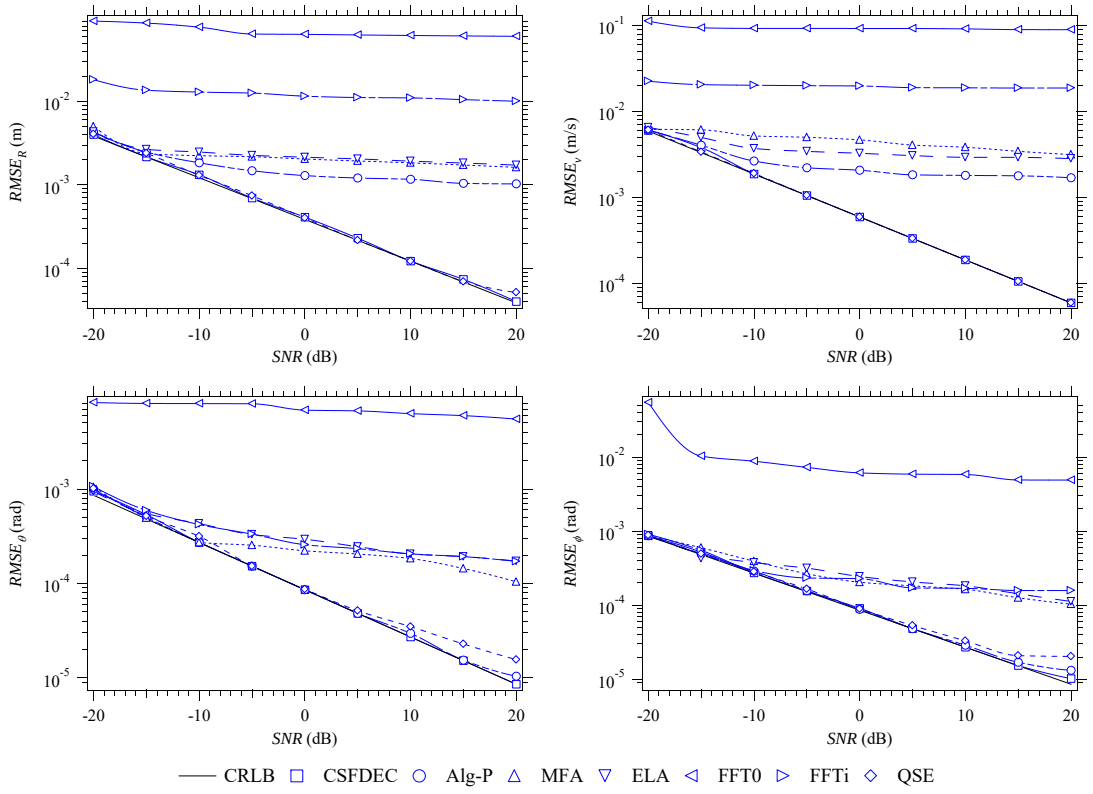

FIGURE 3.7: Root mean square error performance achieved by the considered embodiments of the DRAEC strategy. The third scenario is considered.

2) The CSFDEC and the Alg-P achieve very good accuracy (close to the CRLB) thanks to their use of cancellation and refinement procedures.

3) The QSE performs similarly to the Alg-P (FFTi) in range (angle) estimation and similarly to the CSFDEC in velocity estimation.

4) The FFTi takes advantage of peak interpolation, achieving an estimation accuracy similar to that of the MFA and of the ELA in angular estimation. These considerations, together with those illustrated at point 3), also apply to **S2** and **S3**.

5) The RMSE curves for the FFTi, the MFA and the ELA exhibit a floor at high SNRs. This is due to the fact that the accuracy of the FFTi estimator and the MFA is intrinsically limited by the discretization of their search grid. Further simulation results have evidenced that enlarging the set of trial values improves estimation accuracy; however, this result is achieved at the price of higher computational complexity. As far as the ELA is concerned, its accuracy can also be improved by increasing its number of iterations, but this results in a significant increase in the required computational effort. These considerations apply to all the results shown below for the three algorithms that have been just mentioned.

6) The $\mathrm{RMSE_R}$ and $\mathrm{RMSE_v}$ curves of the Alg-P exhibit a floor at high SNRs. This phenomenon can be related to the fact that the employed estimation algorithm is biased, since it does not include either an iterative refinement process or a leakage compensation procedure for each detected target.

7) The computational efforts required by the FFTi, the CSFDEC, the Alg-P, the MFA, the QSE and the ELA are 1.01, 6.6, 1.1, 10, 1.2 and 49 times higher than that required by the FFT0; these results also hold for **S2** and **S3**.

Further results for **S1** are shown in Fig. 3.5, in which the $\mathrm{RMSE_R}$ curves of the CSFDEC, the Alg-P and the QSE are shown for the cases in which the RDE is executed only once (dashed lines) and twice (solid lines). From this figure, it is easily inferred that:

1) The improvement in range estimation provided by the second instance of the RDE in order is significant for all the proposed techniques; similar results, not shown here, have been found for velocity estimation.

2) The price to be paid for this improvement is an increase in the overall computational effort (this is quantified by the term $\bar{N}_{\mathrm{RDE}}$ appearing in (3.123)).

Note also that running a single instance of the RDE corresponds to what is done in all the related technical manuscripts in which only a subset of the target parameters (range and Doppler, in this case) is estimated, whereas the other parameters are kept fixed and/or are not successively compensated for (e.g., see [23] where the angular parameters are not estimated). For this reason, these results evidence the importance of estimating all the target parameters jointly.

Some numerical results referring to **S2** are shown Fig. 3.6, where the performance index RMSE_X (with $X = R$, v, θ or ϕ), characterizing all the considered algorithms, is shown for $\mathrm{SNR} \in [-20, 20]$ dB. These results lead to the following conclusions:

1) The FFTi, the MFA, and the ELA achieve similar accuracy in the estimation of angular parameters and exhibit similar trends (and, in particular, a floor); however, the FFTi is outperformed by the MFA and the ELA in range and Doppler estimation.

2) The RMSE_θ and RMSE_ϕ referring to the Alg-P and the QSE are quite flat. This is due to the fact that the two targets are located in the same range-Doppler bin. This affects the quality of the signal generated by the AE in compensating for the range and Doppler of each target (see (3.49)) and passed to the RDE. Moreover, the performance of the QSE is appreciably influenced by the selection of the shifting parameters (i.e., q_V and q_H for the AE). The values of these parameters have been optimized according to [71, Sec. III, eqs. (40) and (45)].

3) The CSFDEC performs substantially better than all the other embodiments in the estimation of azimuth and elevation, and similarly as the QSE in range and velocity estimation (the accuracy of both embodiments is very close to the CRLB).

Some numerical results obtained for **S3** are illustrated in Fig. 3.7, showing again the dependence of the RMSEs on the SNR, with $\text{SNR} \in [-20, 20]$ dB. These results lead to the following conclusions:

1) The CSFDEC and the QSE achieve the best estimation accuracy (very close to the CRLB) for all the considered parameters, whereas the Alg-P performs similarly in angle estimation only.

2) The accuracy provided by the MFA in azimuth and elevation estimation is slightly better than that characterizing the ELA and the FFTi.

3) The accuracy achieved by the MFA in range and velocity estimation is similar to that provided by the Alg-P and the ELA; moreover, the trend of their RMSE_R and RMSE_v curves remains flat even at high SNR values.

The last results refer to **S4** and are shown in Fig. 3.8 and in Fig. 3.9. In particular, in Fig. 3.8 the NRMSE characterizing all the considered embodiments at a given SNR and in the presence of a variable number of targets is shown. These results lead to the following conclusions:

1) The NRMSE_X increases with the overall number of targets (i.e., the RMSE_X departs from the associated CRLB), with $X = R$, v, F_V or F_H. This is due to the fact that increasing K results in a stronger spectral *leakage* and, consequently, in poorer estimation accuracy of each algorithm.

2) The CSFDEC, the Alg-P and the QSE perform similarly in range and velocity estimation, whereas the CSFDEC performs better in the estimation of azimuth and elevation. This confirms once again that the CSFDEC algorithm better exploits the limited information available in the angular domain[22] and takes advantage of its *leakage compensation* mechanism.

3) The QSE represents the best option in the case of a single target. However, if the overall number of targets increases, it is outperformed by the CSFDEC and the Alg-P; this is due

[22]The estimation of angular parameters is based on the $N_\text{T} \times N_\text{R}$ matrix $\check{\mathbf{H}}_k$; see Section 3.3.2.

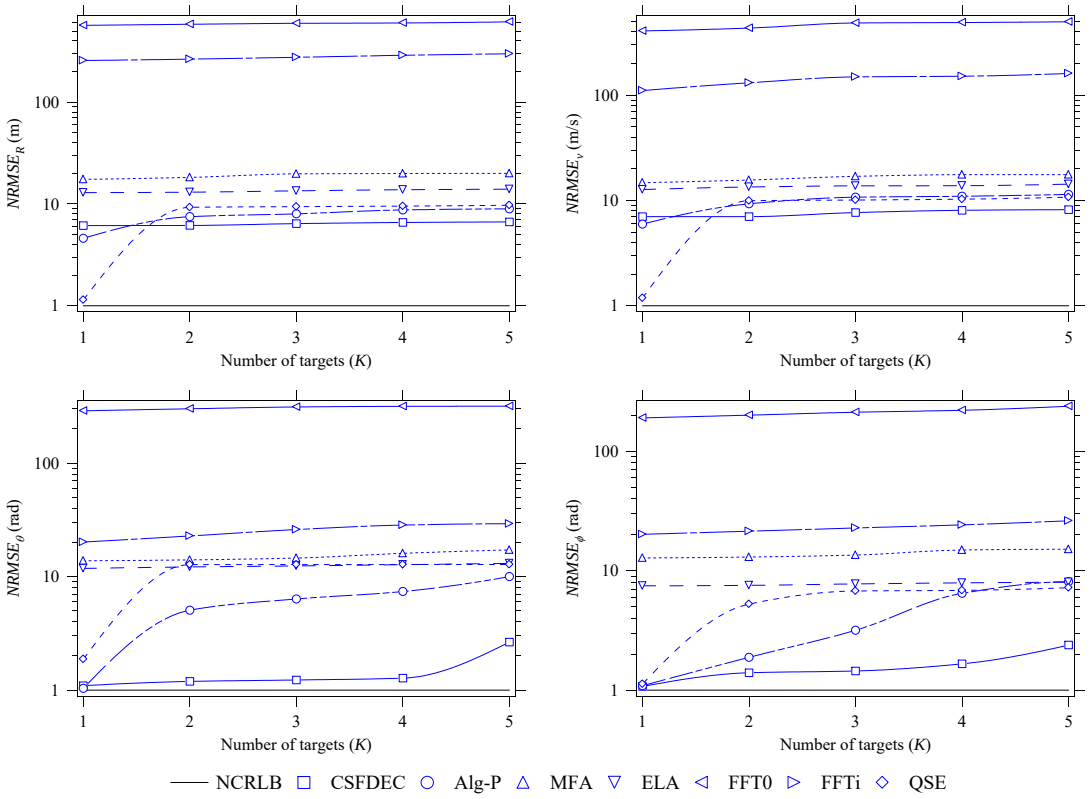

FIGURE 3.8: Root mean square error performance achieved by the considered embodiments of the DRAEC strategy. The fourth scenario is considered.

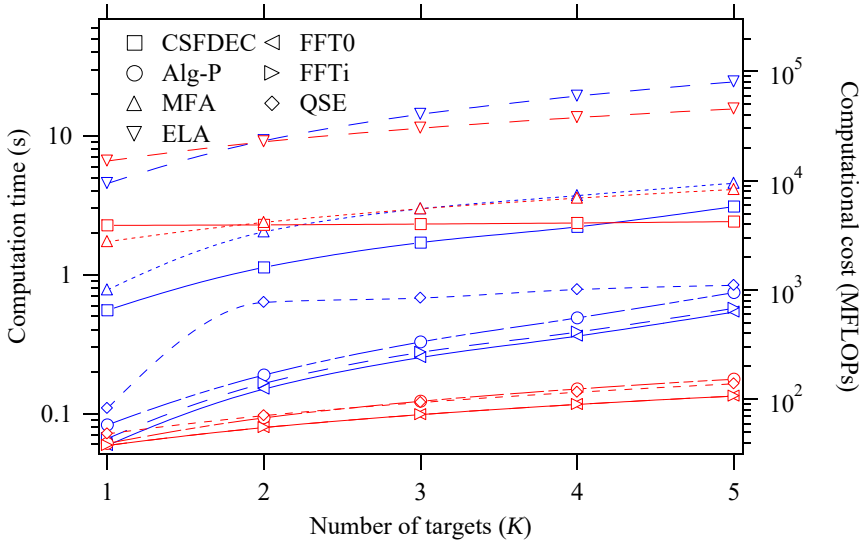

FIGURE 3.9: *Computation time* (blue lines) and *computational cost* (red lines) characterizing the analyzed embodiments in the presence of a variable number of targets. The fourth scenario is considered.

to the fact that the CSFDEC algorithm and the Alg-P make use of a serial cancellation procedure.

4) The ELA performs better than the MFA in the considered scenario.

5) The FFT0 and the FFTi are less accurate than all the other techniques.

In Fig. 3.9, instead, the computational complexity of all the embodiments is represented for a variable number of targets; both the *computational cost*, measured in *mega* FLOPs (MFLOPs), and the CT[23] are taken into consideration. From this figure, it is easily inferred that:

1) The trend of most of the CT curves is similar and in agreement with that characterizing the corresponding curves of the computational cost; the only exception is represented by the CSFDEC, for which the trend of the computational cost appears to be flatter than that of the CT.

2) The slopes of all the curves (i.e., the relative increase in complexity as K gets larger) are similar.

3) The CT of the Alg-P is very close to that required by the FFT0 and the FFTi; moreover, the last two methods require similar CTs.

4) Even if the complexity of the QSE is similar to that of the Alg-P, the CT of the former embodiment tends to be larger than that of the latter; this is mainly due to the fact that their estimators have different initializations. In fact, in the case of the QSE (the Alg-P), the search for K local maxima (for a single maximum) is required.

The results shown in this section evidence that the CSFDEC represents the winning option among the set of considered embodiments, since it achieves the best performance-complexity trade-off.

3.7 Conclusions

In this chapter, a novel general strategy to develop sub-optimal methods for the detection of multiple targets and the estimation of their parameters in a MIMO OFDM-based JCAS system has been proposed. This strategy is based on the idea of splitting a complicated multidimensional optimization problem into a couple of simpler (but interacting) sub-problems. Seven different embodiments of it have been described, their complexity has been assessed and their estimation accuracy has been compared in four different scenarios. The numerical results, based on synthetically generated data referring to four distinct scenarios, evidence that all the proposed embodiments perform reasonably well, but may require substantially different computational efforts. Moreover, the estimation accuracy of the majority of the algorithms exhibits a floor as the SNR increases. This phenomenon

[23]These metrics allow us to compare the impact of different 2D estimators available in the technical literature on the overall computational effort required by the DRAEC, since this mainly depends on the complexity of the specific algorithm adopted in its two core blocks.

is due to the lack of an iterative procedure for refining the coarse estimates of the detected targets or to the use of a sub-optimal refinement procedure or to the adoption of a (discretized) search grid.

We believe that this work sheds new light on a complicated technical problem, which plays a key role in the development of future JCAS systems; in fact, it provides an in-depth analysis of the accuracy-complexity trade-off characterizing different solutions to it. In a number of applications, achieving good estimation accuracy represents a fundamental requirement; at the same time, real-time operation is also needed, so that substantial attention must be paid to the computational effort required by the adopted estimation algorithms. All in all, we believe the detection and estimation algorithms based on the strategy we propose can represent good candidates for the processing to be accomplished in OFDM-based 4D radars. The next chapter introduces multicarrier modulation formats to be employed for JCAS applications within the context of high-mobility communications, with a particular focus on OTFS, a format designed to be resilient against doubly-selective fading communication channels.

4

Multicarrier modulations in high mobility scenarios

This chapter discusses focuses on the challenges of wireless communication systems when rapid channel variations and Doppler effects are present. Orthogonal Frequency Division Multiplexing (OFDM) has been widely adopted due to its robustness against multipath fading and its efficient implementation using Fast Fourier Transform (FFT). However, its performance degrades in high-mobility environments due to its sensitivity to Doppler shifts. To address these challenges, Orthogonal Time Frequency Space (OTFS) has emerged as a promising alternative. OTFS transforms the time-frequency domain into the delay-Doppler domain, providing resilience against channel variations and improving performance in high-mobility scenarios. In particular, in this chapter, we investigate the implications of adopting a double cyclic prefix in the acOTFS modulation. The study in this chapter first focuses on the analysis of the modulated signal and on the development of a useful model for the received signal in the presence of a doubly selective fading channel. On the one hand, the obtained mathematical results allow us to accurately assess the impact of pulse shaping on the structure of the transmitted waveform and on its power spectral density. On the other hand, the resulting models pave the way for developing some simple rules for allocating pilot symbols within each OTFS symbol and develop novel strategies for channel estimation and equalization.

4.1 Introduction

In the near future, 6G wireless networks are expected to provide high-quality wireless connectivity as well as highly accurate and robust sensing capability. One of the key challenges in 6G network research is represented by the development of new communication waveforms that are able to support communication and sensing functionalities in high-mobility environments at very high frequencies. In the last two decades, a multicarrier modulation format, known OFDM, has played a fundamental role in new standards for local area and mobile wireless networks. Recently, substantial efforts have been devoted to investigating its use for Integrated Sensing and Communication (ISAC) in future wireless networks [75, 76]. Unluckily, one of the main weaknesses of OFDM-based digital communications is represented by the severe ICI experienced at the RX side in the presence of a doubly selective fading channel characterized by strong Doppler [77]. From this perspective, a more appealing alternative[1] is represented by a 2D modulation technique called OTFS [79]. In fact, it has been shown that, since in that case data are modulated in the DD domain rather than in the conventional TF domain, the communication channel has

[1]Another alternative to OFDM, in the ISAC context, is represented by Affine Frequency Division Multiplexing (AFDM) (see [78]) for further details).

approximately the same impact on all the channel symbols of the same OTFS symbol and its full diversity can be potentially extracted through proper equalization methods [80].

It is important to mention that *Hadani et al.*, in their seminal manuscript [79], presented the OTFS modulation as a 2D generalization of the OFDM format, but did not focus on the problem of adopting, in a similar way as OFDM, a proper CP to impart a quasi-periodic structure to the transmitted signal; this issue has been also ignored in their later manuscript [80]. Note that the presence of a CP plays a fundamental role in OFDM communications over a *frequency selective* (i.e., time dispersive) communication channel, as it allows to represent the effect of the communication channel on the transmitted signal as a cyclic convolution in the TD, thereby drastically simplifying channel equalization at the RX side; moreover, it eliminates the interference between consecutive OFDM symbols [81, Sec. 3.7]. Note, however, these advantages are obtained at the price of a reduction of energy efficiency. Since the OTFS modulation generalizes OFDM by expanding the last format along the frequency dimension, in the light of the TF *duality principle* developed by *Bello* in [82], the use of an additional CP in that dimension in the presence of a *frequency dispersive* (i.e., time dispersive) communication channel appears to be a natural choice. This unavoidably increases the bandwidth of the modulated signal and, consequently, reduces its spectral efficiency. However, based, once again, on the duality principle, we should expect that the presence of the second prefix will allow us to represent the effect of frequency dispersion (i.e., Doppler) on the transmitted signal as a cyclic convolution in the FD and, consequently, will simplify the processing to be accomplished at the RX to compensate for the resulting distortions.

As far as we know, the use of a CP in the OTFS modulation has been taken into consideration for the first time in [83, 84] and, later, in [85]. In all these manuscripts, however, the CP is adopted *along the time dimension only*. When this occurs, interference between OTFS symbols (i.e., ISI) is avoided if the CP is long enough [86]; otherwise, this phenomenon has to be taken into account in the received signal model [87, 88]). Another significant contribution related to the CP issue can be found in [85], where a derivation of the OTFS modulation based on the Zak transform [89] is provided. The use of this transform makes an entire OTFS frame appear periodic to the communication channel along the Doppler direction and "quasi-periodic" along the delay direction. The work illustrated in [85] effectively encompasses the concept of imparting 2D periodicity to the modulated signal. However, in our opinion, it does not fully unveil the implications of the use of a CP along the frequency dimension.

In this chapter, we focus on the use of a Double Cyclic Prefix (DCP) in the OTFS modulation and on its implications on pulse shaping and pilot-aided channel estimation. More specifically, the following contributions are provided:

1) The dual of the OFDM modulation, called Dual Orthogonal Frequency Division Multiplexing (DOFDM), is derived by applying the duality concept to OFDM. Moreover, its use in a digital communication system operating over a *time selective* communication channel is illustrated. This allows us to show that the adoption of a FD CP in DOFDM drastically simplifies channel equalization at the RX side.

2) It is shown that the OTFS modulation can be developed by jointly exploiting a few essential principles on which OFDM and DOFDM are based. This leads to extending

OTFS symbols by incorporating a CP in the TD and one in the FD in a natural fashion; the resulting modulation format is called OTFS with DCP (OTFS-DCP, briefly) in the following.

3) The impact of the TX pulse on the overall structure of OTFS-DCP signals is assessed in a rigorous way. The conducted analysis is based on representing the complex envelope of the modulated signal and its spectrum through their Fourier series; the adoption of this mathematical tool is made possible by the cyclic structure of the modulated signal along the time and the frequency dimensions. Note that, in the technical literature, a rectangular TX pulse is usually selected because of its simplicity and the simplifications it offers in signal modeling (e.g., see [83, 84, 88, 90–92]). We show, instead, that the choice of a pulse having a Root of a Raised Cosine (RRC) spectrum represents a better choice. In addition, differently from [93, 94], which primarily focus on the influence of pulse shaping on the architecture of OTFS receivers, in this chapter a specific pulse shape imparting a simple multicarrier structure to the modulated signal is proposed; this, in turn, simplifies the processing to be executed at the RX side for channel estimation and equalization.

4) The Power Spectral Density (PSD) of the OTFS-DCP format is derived and analyzed.

The remaining part of this chapter is organized as follows. Section 4.2 is devoted to briefly describing OFDM and its dual modulation scheme, and to showing how the OTFS-DCP format is related to them. In the analysis of the OTFS modulation format, we take into consideration not only the baseband model of the transmitted signal, but also show how channel equalization and detection of channel symbols should be accomplished at the RX side. Moreover, the impact of pulse shaping on the inner structure of the OTFS-DCP format and its PSD are investigated. Finally, some conclusions are offered in Section 4.3.

4.2 Signal and System Models

In this section, we illustrate: 1) the derivation of three distinct digital modulations; 2) the signal models at the RX side of a communication system employing each of these modulations and operating in the presence of different types of fading channels. First, we briefly describe how an OFDM signal is generated and derive the corresponding RX signal model in the presence of a *frequency selective* fading channel. Then, following the same line of reasoning and, based on the duality concept, we introduce the dual of the OFDM format (briefly, *dual* OFDM, DOFDM) and develop the corresponding RX signal model in the presence of a *time selective* fading channel. Finally, we show how the signal model of the OTFS-DCP modulation can be derived from most of the previously obtained results in a natural fashion; moreover, we develop the received signal model for a communication system employing that modulation format and operating over a *doubly selective* fading channel.

4.2.1 Signal Models in an OFDM-Based Communication System

In this subsection, the derivation of various signal models is sketched for a communication system employing the OFDM modulation. In the following mathematical developments

we focus on the transmission of the N-dimensional vector $\mathbf{c}_N \triangleq [c_0, c_1, ..., c_{N-1}]^T$, representing the message and collecting N *channel symbols*, each of which belongs to an M_{c}ary constellation; this vector represents a single OFDM *symbol*. To begin, we assume that $\mathbf{c}_N$ undergoes the one-to-one transformation $\mathbf{g} : \mathbb{C}^N \to \mathbb{C}^N$; this yields the N-dimensional vector

$$\mathbf{x}_N \triangleq [x_0, x_1, ..., x_{N-1}]^T = \mathbf{g}\left(\mathbf{c}_N\right) \tag{4.1}$$

conveying the same information as $\mathbf{c}_N$. The last vector is employed to generate the periodic sequence $\{x_k\}$ by repeating it with period N, so that

$$x_k = x_{R_N[k]}, \tag{4.2}$$

for any $k \notin \{0, 1, ..., N-1\}$. This sequence feeds a pulse amplitude modulator, that produces the baseband periodic signal

$$s\big(t; \mathbf{c}_N\big) = \sum_{k=-\infty}^{+\infty} x_k \, p(t - kT_{\mathrm{s}}), \tag{4.3}$$

where $p(t)$ is the *modulator impulse response* and T_{s} is the *symbol interval*. Since the period of $s(t; \mathbf{c}_N)$ in (4.3) is $T = NT_{\mathrm{s}}$, this signal can be represented through its Fourier series as

$$s(t; \mathbf{c}_N) = \sum_{m=-\infty}^{+\infty} S_m^{(\mathrm{TD})}\left(\mathbf{c}_N\right) \exp\left(j2\pi f_m t\right), \tag{4.4}$$

where $f_m \triangleq m/T = m/(NT_{\mathrm{s}})$ is the mth harmonic frequency and

$$S_m^{(\mathrm{TD})}\left(\mathbf{c}_N\right) \triangleq \frac{1}{T} \int_0^T s\left(t; \mathbf{c}_N\right) \exp\left(-j2\pi f_m t\right) dt \tag{4.5}$$

is the mth Fourier coefficient. Substituting the RHS of (4.3) in that of (4.5) yields, after some manipulation,

$$S_m^{(\mathrm{TD})}\left(\mathbf{c}_N\right) = \frac{1}{\sqrt{N} T_{\mathrm{s}}} P_m \, X_m, \tag{4.6}$$

for any m; here, $P_m \triangleq P(f_m) = P(m/(NT_{\mathrm{s}}))$,

$$P(f) = \mathrm{FCT}\left[p(t)\right] \triangleq \int_{-\infty}^{+\infty} p(t) \exp(-j2\pi f t) dt \tag{4.7}$$

is the Fourier Continuous Transform (FCT) of $p(t)$ and

$$X_m \triangleq \frac{1}{\sqrt{N}} \sum_{l=0}^{N-1} x_l \exp\Big(-j2\pi \frac{l}{N} m\Big) \tag{4.8}$$

is the mth coefficient of the order N DFT of the vector $\mathbf{x}_N$, in (4.1). Note that the last equation can be rewritten in vector form as

$$\mathbf{X}_N \triangleq [X_0, X_1, ..., X_{N-1}]^T \triangleq \mathrm{DFT}_N[\mathbf{x}_N] \triangleq \mathbf{\Xi}_N \, \mathbf{x}_N, \tag{4.9}$$

where $\mathbf{\Xi}_N$ is the order N DFT matrix. Then, if the transformation $\mathbf{g}(\cdot)$ in (4.1) is an order N IDFT, i.e., if

$$\mathbf{x}_N = \mathrm{IDFT}_N[\mathbf{c}_N] \triangleq \mathbf{\Xi}_N^H \mathbf{c}_N, \tag{4.10}$$

we have that (see (4.9))

$$\mathbf{X}_N = \mathbf{\Xi}_N \mathbf{\Xi}_N^H \mathbf{c}_N = \mathbf{c}_N. \tag{4.11}$$

Similarly as $\mathbf{x}_N$, $\mathbf{X}_N$ can be cyclically extended to generate the periodic sequence $\{X_k\}$, having period equal to N; from (4.11) it is easily inferred that

$$X_k = c_{R_N[k]} \tag{4.12}$$

for any $k \notin \{0, 1, ..., N-1\}$. Substituting the RHS of (4.12) in that of (4.6) and, then, the resulting expression in the RHS of (4.4) yields

$$s\big(t; \mathbf{c}_N\big) = \frac{1}{\sqrt{N} T_\mathrm{s}} \sum_{m=-\infty}^{+\infty} P_m \, c_{R_N[m]} \exp\left(j 2\pi f_m t\right). \tag{4.13}$$

The last expression can be reformulated by replacing the (single) index m with the couple (n, k), such that $m = n + kN$, with $n = 0, 1, ..., N-1$ and k arbitrary integer. This produces

$$s\left(t; \mathbf{c}_N\right) = \frac{1}{\sqrt{N} T_\mathrm{s}} \sum_{n=0}^{N-1} c_n \, g_n(t), \tag{4.14}$$

where

$$g_n(t) \triangleq \sum_{k=-\infty}^{+\infty} P_{n+kN} \exp\left(j 2\pi f_{n+kN} \, t\right). \tag{4.15}$$

The RHS of (4.14) is required to represent a multicarrier signal, i.e., to consist of the superposition of N complex exponentials, characterized by distinct frequencies, having the same amplitude and conveying different channel symbols. This result is achieved if only a single term and, in particular, the one associated with $k = 0$, survives in the sum appearing in the RHS of (4.15), i.e., if $P_{n+kN} = 0$ for any $k \neq 0$; this means that $p(t)$ should be bandlimited and its spectrum $P(f)$ should ensure that the spectral samples $\{P_n; n = 0, 1, ..., N-1\}$ are identical. In [81, Subsec. 3.7] it is shown that a good option for $p(t)$ is represented by a pulse whose spectrum $P(f)$ is the RRC[2] with *roll-off* factor α (e.g., see [81, Subsect. 3.5.4, eq. (3.90)])

$$P(f) = \begin{cases} \sqrt{T_\mathrm{s}} & |f| < f_{1-\alpha} \\ \sqrt{T_\mathrm{s}} \cos\big(\pi \frac{|2fT_\mathrm{s}| - 1 + \alpha}{4\alpha}\big) & f_{1-\alpha} \leq |f| \leq f_{1+\alpha} \\ 0 & |f| > f_{1+\alpha} \end{cases}, \tag{4.16}$$

where $f_{1\pm\alpha} \triangleq (1 \pm \alpha)/(2T_\mathrm{s})$, with $0 \leq \alpha \leq 1$. However, in this case, the contribution of some of the functions $\{g_n(t)\}$ appearing in the RHS of (4.14) needs to be *suppressed*, since they consist of the superposition of a *couple*[3] of complex exponentials, whose frequencies are spaced apart by $1/T_\mathrm{s}$ Hz (see [81, Sebsect. 3.7.2, eq. (3.257)]). The suppression of

[2]This spectrum is characterized by a flat top; the identical spectral samples $\{P_n\}$ originate from it.

[3]If subcarrier suppression was not used, this would result in the presence of a form of *self-interference*.

such functions is obtained by setting $N_{sc} \triangleq N - 2N_\alpha - 1$ consecutive elements of $\mathbf{c}_N$ (and, in particular, the elements whose index runs from N_α to $N - N_\alpha - 1$) to zero; here,

$$N_\alpha \triangleq \left\lfloor \frac{N(1-\alpha)}{2} \right\rfloor . \tag{4.17}$$

Then, (4.14) turns into

$$s\left(t; \mathbf{c}_N\right) = \frac{1}{\sqrt{NT_s}} \sum_{n=-N_\alpha}^{N_\alpha} c_{R_N[n]} \exp\left(j2\pi f_n t\right). \tag{4.18}$$

Note that: 1) in the last equation, $c_{R_N[n]} = c_n$ for $n = 0, 1, ..., N_\alpha$ and $c_{R_N[n]} = c_{N+n}$ for $n = -N_\alpha, -N_\alpha + 1, ..., -1$; 2) the number of *useful subcarriers* is equal to $N_u = 2N_\alpha + 1$ and increases as the roll-off factor gets closer to zero at the price of a longer $p(t)$; 3) the number of Suppressed Carriers (SCs) is equal to $N - N_u$; 4) the subcarrier spacing is equal to $1/(NT_s)$; 5) the pulse $p(t)$ characterized by the spectrum $P(f)$ (4.16) needs to be truncated to L_p symbol intervals (where L_p is an integer parameter) in order to ensure that the transmission of each OFDM symbol is accomplished over a finite time interval; 6) since the truncation interval adopted for $p(t)$ is required to capture most of the energy of this pulse, its duration should increase as α gets smaller.

Let us assume now that the signal $s(t; \mathbf{c}_N)$ (4.18) is sent over a time-invariant frequency selective wireless channel having impulse response

$$h(\tau) \triangleq \sum_{l=0}^{L-1} h_l \delta(\tau - \tau_l), \tag{4.19}$$

where h_l and τ_l represent the complex gain and the delay, respectively, of the lth path, with $l = 0, 1, ..., L-1$, and L is the overall number of multi-path components. The useful component of the baseband signal available at the output of the RX filter can be written as

$$r\big(t; \mathbf{c}_N\big) \triangleq s\big(t; \mathbf{c}_N\big) * h(t) * g(t), \tag{4.20}$$

where $g(t)$ represents the impulse response of the RX filter, which is assumed to be *matched*[4] to $p(t)$ (i.e., $g(t) = p^*(-t)$), so that $G(f) \triangleq \mathrm{FCT}[g(t)] = P^*(f)$. Then, under this assumption, substituting the RHS of (4.18) in that of (4.20) produces

$$r\left(t; \mathbf{c}_N\right) = \frac{1}{\sqrt{N}} \sum_{n=-N_\alpha}^{N_\alpha} c_{R_N[n]}\, H_{R_N[n]} \exp\left(j2\pi f_n t\right), \tag{4.21}$$

where $H_n \triangleq H(f_n)$ and $H(f) \triangleq \mathrm{FCT}[h(t)]$. Note that, if (4.19) holds, we have that

$$H(f) = \sum_{l=0}^{L-1} h_l \exp(-j2\pi f \tau_l), \tag{4.22}$$

Comparing (4.21) with (4.18) leads to the conclusion that:

[4]The adoption of this filter follows from the model (4.3), that represents the complex envelope of an OFDM signal at the output signal of baseband pulse amplitude modulator.

1) $r(t;\mathbf{c}_N)$ retains the same structure as the signal feeding the channel input;

2) the effect of the communication channel on the nth subcarrier of the transmitted signal is represented by the complex coefficient $H_{R_N[n]}$. Moreover, given $r(t;\mathbf{c}_N)$ in (4.21), the extraction of the transmitted message can be accomplished by: a) uniformly sampling this signal N times in the interval $[0, NT_\mathrm{s}]$; b) evaluating an order N DFT on the resulting sample vector; c) compensating for the channel distortion on a subcarrier-by-subcarrier basis (i.e., *equalizing* the received signal in the FD); d) accomplishing symbol detection the basis of the equalized samples (once again, on a subcarrier-by-subcarrier basis). In practice, sampling $r(t;\mathbf{c}_N)$ in (4.21) at the instant $t_{\tilde{n}} \triangleq \tilde{n}T_\mathrm{s}$ yields

$$r_{\tilde{n}} \triangleq r\left(t_{\tilde{n}};\mathbf{c}_N\right) = \frac{1}{\sqrt{N}} \sum_{n=-N_\alpha}^{N_\alpha} c_{R_N[n]}\, H_{R_N[n]} \exp\Big(j2\pi \frac{\tilde{n}}{N} n\Big), \tag{4.23}$$

with $\tilde{n} = 0, 1, ..., N-1$. The last equation can be easily written in vector form as

$$\mathbf{r}_N \triangleq [r_0, r_1, ..., r_{N-1}]^T = \mathbf{\Xi}_N^H(\mathbf{c}_N \odot \mathbf{H}), \tag{4.24}$$

where $\mathbf{H} \triangleq [H_0, H_1, ..., H_{N-1}]^T$. Performing an order N DFT of the N-dimensional vector $\mathbf{r}_N$ produces the N-dimensional vector

$$\mathbf{R}_N = \mathbf{\Xi}_N \mathbf{\Xi}_N^H(\mathbf{c}_N \odot \mathbf{H}) = \mathbf{c}_N \odot \mathbf{H}, \tag{4.25}$$

whose nth element is

$$R_n = \frac{1}{N} c_n\, H_n \tag{4.26}$$

for $0 \leq n \leq N_\alpha$ and $N - N_\alpha \leq n \leq N-1$ (the remaining N_{sc} elements of $\mathbf{R}_N$ are irrelevant since, being associated with the SCs, are discarded). Note that the simplicity and the elegance of the model (4.26) follows from the *orthogonality* of the complex exponentials appearing in the RHS of (4.23). Moreover, from (4.26) it is easily inferred that c_n can be detected on the basis of R_n after compensating for the complex channel gain H_n. This elegant result has been obtained under the assumption that the complex envelope of the transmitted signal is expressed by (4.3), since this allows, under certain assumptions, to put it in the multicarrier form expressed by (4.18); this, in turn, leads easily to (4.21). Unluckily, all these signals have an infinite duration, so that, seemingly, an unlimited time interval is required for the transmission of a symbol vector of limited size. In practice, if the temporal supports of $p(t)$ and $h(t)$ are limited and, in particular, are the intervals $[0, L_pT_\mathrm{s}]$ and $[0, L_hT_\mathrm{s}]$ (where L_p and L_h are integer parameters), respectively, and if the integer parameter $N_{cp}^{(\mathrm{TD})}$, representing the size of the CP, is not smaller than[5] $(2L_p + L_h)$, it can be shown that (4.23) still holds in the interval $(0, NT_\mathrm{s})$ provided that (4.3) is replaced by its time limited counterpart

$$s\left(t;\mathbf{c}_N\right) = \sum_{k=-N_{cp}^{(\mathrm{TD})}}^{N-1} x_k\, p(t - kT_\mathrm{s}). \tag{4.27}$$

[5]Note that the duration of $p(t)$ plays an important role in determining the value of $N_{cp}^{(\mathrm{TD})}$.

Finally, it is useful to note that the interval devoted to the transmission of the CP can be also considered as a *guard interval* for avoiding the interference between consecutive OFDM symbols, i.e., the so-called Inter-Block Interference (IBI). Moreover, if the duration of the CP exceeds its minimum value, the performance of the considered communication system is not affected by a limited sampling offset. In fact, such an offset, that results in a phase rotation of all channel symbols, is compensated for through FD equalization.

4.2.2 Signal Models in a DOFDM-Based Communication System

In this subsection, we focus on the derivation of various signal models for a communication system employing the DOFDM modulation; the considered approach parallels that provided for OFDM in the previous subsection and relies on the use of the duality principle. This means, for instance, that each DFT is replaced by an IDFT (and vice-versa) and that TD signal models are replaced by the corresponding FD counterparts (and vice-versa).

In the following, we take into consideration the transmission of a digital message represented by the M-dimensional vector $\mathbf{c}_M \triangleq [c_0, c_1, ..., c_{M-1}]^T$; we assume that each of its elements are *channel symbols* belonging to an $M_c$ary constellation and that M is even. The vector $\mathbf{c}_M$ undergoes an order M DFT (see (4.9)) at the TX side. This produces the M-dimensional vector

$$\mathbf{y}_M = \mathrm{DFT}_M[\mathbf{c}_M] = \mathbf{\Xi}_M \mathbf{c}_M, \tag{4.28}$$

which is periodically extended to generate the sequence $\{y_k\}$ having period M. In other words, the kth element of this sequence is expressed by

$$y_k = y_{R_M[k]} \tag{4.29}$$

for any $k \notin \{0, 1, ..., M-1\}$. This sequence is conveyed by the complex signal $s_D(t; \mathbf{c}_M)$, characterized by the *periodic spectrum*

$$S_D(f; \mathbf{c}_M) = \sum_{k=-\infty}^{+\infty} y_k P(f - k\Delta_f), \tag{4.30}$$

that represents the dual of $s(t; \mathbf{c}_N)$ (4.3); here, $P(f)$ is the FCT of the pulse $p(t)$ employed in the generation of the modulated signal (further details about the properties of this pulse are provided below). Since the period of $S_D(f; \mathbf{c}_M)$ in (4.30) is equal to $B \triangleq M\Delta_f$, this spectrum can be represented through its Fourier series as

$$S_D(f; \mathbf{c}_M) = \sum_{q=-\infty}^{+\infty} s_q^{(\mathrm{FD})}(\mathbf{c}_M) \exp(-j2\pi f t_q), \tag{4.31}$$

where $t_q \triangleq q/B = q/(M\Delta_f)$ and

$$s_q^{(\mathrm{FD})}(\mathbf{c}_M) \triangleq \frac{1}{B} \int_{-M\Delta_f/2}^{M\Delta_f/2} S_D(f; \mathbf{c}_M) \exp(j2\pi f t_q)\, df \tag{4.32}$$

is the qth Fourier coefficient of $S_D(f;\mathbf{c}_M)$. Substituting the RHS of (4.30) in that of (4.32) and exploiting the periodicity of the sequence $\{y_k\}$ produces, after some manipulation,

$$s_q^{(\mathrm{FD})}(\mathbf{c}_M) = \frac{1}{\sqrt{M}\Delta_f} p_q \, c_{R_M[q]}, \tag{4.33}$$

where

$$p_q \triangleq p(t_q) = p\left(\frac{q}{B}\right) = p\left(\frac{q}{M\Delta_f}\right). \tag{4.34}$$

Then, substituting the RHS of (4.33) in that of (4.31) yields

$$S_D(f;\mathbf{c}_M) = \frac{1}{\sqrt{M}\Delta_f} \sum_{q=-\infty}^{+\infty} p_q \, c_{R_M[q]} \exp\left(-j2\pi f t_q\right). \tag{4.35}$$

The last equation can be further simplified following the same approach as that illustrated for (4.13); for this reason, the index q is replaced by the couple (m,k) such that $q = m + kM$, with $m = 0, 1, ..., M-1$ and k arbitrary integer. This allows us to rewrite (4.35) as

$$S_D(f;\mathbf{c}_M) = \frac{1}{\sqrt{M}\Delta_f} \sum_{m=0}^{M-1} c_m G_m(f), \tag{4.36}$$

where

$$G_m(f) \triangleq \sum_{k=-\infty}^{+\infty} p_{m+kM} \exp\left(-j2\pi t_{m+kM} f\right). \tag{4.37}$$

Based on similar considerations as those illustrated for (4.14) and (4.15), we require $G_m(f)$ to consist of a single complex exponential; this means that, for any m, only a single term should survive in the sum appearing in the RHS of (4.37). From (4.37) it is easily inferred that this result is achieved if $p(t)$ is *time-limited* and, in particular, if its duration does not exceed $1/\Delta_f$. Note that, when this occurs, $S_D(f;\mathbf{c}_M)$ consists of the superposition of M complex exponentials that are *orthogonal* in the frequency range $\mathcal{I}_f \triangleq (-B/2, B/2)$ (i.e., over a single period of this spectrum). In the following, we assume that:

1) The support of $p(t)$ is contained in the interval $[-1/(2\Delta_f), 1/(2\Delta_f)]$ and $p_q = \sqrt{\Delta_f}$ for $q = -N_\beta, -N_\beta+1, ..., -1, 0, 1, ..., N_\beta$, where N_β is a positive integer depending on the pulse shape and such that $N_\mathrm{u} = (2N_\beta + 1) < M$.

2) $N_{sc} \triangleq M - N_\mathrm{u}$ consecutive elements of $\mathbf{c}_M$ (and, in particular, the elements whose index runs from N_β to $M - N_\beta - 1$) are set to zero. Under these assumptions (4.36) becomes

$$S_D(f;\mathbf{c}_M) = \frac{1}{\sqrt{M\Delta_f}} \sum_{m=-N_\beta}^{N_\beta} c_{R_M[m]} \exp\left(-j2\pi f t_m\right), \tag{4.38}$$

so that it takes the form described above. This representation of $S_D(f;\mathbf{c}_M)$ holds in a single period (say, in the interval $\mathcal{I}_f$) if $p(t)$ is bandlimited (with bandwidth B_p). In this case, the sum appearing in the RHS of (4.30) can be properly truncated to limit the

number of its terms; this leads to the new spectrum[6]

$$Y_D\left(f;\mathbf{c}_M\right) = \sum_{k=-(M/2+N_{cp}^{(\mathrm{FD})})}^{M/2-1+N_{cpo}^{(\mathrm{FD})}} y_k P\Big(f-k\Delta_f\Big), \tag{4.39}$$

where the integer parameters $N_{cp}^{(\mathrm{FD})}$ and $N_{cpo}^{(\mathrm{FD})}$ denote the size of the CP and that of the Cyclic Postfix (CPO), respectively. Similarly as OFDM, the use of a CP and a CPO is needed to guarantee that, over the considered frequency range, the observed spectrum looks periodic, i.e., that it has a *quasi-periodic structure* (details about the selection of $N_{cp}^{(\mathrm{FD})}$ and $N_{cpo}^{(\mathrm{FD})}$ are provided below). Given the spectrum in (4.39), the complex envelope $y_D(t;\mathbf{c}_M)$ of the transmitted signal is expressed by its Inverse Fourier Continuous Transform (IFCT), that is

$$y_D\big(t;\mathbf{c}_M\big) \triangleq \mathrm{IFCT}\Big[Y_D\big(f;\mathbf{c}_M\big)\Big] = p(t) \sum_{k=-(M/2+N_{cp}^{(\mathrm{FD})})}^{M/2-1+N_{cpo}^{(\mathrm{FD})}} y_k \exp\big(j2\pi k\Delta_f t\big). \tag{4.40}$$

This means that the complex envelope of the DOFDM modulation is the superposition of multiple complex exponentials windowed by $p(t)$. Note that this signal model is structurally similar to the model (4.18) developed for OFDM, but is characterized by a subcarrier spacing equal to Δ_f. However, in the case of DOFDM, the set of channel symbols $\{c_{R_N[n]}\}$ is replaced by the set of their DFT coefficients (namely, by the set $\{y_k\}$), and the presence of both a CP and a CPO is required; moreover, the role of $p(t)$, acting as a TD window, is also clear.

Let us consider now the transmission of $y_D(t;\mathbf{c}_M)$ in (4.40) on the dual of a frequency selective channel, i.e., on a *time selective channel*. This channel introduces the TD multiplicative distortion (see [81, eq. (2.134)])

$$a(t) \triangleq \sum_{l=0}^{L-1} a_l \exp\left(j2\pi\nu_l t\right); \tag{4.41}$$

here, a_l and ν_l represent the lth complex gain and the corresponding Doppler shift (with $l=0,1,...,L-1$), respectively, and L is the overall number of Doppler shifts characterizing the communication channel. Let also

$$B_D \triangleq 2\max_l |\nu_l| \tag{4.42}$$

denote the *Doppler bandwidth* of the communication channel. The spectrum of the channel response $z_D(t;\mathbf{c}_M)$ to $y_D(t;\mathbf{c}_M)$ in (4.40) can be evaluated as

$$Z_D\big(f;\mathbf{c}_M\big) = Y_D\big(f;\mathbf{c}_M\big) * A(f) = \sum_{k=-(M/2+N_{cp}^{(\mathrm{FD})})}^{M/2-1+N_{cpo}^{(\mathrm{FD})}} y_k P_{\mathrm{a}}(f-k\Delta_f), \tag{4.43}$$

[6]Note that a larger value of B_{p} results in a longer prefix and in a longer postfix; i.e., requires increasing the values of $N_{cp}^{(\mathrm{FD})}$ and $N_{cpo}^{(\mathrm{FD})}$.

where $A(f)$ denotes the FCT of $a(t)$ (4.41) and

$$P_{\rm a}(f) = P(f) * A(f) \tag{4.44}$$

represents the FCT of the pulse $p(t)$ distorted by the communication channel, i.e., of the signal[7]

$$p_{\rm a}(t) \triangleq \text{IFCT}[P_{\rm a}(f)] = p(t)\, a(t). \tag{4.45}$$

Note that, if (4.41) holds, we have that

$$P_{\rm a}(f) = \sum_{l=0}^{L-1} a_l P(f - \nu_l). \tag{4.46}$$

At the RX side, matched filtering is executed in the FD; this means that the signal $Z_D(f; \mathbf{c}_M)$, in (4.43), is applied to a filter matched to $P(f)$, i.e., to a filter whose impulse response is $P^*(-f)$. The filter output is the spectrum

$$R_D\big(f; \mathbf{c}_M\big) = Z_D\big(f; \mathbf{c}_M\big) * P^*(-f). \tag{4.47}$$

The spectrum $Z_D(f; \mathbf{c}_M)$, in (4.43), looks periodic over the interval $\mathcal{I}_f$ and, consequently, can be represented as (see (4.38))

$$Z_D\big(f; \mathbf{c}_M\big) = \frac{1}{\sqrt{M\Delta_f}} \sum_{m=-N_\beta}^{N_\beta} c_{R_M[m]}\, a_{R_M[m]} \exp\big(-j2\pi f t_m\big) \tag{4.48}$$

in that interval; here,

$$a_m \triangleq a(t_m) = a\big(m/B\big) = a\big(m/(M\Delta_f)\big) \tag{4.49}$$

for any m. Then, substituting the RHS of (4.48) in that of (4.47) yields

$$R_D\big(f; \mathbf{c}_M\big) = \frac{1}{\sqrt{M\Delta_f}} \sum_{m=-N_\beta}^{N_\beta} c_{R_M[m]}\, a_{R_M[m]} \exp\big(-j2\pi f t_m\big) p^*(t_m) \tag{4.50}$$

Sampling $R_D(f; \mathbf{c}_M)$ at the frequency $\bar{f}_k = k\Delta_f$, with $k = -M/2, -M/2{+}1, ..., -1, 0, 1, ..., M/2{-}1$, gives

$$R_{D,k} \triangleq R_D\big(\bar{f}_k; \mathbf{c}_M\big) = \frac{1}{\sqrt{M}} \sum_{m=-N_\beta}^{N_\beta} c_{R_M[m]} a_{R_M[m]} \exp\big(-j2\pi k \frac{m}{M}\big). \tag{4.51}$$

The last equation can be easily written in vector form as

$$\mathbf{R}_{D,M} \triangleq [R_{D,0}, R_{D,1}, ..., R_{D,M-1}]^T = \mathbf{\Xi}_M(\mathbf{c}_M \odot \mathbf{a}), \tag{4.52}$$

[7]Note that the bandwidth of $p_{\rm a}(t)$ is equal to $B_{\rm p} + B_D$. Therefore, it is larger than that of $p(t)$ because of the spectral broadening due to the Doppler phenomenon.

where $\mathbf{a} \triangleq [a_0, a_1, ..., a_{M-1}]^T$. Performing an order M IDFT of the vector $\mathbf{R}_{D,M}$ produces the M-dimensional vector

$$\mathbf{r}_{D,M} = \mathbf{\Xi}_M^H \mathbf{\Xi}_M (\mathbf{c}_M \odot \mathbf{a}) = \mathbf{c}_M \odot \mathbf{a}, \tag{4.53}$$

whose mth element is given by

$$r_{D,m} = \frac{1}{M} c_m a_m, \tag{4.54}$$

for $0 \leq n \leq N_\beta$ and $M - N_\beta \leq n \leq M - 1$ (the remaining N_{sc} elements of $\mathbf{r}_{D,M}$ are irrelevant since, being associated with the zeroed elements of $\mathbf{c}_M$, they are discarded). The last result represents the TD counterpart of the FD formula (4.26). For this reason, symbol detection can be carried out in a similar way after equalizing the communication channel; this task, in turn, requires estimating the complex samples $\{a_m\}$, i.e., multiple samples of the multiplicative distortion introduced by the communication channel.

Finally, it is important to point out that:

1) A TD pulse having a RRC shape could be adopted for $p(t)$. The value of N_β for this pulse depends on the value of the RRC roll-off (similarly to OFDM, a smaller roll-off results in a wider flat top of the pulse and, consequently, in a larger N_β).

2) The value of both the CP $N_{cp}^{(\mathrm{FD})}$ and the CPO $N_{cpo}^{(\mathrm{FD})}$ should not be smaller than $\lceil (2B_\mathrm{p} + B_D)/(2\Delta_f) \rceil$ in order to ensure the property of *spectral cyclicity* in the frequency range of interest (namely, $\mathcal{I}_f \triangleq (-B/2, B/2)$).

3) The TD counterpart of (4.47) is

$$r_D\big(t; \mathbf{c}_M\big) = z_D\big(t; \mathbf{c}_M\big) p^*(t), \tag{4.55}$$

where $r_D(t; \mathbf{c}_M)$ and $z_D(t; \mathbf{c}_M)$ represent the IFCT of $R_D(f; \mathbf{c}_M)$ and $Z_D(f; \mathbf{c}_M)$, respectively. This means that, in practice, the received signal $r_D(t; \mathbf{c}_M)$ undergoes windowing (represented by a multiplication by $p^*(t)$) and, then, spectral analysis for the evaluation of the samples $\{R_D(\bar{f}_k; \mathbf{c}_M)\}$. The last task can be executed by sampling $r_D(t; \mathbf{c}_M)$ at a proper rate and accomplishing a DFT on the resulting sample sequence.

4.2.3 Signal Models in an OTFS-Based Communication System

In this subsection, we first show how the mathematical results illustrated in the previous two subsections can be exploited to: 1) develop various models for the complex envelope of an OTFS signal incorporating a DCP; 2) derive the corresponding received signal model in the presence of both an *ideal* communication channel (i.e., a channel not introducing any distortion and noise) and a doubly selective fading channel. Then, we analyze the implications of adopting a specific pulse shape in the OTFS signal model. The following approach is inspired by the basic principles illustrated for OFDM and its dual, and aims at developing a digital modulation format whose detection and equalization can be implemented at a reasonable complexity in the presence of a doubly selective communication channel. As shown below, the property of double cyclicity of the modulated signal plays a fundamental role in the next derivations.

4.2.3.1 Transmitted signal model

In the following, we take into consideration the transmission of the $M \times N$ matrix[8] $\mathbf{C} \triangleq [c_{m,n}]$ (with $m = 0, 1, ..., M-1$ and $n = 0, 1, ..., N-1$), collecting MN channel symbols, each of which belongs to an $M_c$ary constellation; this matrix represents a single OTFS *symbol*. Let us assume that the matrix $\mathbf{C}$ undergoes a one-to-one transformation $\mathbf{g} : \mathbb{C}^{M\times N} \rightarrow \mathbb{C}^{M\times N}$, generating the new symbol matrix

$$\mathbf{X} \triangleq [x_{m,n}] = \mathbf{g}(\mathbf{C}), \tag{4.56}$$

having the same size as $\mathbf{C}$. The matrix $\mathbf{X}$ is *periodically extended along both its dimensions* to generate the 2D periodic sequence

$$x_{k,l} = x_{R_M[k],R_N[l]}, \tag{4.57}$$

for any value of the couple (k, l) not belonging to the set of indices of the elements of $\mathbf{X}$ (4.56). The matrix $\mathbf{X}$ is transmitted by generating a modulated signal that exhibits the property of *cyclicity in both the TD and the FD*. As shown in Section 4.2.1 and Section 4.2.2, cyclicity in the TD over an interval lasting NT_s s and in the FD over the frequency range $(-M\Delta_f/2, M\Delta_f/2)$ can be guaranteed by generating the complex envelope (see (4.27))

$$s(t; \mathbf{C}) \triangleq \sum_{l=-N_{cp}^{(\mathrm{TD})}}^{N-1} s_l^{(\mathrm{FD})}\Big(t - lT_\mathrm{s}; \mathbf{C}\Big), \tag{4.58}$$

with (see (4.40))

$$s_l^{(\mathrm{FD})}\big(t; \mathbf{C}\big) \triangleq p(t) \sum_{k=-(M/2+N_{cp}^{(\mathrm{FD})})}^{M/2-1+N_{cpo}^{(\mathrm{FD})}} x_{k,l} \exp\big(j2\pi k\Delta_f t\big); \tag{4.59}$$

here, $p(t)$ is a bandlimited pulse (whose temporal support is the interval $[0, L_pT_\mathrm{s}]$, L_p being an integer parameter), T_s is the symbol interval, Δ_f is a frequency spacing, and the integer parameters $N_{cp}^{(\mathrm{TD})}$, $N_{cp}^{(\mathrm{FD})}$ and $N_{cpo}^{(\mathrm{FD})}$ have the same meaning and scope as that illustrated for the corresponding parameters which have been defined in the description of OFDM and DOFDM, respectively. Note that the DCP insertion entails the transmission of

$$N_{cp} \triangleq N_{cp}^{(\mathrm{TD})} M + (N + N_{cp}^{(\mathrm{TD})})(N_{cp}^{(\mathrm{FD})} + N_{cpo}^{(\mathrm{FD})}) \tag{4.60}$$

additional channel symbols, so that

$$\Lambda_{cp} \triangleq \frac{N_{cp}}{MN + N_{cp}} \tag{4.61}$$

[8]The values of the parameters M and N are assumed to be even in the following.

represents the fraction of channel symbols assigned to the TD prefix and to the FD prefix & postfix. Substituting the RHS of (4.59) in that of (4.58) yields the signal model

$$s(t;\mathbf{C}) = \sum_{l=-N_{cp}^{(\mathrm{TD})}}^{N-1} \sum_{k=-(M/2+N_{cp}^{(\mathrm{FD})})}^{M/2-1+N_{cpo}^{(\mathrm{FD})}} x_{k,l} p\big(t - lT_{\mathrm{s}}\big) \exp\big(j2\pi k\Delta_f\big(t - lT_{\mathrm{s}}\big)\big), \tag{4.62}$$

that has the same structure as [79, Sec. II-A, eq. (5)], but, unlike that, includes a *double cyclic extension*. Note also that (4.62) can be easily rewritten as

$$s(t;\mathbf{C}) = \sum_{k=-(M/2+N_{cp}^{(\mathrm{FD})})}^{M/2-1+N_{cpo}^{(\mathrm{FD})}} s_k^{(\mathrm{TD})}(t;\mathbf{C}), \tag{4.63}$$

where

$$s_k^{(\mathrm{TD})}(t;\mathbf{C}) \triangleq \sum_{l=-N_{cp}^{(\mathrm{TD})}}^{N-1} x_{k,l}\, p(t - lT_{\mathrm{s}}) \exp\big(j2\pi k\Delta_f(t - lT_{\mathrm{s}})\big), \tag{4.64}$$

and that the last signal can be interpreted as a *frequency shifted version of an* OFDM *signal* (characterized by the frequency shift $k\Delta_f$; see (4.27)); consequently, $s(t;\mathbf{C})$ (4.63) can be seen as the superposition of multiple (namely, $M + N_{cp}^{(\mathrm{FD})} + N_{cpo}^{(\mathrm{FD})}$) OFDM signals, characterized by distinct central frequencies. Let us select now[9]

$$\Delta_f = 1/T_{\mathrm{s}}, \tag{4.65}$$

so that $s_k^{(\mathrm{TD})}(t;\mathbf{C})$ (4.64) looks periodic in the interval $[0, T]$, thanks to presence of its TD CP, and its period is

$$T = NT_{\mathrm{s}}. \tag{4.66}$$

Therefore, in that interval, it can be represented through its Fourier Series (FS) (see (4.4) and (4.5))

$$s_k^{(\mathrm{TD})}(t;\mathbf{C}) = \sum_{q=-\infty}^{+\infty} S_{k,q}^{(\mathrm{TD})}(\mathbf{C}) \exp\Big(j2\pi q\frac{t}{T}\Big), \tag{4.67}$$

where

$$S_{k,q}^{(\mathrm{TD})}(\mathbf{C}) \triangleq \frac{1}{T}\int_0^T s_k^{(\mathrm{TD})}(t;\mathbf{C}) \exp\Big(-j2\pi q\frac{t}{T}\Big) dt \tag{4.68}$$

is the qth Fourier coefficient. The coefficient $S_{k,q}^{(\mathrm{TD})}(\mathbf{C})$ (4.68) can be evaluated by:

1) replacing the extremes $(-N_{cp}^{(\mathrm{TD})})$ and $(N-1)$ of the summation in (4.64) with $-\infty$ and $+\infty$, respectively[10];

2) Substituting the RHS of the resulting formula in that of (4.68).

[9] This assumption is commonly made in the technical literature (e.g., see [88]); this corresponds to selecting an OFDM subcarrier spacing equal to Δ_f/N, i.e., N times smaller than that characterizing DOFDM (see the comments above (4.19) and those following (4.40)).

[10] Note that this does not have any impact on the representation of $s_k^{(\mathrm{TD})}(t;\mathbf{C})$ (4.64) over the limited interval $[0, T]$.

3) replacing the index l with the couple $(\tilde{l}, u)$ such that $l = \tilde{l} + uN$, with $\tilde{l} = 0, 1, ..., N-1$ and u arbitrary integer.

4) Exploiting the periodicity, with period N, of the sequence $\{x_{k,l}\}$ in the index l (see (4.57)). This yields, after some manipulation[11],

$$S_{k,q}^{(\mathrm{TD})}(\mathbf{C}) = \frac{1}{\sqrt{N}T_{\mathrm{s}}} X_{k,q} P\Big(\frac{q - kN}{T}\Big), \tag{4.69}$$

where $P(f)$ is the FCT of $p(t)$ and

$$X_{k,q} \triangleq \frac{1}{\sqrt{N}} \sum_{n=0}^{N-1} x_{k,n} \exp\Big(-j2\pi \frac{n}{N} q\Big) \tag{4.70}$$

represents the qth element of the order N DFT of the sequence $\{x_{k,n}\}$ evaluated with respect to the index n.

The mathematical results developed until now (and, in particular, the FS representation (4.67)) allow us to analyze easily what happens at the RX side when $s(t; \mathbf{C})$ (4.62) is transmitted on an *ideal communication channel*, i.e., on a channel that does not introduce distortion and noise (channel delay is also neglected for simplicity). The study of this scenario, which is described in the following paragraph, allows us to:

1) discover the nature of the transformation $\mathbf{g}(\cdot)$ to be adopted in (4.56).

2) assess the impact of TX and RX filtering.

4.2.3.2 Received signal model in the presence of an ideal communication channel

In this paragraph, we develop a mathematical model of the received signal under the assumption that it coincides with the transmitted signal $s(t; \mathbf{C})$ (4.62). Following [95, 96], we assume that the first stage in the baseband model of the receiver for the modulation format described in the previous paragraph is a *filter bank*[12], consisting of M distinct *matched filters*. The frequency response and the impulse response of the $\tilde{k}$th filter (matched to $p(t)\exp(j2\pi k\Delta_f t)$) are

$$\Phi_{\tilde{k}}(f) = P^*\big(f - \tilde{k}\Delta_f\big) = P^*\big(f - \tilde{k}N/T\big) \tag{4.71}$$

and

$$\phi_{\tilde{k}}(t) = p^*(-t)\exp\big(j2\pi\tilde{k}t/T_{\mathrm{s}}\big), \tag{4.72}$$

respectively, with $\tilde{k} = -M/2, -M/2+1, ..., M/2-1$. Based on the signal decomposition (4.63), the overall response of this filter to the signal $s(t; \mathbf{C})$ (4.62), can be computed by

[11] The derivation of the following result is similar to that illustrated for (4.6) (obtained from (4.5)); further details can be found in Appendix A.3.1.

[12] This choice is optimal in the maximum likelihood sense in this case, but is sub-optimal in the case of a multipath fading channel.

first evaluating its response to $s_k^{(\mathrm{TD})}(t;\mathbf{C})$ (4.64) and then summing over k. Based on the FS representation (4.67) of $s_k^{(\mathrm{TD})}(t;\mathbf{C})$ and (4.71), the last response can be expressed as

$$r_{k,\tilde{k}}(t;\mathbf{C}) = \frac{1}{\sqrt{N}} \sum_{q=-\infty}^{+\infty} X_{k,q}\, G_{k,\tilde{k},q} \exp\Big(j2\pi q \frac{t}{T}\Big), \tag{4.73}$$

in the interval[13] $[0,T]$; here,

$$G_{k,\tilde{k},q} \triangleq \frac{1}{T_\mathrm{s}} P\Big(\frac{q-kN}{T}\Big) P^*\Big(\frac{q-\tilde{k}N}{T}\Big) \tag{4.74}$$

for any k, $\tilde{k}$ and q. The output of the $\tilde{k}$th matched filter (with $\tilde{k} = -M/2, -M/2+1, ..., M/2-1$) is sampled at the instant $t_{\tilde{n}} = \tilde{n}T_\mathrm{s}$, with $\tilde{n} = 0, 1, ..., N-1$. Sampling $r_{k,\tilde{k}}(t;\mathbf{C})$ (4.73) at that instant produces[14]

$$r_k[\tilde{k},\tilde{n}] \triangleq r_{k,\tilde{k}}(t_{\tilde{n}};\mathbf{C}) = \frac{1}{\sqrt{N}} \sum_{q=-\infty}^{+\infty} X_{k,q}\, G_{k,\tilde{k},q} \exp\Big(j2\pi \frac{q}{N}\tilde{n}\Big). \tag{4.75}$$

The last expression can be easily rewritten by: 1) replacing the index q with the couple $(\tilde{q},u)$, with $\tilde{q} = 0, 1, ..., N-1$ and u arbitrary integer; 2) replacing $\tilde{q}$ with q; 3) exploiting the periodicity of the sequence $\{X_{k,q}\}$ in the index q (with period N) thanks to the presence of the TD CP[15]. This yields

$$r_k[\tilde{k},\tilde{n}] = \frac{1}{\sqrt{N}} \sum_{q=0}^{N-1} X_{k,q}\, \hat{G}_{\tilde{k}-k,q} \exp\Big(j2\pi \frac{q}{N}\tilde{n}\Big), \tag{4.76}$$

where

$$\hat{G}_{x,q} \triangleq \frac{1}{T_\mathrm{s}} \sum_{u=-\infty}^{+\infty} P\Big(\frac{q+(u+x)N}{T}\Big) P^*\Big(\frac{q+uN}{T}\Big) \tag{4.77}$$

for any integer x. Given (4.76), the output $r[\tilde{k},\tilde{n}]$ of the $\tilde{k}$th matched filter at the instant $t_{\tilde{n}} = \tilde{n}T_\mathrm{s}$ can be evaluated as

$$r[\tilde{k},\tilde{n}] = \sum_{k=-\infty}^{+\infty} r_k[\tilde{k},\tilde{n}]. \tag{4.78}$$

Then, substituting the RHS of (4.76) in that of the last equation gives, after some manipulations

$$r[\tilde{k},\tilde{n}] = \frac{1}{\sqrt{MN}} \sum_{p=0}^{M-1} \sum_{q=0}^{N-1} \bar{X}_{p,q}\, \bar{g}_{p,q} \exp\Big(-j2\pi\big(\frac{p}{M}\tilde{k} - \frac{q}{N}\tilde{n}\big)\Big), \tag{4.79}$$

[13] Despite RX filtering, this interval remains the same as that in which (4.67) holds, thanks to the fact that the employed matched filters are assumed not to be causal for simplicity (see (4.72)).

[14] In the following, the dependence on $\mathbf{C}$ is omitted to ease notation.

[15] Note that this is the *first* time that the double cyclicity of the modulated signal is exploited at the RX side.

where

$$\bar{X}_{p,q} \triangleq \frac{1}{\sqrt{M}} \sum_{m=0}^{M-1} X_{m,q} \exp\Big(j2\pi \frac{p}{M} m\Big) \tag{4.80}$$

is the pth element of the order M IDFT of the sequence $\{X_{m,q}\}$ in the index m and

$$\bar{g}_{p,q} \triangleq \sum_{u=-\infty}^{+\infty} \hat{G}_{u,q} \exp\Big(j2\pi \frac{p}{M} u\Big) \tag{4.81}$$

represents the *frequency response*, evaluated at the normalized frequency (p/M), of the digital filter characterized by the impulse response $\{\hat{G}_{u,\cdot}\}$ (further details can be found in Appendix A.3.2). It is important to point out that: 1) the derivation of (4.79) relies on the order M periodicity of the sequence $\{X_{k,q}\}$ (4.70) in k, i.e., on the presence of the FD CP and CPO; 2) ciclicity is exploited for the *second* time in deriving the proposed received signal model (further mathematical details can be found in Appendix A.3.2). Moreover, (4.79) leads to the conclusion that the 2D sequence $\{r[\tilde{k}, \tilde{n}]\}$ consists of the *superposition of MN distinct complex exponentials* and that the complex gain associated with the couple of indices (p, q) is given by the product between $\bar{X}_{p,q}$ (conveying the transmitted message) and $\bar{g}_{p,q}$ (depending on TX and RX filtering only). Based on the last results, we can: 1) select properly the transformation $\mathbf{g}(\cdot)$; 2) assess the impact of the pulse $p(t)$ on the structure of the received signal samples. In the remaining part of this paragraph, we concentrate on the first issue only (a detailed discussion on the second one can be found in Section 4.2.3.4). As far as $\mathbf{g}(\cdot)$ is concerned, substituting the RHS of (4.70) in that of (4.80) gives

$$\bar{X}_{p,q} \triangleq \frac{1}{\sqrt{MN}} \sum_{m=0}^{M-1} \sum_{n=0}^{N-1} x_{m,n} \exp\Big(j2\pi\big(\frac{m}{M}p - \frac{n}{N}q\big)\Big), \tag{4.82}$$

that can be interpreted as the coefficient (p, q) of the order (M, N) DSFT of the $M \times N$ complex matrix $\mathbf{X}$ [87, 88]. In addition, (4.82) can be rewritten in matrix form as

$$\bar{\mathbf{X}} = \mathrm{DSFT}_{M,N}[\mathbf{X}] \triangleq \mathbf{\Xi}_M^H \, \mathbf{X} \, \mathbf{\Xi}_N, \tag{4.83}$$

where $\bar{\mathbf{X}} \triangleq [\bar{X}_{p,q}]$ is an $M \times N$ complex matrix This suggests to select an order (M, N) Inverse Discrete Symplectic Fourier Transform (IDSFT) for the transformation $\mathbf{g}(\cdot)$ appearing in the RHS of (4.56), so that

$$\mathbf{X} = \mathrm{IDSFT}_{M,N}[\mathbf{C}] \triangleq \mathbf{\Xi}_M \, \mathbf{C} \, \mathbf{\Xi}_N^H. \tag{4.84}$$

In fact, (4.83) implies that

$$\bar{\mathbf{X}} = \mathbf{\Xi}_M^H \, \mathbf{\Xi}_M \, \mathbf{C} \, \mathbf{\Xi}_N^H \, \mathbf{\Xi}_N = \mathbf{C} \tag{4.85}$$

and, consequently, that

$$\bar{X}_{p,q} = c_{R_M[p], R_N[q]}, \tag{4.86}$$

for any p and q, and (see (4.79))

$$r[\tilde{k}, \tilde{n}] = \frac{1}{\sqrt{MN}} \sum_{p=0}^{M-1} \sum_{q=0}^{N-1} c_{p,q} \, \bar{g}_{p,q} \exp\Big(-j2\pi\big(\frac{p}{M}\tilde{k} - \frac{q}{N}\tilde{n}\big)\Big). \tag{4.87}$$

The last result can be easily rewritten in matrix form as

$$\mathbf{r}(\mathbf{C}) = \mathbf{\Xi}_M(\mathbf{C} \odot \bar{\mathbf{G}})\mathbf{\Xi}_N^H, \tag{4.88}$$

where $\mathbf{r}(\mathbf{C}) \triangleq [r[\tilde{k}, \tilde{n}]]$ and $\bar{\mathbf{G}} \triangleq [\bar{g}_{p,q}]$ are $M \times N$ matrices collecting the received signal samples acquired at the output of whole filter bank over the observation interval and the complex gains $\{\bar{g}_{p,q}\}$ (evaluated on the basis of (4.81)), respectively. Moreover, based on (4.88), a simple detection method, conceptually similar to those illustrated for OFDM and DOFDM, can be easily developed. In fact, the evaluation of an order (M, N) DSFT of $\mathbf{r}(\mathbf{C})$ (4.88) produces the $M \times N$ complex matrix

$$\mathbf{Y}(\mathbf{C}) \triangleq \mathrm{DSFT}_{M,N}[\mathbf{r}(\mathbf{C})] = \mathbf{C} \odot \bar{\mathbf{G}}, \tag{4.89}$$

whose element (m, n) is

$$Y[m, n] = \frac{1}{MN} c_{m,n} \bar{g}_{m,n}, \tag{4.90}$$

with $m = 0, 1, ..., M-1$ and $n = 0, 1, ..., N-1$. Then, for any m and n, the channel symbol $c_{m,n}$ has to be detected on the basis of $Y[m, n]$ only, after compensating for the complex gain $\bar{g}_{m,n}$.

Finally, it is important to point out that:

1) Equations (4.84) and (4.86) entail that

$$x_{m,n} \triangleq \frac{1}{\sqrt{MN}} \sum_{p=0}^{M-1} \sum_{q=0}^{N-1} c_{p,q} \exp\Big(-j2\pi\big(\frac{p}{M}m - \frac{q}{N}n\big)\Big), \tag{4.91}$$

with $m = 0, 1, ..., M-1$ and $n = 0, 1, ..., N-1$.

2) The mathematical result expressed by (4.90) can be seen as a generalization of (4.26) and (4.54), that have been derived for OFDM and DOFDM, respectively. Note that the absence of any form of ISI affecting $Y[m, n]$ (4.90) is made possible by the use of a DCP[16]. In fact, this property would disappear if the TD CP and/or the FD CP & CPO were removed. Note also that, since the communication channel we are considering does not introduce any distortion, the coefficient $\bar{g}_{m,n}$ depends exclusively on the spectrum $P(f)$ (see (4.81) and (4.77)).

3) Ideally, the pulse $p(t)$ should be selected in a way that all the elements of the resulting gain matrix $\bar{\mathbf{G}}$ have similar amplitudes (see (4.89)); in fact, this would ensure that all the channel symbols are treated fairly, i.e., that the 2D complex exponentials conveying them exhibit similar strengths (see (4.79)). It should be expected, however, that, similarly to what happens in the case of OFDM and DOFDM, since this condition cannot be met for all the elements of the matrix $\mathbf{C}$, even in an approximate fashion, a portion of such elements has to be suppressed (i.e., set to zero). These issues are discussed in detail in Section 4.2.3.4.

[16] In the absence of a DCP, (4.76), (A.48) (see Appendix A.3.2) and, consequently, (4.79), would not hold. This would result in the presence of a 2D ISI term in the RHS of (4.90).

4.2.3.3 Received signal model in the presence of a doubly selective fading channel

Let us focus now on the reception on a multipath fading channel characterized by Channel Impulse Response (CIR)[17]

$$h(t,\tau) = \sum_{l=0}^{L-1} \tilde{h}_l(t,\tau), \tag{4.92}$$

where

$$\tilde{h}_l(t,\tau) = a_l \exp\left(j2\pi\nu_l t\right) \delta(\tau - \tau_l) \tag{4.93}$$

represents the CIR component associated with the lth path, characterized by the gain a_l, the delay τ_l and the Doppler shift ν_l, and L is the overall number of paths. In the following, we assume that the CIR components are organized according to increasing delays, so that τ_0 and τ_{L-1} represent the minimum and maximum delays, respectively. In the remaining part of this subsection, we derive a mathematical model for the $M \times N$ matrix $\mathbf{r}(\mathbf{C})$ collecting the samples acquired at the output of the above mentioned filter bank (see (4.88)) in the new scenario. The subsequent analytical developments follow closely those illustrated above for an ideal communication channel. To begin, we evaluate the response

$$z_{k,l}(t;\mathbf{C}) \triangleq \int_{-\infty}^{+\infty} s_k^{(\mathrm{TD})}(\tau;\mathbf{C}) \tilde{h}_l(\tau, t-\tau)\, d\tau \tag{4.94}$$

of the lth CIR contribution (namely, $\tilde{h}_l(t,\tau)$ (4.93)) to $s_k^{(\mathrm{TD})}(t;\mathbf{C})$ (4.64). Once again, in doing so, the FS representation (4.67) of $s_k^{(\mathrm{TD})}(t;\mathbf{C})$ is exploited; based on this, it is easy to prove that

$$z_{k,l}(t;\mathbf{C}) = \tilde{a}_l \sum_{q=-\infty}^{+\infty} Z_{k,q,l}(\mathbf{C}) \exp\Big(j2\pi\big(\frac{q}{T} + \nu_l\big)t\Big) \tag{4.95}$$

in the interval $[\tau_{L-1}, T + \tau_{L-1}]$; here,

$$Z_{k,q,l}(\mathbf{C}) \triangleq \frac{1}{\sqrt{N}T_{\mathrm{s}}} X_{k,q} P\Big(\frac{q - kN}{T}\Big) \exp\Big(-j2\pi q \frac{\tau_l}{T}\Big) \tag{4.96}$$

and

$$\tilde{a}_l \triangleq a_l \exp\big(j2\pi\nu_l\tau_l\big). \tag{4.97}$$

Note that the difference between the coefficient (4.96) and its counterpart $S_{k,q}^{(\mathrm{TD})}(\mathbf{C})$ (4.69) obtained for an ideal channel is represented by a complex exponential, that accounts for the delay τ_l introduced by the lth path of the communication channel.

Given (4.95), the response

$$r_{k,\tilde{k},l}(t;\mathbf{C}) = z_{k,l}(t;\mathbf{C}) * \phi_{\tilde{k}}(t) \tag{4.98}$$

[17] *Channel sparsity* is usually assumed in the OTFS literature (e.g., see [79,87,88,97]). This assumption is not required in the following derivations.

of the $\tilde{k}$th matched filter (see (4.71) and (4.72)) to $z_{k,l}(t;\mathbf{C})$ can be expressed as

$$r_{k,\tilde{k},l}(t;\mathbf{C}) = \tilde{a}_l \sum_{q=-\infty}^{+\infty} Z_{k,q,l}(\mathbf{C}) P^*\Big(\frac{q-\tilde{k}N}{T}+\nu_l\Big)\exp\Big(j2\pi\Big(\frac{q}{T}+\nu_l\Big)t\Big). \tag{4.99}$$

Then, substituting the RHS of (4.96) in that of the last equation and sampling the resulting signal at the instant $t_{\tilde{n}} = \tau_{L-1} + \tilde{n}T_{\rm s}$ produces

$$r_{k,l}[\tilde{k},\tilde{n}] \triangleq r_{k,\tilde{k},l}(t_{\tilde{n}};\mathbf{C}) = \frac{A_l}{\sqrt{N}}\exp\left(j2\pi\tilde{n}F_{\nu_l}\right)\sum_{q=-\infty}^{+\infty} X_{k,q}\, G_{k,\tilde{k},q,l} \cdot \exp\left(-j2\pi q\frac{F_{\tau_l}}{N}\right)\exp\left(j2\pi\frac{q}{N}\tilde{n}\right), \tag{4.100}$$

with $\tilde{n} = 0, 1, ..., N-1$; here,

$$G_{k,\tilde{k},q,l} \triangleq \frac{1}{T_{\rm s}} P\Big(\frac{q-kN}{T}\Big)P^*\Big(\frac{q-\tilde{k}N}{T}+\nu_l\Big), \tag{4.101}$$

and

$$A_l \triangleq \tilde{a}_l \exp(j2\pi\nu_l\tau_{L-1}), \tag{4.102}$$

$$F_{\tau_l} \triangleq \frac{\tau_l - \tau_{L-1}}{T_{\rm s}} \tag{4.103}$$

and

$$F_{\nu_l} \triangleq \nu_l T_{\rm s} \tag{4.104}$$

denote a complex gain, the *normalized delay* and the *normalized Doppler shift* associated with the lth path, respectively. Given (4.100), the expression of the overall output of the $\tilde{k}$th RX filter due to the lth path and to all the components of $s(t;\mathbf{C})$ at the $\tilde{n}$th sampling instant is evaluated by summing over k; this produces

$$r_l[\tilde{k},\tilde{n}] = \frac{A_l}{\sqrt{MN}}\exp\big(-j2\pi\tilde{k}F_{\tau_l}\big)\exp\left(j2\pi\tilde{n}F_{\nu_l}\right)\sum_{p=0}^{M-1}\sum_{q=0}^{N-1}\bar{X}_{p,q}\,\bar{g}_{p,q}(F_{\tau_l},F_{\nu_l}) \cdot \exp\Big(-j2\pi\Big(\frac{p}{M}\tilde{k}-\frac{q}{N}\tilde{n}\Big)\Big). \tag{4.105}$$

Note that validity of this result relies on the assumption of double periodicity of the sequence $\{X_{k,q}\}$ (4.82), i.e., on the presence of the DCP[18]. In (4.105), $\bar{X}_{p,q}$ is still expressed by (4.82), whereas

$$\bar{g}_{p,q}(F_{\tau_l},F_{\nu_l}) \triangleq \sum_{u=-\infty}^{\infty}\hat{G}_{u,q}(F_{\tau_l},F_{\nu_l})\exp\Big(j2\pi\frac{u}{M}p\Big) \tag{4.106}$$

represents the counterpart of $\bar{g}_{p,q}$ (4.81). Note that (4.105) can be rewritten as

$$r_l[\tilde{k},\tilde{n}] = h_l[\tilde{k},\tilde{n}]T_l[\tilde{k},\tilde{n}], \tag{4.107}$$

[18]This is the *third* time that the property of double cyclicity is exploited in the derivations referring to the RX side (further mathematical details are provided in Appendix A.3.3).

where

$$h_l[\tilde{k},\tilde{n}] \triangleq A_l \exp\big(-j2\pi\tilde{k}F_{\tau_l}\big)\exp\left(j2\pi\tilde{n}F_{\nu_l}\right) \tag{4.108}$$

depends on the parameters of the lth path only, whereas

$$T_l[\tilde{k},\tilde{n}] \triangleq \frac{1}{\sqrt{MN}}\sum_{p=0}^{M-1}\sum_{q=0}^{N-1} c_{p,q}\,\bar{g}_{p,q}(F_{\tau_l},F_{\nu_l})\exp\Big(-j2\pi\big(\frac{p}{M}\tilde{k}-\frac{q}{N}\tilde{n}\big)\Big) \tag{4.109}$$

depends on: 1) the channel symbols $\{c_{p,q}\}$; 2) the pulse shape, and the lth *normalized delay* and *Doppler shift* through $\bar{g}_{p,q}(F_{\tau_l},F_{\nu_l})$.

Equation (4.105) describes the contribution given to the output of the $\tilde{k}$th RX filter by the lth path only. The contribution of all the paths can be accounted for by summing over the index l (see (4.92)); this produces (see (4.107))

$$r[\tilde{k},\tilde{n}] \triangleq \sum_{l=0}^{L-1} r_l[\tilde{k},\tilde{n}] = \sum_{l=0}^{L-1} h_l[\tilde{k},\tilde{n}]T_l[\tilde{k},\tilde{n}] \tag{4.110}$$

that, similarly as (4.79), expresses the $\tilde{n}$th sample taken at the output of the $\tilde{k}$th RX filter. The samples acquired at the output of the filter bank at all the considered sampling instants are collected in the $M\times N$ matrix $\mathbf{r}(\mathbf{C}) \triangleq [r[\tilde{k},\tilde{n}]]$, that, similarly as the case of an ideal channel, undergoes DSFT processing (see (4.89)); this yields

$$\mathbf{Y}(\mathbf{C}) \triangleq [Y[m,n]] = \mathrm{DSFT}_{M,N}[\mathbf{r}(\mathbf{C})]. \tag{4.111}$$

It is easy to prove that the element (m,n) of $\mathbf{Y}(\mathbf{C})$ (4.111) is

$$Y[m,n] = \frac{1}{MN}\sum_{p=0}^{M-1}\sum_{q=0}^{N-1} c_{p,q}\left[\sum_{l=0}^{L-1} A_l\,\bar{g}_{p,q}(F_{\tau_l},F_{\nu_l})\Psi_M\left(m-p,-F_{\tau_l}\right)\Psi_N\left(n-q,F_{\nu_l}\right)\right], \tag{4.112}$$

where

$$\Psi_V(v,F) \triangleq \frac{\exp\left(j2\pi(v+FV)\right)-1}{\exp\left(j2\pi\left(\frac{v+FV}{V}\right)\right)-1} \tag{4.113}$$

and F is a normalized frequency belonging to the interval $[0,1]$. Comparing (4.90) with (4.112) evidences that:

1) The presence of time dispersion (i.e., multipath) and frequency dispersion (i.e., Doppler) results in the presence of 2D ISI[19]. In fact, the RHS of (4.112) depends not only on $c_{m,n}$, but also on all the other channel symbols belonging to the same OTFS symbol.

[19]In a part of the technical literature on OTFS, the 2D ISI is often split into two components (e.g., see [87]). In practice, on the one hand, the term ISI usually refers to the interference affecting TD samples due to the presence of a fractional component in the delay introduced by the communication channel; on the other hand, the term Inter-Doppler Interference (IDI) is adopted for the interference affecting frequency domain samples and due to the presence of a fractional component in the Doppler shift. The 2D ISI turns into 1D ISI in the absence of time dispersion (i.e., multipath) or frequency dispersion (i.e., Doppler).

2) The amplitude $\bar{g}_{m,n}$ appearing in the RHS of (4.90) is replaced by the quantity (which is associated with $(p,q)=(m,n)$; see (4.112))

$$\hat{g}_{m,n}(\mathbf{F}_\tau,\mathbf{F}_\nu) \triangleq \sum_{l=0}^{L-1} \hat{g}_{m,n}(F_{\tau_l},F_{\nu_l}) = \sum_{l=0}^{L-1} A_l\, \bar{g}_{m,n}(F_{\tau_l},F_{\nu_l}) \Psi_M\left(0,-F_{\tau_l}\right) \Psi_N\left(0,F_{\nu_l}\right); \tag{4.114}$$

here, $\mathbf{F}_\tau \triangleq [F_{\tau_0},F_{\tau_1},...,F_{\tau_{L-1}}]^T$ and $\mathbf{F}_\nu \triangleq [F_{\nu_0},F_{\nu_1},...,F_{\nu_{L-1}}]^T$. Therefore, the amplitude of the term conveying $c_{m,n}$ in $Y[m,n]$ is influenced by *all the parameters of the communication channel* (namely, its overall number of paths, its Doppler shifts and its path delays).

3) In the presence of a single path (i.e., for $L=1$), (4.114) turns into

$$\hat{g}_{m,n}(F_{\tau_0},F_{\nu_0}) = A_0\, \bar{g}_{m,n}(F_{\tau_0},F_{\nu_0}) \Psi_M(0,-F_{\tau_0}) \Psi_N(0,F_{\nu_0}). \tag{4.115}$$

This shows that, even in the presence of a single propagation path in the communication channel, the amplitude of the term conveying $c_{m,n}$ in $Y[m,n]$ (4.112) depends not only on $p(t)$ (through $\bar{g}_{m,n}(\cdot,\cdot)$), but also on the path delay and Doppler.

A thorough understanding of the ISI phenomenon affecting $Y[m,n]$ (4.112) requires analyzing the dependence of function $\Psi_V(v,F)$, that appears in the RHS of (4.112), on the variable v for a given F. To this aim, it is useful to express the variable F as $F=\bar{F}/V+F_r$, where $\bar{F}$ is an integer and F_r is a real quantity belonging to interval $[-0.5/V,\, 0.5/V]$ ($\bar{F}$ and F_r represent the so-called *integer part* of F and its *fractional part*, respectively). In fact, it is easy to prove that, in general, the function $\Psi_V(v,F)$ exhibits a peak at $v=\bar{F}$ and, if $F_r=0$, the function $\Psi_V(v,F)=\Psi_V(\bar{F}/V,F)$ turns into a Kronecker delta, i.e.,

$$\delta(v,F) = \begin{cases} 1 & \text{if } v=\bar{F} \\ 0 & \text{otherwise} \end{cases}; \tag{4.116}$$

otherwise, it exhibits *tails* that decay slowly and that become more pronounced if $|F_r|$ approaches $0.5/V$. Because of the behavior of the function $\Psi_V(v,F)$, the terms $\Psi_M(0,-F_{\tau_l})$ and $\Psi_N(0,F_{\nu_l})$ appearing in the RHS of (4.112) are responsible for:

1) A *cyclic shift* of all the elements $\{c_{p,q}\}$ of the OTFS symbol matrix $\mathbf{C}$; the horizontal shift and the vertical one are quantified by the integer part of F_{τ_l} and F_{ν_l}, respectively.

2) The presence of *leakage* (i.e., ISI) when one or both the *fractional* parts of the normalized frequencies F_{τ_l} and F_{ν_l} are different from zero.

Based on these results, we can conclude that, even if a DCP is employed, the estimation of the transmitted OTFS symbol requires a form of 2D *equalization*, which is substantially more complicated than its 1D counterparts illustrated for OFDM and DOFDM in the previous two subsections. Equalization, in turn, needs *channel estimation*; this task is usually accomplished through *pilots*, i.e., through the exploitation of known symbols surrounded by guard symbols (i.e., by zero symbols placed around pilots) for mitigating mutual interference [88, 98].

4.2.3.4 Pulse-shaping

Let us focus now on the *pulse shaping problem*, i.e., on how to select the pulse $p(t)$. In the technical literature, the use of a rectangular pulse is often taken into consideration, since its simple shape makes mathematical derivations easier [83, 84, 87, 88, 99–101]. However, this choice is not in agreement with the fact that:

1) as illustrated in Section 4.2.3.1, an OTFS signal can be seen as the superposition of multiple OFDM signals, characterized by distinct central frequencies.

2) The generation of an OFDM signal requires the use of a bandlimited pulse, whose amplitude spectrum exhibits a flat top[20] (see Section 4.2.1). Based on these considerations, in this work, the following choices have been made:

1) The same pulse as the one adopted in the OFDM signal model has been selected for $p(t)$ (therefore, its spectrum $P(f)$ is expressed by (4.16)). Note that, for any value of its roll-off factor α, its bandwidth is equal to $(1+\alpha)/(2T_s)$ and, consequently, never exceeds $\Delta_f = 1/T_s = N/T$.

2) Subcarrier suppression has been employed to ensure that the useful subcarriers of the multiple OFDM signals, which the OTFS signal is made of, have identical amplitudes and that self-interference is avoided (see Section 4.2.1).

Regarding point 1), if the above mentioned pulse is selected, only the terms associated with $u \in \{-1, 0, 1\}$ survive in the sums appearing in the RHS of (4.77) and (4.81), because of the limited bandwidth of $p(t)$. As far as point 2) is concerned, instead, following the rules illustrated for OFDM, *subcarrier suppression* SC can be achieved by simply setting to zero $N_{sc} \triangleq N - 2N_\alpha - 1$ consecutive columns[21] of the matrix $\mathbf{C}$; this means that

$$\bar{N}_{sc} \triangleq M(N - 2N_\alpha - 1) \tag{4.117}$$

elements of the matrix $\mathbf{C}$ do not convey channel symbols, being zeroed. Note also that:

1) Subcarrier suppression ensures that, in principle, the coefficients $\{\bar{g}_{m,n}\}$ (see (4.81)) associated with the unsuppressed channel symbols $\{c_{m,n}\}$, in (4.87), have exactly the same amplitude (and, in particular, a unit amplitude for the selected pulse).

2) If this occurs, (4.91) can be rewritten as

$$x_{m,n} \triangleq \frac{1}{\sqrt{MN}} \sum_{p=0}^{M-1} \sum_{q=-N_\alpha}^{N_\alpha} c_{p,R_N[q]} \exp\Big(j2\pi\big(\frac{q}{N}n - \frac{p}{M}m\big)\Big), \tag{4.118}$$

with $m = 0, 1, ..., M-1$ and $n = 0, 1, ..., N-1$.

The overall number of channel symbols conveyed by a single OTFS symbol can be increased a little bit by relaxing the above-mentioned amplitude constraint at the price of introducing

[20] This choice, as noted in Section 4.2.1, ensures uniform amplitude for the useful (i.e., unsuppressed) subcarriers of an OFDM signal.

[21] In particular, the columns whose index runs from $N_\alpha + 1$ to $N - N_\alpha - 1$.

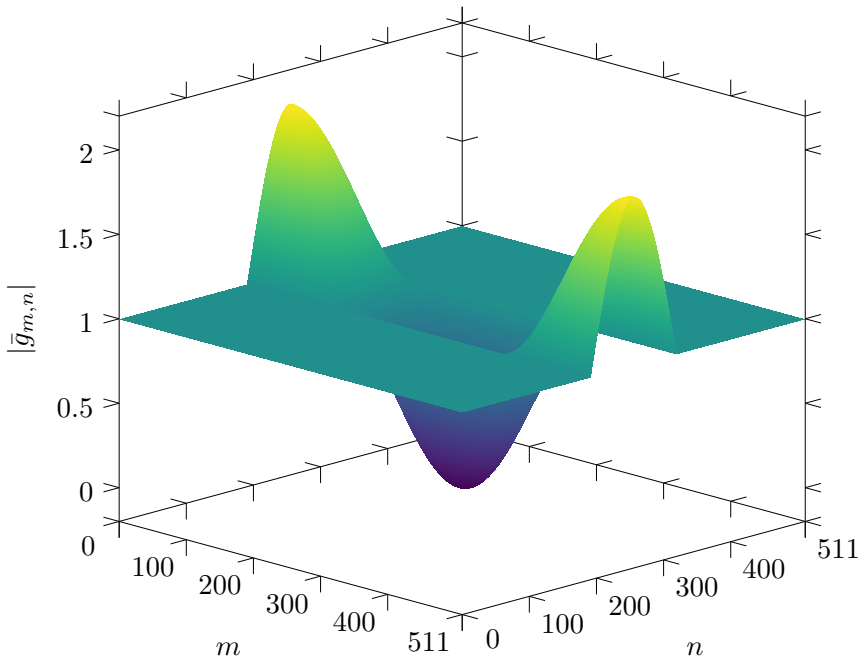

FIGURE 4.1: Representation of the 2D sequence $\{|\bar{g}_{m,n}|\}$ for $M = N = 512$. The spectrum $P(f)$ is expressed by (4.16) with $\alpha = 0.25$.

a limited amount of self-interference. In the considered case, this result can be achieved by exploiting all the elements of the matrix $\mathbf{C}$ whose indexes (m, n) belong to the set

$$\Gamma_\varepsilon(\alpha) \triangleq \{(m,n) : (1-\varepsilon) \leq |\bar{g}_{m,n}| \leq (1+\varepsilon)\}; \tag{4.119}$$

here, $m = 0, 1, ..., M-1$, $n = 0, 1, ..., N-1$, whereas ε denotes a real (and small) positive parameter representing the maximum tolerable deviation from a unitary amplitude. These concepts are exemplified by Fig. 4.1, in which the amplitude of the complex 2D sequence $\{\bar{g}_{m,n}\}$ is represented for $M = N = 512$ and $\alpha = 0.25$. In this case, if $\varepsilon = 0$ is selected, 386 subcarriers are available for data transmission. On the other hand, if $\varepsilon = 0.01$ and $\varepsilon = 0.05$ are chosen, the overall number of useful subcarriers increases to 388 and 401, respectively. The small increase observed in this case is due to the fast variations observed in the sequence $\{|\bar{g}_{m,n}|\}$ out of its flat region; this is evidenced by the two heat maps shown in Fig. 4.2, that represent the behavior of the sequence $\{|\bar{g}_{m,n}|\}$ in the 2D region $\Gamma_\varepsilon(\alpha)$ (4.119) for $\varepsilon = 0.01$ and $\varepsilon = 0.05$. Note also that a larger cardinality of the set $\Gamma_\varepsilon(\alpha)$ results in a higher transmission rate; the impact of the roll-off factor on this can be assessed by evaluating the Spectral Efficiency (SE) [83, 85]

$$\eta_\varepsilon(\alpha) \triangleq \frac{N_\varepsilon(\alpha)}{MN}, \tag{4.120}$$

where $N_\varepsilon(\alpha)$ denotes the cardinality of the set $\Gamma_\varepsilon(\alpha)$ (4.119) (i.e., the overall number of useful channel symbols conveyed by a single OTFS symbol). A representation of $\Gamma_\varepsilon(\alpha)$ and that of its Lower Bound (LB)

$$\eta_{\text{lb}}(\alpha) \triangleq \frac{(2N_\alpha + 1)M}{MN} = \frac{2N_\alpha + 1}{N} \tag{4.121}$$

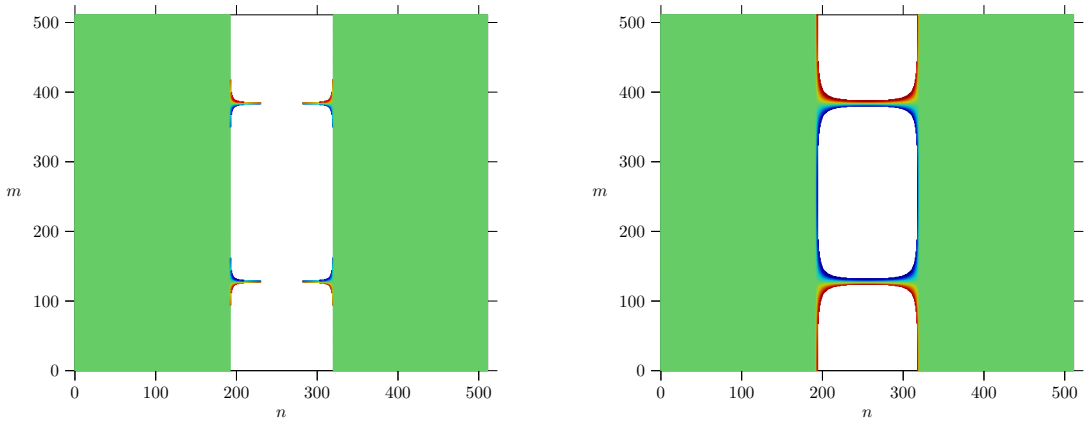

FIGURE 4.2: Heat maps representing the behavior of the sequence $\{|\bar{g}_{m,n}|\}$ in the 2D region $\Gamma_\varepsilon(\alpha)$ (4.119) for a) $\varepsilon = 0.01$ and b) $\varepsilon = 0.05$; $\alpha = 0.25$ is assumed in both cases.

versus α is provided in Fig. 4.3 for $\alpha \in [0.2; 0.45]$; $\varepsilon = 0.05$ and $M = N = 512$ have been selected in this case. From this figure, it is easily inferred that reducing α improves the spectral efficiency of the communication system; this is due to the decrease of the overall number of zeroed symbols. However, this result is achieved at the price of an increase in the duration of $p(t)$ and, consequently, of a longer CP in the TD (i.e., a higher value of $N_{cp}^{(\mathrm{TD})}$).

The considerations made in this paragraph until this point refer to the inner structure of the transmitted signal. As shown in Section 4.2.3.3, this structure may be substantially modified by a doubly selective communication channel. In particular, as illustrated at the end of that paragraph, the complex amplitude $\bar{g}_{m,n}$ associated with the channel symbol $c_{m,n}$ in $Y[m,n]$ (4.90) is replaced by $\hat{g}_{m,n}(F_{\tau_0}, F_{\nu_0})$ (see (4.115)) in the presence of a single path in the communication channel (i.e., for $L = 0$). Let us now analyze the impact of this simple communication channel on the transmitted signal under the assumption that, once again, $P(f)$ is expressed by (4.16). Some numerical results referring to the considered scenario are shown in Fig. 4.4, in which the amplitude of the complex factor $\hat{g}_{m,n}(F_{\tau_0}, F_{\nu_0})$ versus n is illustrated under the assumption that: 1) $M = N = 512$; 2) $T_s = 4$ µs; 3) path gain $A_0 = 1$; 4) $F_{\tau_0} = 4 \cdot 10^{-4}$ (this value corresponds to the path length $R_0 = 250$ m); 5) $F_{\nu_0} = 0.0222$ (this value corresponds to the velocity $v_0 = 250$ km/h if the carrier frequency $f_c = 24$ GHz is employed); 6) $\alpha = 0.25$; 7) $m = M/2 - 1$ (this choice allows us to assess the impact of the Doppler introduced by the communication channel on a specific row of the $M \times N$ matrix $[\hat{g}_{m,n}(F_{\tau_0}, F_{\nu_0})]$). Comparing the amplitude $|\hat{g}_{M/2-1,n}(F_{\tau_0}, F_{\nu_0})|$ with its counterpart $|\bar{g}_{M/2-1,n}|$ referring to an ideal scenario leads to the conclusion that, in the considered case, such amplitudes are close; moreover, similar results are observed for other values of m. The obtained numerical results have also evidenced that limited changes are also observed in the phase of the sequence $\{\hat{g}_{M/2-1,n}(F_{\tau_0}, F_{\nu_0})\}$ with respect to the phase of $\{\bar{g}_{M/2-1,n}\}$ in the flat region of its amplitude. Based on these results, we can assume that

$$\bar{g}_{p,q}(F_{\tau_l}, F_{\nu_l}) \cong \bar{g}_{p,q} \tag{4.122}$$

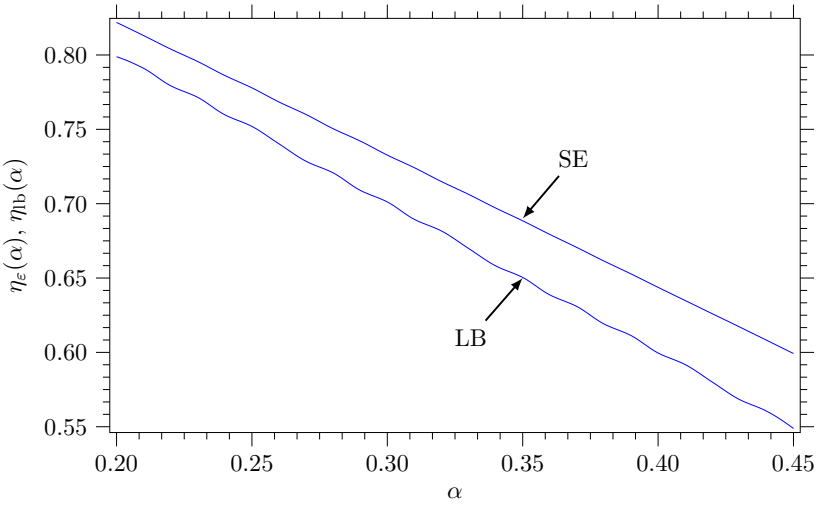

FIGURE 4.3: Representation of $\eta_\varepsilon(\alpha)$ (4.120) (SE) and its lower bound $\eta_{\rm lb}(\alpha)$ (4.121) (LB) versus α for $\alpha \in [0.2; 0.45]$; $\varepsilon = 0.05$ and $M = N = 512$ have been selected.

for any l and (p, q). This approximation, obtained for a specific pulse, has the following relevant implications: 1) the SC positions can be unambiguously identified at the RX side; 2) the approximation

$$T_l[\tilde{k}, \tilde{n}] \cong T[\tilde{k}, \tilde{n}] = \frac{1}{\sqrt{MN}} \sum_{p=0}^{M-1} \sum_{q=0}^{N-1} c_{p,q}\, \bar{g}_{p,q} \exp\Big(-j2\pi\big(\frac{p}{M}\tilde{k} - \frac{q}{N}\tilde{n}\big)\Big) \tag{4.123}$$

can be adopted in the RHS of (4.109), so that (see (4.110))

$$r[\tilde{k}, \tilde{n}] \cong T[\tilde{k}, \tilde{n}] h[\tilde{k}, \tilde{n}], \tag{4.124}$$

where (see (4.108))

$$h[\tilde{k}, \tilde{n}] \triangleq \sum_{l=0}^{L-1} h_l[\tilde{k}, \tilde{n}] = \sum_{l=0}^{L-1} A_l \exp\big(-j2\pi\tilde{k}F_{\tau_l}\big) \exp\big(j2\pi\tilde{n}F_{\nu_l}\big) \tag{4.125}$$

represents the multiplicative distortion introduced by the communication channel. Note that, if (4.124) holds, channel equalization is tantamount to compensating for the factor $h[\tilde{k}, \tilde{n}]$ (4.125) that appears in the RHS of that equation.

Since the selection of $p(t)$ influences the structure of the OTFS-DCP signal (4.62), it should be expected that it has a major impact on the spectral properties of that modulation format. In Appendix A.3.4, the derivation of the PSD $S_s(f)$ of the OTFS-DCP complex envelope $s(t; \mathbf{C})$ (4.62) is sketched for the pulse shape considered in this paragraph; in particular, it is shown that

$$S_s(f) = \sum_{k=-(M/2+N_{cp}^{(\rm FD)})}^{M/2-1+N_{cpo}^{(\rm FD)}} S(f - k\Delta_f), \tag{4.126}$$

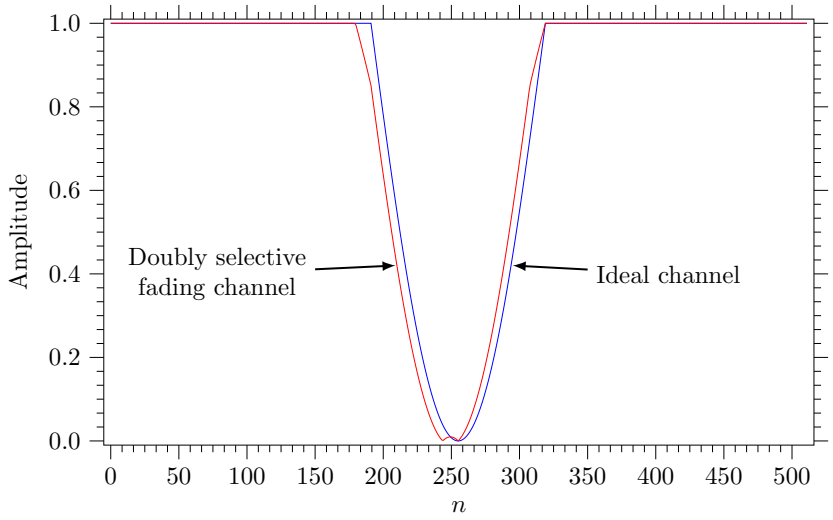

FIGURE 4.4: Representation of the sequences $\{|\hat{g}_{M/2-1,n}(F_{\tau_0}, F_{\nu_0})|\}$ and $\{|\bar{g}_{M/2-1,n}|\}$; a single path doubly selective fading channel characterized by $A_0 = 1$ and $(F_{\tau_0}, F_{\nu_0}) = (4 \cdot 10^{-4}, 0.0222)$ is assumed in the evaluation of the first sequence. Here, $M = N = 512$ and a roll-off value $\alpha = 0.25$ for $p(t)$ are selected.

where $S(f - k\Delta_f)$ is the PSD of the signal $s_k^{(\mathrm{TD})}(t; \mathbf{C})$ (4.64),

$$S(f) \triangleq \frac{\sigma_c^2}{T(N + N_{cp}^{(\mathrm{TD})})} \left|P\big(f\big)\right|^2 \sum_{l=-N_\alpha}^{N_\alpha} S_{\mathrm{sub}}(f - f_l), \tag{4.127}$$

σ_c^2 is the variance of the adopted channel symbol constellation[22], $S_{\mathrm{sub}}(f - f_l)$ is the contribution of the lth subcarrier[23] to the PSD $S(f)$ and

$$S_{\mathrm{sub}}(f) \triangleq \frac{\sin^2\left(\pi(N + N_{cp}^{(\mathrm{TD})})fT_s\right)}{\sin^2\left(\pi f T_s\right)}. \tag{4.128}$$

It is important to point out that:

1) If the pulse $p(t)$ selected for the OTFS signal is bandlimited, the OTFS spectrum $S_s(f)$ (4.126) is also bandlimited (see (4.127)).

2) The bandwidth B_s of the OTFS-DCP format proposed in this chapter can be approximated as

$$B_s \cong (M + N_{cp}^{(\mathrm{FD})} + N_{cpo}^{(\mathrm{FD})})\Delta_f. \tag{4.129}$$

A portion of this bandwidth is exploited to transmit the FD CP and CPO (i.e., $N_{cp}^{(\mathrm{FD})} + N_{cpo}^{(\mathrm{FD})}$ OFDM signals); this implies a loss in spectral efficiency (such a loss is quantified by Λ_{cp} (4.61)).

[22]The expression of σ_c^2 for different types of constellation can be found in [81, Subsect. (3.5.4)].

[23]This subcarrier is characterized by the frequency $f_{k,l} \triangleq k\Delta_f + l/T = k\Delta_f + l/(NT_s)$ if $s_k^{(\mathrm{TD})}(t; \mathbf{C})$ is considered.

3) In real world communication systems, a causal and time-limited approximation of the TX pulse $p(t)$ proposed above (and having a RRC spectrum) needs to be used. This can be generated by first delaying the pulse by $L_pT_s/2$ s and, then, by truncating it to the interval $[0, L_pT_s]$, where L_p is an integer parameter. In doing so, it is important to keep in mind that the tails of $p(t)$ become more and more pronounced as its roll-off α approaches 0; for this reason, the duration of its truncation interval has to be increased if a given fraction of the unlimited pulse energy has to be captured. Nevertheless, a larger L_p unavoidably results in a longer TD CP, since,in general, $N_{cp}^{(\mathrm{TD})}$ is required to be not smaller than $(2L_p + L_h)$ (i.e., than the *overall channel memory*, that includes TX/RX filtering).

4) The superposition of multiple subcarriers in $S(f)$ (4.127) results in the presence of fast oscillations in the overall PSD $S_s(f)$ (4.126) within its lower and upper band limits.

4.3 Conclusions

In this chapter, a novel modulation format, resulting from the insertion of a DCP in the OTFS modulation, has been proposed. The impact of pulse shaping on the inner structure of the modulated signal has been analyzed and a specific proposal for pulse selection has been made. Moreover, a receiver architecture for the considered modulation format has been described. The next chapter describes 1) simple rules for allocating one or multiple pilots in the OTFS symbol and 2) novel algorithms for pilot-aided channel estimation with a particular focus for JCAS applications. The developed algorithms are able to estimate the inner structure of a multipath communication channel with better accuracy than other technical alternatives at the price of limited complexity.

5

Novel Channel Estimation and Equalization Algorithms for Orthogonal Time-Frequency Space Modulation with Double Cyclic Prefix

In this chapter, a digital communication system employing the orthogonal time-frequency space modulation with a double cyclic prefix and operating over a doubly selective fading is considered. After providing some guidelines for the allocation of pilot symbols within a single orthogonal time-frequency space modulation symbol, novel algorithms for pilot-aided channel estimation and equalization are illustrated. The proposed channel estimator is able to provide a description of the inner structure of the communication channel; therefore, it can be also employed at the transmit side for sensing applications. The numerical results evidence that the proposed algorithms outperform two technical alternatives outlined in the literature at the price of a limited increase in the required computational effort.

5.1 Introduction

In the last few years, substantial research efforts have been devoted to the investigation of modulation schemes that can be used for JCAS applications in future wireless networks operating at very high frequencies [76]. The considered technical options include OFDM and the OTFS modulation. Unluckily, OFDM suffers from severe ICI in high-mobility conditions. This has motivated the study of alternative communication waveforms and, in particular, of the OTFS modulation. The last modulation scheme has been proposed by *Hadani et al.* to benefit from the diversity offered by doubly selective communication channels [79].

Two important research problems in the field of OTFS-based systems for JCAS are represented by: 1) the development of novel methods for pilot-aided channel estimation; 2) the design of computationally simple equalization techniques. Both problems have been tackled in [83, 91, 92, 101]. However, the solutions developed in those manuscripts suffer from the following limitations: a) the cyclicity property of the modulated signal along the frequency direction, imparted by the introduction of a FD CP and a CPO has never been taken into consideration; b) the presence of a single known channel symbol within each OTFS symbol is assumed for pilot-aided channel estimation; c) the impact of pulse shaping on the positioning of the pilot channel symbol is ignored; d) the property of sparsity is assumed for the communication channel. This chapter presents new findings in the field of pilot-aided channel estimation and equalization to be adopted in a communication system

using the OTFS modulation scheme. This study introduces the concept of DCP, which consists of one CP in the TD and a CP & CPO in the FD. The inner structure of the resulting OTFS signal, referred to as OTFS-DCP, is analyzed in detail in the previous chapter (see Chapter 4).

More specifically, the contributions of this chapter can be summarized as follows.

1) Novel criteria for arranging multiple pilots in each OTFS symbol are illustrated.

2) The improvement provided by multiple pilots in channel estimation is assessed.

3) A low-complexity off-grid algorithm for pilot-aided channel estimation is described. The Channel State Information (CSI) generated by this algorithm can be exploited for target detection and estimation at the TX side in sensing applications or to compute the channel equalizer coefficients at the RX side.

4) A simple channel equalization algorithm is proposed. This algorithm, unlike the alternatives available in the technical literature [83, 101], does not rely on the assumption of channel sparsity[1].

The remaining part of this chapter is organized as follows. In Section 5.2, the architecture of the considered communication system and some relevant signal models referring to it are illustrated. The proposed algorithm for pilot-aided channel estimation and equalization is analyzed in Section 5.3. The algorithm is compared with two technical alternatives in Section 5.4 and its performance, together with those of the other two techniques, is shown in Section 5.5. Finally, some conclusions are given in Section 5.6.

5.2 System and Signal Models

In this section, we focus on a communication system whose architecture is described by the baseband model shown in Fig. 5.1. We assume that:

1) the OTFS-DCP modulation described in Chapter 4 is employed at its TX side;

2) the signal $s(t; \mathbf{C})$, denoting the baseband equivalent of the modulated signal, conveys the $M \times N$ matrix $\mathbf{C} \triangleq [c_{m,n}]$ (with $m = 0, 1, ..., M-1$ and $n = 0, 1, ..., N-1$), that represents a single OTFS *symbol*;

3) the communication channel is *doubly selective*[2] and is characterized by the CIR

$$h(t, \tau) = \sum_{l=0}^{L-1} a_l \, \exp(j2\pi\nu_l t) \, \delta(\tau - \tau_l), \tag{5.1}$$

[1] In this context, sparsity refers to the fact that leakage caused by fractional delays and Doppler frequencies is limited to few adjacent bins. It is worth noting that this property does not generally hold in all scenarios [88].

[2] Channel noise is neglected for simplicity.

where a_l, τ_l and ν_l represent the gain, the delay[3] and the Doppler shift associated with the lth channel path, respectively, and L is the overall number of paths.

Following the methodology described in Section 4.2.3.1, we also assume that

$$s(t;\mathbf{C}) = \sum_{k=-(M/2+N_{cp}^{(\mathrm{FD})})}^{M/2-1+N_{cpo}^{(\mathrm{FD})}} s_k^{(\mathrm{TD})}(t;\mathbf{C}), \tag{5.2}$$

where

$$s_k^{(\mathrm{TD})}(t;\mathbf{C}) \triangleq \sum_{l=-N_{cp}^{(\mathrm{TD})}}^{N-1} x_{k,l}\, p(t-lT_\mathrm{s}) \exp\big(j2\pi k\Delta_f (t-lT_\mathrm{s})\big), \tag{5.3}$$

$x_{k,l}$ is the element (k,l) of the $M \times N$ matrix

$$\mathbf{X} \triangleq [x_{m,n}] = \mathrm{IDSFT}_{M,N}[\mathbf{C}] \triangleq \mathbf{\Xi}_M\, \mathbf{C}\, \mathbf{\Xi}_N^H \tag{5.4}$$

for $k \in \{0,1,...,M-1\}$ and $l \in \{0,1,...,N-1\}$ ($x_{k,l} = x_{R_M[k],R_N[l]}$ otherwise), $p(t)$ is the TX pulse, $\Delta_f = 1/T_\mathrm{s}$ [101], T_s is the *symbol interval*, and $N_{cp}^{(\mathrm{TD})}$, $N_{cp}^{(\mathrm{FD})}$ and $N_{cpo}^{(\mathrm{FD})}$ represent the sizes of the TD CP, the FD CP and the FD CPO; moreover, $\mathrm{IDSFT}_{M,N}[\mathbf{X}]$ denotes an order (M,N) IDSFT (see [101]).

In Section 4.2.3.1, it is proved that, for any k, $s_k^{(\mathrm{TD})}(t;\mathbf{C})$ (5.3) can be seen as the frequency-shifted version of the complex envelope of an OFDM signal, characterized by a CP size equal to $N_{cp}^{(\mathrm{TD})}$ and by a frequency shift equal to $k\Delta_f$, if:

a) the spectrum $P(f)$ of $p(t)$ is the RRC function with *roll-off factor* $\alpha \in [0,1]$ (see (4.16));

b) $N_\mathrm{r} \triangleq M(N-2N_\alpha-1)$ elements of the matrix $\mathbf{C}$ are set to zero (that is, *subcarrier suppression*, SC, is accomplished); here, $N_\alpha \triangleq \lfloor N(1-\alpha)/2 \rfloor$, where $\lfloor\cdot\rfloor$ denotes the *floor* operator. In practice, $c_{p,q} = 0$ for any $(p,q) \in \Gamma_\mathrm{sc}(\alpha)$ with

$$\Gamma_\mathrm{sc}(\alpha) \triangleq \{(p,q);\, p = 0,1,...,M-1, N_\alpha+1 \le q \le N-N_\alpha-1\}. \tag{5.5}$$

Then, under the last assumptions, we have that: 1) $s(t;\mathbf{C})$ (5.2) can be interpreted as the superposition of $M + N_{cp}^{(\mathrm{FD})} + N_{cpo}^{(\mathrm{FD})}$ distinct OFDM signals; 2) $N_\mathrm{u} \triangleq MN - N_\mathrm{r}$ elements of $\mathbf{C}$ are available for the transmission of pilot and information channel symbols, since the remaining ones are set to zero (i.e., are suppressed).

The channel response to $s(t;\mathbf{C})$ (5.2), denoted $r(t;\mathbf{C})$, is applied to a *filter bank* consisting of M distinct *matched filters*; $\phi_{\tilde{k}}(t) \triangleq p^*(-t)\exp(j2\pi\tilde{k}t/T_\mathrm{s})$ is the impulse response of the $\tilde{k}$th filter (with $\tilde{k} = -M/2, ... -1, 0, 1, ...M/2-1$). The output of each filter is then sampled at the instants $t_{\tilde{n}} = \tau_{L-1} + \tilde{n}T_\mathrm{s}$, with $\tilde{n} = 0,1,...,N-1$. Note that the DCP ensures that any shift in both time and frequency directions caused by each path of the doubly selective channel does not result in a loss of useful data, thanks to the availability of redundant information. Thanks to the property of *double cyclicity* of the transmitted

[3]We assume the CIR components are arranged in ascending order of delays, so that τ_0 and τ_{L-1} are the minimum and maximum delays, respectively.

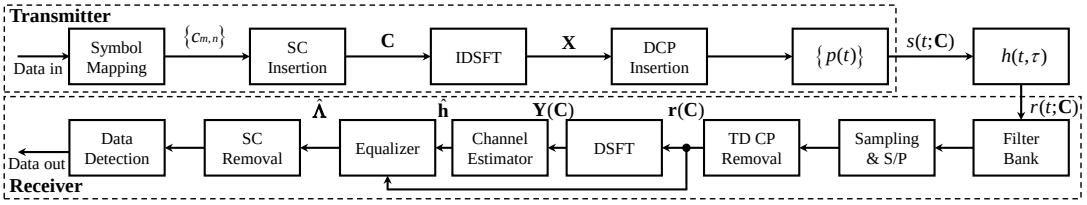

FIGURE 5.1: Baseband model of the developed OTFS-DCP-based communication system.

signal, the $M \times N$ matrix $\mathbf{r}(\mathbf{C})$, collecting the MN samples acquired through the filter bank, can be put in the form (see Section 4.2.3.4)

$$\mathbf{r}(\mathbf{C}) \triangleq [r[\tilde{k},\tilde{n}]] = \mathbf{h} \odot \mathbf{T}(\mathbf{C}), \tag{5.6}$$

where $r[\tilde{k},\tilde{n}]$ is the $\tilde{n}$th sample of the $\tilde{k}$th matched filter output, $\mathbf{h}$ is an $M \times N$ CSI matrix whose element $(\tilde{k},\tilde{n})$ (with $\tilde{k} = 0,1,...,M-1$ and $\tilde{n} = 0,1,...,N-1$) is expressed by

$$h[\tilde{k},\tilde{n}] \triangleq \sum_{l=0}^{L-1} A_l \exp(-j2\pi\tilde{k}F_{\tau_l}) \exp(j2\pi\tilde{n}F_{\nu_l}), \tag{5.7}$$

$A_l \triangleq a_l \exp(j2\pi\nu_l(\tau_l + \tau_{L-1}))$, $F_{\tau_l} \triangleq (\tau_l - \tau_{L-1})/T_\mathrm{s}$ and $F_{\nu_l} \triangleq \nu_l T_\mathrm{s}$ represent the complex gain, the *normalized delay* and *normalized Doppler shift* associated with the lth channel path, respectively, and (see (5.6))

$$\mathbf{T}(\mathbf{C}) = \mathbf{\Xi}_M(\mathbf{C} \odot \bar{\mathbf{G}})\,\mathbf{\Xi}_N^H \tag{5.8}$$

is an $M \times N$ matrix accounting for the channel symbols through $\mathbf{C}$ and the impact of $p(t)$ through[4] $\bar{\mathbf{G}} \triangleq [\bar{g}_{p,q}]$. The matrix $\mathbf{r}(\mathbf{C})$ (5.6) undergoes an order (M,N) DSFT; this produces the DD domain $M \times N$ complex matrix

$$\mathbf{Y}(\mathbf{C}) \triangleq [Y[m,n]] = \mathrm{DSFT}_{M,N}[\mathbf{r}(\mathbf{C})] \triangleq \mathbf{\Xi}_M^H \mathbf{r}(\mathbf{C}) \mathbf{\Xi}_N, \tag{5.9}$$

whose element (m,n) can be expressed as

$$Y[m,n] = \frac{1}{MN} \sum_{p=0}^{M-1} \sum_{q=0}^{N-1} c_{p,q}\, \bar{g}_{p,q} \sum_{l=0}^{L-1} A_l \Psi_M(m-p,-F_{\tau_l}) \Psi_N(n-q,F_{\nu_l}), \tag{5.10}$$

where

$$\Psi_V(v,F) \triangleq \frac{\exp(j2\pi(v+FV)) - 1}{\exp(j2\pi(v/V+F)) - 1} \tag{5.11}$$

for any integer v and normalized frequency $F \in [0,1]$. To understand the properties of $\Psi_V(v,F)$ (5.11) and its impact on the signal (5.10), it is useful to express the variable F, appearing in (5.11) as $F = \bar{F}/V + F_r$, where $\bar{F}$ is an integer parameter (called *integer part*) and F_r is a real parameter, called *fractional part* and whose value belongs to the interval $[-0.5/V, 0.5/V]$. In general, $\Psi_V(v,F)$ exhibits a peak at $v = \bar{F}$, and, when $F_r = 0$, it turns into a Kronecker delta. Otherwise, it displays tails that decay gradually, becoming more prominent as $|F_r|$ approaches $0.5/V$.

[4]The expression of $\bar{g}_{p,q}$ is given in (4.81).

Finally, based on the RX signal models (5.6) and (5.9) and on the previous comments about $\Psi_V(v, F)$ (5.11), the following conclusions can be inferred:

1) If the CSI matrix $\mathbf{h}$ (or an estimate of it) is available, channel equalization can be easily accomplished by compensating for the channel gains appearing in the TF domain matrix $\mathbf{r}(\mathbf{C})$ (5.6). This allows recovering the matrix $\mathbf{T}(\mathbf{C})$ (5.8), from which the OTFS symbol $\mathbf{C}$ can be estimated through an order (M, N) DSFT, followed by element-by-element detection.

2) Two-dimensional *cyclic shifts* of all the symbols $\{c_{p,q}\}$ may appear in the DD domain signal (5.9), because of the properties of $\Psi_V(v, F)$. This occurs when the integer part of one or more of the *normalized delays* $\{F_{\tau_l}\}$ and/or the *normalized Doppler shifts* $\{F_{\nu_l}\}$ is different from zero.

3) The DD domain signal (5.9) is affected by *leakage* (i.e., by a form of ISI) if the *fractional* part of the *normalized delays* $\{F_{\tau_l}\}$ and/or the *normalized Doppler shifts* $\{F_{\nu_l}\}$ is different from zero.

5.3 Pilot-aided channel estimation & equalization method

In this section, we focus on pilot-aided channel estimation and equalization algorithms that can be employed in the communication system illustrated in Fig. 5.1. The algorithm we propose relies on the availability of multiple (say, N_{pil}) pilot channel symbols in each received OTFS symbol. The pilot symbol arrangement is based on the following criteria:

1) The vth pilot symbol, denoted x_v (with $v = 0, 1, ..., N_{\text{pil}} - 1$), is surrounded[5] by a *rectangular guard region*, containing multiple null symbols; in practice, we have that $c_{p,q} = 0$ for any $(p, q) \in \Gamma_{\text{g}}^{(v)} \setminus \{(p_v, q_v)\}$, with

$$\Gamma_{\text{g}}^{(v)} \triangleq \{(R_M[p_v + k], R_N[q_v + l]);\ |k| \leq p_\tau, |l| \leq 2q_\nu\}; \tag{5.12}$$

here, the couple (p_v, q_v) denotes the coordinates of x_v within the OTFS symbol matrix[6] $\mathbf{C}$, and p_τ and q_ν are integer parameters defining the vertical and horizontal width, respectively, of the rectangular guard.

Note that p_τ and q_ν cannot be arbitrarily small, since their values should be selected on the basis of the maximum delay $\tau_{\max}$ and the maximum Doppler shift $\nu_{\max}$, respectively, envisaged for the communication channel[7]. More specifically, we should select

$$p_\tau = \lceil \tau_{\max}/\tau_{\text{res}} \rceil \tag{5.13}$$

and

$$q_\nu = \lceil \nu_{\max}/\nu_{\text{res}} \rceil, \tag{5.14}$$

[5] In the considered communication system, the pilot configuration is assumed to be time invariant, meaning it does not change over consecutive OTFS symbols.

[6] Note that (p_v, q_v) belong to the unsuppressed region of $\mathbf{C}$ for any v.

[7] Do not forget that the presence of a delay and a Doppler shift results in a 2D cyclic shift of all the elements of the each OTFS symbol. In the following, we assume that $\tau_{\max}$ and $\nu_{\max}$ do not exceed $T_{\text{s}}/2$ and $\Delta_f/2$, respectively, in order to avoid any ambiguity in the interpretation of the detected OTFS symbols.

where $\tau_{\text{res}} \triangleq T_{\text{s}}/M$ and $\nu_{\text{res}} \triangleq \Delta_f/N$ represent the *delay resolution* and *Doppler frequency resolution*, respectively. If these choices are made, we can extract, from the DD domain matrix $\mathbf{Y}(\mathbf{C})$ (5.9), N_{pil} distinct $P \times Q$ submatrices, each containing a single channel pilot symbol; here,

$$P \triangleq p_\tau + 1 \tag{5.15}$$

and

$$Q \triangleq 2q_\nu + 1. \tag{5.16}$$

are selected in a way that no information symbol has stepped inside each submatrix because of path delays and/or Doppler shifts (further details are provided below), so that the submatrix content depends on a single pilot symbol only.

It is easy to understand that the elements of $\mathbf{C}$ that are not occupied by the N_{pil} pilots or their guards, or that have not been zeroed for SC (see Section 4.2.3.4), can be exploited to convey information symbols.

2) In general, the transmission rate loss due to the considered pilot arrangement scheme can be quantified by evaluating the parameter

$$\Lambda_{\text{loss}} \triangleq \frac{1}{MN} \sum_{v=0}^{N_{\text{pil}}-1} \#\Big(\Gamma_{\text{pil}}^{(v)}(\alpha)\Big); \tag{5.17}$$

here, $\#(\Gamma)$ denotes the cardinality of the set Γ and

$$\Gamma_{\text{pil}}^{(v)}(\alpha) \triangleq \Gamma_{\text{g}}^{(v)} \setminus \Gamma_{\text{g}}^{(v)} \cap \Gamma_{\text{sc}}(\alpha) \tag{5.18}$$

represents a measure of the overhead due to the vth pilot.

3) The proposed pilot arrangement can be easily employed in MIMO OTFS-based JCAS systems, due to the use of disjoint guardbands (e.g., see [102]).

4) The N_{pil} guard regions overlap as much as possible with the portions of $\mathbf{C}$ zeroed because of SC. This choice aims to minimize the impact of the guard region on the transmission rate.

These concepts are exemplified by Fig. 5.2, which refers to an OTFS symbol characterized by $M = 16$ and $N = 32$. In this context, $N_{\text{pil}} = 2$ pilot symbols are considered; even if their associated guardbands are both characterized by $p_\tau = 4$ and $q_\nu = 1$, the pilot positioning has a significant impact on the transmission rate loss (5.17). In fact, as it can be inferred from Fig. 5.2, the guardband of x_0 partially overlaps with the 16×7 null submatrix representing the contribution of the suppressed carriers, but this does not happen for the guardband of x_1. The overheads associated with x_0 and x_1 are $\#(\Gamma_{\text{pil}}^{(0)}(\alpha)) = 27$ and $\#(\Gamma_{\text{pil}}^{(1)}(\alpha)) = 45$ (see (5.18)), respectively; here a roll-off factor $\alpha = 0.25$ has been considered. Therefore, arranging the pilots as done for x_0 reduces the pilot overhead and consequently, the overall transmission rate loss.

Let us focus now on the problem of estimating the *inner structure* of the communication channel. This requires estimating the L triplets $\{(A_l, F_{\tau_l}, F_{\nu_l}); l = 0, 1, ..., L-1\}$ and

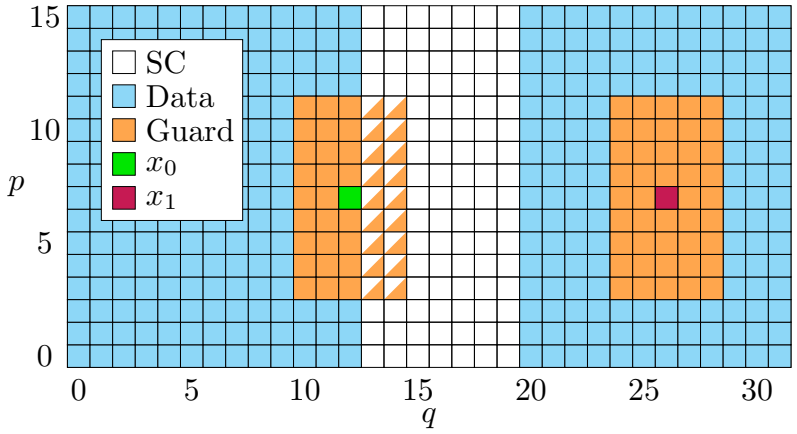

FIGURE 5.2: Representation of the guard regions associated with a couple of pilot symbols. Such symbols are conveyed by an OTFS symbol $\mathbf{C}$ characterized by $M = 16$ and $N = 32$. The guard region of x_0 partially overlap with the portion of $\mathbf{C}$ conveying null symbols because of *subcarrier suppression* (SC). For this reason, the pilot overhead required by the guardband of x_1 is larger than that required by that of x_0.

the parameter L; in fact, these provide a full description of the communication channel, described by the $M \times N$ matrix $\mathbf{h} \triangleq [h[\tilde{k}, \tilde{n}]]$ (see (4.125)).

First of all, let us assume, for simplicity, that the matrix $\mathbf{C}$ conveys a *single pilot channel symbol* (denoted x_0 and having coordinates $(p_0, q_0) \in \Gamma_\varepsilon(\alpha)$) and that all the remaining elements of it form the guardband of that symbol (this scenario is denoted Full Guard (FG), in the following). Under this assumption, based on (4.122), the element $(\tilde{k}, \tilde{n})$ of the channel matrix $\mathbf{h}$ can be approximately expressed as[8] (see (4.123) and (4.124))

$$h[\tilde{k}, \tilde{n}] \cong \hat{h}[\tilde{k}, \tilde{n}] \triangleq \frac{\sqrt{MN}}{x_0} \exp\Big(j2\pi\big(\frac{p_0}{M}\tilde{k} - \frac{q_0}{N}\tilde{n}\big)\Big) r[\tilde{k}, \tilde{n}]. \tag{5.19}$$

From the last equation it is easily inferred that an estimate $\hat{h}[\tilde{k}, \tilde{n}]$ of the element $(\tilde{k}, \tilde{n})$ of $\mathbf{h}$ can be easily evaluated on the basis of the received signal $r[\tilde{k}, \tilde{n}]$, for any $\tilde{k}$ and $\tilde{n}$ (see (4.124)). Note that:

1) The set of complex gains $\{\hat{h}[\tilde{k}, \tilde{n}]\}$ does not directly provide full knowledge of the communication channel, since the inner structure of the channel, in terms of the number of paths, delays, and Doppler shifts, cannot be immediately inferred from that set. For this reason, in the following, this set is considered as a form of partial CSI[9].

2) Thanks to (4.125), the 2D sequence $\{\hat{h}[\tilde{k}, \tilde{n}]\}$ can be seen as the noisy superposition of 2D complex exponentials whose parameters (namely, complex amplitude and normalized frequencies) completely describe the inner structure of the communication channel. For this reason, the set of those parameters, that represent a form of *full* CSI, can be estimated by applying the 2D sequence $\{\hat{h}[\tilde{k}, \tilde{n}]\}$ to an algorithm for Multidimensional Harmonic Retrieval (MHR).

[8] The term $\bar{g}_{p_v, q_v}$ (for $v = 0$) is absent from the RHS of (5.19), as its value is assumed to be unitary for any pair of indices $(p, q) \in \Gamma_\varepsilon(\alpha)$ (4.119). This assumption extends to all v thereafter.

[9] Another form of partial CSI is represented by the DSFT of $\{\hat{h}[\tilde{k}, \tilde{n}]\}$, i.e., its DD domain representation.

3) The FG option described above should only be considered in two distinct scenarios. In the first scenario, a single OTFS (pilot) symbol is transmitted solely for sensing purposes. In the second scenario, the OTFS pilot symbol is included in a frame and is followed by multiple OTFS symbols carrying data. In this case, the channel estimates obtained from the pilot symbol are either directly utilized for channel equalization if channel variations are deemed negligible over the whole frame, or they serve as initial values for decision-directed channel tracking if the latter assumption does not hold.

Algorithm 5: The MTEE algorithm.

Input: a) the noisy matrices $\mathbf{r}(\mathbf{C})$ (5.6) and $\mathbf{Y}(\mathbf{C})$ (5.9); b) the set of pilot symbols $\{x_v; v = 0, 1, ..., N_{\text{pil}} - 1\}$; c) an estimate $\hat{\sigma}^2$ of the noise variance σ^2.

1 **Extraction of pilot submatrices:** Extract the set $\{\mathbf{Y}^{(v)}; v = 0, 1, ...N_{\text{pil}} - 1\}$ from $\mathbf{Y}(\mathbf{C})$ (5.9) (see (5.25)).

2 **Channel estimation:**

a- Evaluation of the reduced dimension TF model: Compute the matrix

$$\hat{\mathbf{h}}_{\text{w}} = \text{IDSFT}_{P,Q}[\hat{\mathbf{H}}_{\text{w}}], \tag{5.20}$$

where

$$\hat{\mathbf{H}}_{\text{w}} \triangleq \frac{1}{N_{\text{pil}}} \sum_{v=0}^{N_{\text{pil}}-1} \mathbf{Y}^{(v)}/x_v. \tag{5.21}$$

b- Channel parameter estimation: Run the CSFDEC algorithm, fed by the matrix $\hat{\mathbf{h}}_{\text{w}}$, to generate the estimates $\{(\hat{A}_l, \hat{F}_{\tau_l}, \hat{F}_{\nu_l}); l = 0, ..., \hat{L} - 1\}$ and $\hat{L}$ of $\{(A_l, F_{\tau_l}, F_{\nu_l}); l = 0, ..., L - 1\}$ and L, respectively.

c- CSI reconstruction: Compute an estimate $\hat{\mathbf{h}} \triangleq [\hat{h}[\tilde{k}, \tilde{n}]]$ (with $\tilde{k} = 0, 1, ..., M - 1$ and $\tilde{n} = 0, 1, ..., N - 1$) of $\mathbf{h}$ on the basis of (5.7); in doing so, $A_l = \hat{A}_l$, $F_{\tau_l} = \hat{F}_{\tau_l}$, $F_{\nu_l} = \hat{F}_{\nu_l}$ and $L = \hat{L}$ are assumed.

3 **Equalization:**

d- Evaluation of the MMSE equalizer gains: Compute the $M \times N$ matrix $\mathbf{G}_{\text{mmse}} \triangleq [G_{\text{mmse}}[\tilde{k}, \tilde{n}]]$, where

$$G_{\text{mmse}}[\tilde{k}, \tilde{n}] \triangleq \hat{h}^*[\tilde{k}, \tilde{n}](\hat{h}[\tilde{k}, \tilde{n}]\hat{h}^*[\tilde{k}, \tilde{n}] + \hat{\sigma}^2)^{-1}. \tag{5.22}$$

e- Element-wise equalization: Perform equalization in the TF domain by computing

$$\hat{\mathbf{T}} = \mathbf{r}(\mathbf{C}) \odot \mathbf{G}_{\text{mmse}}. \tag{5.23}$$

f- TF to DD domain conversion: Evaluate the equalized symbol matrix in the DD domain as

$$\hat{\mathbf{\Lambda}} \triangleq \text{DSFT}_{M,N}[\hat{\mathbf{T}}]. \tag{5.24}$$

Output: The set $\{(\hat{A}_l, \hat{F}_{\tau_l}, \hat{F}_{\nu_l}); l = 0, ..., \hat{L} - 1\}$, the number of channel paths $\hat{L}$ and the equalized matrix $\hat{\mathbf{\Lambda}}$ (to be employed for channel symbol detection).

Thanks to the presence of N_{pil} pilots, each surrounded by a guard region, N_{pil} non-overlapping $P \times Q$ submatrices, with $P \triangleq p_\tau + 1 \leq M$ and $Q \triangleq 2q_\nu + 1 \leq N$, can be extracted from $\mathbf{Y}(\mathbf{C})$ (5.9) at the RX side. In practice, the vth submatrix $\mathbf{Y}^{(v)}$ (where $v = 0, 1, ..., N_{\text{pil}} - 1$) is obtained by selecting elements from $\mathbf{Y}(\mathbf{C})$ with coordinates (p, q)

in the set

$$\Gamma_{\mathrm{w}}^{(v)} \triangleq \{(R_M[p_v + k], R_N[q_v + l]); 0 \leq k \leq p_\tau, |l| \leq q_\nu\}. \tag{5.25}$$

This choice ensures that, for any v, $\mathbf{Y}^{(v)}$ depends on the vth pilot channel symbol only, if spectral leakage can be neglected. The proposed *channel estimation* algorithm combines the N_{pil} matrices of the set $\{\mathbf{Y}^{(v)}; v = 0, 1, ..., N_{\mathrm{pil}} - 1\}$ in a single $P \times Q$ matrix, denoted $\hat{\mathbf{H}}_{\mathrm{w}}$; this matrix undergoes an order (P, Q) IDSFT, whose output is processed by an algorithm for 2D harmonic retrieval.

The last algorithm generates an estimate of all the channel parameters (namely, of the L triplets $\{(A_l, F_{\tau_l}, F_{\nu_l})\}$ and L); given the estimates of such parameters, CSI reconstruction becomes possible (see (5.7)). In this chapter, the CSFDEC algorithm, derived in Chapter 1, has been employed for MHR because of its accuracy and limited complexity.

The proposed *equalization* algorithm, instead, exploits the reconstructed CSI (5.7) to compensate for the channel distortion affecting the TF domain matrix[10] (5.6) employing a Minimum Mean Square Error (MMSE) equalization technique in TF domain.

The overall strategy sketched above (and combining channel estimation and channel equalization) is dubbed *multiple tone estimation* and *equalization* (MTEE), and is represented by Algorithm 5. In analyzing the structure of this algorithm, readers should keep in mind that:

1) Step **2a** aims at improving the accuracy of channel estimation through the constructive combination of the N_{pil} submatrices $\{\mathbf{Y}^{(v)}; v = 0, 1, ..., N_{\mathrm{pil}} - 1\}$, in particular at low SNR values. This step involves an element-wise division procedure, which can be further refined using an MMSE approach, as proposed in [103, Eq. (22)], provided that both the data-induced interference and noise variance are known.

2) The estimates of the channel parameters obtained at step **2b** can be employed for target detection and estimation in JCAS systems.

3) For any l, the normalized frequencies $\hat{F}_{\tau_l}$ and $\hat{F}_{\nu_l}$ provided by step **2b** need to be multiplied by P/M and Q/N, respectively, before being employed in the evaluation of the estimate $\hat{\mathbf{h}}$ of $\mathbf{h}$ in step **2c**.

4) All the elements of the matrix $\hat{\mathbf{\Lambda}}$ (5.24) associated with suppressed channel symbols are discarded, whereas the remaining elements undergo channel symbol detection (see Fig. 5.1).

5.4 Comparison with other channel estimation & equalization techniques

The technique for channel estimation & equalization described in the previous section is conceptually related to: a) the threshold-based approach developed by Raviteja *et al.* [83]

[10] In the proposed simulations, all the elements of $\mathbf{r}(\mathbf{C})$ (5.6) are affected by AWGN; the variance of noise samples is denoted σ^2.

and denoted Alg-R in the following; b) the frequency estimation algorithm proposed by *Wu et al.* [91] and denoted Alg-W in the following. In fact, both these algorithms rely on the transmission of pilot symbols to extract partial or full CSI. Despite their similarities, they exhibit various differences concerning the six specific issues listed below.

1) *Assumptions on delays and Doppler shifts* - Alg-R has been developed under the restrictive assumption that the fractional part of all the normalized delays $\{F_{\tau_l}\}$ is equal to zero. This assumption does not hold; instead, for the derivation of the MTEE algorithm and Alg-W. Keep in mind that the presence of a fractional part in the normalized delays makes the problems of channel estimation and data detection significantly more challenging.

2) *Pilot symbol arrangement* - In Alg-R and Alg-W, a single pilot symbol is employed for channel estimation (e.g. see [83, Figs. 1-2]); moreover, its position does not take into account the impact of pulse shaping (see Section 4.2.3.4). The MTEE algorithm, instead, can benefit from the use of multiple pilot symbols, whose position is carefully selected on the basis of the adopted pulse shape and the suppressed channel symbols.

3) *Channel estimation method* - The channel estimation technique adopted in Alg-R exploits a threshold-based approach to extract partial CSI only (represented by the matrix $\hat{\mathbf{H}}_{\mathrm{w}}$ (5.21)); then, this information is exploited in an iterative data detection process. On the other hand, a DFT-based approach initialized through Alg-R is employed by Alg-W. The last algorithm is able, similarly to the MTEE algorithm, to estimate both integer and fractional components of the normalized delays $\{F_{\tau_l}\}$ and the normalized Doppler shifts $\{F_{\nu_l}\}$ (see the frequency estimation algorithm described in [91, Sec. IV-A]).

4) *Use of channel estimates for sensing purposes* - Even if the exploitation of the channel estimates generated by Alg-R for sensing purposes has not been investigated in [83], the threshold-based approach on which this algorithm is based paves the way for the estimation of the integer parts of normalized delays and Doppler shifts; these can be considered as *coarse* estimates of target parameters. Alg-W, instead, has been proposed for sensing only; for this reason, it does not solve the problems of channel equalization and data detection. On the other hand, the MTEE algorithm can be employed for JCAS in the proposed OTFS-DCP-based communication system.

5) *Channel equalization* - A message passing detection and interference cancellation algorithm to be used jointly with Alg-R has been developed in [87]; it relies on a *sparse model* of the received signal. Sparsity entails a significant reduction in the complexity of iterative detection methods. However, if the RX signal matrix in the TF domain or in the DD one is not sufficiently sparse (because of the presence of fractional components in the channel delays and/or Doppler shifts [88, 98]), iterative detectors become infeasible because of their highly increasing complexity, may produce significant detection errors, and may not even converge. On the other hand, the MTEE algorithm is not based on a sparse signal model (see (4.124)); moreover, it makes use of an MMSE equalizer, fed by the full CSI (represented by the set $\{(\hat{A}_l, \hat{F}_{\tau_l}, \hat{F}_{\nu_l}); l = 0, 1, ..., \hat{L}-1\}$ and the parameter $\hat{L}$; see step **3e** in Algorithm 5). Finally, in the development of Alg-W, the problem of channel equalization has not been taken into consideration.

6) *Computational complexity*: The computational complexity orders of Alg-R, MTEE and Alg-W are listed in Table 5.1, where the partial contributions due to *channel estimation*,

sensing and *equalization* steps are also provided. From the provided formulas, the following conclusions can be easily inferred:

TABLE 5.1: Computational complexity order of Alg-R, MTEE and Alg-W.

Technique	Channel estimation $\mathcal{O}(\cdot)$	Sensing $\mathcal{O}(\cdot)$	Equalization $\mathcal{O}(\cdot)$
Alg-R	PQ	–	MNS
MTEE	$(N_{\text{pil}} + \log_2(PQ))PQ$	$13\big[P_0Q_0\log_2(P_0Q_0) + L^2N_{\text{it}}N_{\text{ref}}I_{\text{p}}I_{\text{q}}\big]$	$MN\log_2(MN)$
Alg-W	$(1 + \log_2(PQ))PQ$	$P_0Q_0\log_2(P_0Q_0) + LN_{\text{it}}8PQ$	–

a) In channel estimation, Alg-R evaluates the matrix $\hat{\mathbf{H}}_{\text{w}}$ (5.21) under the assumption that a single pilot symbol is transmitted (i.e., $N_{\text{pil}} = 1$). On the other hand, both the MTEE algorithm and Alg-W also require the estimation of the matrix $\hat{\mathbf{h}}_{\text{w}}$ (5.20), which is processed by a MHR algorithm for sensing purposes. The only difference between the MTEE algorithm and Alg-W is represented by the fact that the last method uses a single pilot for channel estimation.

b) The computational cost of the sensing step of the MTEE algorithm is given by the sum of different contributions (see (1.65)). The first contribution is the cost of *initialization*; this requires the evaluation of the order (P_0, Q_0) DSFT of $\hat{\mathbf{h}}_{\text{w}}$ (5.20) and its first three derivatives[11]. In general, $P_0 \geq P$ and $Q_0 \geq Q$, since *oversampling* is employed along one or both dimensions in order to improve the sensing accuracy. The second contribution, instead, is given by the cost of *refinements*; the cost of each refinement depends on the overall number of targets L and on the interpolation technique[12] adopted in each refinement step of the CSFDEC algorithm employed for 2D harmonic retrieval in **S2**. Note that the overall refinement step can be run N_{ref} times.

c) The Alg-W cost (see [91, Sec. IV-B]) also results from the sum of the costs of its initialization (requiring the evaluation of a single 2D spectrum) with that of an iterative refinement step based on DFT coefficients.

d) In accomplishing channel equalization, Alg-R exploits the sparsity of the channel model proposed in [83]; the complexity of the proposed iterative equalizer depends on an integer parameter, denoted S and quantifying the sparsity of the channel model[13].

e) The computational cost of the proposed MMSE equalization is $N_{\text{mmse}} = N_{\text{eq}} + N_{\text{dd}}$, where $N_{\text{eq}} = \mathcal{O}(MN)$ and $N_{\text{dd}} = \mathcal{O}(MN\log_2(MN))$ are the costs of computing (5.22), (5.23) and (5.24), respectively. From the last result, it can be inferred that the overall computational cost of the MMSE equalizer is approximately of order $\mathcal{O}(N_{\text{mmse}})$, where

$$N_{\text{mmse}} = MN\log_2(MN). \tag{5.26}$$

It is important to highlight that this last computational cost is much lower than that required by the MMSE or Zero Forcing (ZF) techniques operating in the DD domain and

[11] The overall number of derivatives to be computed is equal to 12; the matrices corresponding to the derivatives of order $(0,3)$, $(3,0)$ and $(3,3)$ of the DSFT of $\hat{\mathbf{h}}_{\text{w}}$ (5.20) are not needed (see Section 1.3.3).

[12] In the following, the interpolation orders employed for the rows and columns of the spectrum and its derivatives are denoted I_p and I_q, respectively Algorithm 1.3.

[13] Note that S is usually greater than L.

adopted in [88, 99]; in fact, these involve matrix inversion (as opposed to element-wise division in (5.23)) and thus require $\mathcal{O}((MN)^3)$ operations (e.g., see [88, Eq. (48)]).

5.5 Numerical Results

Extensive computer simulations have been run to compare the MTEE algorithm, Alg-R and Alg-W from two different perspectives. In fact, on the one hand, we have assessed their ability to accurately estimate the inner structure of the communication channel and, in particular, to estimate the delays and Doppler shifts characterizing its paths. This issue is relevant not only for digital communications, but also for sensing in JCAS systems. On the other hand, we have evaluated the error performance achievable on different doubly selective channels when the considered algorithms are used for channel estimation and the resulting estimates are exploited for channel equalization. Ensuring a fair comparison between the considered algorithms has required adapting Alg-R and Alg-W to the considered scenarios. More specifically, the following choices have been made in the implementation of these last two algorithms:

1) The same pilot symbol configuration as the MTEE algorithm has been adopted; this involves N_{pil} pilot channel symbols. In Section 5.3 we have mentioned that, if the guard-bands surrounding pilot symbols are of proper size, the use of multiple pilots represents a viable way to improve the quality of the full CSI conveyed by the matrix $\hat{\mathbf{H}}_{\text{w}}$ (5.21).

2) A 2D *spline* interpolation technique[14] has been employed in Alg-R to increase the number of rows of the matrix $\hat{\mathbf{H}}_{\text{w}}$ (5.21) and that of its columns from P and Q to P_0 and Q_0, respectively. This improves channel estimation accuracy by enhancing the resolution in both delay and Doppler domains.

3) In Alg-R, the matrix $\hat{\mathbf{H}}_{\text{w}}$ (5.21) has been processed to detect its L most relevant amplitude peaks (that are associated with relevant normalized delays and Doppler shifts); this is conceptually similar to the peak search in a 2D *periodogram* (e.g., see Section 2.3.1.1).

4) In Alg-W, sensing consists of the following two consecutive steps: a) Alg-R is run on the matrix $\hat{\mathbf{H}}_{\text{w}}$ (5.21) to detect its L most relevant peaks, whose indices are collected in the set $\{(\hat{p}_l, \hat{q}_l); l = 0, 1, ..., L-1\}$; b) a serial refinement procedure, based on the matrix $\hat{\mathbf{h}}_{\text{w}}$ (5.20), is accomplished for each peak $(\hat{p}_l, \hat{q}_l)$. This procedure can be repeated up to N_{it} times for each detected peak and closely follows what is described in [91, Algorithm 2], where the input parameters $\tilde{X}_n^{(p)}[l]$, $(\tilde{l}_p, \tilde{n}_p)$ and N_{iter} are replaced by the element (p', q') (with $p' = 0, 1, ..., P-1$ and $q' = 0, 1, ..., Q-1$) of $\hat{\mathbf{h}}_{\text{w}}$, the couple of indices $(\hat{p}_l, \hat{q}_l)$ and the number of iterations to be accomplished in each refinement step (i.e., N_{it}), respectively.

5) The MMSE equalizer described in Section 5.3 (see step **3e** of Algorithm 5) has also been employed by Alg-R and Alg-W.

In the simulations, five different scenarios, denoted **SC1**, **SC2**, **SC3**, **SC4** and **SC5**, have been considered. The **first scenario** is characterized by a single path (corresponding to the presence of a single target in sensing), i.e., by $L = 1$. The path amplitude is set to unity,

[14] In the considered simulations, the MatlabR2023b *spline* 2D interpolation has been used.

whereas both its delay and Doppler frequency are generated randomly to ensure that their fractional parts are usually different from zero (see comments below (5.13) and (5.14)). In sensing, the path delay τ_0 and Doppler shift ν_0 can be easily related to target range R_0 and velocity v_0 as $\tau_0 = 2R_0/c$ and $\nu = 2f_c\, v_0/c$, respectively (here, f_c and c denote the carrier frequency and the speed of light, respectively). In the simulations, R_0 and v_0 are generated in an independent fashion and are uniformly distributed in $[R_{\min}, R_{\max}]$ and $[v_{\min}, v_{\max}]$, respectively, with $R_{\min} = 0$, $R_{\max} = 30$ m, $v_{\min} = -50$ km/h and $v_{\max} = 50$ km/h.

The **second scenario**, instead, is characterized by a couple of paths having unitary amplitude. The range R_0 and the speed v_0 characterizing the first path are generated in the same way as the corresponding parameters defined for **SC1**; however, $R_{\max} = 26$ m, $v_{\min} = -90$ km/h and $v_{\max} = 90$ km/h have been selected. The range R_1 and the velocity v_1 characterizing the second path are evaluated as

$$R_1 = R_0 + (\bar{\rho}_{\rm r} + \rho_{\rm r})R_{\rm bin} \tag{5.27}$$

and

$$v_1 = v_0 + (\bar{\rho}_{\rm v} + \rho_{\rm v})v_{\rm bin}, \tag{5.28}$$

respectively; here, we have that: 1) $R_{\rm bin} = {\rm c}/(2M\Delta_f)$ and $v_{\rm bin} = {\rm c}/(2NT_{\rm s}f_{\rm c})$ represent the *bin resolutions* for range and velocity, respectively; 2) $\bar{\rho}_{\rm r} = 3$ and $\bar{\rho}_{\rm v} = 3$ denote the normalized range and velocity bin spacing, respectively; 3) $\rho_{\rm r}$, and $\rho_{\rm v}$ are independent random parameters, and each of them is uniformly distributed between 0 and 0.5.

The **third scenario** is characterized by three paths, all having unitary amplitude. In this case, the range R_0 characterizing the first path is generated in the same way as the corresponding parameter defined for **SC1**; however, $R_{\max} = 25$ m has been chosen. On the other hand, the ranges characterizing the other two paths have been generated as

$$R_l = R_0 + l\bar{\rho}_{\rm r}R_{\rm bin}, \tag{5.29}$$

with $l = 1$ and 2; moreover, the parameter $\bar{\rho}_{\rm r}$ is set to 2. The velocities associated with the considered paths have been generated according to Jake's formula (e.g., see [83]), that is as

$$v_l = v_{\max}\cos(\theta_l), \tag{5.30}$$

with $l = 0, 1$ and 2; here, $v_{\max} = 250$ km/h and θ_l is a random parameter uniformly distributed over $[-\pi, \pi]$.

The **fourth scenario** is very similar to **SC2**, the only difference being represented by the fact that $\bar{\rho}_{\rm r} = \bar{\rho}_{\rm v} = 1.4$ in the generation of R_1 and v_1 according to (5.27) and (5.28), respectively.

In the **fifth scenario** the following assumptions regarding the communication channel have been made: 1) the channel *power delay profile* is a truncated exponential with maximum delay $\tau_{\max} = 0.67$ µs; 2) the channel *Doppler spectrum* is the Jake's power spectrum with maximum Doppler shift $\nu_{\max} = 5.56$ kHz. The methodology illustrated in [104] and based on Gaussian Quadrature Rules (GQR) has been applied to derive a simple channel model for the simulations in **SC5**. This has resulted in a channel model characterized by $L = 3$

channel paths, characterized by the delays $\tau_1 = 0.07$ µs, $\tau_2 = 0.31$ µs and $\tau_3 = 0.59$ µs, and whose complex amplitudes are represented as the superposition of three complex exponentials (see [104, Table I]).

The selection of the five scenarios defined above can be motivated as follows. The first scenario allows us to assess the performance of the considered algorithms in the absence of interference between different paths; in fact, in this case, the spectral leakage affecting pilot symbols originates from data symbols only. In the second scenario, the contributions due to the couple of paths are adequately spaced in the DD domain (since the spacing corresponds to 3 resolution bins for both range and velocity), but leakage has a random impact because of the presence of the terms ρ_{r} and ρ_{v} in (5.27) and (5.28), respectively; this makes the task of channel estimation harder. In the third scenario, the overall number of paths is larger than that of the other two, and Doppler shifts are randomly distributed according to the widely adopted Jake's spectrum (e.g., see [81, Example 2.2.8]). This scenario allows us to assess how the considered algorithms perform when we use: a) a couple of pilots; b) a single pilot surrounded by a guard wide enough to accommodate a Doppler shift corresponding to twice its maximum value (with the aim of leakage mitigation). The fourth scenario allows us to assess the performance of the considered algorithms when the contributions of the two paths are closely spaced in the DD domain (since the spacing corresponds to 1.4 resolution bins for both range and velocity). Finally, the fifth scenario takes into account a distinct delay profile compared to the first four scenarios, with each path distinguished by varying amplitudes.

In the computer simulations, the following parameters have been selected for the OTFS modulation: 1) $M = 512$ and $N = 512$ for the data matrix $\mathbf{C}$; 2) frequency spacing $\Delta_f = 250$ kHz; 3) TD cyclic prefix size $N_{cp}^{(\mathrm{TD})} = N/32$; 4) FD cyclic prefix and postfix sizes[15] $N_{cp}^{(\mathrm{FD})} = N_{cpo}^{(\mathrm{FD})} = M/32$; 5) carrier frequency $f_{\mathrm{c}} = 24$ GHz; 6) roll-off factor and truncation length for the RRC pulse $\alpha = 0.25$ and $L_p = 19$, respectively; 7) gain tolerance adopted in the evaluation of the overall number of SCs $\varepsilon = 0.05$; 8) cardinality of the PSK modulation $M_{\mathrm{c}} = 4$ (Gray coding is used in symbol mapping). The choice of these parameters entails that: 1) $T_{\mathrm{s}} = 1/\Delta_f = 4$ µs; 2) the bin sizes along range and velocity are $R_{\mathrm{bin}} = 1.17$ m and $v_{\mathrm{bin}} = 3.05$ m/s, respectively; 3) the percentage of overhead due to the insertion of the DCP is 8.73% (see (4.61)). The only changes in the parameters listed above have been made for the evaluation of the PSD (4.126). In fact, in this case, to ease the interpretation of numerical results, the following parameters, different from those listed above, have been selected for the OTFS modulation: 1) $M = 32$, 2) $N_{cp}^{(\mathrm{FD})} = N_{cpo}^{(\mathrm{FD})} = M/8$. The resulting PSD (4.126), normalized with respect to

$$\frac{1}{NT_{\mathrm{s}}} \frac{\sigma_c^2}{N + N_{cp}^{(\mathrm{TD})}}, \tag{5.31}$$

is represented in Fig. 5.3 and in Fig. 5.4 for the following cases:

1) untruncated $p(t)$ (blue curves in both figures);

2) untruncated $p(t)$, and absence of the FD CP and CPO (red curve in Fig. 5.3);

[15] This choice entails a small loss in terms of spectral efficiency with respect to the case FD CP and CPO are not used.

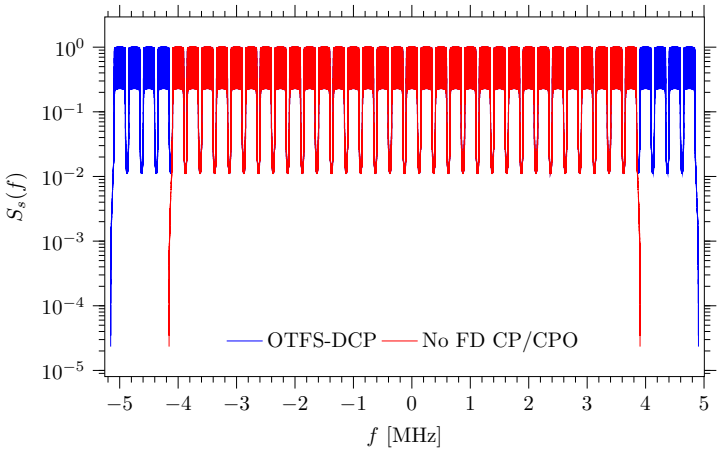

FIGURE 5.3: Normalized PSD of an OTFS signal employing an (untruncated) pulse $p(t)$ characterized by a RRC spectrum with roll-off factor $\alpha = 0.25$. The presence of a DCP (blue curve) and the absence of FD CP/CPO (red curve) are considered.

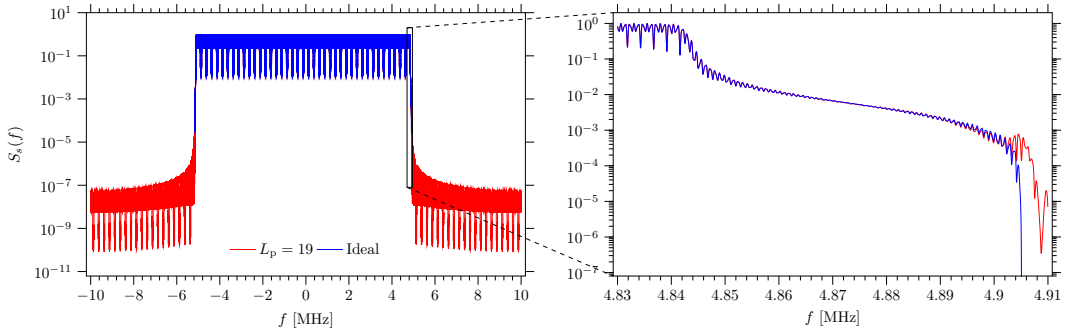

FIGURE 5.4: Normalized PSD of an OTFS signal for a system employing: a) an (untruncated) pulse $p(t)$ characterized by a RRC spectrum with roll-off factor $\alpha = 0.25$ (blue curve); b) a truncated version of it (characterized by the truncation length $L_p = 19$; red curve). The right figure displays the same curves for the frequency range $f \in [4.83, 4.91]$ MHz.

3) truncated pulse $p(t)$ with truncation length $L_p = 19$ (red curve in Fig. 5.4).

These results have allowed us to assess the impact of the FD CP & CPO on the spectral efficiency (see Fig. 5.3) and the effect of pulse truncation on out-of-band emissions (see Fig. 5.4).

These results show that: 1) the signal bandwidth $B_{\rm s}$ (see (4.129)) is approximately equal to 10 MHz and 8 MHz, in the presence of a DCP and in the absence of FD CP/CPO, respectively (see Fig. 5.3); 2) pulse truncation results in spectral widening and in the generation of new side lobes, but it does not have a significant impact on the overall shape of the PSD (see Fig. 5.4). As far as the last point is concerned, we have also found out that, for the given truncation length and roll-off factor, over 99% of the radiated power remains within the bandwidth $B_{\rm s}$.

As far as the transmission of pilot symbols is concerned, the use of a variable number of pilot symbols (in particular, $N_{\text{pil}} \in \{1, 2, 3, 4\}$) has been considered in the first two scenarios. In all cases, the guard $\Gamma_{\text{g}}^{(v)}$ of each pilot is generated according to (5.12). Moreover, the guard parameters $p_\tau = 26$ and $q_\nu = 5$ have been adopted in **SC1** (so that $P = 27$ and $Q = 11$), and $p_\tau = 26$ and $q_\nu = 12$ in **SC2** (so that $P = 27$ and $Q = 25$). Note that the values of p_τ and q_ν have been selected according to (5.13) and (5.14), respectively. In **SC3**, instead, the guard size is the same as **SC2** when two pilots are employed; however, $q_\nu = 24$ has been chosen in the case of a single pilot, in order to double the guard size along Doppler direction. Differently from **SC2**, in **SC4** a single pilot channel symbol has been used, but three different guardband sizes have been considered. In particular, the first guardband configuration, denoted GB_1 is identical to that of **SC2** (therefore, the guard parameters are $p_{\tau_1} = 26$ and $q_{\nu_1} = 12$). In the second guardband configuration, dubbed GB_2, $p_{\tau_2} = 1.5p_{\tau_1}$ and $q_{\nu_2} = 1.5q_{\nu_1}$, whereas in the third guardband configuration, dubbed GB_3, $p_{\tau_3} = 3p_{\tau_1}$ and $q_{\nu_3} = 3q_{\nu_1}$.

The computer simulations have aimed at assessing: a) the Bit Error Rate (BER) achieved by the OTFS-based communication represented in Fig. 5.1 when each of the considered algorithms is used at its RX side; b) the RMSE achieved in range (RMSE_{R}) and velocity (RMSE_{v}) estimation by each of the considered algorithms. Note that the first performance index is meaningful in data communications only, whereas the last two are also relevant for sensing applications. In generating the proposed numerical results referring to the three performance indices mentioned above, the following choices have been made for all the compared algorithms:

1) The oversampling factors $N_{\text{p}} = N_{\text{q}} = 16$ have been adopted for all the algorithms. This implies that, for the first three scenarios, $P_0 = N_{\text{p}}P = 432$, whereas $Q_0 = N_{\text{q}}Q = 176$ and 400 in **SC1** and **SC2**/**SC3**, respectively. As far as **SC4** is concerned, the couple of parameters (P_0, Q_0) is equal to $(432, 400)$, $(648, 600)$ and $(1296, 1200)$ for GB_1, GB_2 and GB_3, respectively.

2) The overall number of paths (L) has been assumed to be known at the RX side.

3) In the MTEE algorithm, $N_{\text{it}} = 5$ refinement steps have been accomplished for the computation of the normalized delay and Doppler residuals, the interpolation orders $I_{\text{p}} = I_{\text{q}} = 7$ have been selected, and $N_{\text{ref}} = 2$ re-estimations have been executed.

4) In Alg-W, $N_{\text{it}} = 5$ refinement steps have been executed.

5) The noise variance σ^2 has been assumed to be known in all the considered scenarios; consequently, $\hat{\sigma}^2 = \sigma^2$ has been adopted in evaluating the gain $G_{\text{mmse}}[\tilde{k}, \tilde{n}]$ (5.22), employed during the equalization step of each algorithm.

The numerical results are illustrated in the following figures. In analyzing them, readers should keep in mind that:

1) Simulation results are represented by labels, whereas solid and dashed lines are drawn to ease reading.

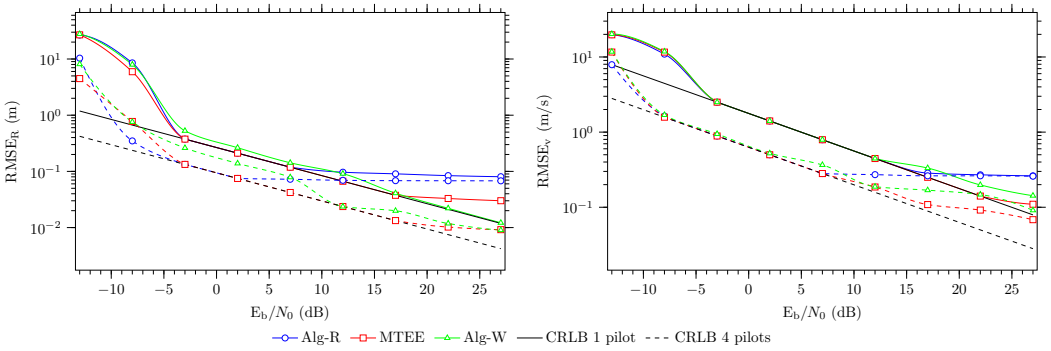

FIGURE 5.5: Root mean square error performance achieved by Alg-R, the MTEE algorithm and Alg-W in range (left figure) and velocity estimation (right figure) in the first scenario. The CRLB is also shown.

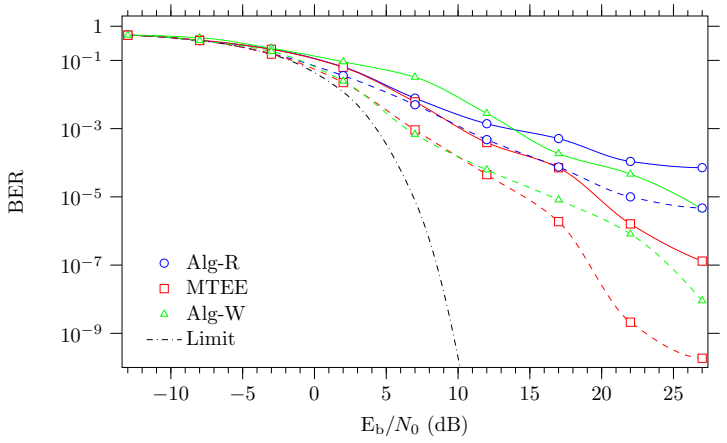

FIGURE 5.6: Bit error rate performance achieved by Alg-R, the MTEE algorithm and Alg-W in the first scenario.

2) In all the figures referring to **SC1** and **SC2**, solid lines refer to the transmission of a single pilot for channel estimation, whereas dashed lines refer to the transmission of 4 pilots in the same OTFS symbol.

3) In the evaluation of the SNR per information bit (E_b/N_0), we have taken into account the energy loss originating from the presence of one or more pilot symbols, but not that due to the use of the DCP for simplicity (this results in an E_b/N_0 loss equal to 0.085 dB).

Some numerical results referring to **SC1** are illustrated in Fig. 5.5 and in Fig. 5.6. In particular, the RMSE$_R$ and RMSE$_v$ characterizing all the considered algorithms are shown for an $E_b/N_0 \in [-13, 27]$ dB; the CRLB[16] is also provided as a reference. The BER performance achievable in the same SNR range through the use of each of the considered algorithms is shown in Fig. 5.6. Moreover, in that figure, the BER performance achieved by the coherent demodulation of an uncoded Quadrature Phase-Shift Keying (QPSK) over

[16]The evaluation of this bound is based on the methodology described in Appendix A.2.1.

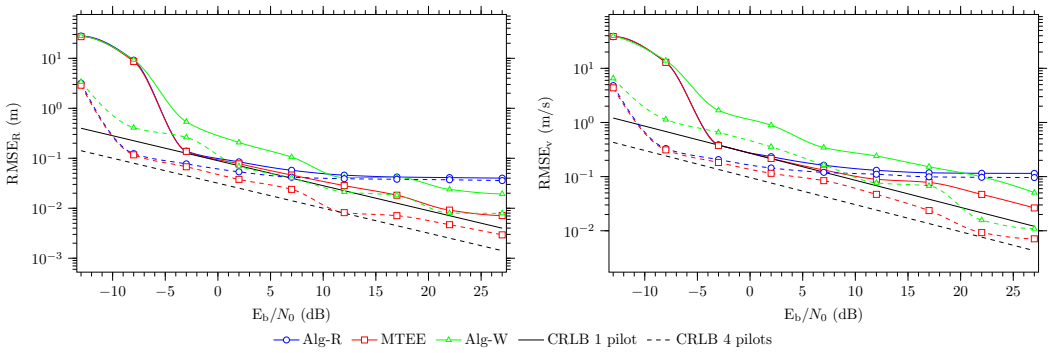

FIGURE 5.7: Root mean square error performance achieved by Alg-R, the MTEE algorithm and Alg-W in range (left figure) and velocity estimation (right figure) in the second scenario. The CRLB is also shown.

an AWGN channel is also shown (see [105, Subsect. 5.2.7, eq. (5.2.59)]), since it provides a lower bound.

The results shown in Fig. 5.5 and in Fig. 5.6 lead to the following conclusions:

1) An E_b/N_0 *threshold* can be easily identified in all the RMSE curves; in all cases, the threshold is lowered by an increase in the number of pilot symbols from one to four.

2) All the techniques exhibit a RMSE *floor* at high values of E_b/N_0. This result can be motivated as follows. On the one hand, Alg-R does not include a refinement step and limits its estimation to peak searching on the matrix $\hat{\mathbf{H}}_w$ (5.21). Conversely, for the other two techniques, their refinement step relies on the input matrix $\hat{\mathbf{h}}_w$ (5.20), which ideally should represent a pure overlap of 2D complex exponentials (this condition is perfectly met in the FG case only).

3) The MTEE algorithm achieves the best estimation accuracy in terms of RMSE$_v$, whereas Alg-W achieves it in terms of RMSE$_R$ at high SNRs. This can be related to the fact that the refinement step of Alg-W converges faster, provided that the 2D tones are adequately spaced.

4) Alg-R and the MTEE algorithm offer the worst and the best BER performance, respectively. Note also that Alg-W is outperformed by Alg-R for an $E_b/N_0 \in [2, 17]$ dB. This can be related to the fact that Alg-R achieves a RMSE$_v$ lower than that of Alg-W in the considered SNR range.

It is also worth mentioning that:

1) The computational complexity for the sensing steps of Alg-W and the MTEE algorithm is 1.1 and 13.1 times higher than that of Alg-R, respectively (see Table 5.1). Even if the MTEE algorithm exhibits a higher complexity (this is due to its initialization cost), it achieves a better complexity-performance trade-off than the other two methods.

2) The percentages of transmission rate loss Λ_{loss} (5.17) due to pilots in **SC1** are 0.44% and 1.76% for 1 and 4 pilots, respectively.

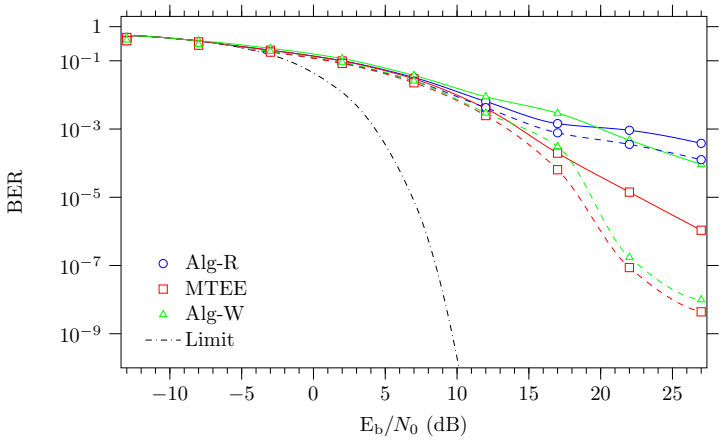

FIGURE 5.8: Bit error rate performance achieved by Alg-R, the MTEE algorithm and Alg-W in the second scenario.

Some numerical results referring to the RMSE and the BER performance achieved in **SC2** are shown in Fig. 5.7 and in Fig. 5.8, respectively. From these results, it can be inferred that:

1) The MTEE algorithm achieves the best accuracy in terms of both range and velocity estimation. This improvement is mainly due to the *serial cancellation* mechanism adopted by the CSFDEC algorithm.

2) Similarly as **SC1**, estimation accuracy improves as the overall number of pilots increases. However, the performance gap between the considered techniques is significantly larger than that observed in **SC1**. This is due to the presence of multiple paths, whose fractional delays and Doppler frequencies generate stronger leakage (i.e., interference) that affects not only pilots but also data symbols.

3) The BER performance of all the algorithms is worse than that observed in **SC1**. Moreover, Alg-R is outperformed by the other two techniques and exhibits a high floor even when four pilots are used.

It is also important to point out that:

1) The computational complexity of the sensing step of Alg-W and the MTEE algorithm is 1.1 and 13.1 times higher than that of Alg-R, respectively (see Table 5.1) as in **SC1**; for this reason, the considerations illustrated for that scenario also apply to **SC2**.

2) The percentages of transmission rate loss Λ_{loss} (5.17) due to pilots in **SC2** are 1% and 4% for 1 and 4 pilots, respectively.

Other numerical results, referring to **SC3**, are illustrated in Fig. 5.9 and in Fig. 5.10. In these figures, solid lines refer to the case in which two pilot symbols are used, whereas dashed lines refer to the use of a single pilot with a guard size doubled along the Doppler direction. The last results evidence that:

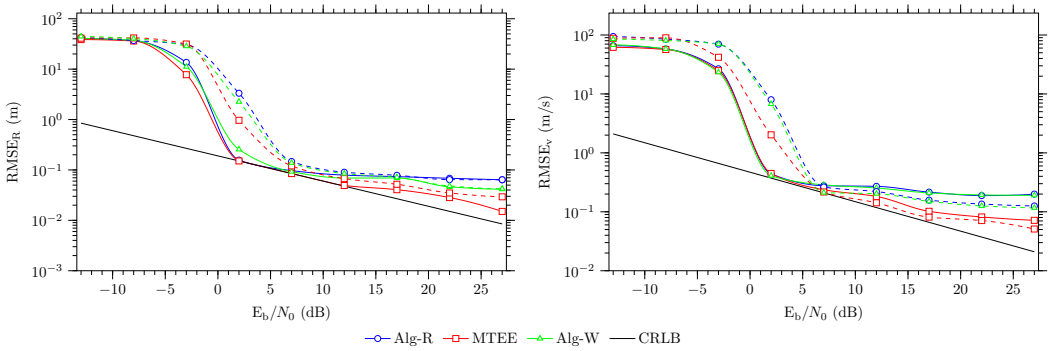

FIGURE 5.9: Root mean square error performance achieved by Alg-R, the MTEE algorithm and Alg-W in range (left figure) and velocity estimation (right figure) in the third scenario.

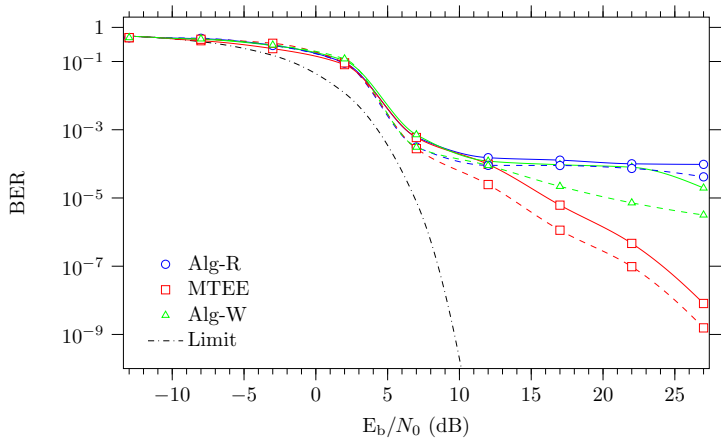

FIGURE 5.10: Bit error rate performance achieved by Alg-R, the MTEE algorithm and Alg-W in the third scenario.

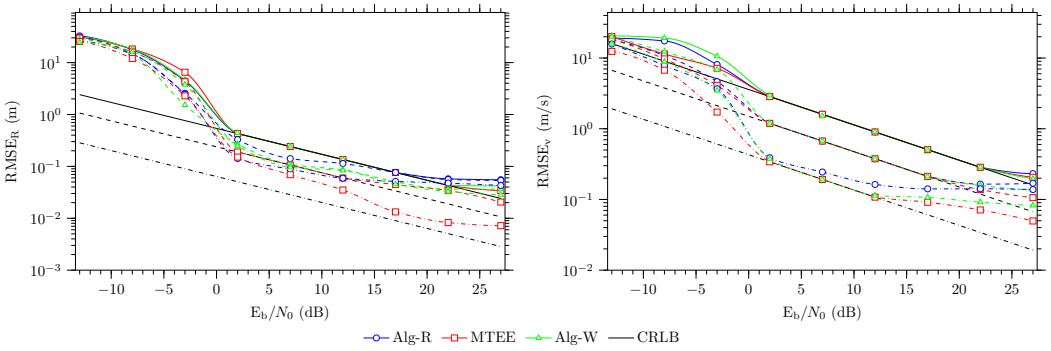

FIGURE 5.11: Root mean square error performance achieved by Alg-R, the MTEE algorithm and Alg-W in range (left figure) and velocity estimation (right figure) in the fourth scenario. Solid, dashed and dash-dotted lines refer to GB_1, GB_2 and GB_3 guardband configurations, respectively. The CRLBs are also shown.

1) All the algorithms exhibit similar thresholds in their RMSE performance. If one or two pilots are used, the E_b/N_0 threshold is approximately 3 dB and 7 dB, respectively.

2) A high floor is visible in the $RMSE_R$ and $RMSE_v$ curves referring to Alg-R.

3) Alg-W performs better than Alg-R in terms of $RMSE_R$, whereas its performance in terms of $RMSE_v$ is comparable to that achieved by Alg-R.

4) The MTEE algorithm performs substantially better than all the other algorithms for high SNRs (more precisely, for $E_b/N_0 \geq 12$ dB).

5) Increasing the guard size along the Doppler dimension improves the estimation accuracy in terms of $RMSE_v$. On the contrary, the use of two pilots with a smaller guard size along the Doppler dimension improves $RMSE_R$.

6) The BER performance achieved in the case of a single pilot with a double guard size is better than that obtained with a couple of pilots. This is mainly due to the fact that **SC3** is characterized by a significant Doppler spread. On the other hand, the delay has a weaker impact, even if it introduces some leakage.

Note that, the percentage of transmission rate loss Λ_{loss} (5.17) is 2% in both the cases considered in **SC3**.

Numerical results referring to **SC4**, are illustrated in Fig. 5.11 and in Fig. 5.12; in these figures, solid, dashed and dash-dotted lines refer to GB_1, GB_2 and GB_3 guardband configurations, respectively. These results evidence that:

1) All the algorithms exhibit similar thresholds in their RMSE performance, regardless of the guardband configuration. The threshold is located at $E_b/N_0 \cong 2$ dB.

2) Despite the RMSE performance improves with increasing guardband sizes, since a higher number of samples becomes available to the harmonic retrieval algorithm, an RMSE floor remains visible at large SNRs for all the considered techniques.

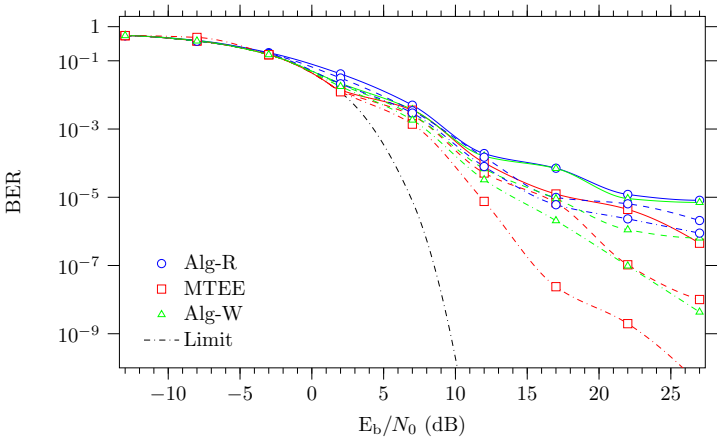

FIGURE 5.12: Bit error rate performance achieved by Alg-R, the MTEE algorithm and Alg-W in the fourth scenario. Solid, dashed and dash-dotted lines refer to GB_1, GB_2 and GB_3 guardband configurations, respectively.

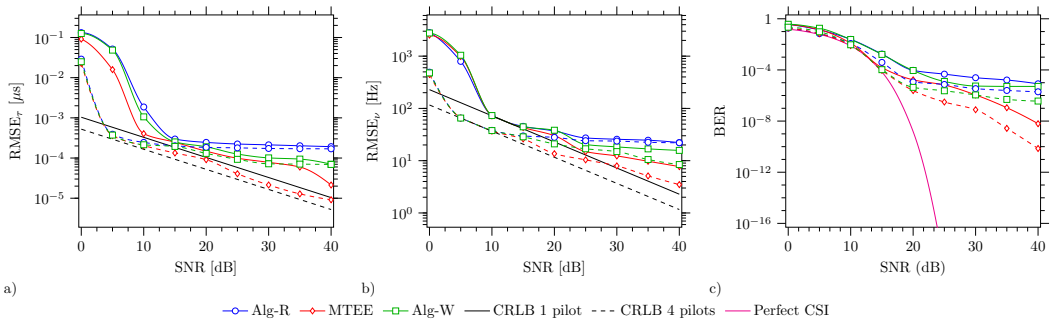

FIGURE 5.13: Root mean square error performance achieved by the MTEE algorithm, Alg-R and Alg-W in a) delay and b) Doppler shift estimation (CRLBs are also shown for comparison). c) Bit error rate performance achieved by the MTEE algorithm, Alg-R and Alg-W (the error performance obtained with perfect CSI is also shown for comparison).

3) Alg-R and MTEE offer the worst and best RMSE & BER performance, respectively, for the same guardband configuration.

4) Better RMSE performance usually results in an improvement in BER performance. However, the price to be paid for this improvement is the adoption of a wider guardband and, consequently, a lower data rate.

The last numerical results, referring to **SC5**, are illustrated in Fig. 5.13-a), -b) and -c), and refer to the cases in which $N_{\text{pil}} = 1$ (solid lines) and $N_{\text{pil}} = 4$ (dashed lines). In particular, some results referring to RMSE_τ and RMSE_ν are shown in Fig. 5.13-a) and in Fig. 5.13-b), respectively; in both figures, the SNR range $[0, 40]$ dB is considered and CRLBs are provided as a reference. Other results referring to the achievable BER performance in the same SNR range are shown, instead, in Fig. 5.13-c); in that figure, the BER obtained when CSI is perfectly known at the RX side (*perfect* CSI case) is also provided as a reference.

From the results shown in Fig. 5.13-a), -b) and -c) the following conclusions can be inferred:

1) A SNR *threshold* can be easily identified in all the RMSE curves; the threshold observed for $N_{\text{pil}} = 4$ is significantly lower than that referring to $N_{\text{pil}} = 1$.

2) All the considered algorithms exhibit a RMSE *floor* at high SNRs. This result can be explained as follows. In Alg-R, the peak search involving the matrix $\hat{\mathbf{H}}_{\text{w}}$ (5.21) is not followed by a refinement step; this limits the estimation accuracy of that algorithm. The MTEE algorithm and Alg-W, instead, execute a refinement procedure that involves the input matrix $\hat{\mathbf{h}}_{\text{w}}$ (see step **2b** of Algorithm 5). This procedure, however, relies on the assumption that the 2D sequence conveyed by the matrix $\hat{\mathbf{h}}_{\text{w}}$ is the overlap of L 2D complex exponentials; unluckily, this condition is perfectly met when the fractional part of all the normalized channel delays and normalized Doppler shifts is equal to zero (this does not occur in the considered simulations).

3) In the SNR range $[22, 35]$ dB, the estimation accuracy provided by the MTEE algorithm in the presence of a single pilot symbol (i.e., $N_{\text{pil}} = 1$) is very close to that offered by Alg-W when four pilot symbols (i.e., $N_{\text{pil}} = 4$) are available.

4) The MTEE algorithm and Alg-R offer the best and worst BER performance, respectively, for a given number of pilots.

5) The computational complexity of step **2b** for Alg-W and the MTEE algorithm is 1.1 and 13.1 times higher, respectively, than that of the same step of Alg-R (see Table 5.1). Despite the computational gap between the MTEE algorithm and the other two algorithms, we can state that the first algorithm achieves a better complexity-performance trade-off than the other two.

Finally, based on all the results illustrated above, we can state that: a) the proposed modulation format (namely, an OTFS modulation incorporating a DCP and employing a pulse shape with RRC spectrum) can be considered a good candidate for future JCAS systems; b) the MTEE algorithm outperforms all the considered technical alternatives over doubly selective fading channels thanks to its ability to accurately estimate fractional delays and Doppler shifts; c) the performance improvement provided by the MTEE algorithm is obtained at the price of a limited complexity increase with respect to other methods.

5.6 Conclusions

In this chapter, a communication system employing the OTFS modulation with a double cyclic prefix has been considered and novel solutions to the problems of pilot-aided channel estimation and equalization have been proposed. First, a pilot arrangement scheme taking into account the impact of pulse shaping and the strategy of using multiple pilots has been described. Then, a novel algorithm for pilot-aided channel estimation to be adopted at the RX side of the communication system (or at its TX side for sensing applications) has been proposed; moreover, it has been shown how the channel estimator output can be exploited for channel equalization. The obtained numerical results have evidenced that the proposed algorithms outperform two technical alternatives at the price of a limited increase in computational complexity. For these reasons, we believe that they represent promising technical solutions for future JCAS systems employing the OTFS modulation.

The next chapter deals with implementing OTFS-DCP modulation on commercial SDRs to conduct experimental measurements about the communication performance of the system in doubly selective channels.

6

On the Use of a Double Cyclic Prefix in Orthogonal Time-Frequency Space Modulation for Communication and Sensing

In this chapter, the problem of implementing, on commercial software defined radios, a digital communication system that employs the OTFS modulation is addressed. In the technical literature, few manuscripts on this issue are available; moreover, they do not take into consideration the use of a cyclic prefix in both the time and frequency domains (i.e., the use of a double cyclic prefix, DCP). In this chapter, we describe the implementation of the OTFS-based communication system developed in Chapter 4 on a couple of software defined radios manufactured by National Instruments. Various technical information about the signal processing algorithms employed at the transmit and receive sides is provided. The obtained experimental results evidence that the implemented communication system is able to reliably operate in the presence of strong Doppler affecting the communication channel.

6.1 Introduction

Future communication systems are expected to support multiple broadband services and perform reliably in heterogeneous propagation conditions. The most challenging communication scenarios are usually characterized by high mobility; in this case, broadband transmissions based on OFDM suffer from severe ICI due to the lack of orthogonality in the presence of fast variations in communication channels. This consideration has motivated the investigation of new modulation formats exhibiting resilience to both multipath and Doppler, and, in particular, has led to the development of the OTFS modulation [79]. This format can be considered as an example of 2D modulation, since it maps data in the DD domain through a 2D transform and, thanks to its inner structure, is able to counteract selectivity in both time and frequency domains. Even if various theoretical results about the OTFS modulation are available in the technical literature, few manuscripts focus on its implementation on programmable radio platforms (i.e., SDR) and analyze its performance in realistic propagation environments. The first implementation has appeared in [106], where two Universal Software Radio Peripheral (USRP) 2943R devices manufactured by National Instruments (NI) have been employed for transmission and reception. Moreover, channel emulation and all the required signal processing algorithms have been implemented in the LABView environment and run on a host Personal Computer (PC). A proof-of-concept static setup has been proposed in [107], where a *single*

Adalm-Pluto [108] SDR operating at 3.5 GHz has been employed; this choice has allowed to circumvent the problem of compensating for a Carrier Frequency Offset (CFO) at the RX side. An implementation based on a pair of X310 SDRs manufactured by ETTUS Research has been described in [109], where the impact of hardware impairments, such as zero frequency (i.e., DC) offset, Timing Offset (TO) and CFO on the received signal is analyzed. Some additional results can be found in [110], in which the same radio setup has been employed. Finally, in [111] and [112], USRP-2953R and USRP-2954 SDRs equipped with Global Positioning System (GPS) synchronization (for minimizing the CFO at the RX side) have been employed; both manuscripts focus on the use of the OTFS modulation for basic JCAS tasks.

It is important to point out that, in all the above-mentioned implementations, a TD CP has always been adopted in the generation of the OTFS modulation. However, the use of an additional CP and a CPO in the FD has never been taken into consideration. We believe that this represents a fundamental issue since, as proved in Section 4.2.3, FD CP & CPO play a similar (dual) role in Doppler mitigation as the TD CP in multipath equalization. This chapter aims at filling this gap by providing some implementation guidelines for the OTFS modulation employing a DCP[1] on SDRs.

This chapter is organized as follows. In Section 6.2 the architecture of an OTFS-DCP based communication system, some essential signal models and relevant signal processing techniques employed at the RX side are described. In Section 6.3 pilot-aided channel estimation and equalization algorithms for OTFS-DCP are proposed. Section 6.4 is devoted to the implementation of the TX and RX chains of the considered system. The performance of the developed algorithms is compared with that provided by two technical alternatives in Section 6.5. Various experimental results acquired in two specific scenarios are analyzed in Section 6.6. Finally, some conclusions are given in Section 6.7.

6.2 System and Signal Models

The overall architecture of the considered communication system is illustrated in Fig. 6.1, where, for simplicity, a detailed representation is provided for the baseband part of the TX and RX sides. In the remaining part of this section, we briefly describe how this system operates and illustrate some essential signal models. Let us focus first on the

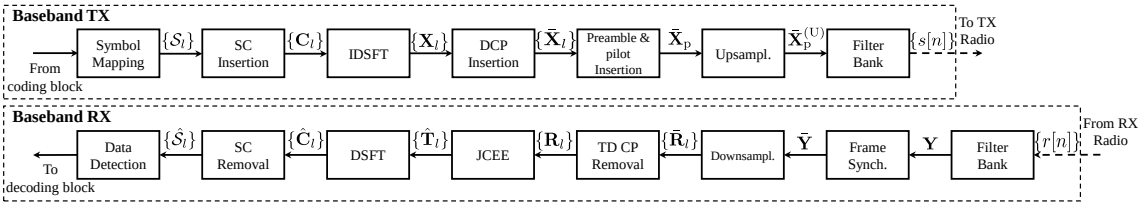

FIGURE 6.1: Block diagram of the considered communication system; all the blocks refer to the baseband processing accomplished at the TX and RX sides (see the upper part and lower part, respectively).

[1]Following the rules for the signal generation described in Section 4.2.3, this modulation format is called OTFS-DCP.

processing accomplished at the TX side. A coded bit stream is mapped into channel symbols, each belonging to an $M_c$ary constellation. Then, such symbols are grouped to generate the sequence $\{\mathbf{C}_l\}$ of OTFS symbols; for any l, the lth OTFS *symbol*, $\mathbf{C}_l \triangleq [c^{(l)}_{m,n}]$ (with $m = 0, 1, ..., M-1$ and $n = 0, 1, ..., N-1$), is an $M \times N$ matrix[2], collecting N_{u} channel symbols and $N_{\mathrm{sc}} \triangleq M(N - N_{\mathrm{u}})$ null symbols identifying the SCs[3]. The matrix $\mathbf{C}_l$ undergoes an order (M, N) IDSFT, generating the $M \times N$ matrix

$$\mathbf{X}_l = [x^{(l)}_{m,n}] \triangleq \mathrm{IDSFT}_{M,N}[\mathbf{C}_l] \triangleq \mathbf{\Xi}_M \, \mathbf{C}_l \, \mathbf{\Xi}_N^H. \tag{6.1}$$

Then, $\mathbf{X}_l$ is cyclically extended along both dimensions, with period N in n (i.e., in the TD) and period M in m (i.e., in the FD); this aims at introducing a TD CP, a FD CP and a FD CPO having sizes $N_{cp}^{(\mathrm{TD})}$, $N_{cp}^{(\mathrm{FD})}$ and $N_{cpo}^{(\mathrm{FD})}$, respectively[4]; note that the new elements of $\mathbf{X}_l$ are generated as $x^{(l)}_{k,i} = x^{(l)}_{R_M[k],R_N[i]}$ for $k \notin \{0, 1, ..., M-1\}$ and $i \notin \{0, 1, ..., N-1\}$. This results in the generation of the $\bar{M} \times \bar{N}$ cyclically extended OTFS symbol $\bar{\mathbf{X}}_l$, with $\bar{M} \triangleq M + N_{cp}^{(\mathrm{FD})} + N_{cpo}^{(\mathrm{FD})}$ and $\bar{N} \triangleq N + N_{cp}^{(\mathrm{TD})}$. The resulting sequence $\{\bar{\mathbf{X}}_l\}$ is cyclically enriched with equally spaced pilot symbols. In particular, every block of $(D-1)$ consecutive elements of $\{\bar{\mathbf{X}}_l\}$ is preceded by an OTFS pilot symbol, which is employed for channel estimation at the RX side; the block and the associated pilot symbol form a transmission *frame*, that consists of D OTFS symbols. Moreover, an $\bar{M}$-dimensional column vector, representing the *frame preamble* and exploited for frame synchronization at the RX side, is concatenated with each pilot symbol. This vector results from: a) evaluating the M order DFT of a Barker sequence of length L_{B}; b) adding a CP and CPO to the DFT output in order to extend it cyclically, so that its size becomes $\bar{M}$. Consequently, concatenating the frame preamble with the OTFS pilot symbol produces a $\bar{M} \times (\bar{N}+1)$ dimensional symbol. The resulting sequence of OTFS symbols is applied to a *filter bank*, which consists of $\bar{M}$ filters running in parallel and generates the complex envelope of the modulated signal. In the following, we concentrate on the transmission and reception of the 0th OTFS symbol (i.e., $\mathbf{C}_0$) for simplicity and drop its subscript to ease reading; its complex envelope can be expressed as (see (4.63))

$$s(t; \mathbf{C}) \triangleq \sum_{k=-(M/2+N_{cp}^{(\mathrm{FD})})}^{M/2+N_{cpo}^{(\mathrm{FD})}-1} s_k^{(\mathrm{TD})}(t; \mathbf{C}), \tag{6.2}$$

with

$$s_k^{(\mathrm{TD})}(t; \mathbf{C}) \triangleq \sum_{l=-N_{cp}^{(\mathrm{TD})}}^{N-1} x_{k,l} \, \phi_k(t - lT_{\mathrm{s}}). \tag{6.3}$$

Here, for any k,

$$\phi_k(t) \triangleq p(t) \exp(j2\pi kt/T_s), \tag{6.4}$$

is the impulse response of the kth filter employed at the TX side, whereas T_{s} and $p(t)$ denote the *symbol interval* and the TX pulse, respectively. In the considered system, following the methodology illustrated in Section 4.2.3.1, $p(t)$ has been selected as the pulse whose

[2]The parameters M and N are supposed to be *even* in the following.

[3]Details about subcarrier suppression are provided in Section 4.2.3.4

[4]Some guidelines for the selection of the TD CP and FD CP & CPO sizes can be found in Section 4.2.3.

the spectrum $P(f)$ is the RRC with *roll-off factor* $\alpha \in [0,1]$ (see (4.16)). Moreover, we have set to zero multiple (i.e., $N_{\rm sc} \triangleq N - N_{\rm u}$, with $N_{\rm u} \triangleq 2N_\alpha + 1$ and $N_\alpha \triangleq \lfloor N(1-\alpha)/2 \rfloor$) columns of the matrix $\mathbf{C}$ to accomplish subcarrier suppression.

It is important to note that the blocks following the DCP insertion, in Fig. 6.1, aim at generating a sampled version of the complex envelope described above.

Let us assume now that the signal $s(t;\mathbf{C})$ (6.2) is sent, after frequency up-conversion, over a doubly selective fading channel, having the baseband CIR

$$h(t,\tau) = \sum_{l'=0}^{L-1} a_{l'} \, \exp(j2\pi\nu_{l'}t) \, \delta(\tau - \tau_{l'}), \tag{6.5}$$

where $a_{l'}$, $\tau_{l'}$ and $\nu_{l'}$ represent the gain, delay[5], and Doppler shift, respectively, of the l'th path (with $l' = 0, 1, ..., L-1$), and L is the overall number of paths. At the RX side, after frequency down-conversion and sampling, the OTFS-DCP signal is processed by a digital filter bank. To simplify the description, we assume that the sampling occurs after a filter bank consisting of M distinct analog *matched filters* (in the proposed implementation, a digital filter bank is employed). According to (4.72), the impulse response of the $\tilde{k}$th matched filter is $\phi^*_{\tilde{k}}(-t) = \phi_{\tilde{k}}(t)$ (see (6.4)), with $\tilde{k} = -M/2, -M/2+1, ..., M/2-1$. Each filter is fed by the complex signal $r(t;\mathbf{C})$ and its output is sampled at the instant $t_{\tilde{n}} = \tau_{L-1} + \tilde{n}T_{\rm s}$, with $\tilde{n} = 0, 1, ..., N-1$; this makes the sample $r[\tilde{k},\tilde{n}]$ available at the output of the $\tilde{k}$th filter. The MN samples acquired through the filter bank for the considered OTFS symbol are collected in the $M \times N$ matrix $\mathbf{R} \triangleq [r[\tilde{k},\tilde{n}]]$. In Section 4.2.3.4, it is proved that, thanks to the property of double periodicity of the transmitted signal and to the specific choice of the pulse $p(t)$, $\mathbf{R}$ can be expressed as

$$\mathbf{R} \triangleq \mathbf{h} \odot \mathbf{T}(\mathbf{C}), \tag{6.6}$$

if channel noise is neglected; here, $\mathbf{h} \triangleq [h[\tilde{k},\tilde{n}]]$ is an $M \times N$ matrix representing the *channel state information* (CSI) and

$$h[\tilde{k},\tilde{n}] \triangleq \sum_{l'=0}^{L-1} A_{l'} \exp(-j2\pi\tilde{k}F_{\tau_{l'}}) \exp(j2\pi\tilde{n}F_{\nu_{l'}}), \tag{6.7}$$

with $\tilde{k} = 0, 1, ..., M-1$ and $\tilde{n} = 0, 1, ..., N-1$. Moreover, $A_{l'} \triangleq a_{l'} \exp(j2\pi\nu_{l'}(\tau_{l'} + \tau_{L-1}))$, $F_{\tau_{l'}} \triangleq (\tau_{l'} - \tau_{L-1})/T_{\rm s}$ and

$$F_{\nu_{l'}} \triangleq \nu_{l'} T_{\rm s} \tag{6.8}$$

represent the complex gain, the *normalized delay* and *normalized Doppler shift* associated with the l'th channel path, respectively, and (see (6.6))

$$\mathbf{T}(\mathbf{C}) \triangleq [T[\tilde{k},\tilde{n}]] = \mathbf{\Xi}_M(\mathbf{C} \odot \bar{\mathbf{G}}) \, \mathbf{\Xi}_N^H \tag{6.9}$$

[5]The CIR components are ordered by increasing delay, with τ_0 and τ_{L-1} being the minimum and maximum delays, respectively.

is an $M \times N$ matrix accounting for the channel symbols through $\mathbf{C}$ and the pulse shape through $\bar{\mathbf{G}} \triangleq [\bar{g}_{p,q}]$. As shown in Eq. (4.122) of Section 4.2.3.4, $\bar{g}_{p,q}$ exhibits a weak dependence on the normalized frequencies $F_{\tau_{l'}}$ and $F_{\nu_{l'}}$. For this reason, the coefficients $\{\bar{g}_{p,q}\}$ corresponding to the MN_{u} unsuppressed channel symbols are characterized by similar amplitudes (and, in particular, by a unitary amplitude for the selected pulse).

6.3 Channel Estimation & Equalization Techniques

Let us focus now on the problem of identifying the inner structure of the communication channel, i.e., estimating the L triplets $\{(A_l, F_{\tau_l}, F_{\nu_l}); l = 0, 1, ..., L-1\}$ and the parameter L; in fact, all these quantities provide a full description of the communication channel $\mathbf{h} \triangleq [h[\tilde{k}, \tilde{n}]]$ (see (6.7)). To achieve this goal, we consider the transmission of a single OTFS *frame* consisting of a single OTFS *pilot symbol* (conveying a *single pilot channel symbol* and $(MN-1)$ null symbols) followed by $(D-1)$ OTFS symbols carrying information symbols only; consequently, the pilot symbol rate is equal to $1/D$. In the following, the OTFS pilot symbol is denoted $\mathbf{C}_0$, whereas the remaining OTFS symbols $\{\mathbf{C}_d = [c^{(d)}_{m,n}]; d = 1, 2, ..., D-1\}$; moreover, the received signal matrix $\mathbf{r}$ associated with the dth OTFS symbol is denoted $\mathbf{r}_d$.

In addition, we assume that:

1) all the elements of the matrix $\mathbf{r}_d$ (6.6) are affected by AWGN with variance σ^2 for any d.

2) The position of the single pilot channel symbol, denoted x_0, is identified by its coordinates (p_0, q_0), which fall in the unsuppressed region of $\mathbf{C}$ (the remaining elements of the OTFS pilot symbol are equal to zero and form the *guardband* of x_0);

3) The channel changes between consecutive OTFS symbols can be deemed negligible.

4) Thanks to the last assumption, CSI can be estimated on the basis of $\mathbf{C}_0$ and, then, be exploited for channel equalization over the other $(D-1)$ OTFS symbol intervals of the same frame.

Under these assumptions, the element $(\tilde{k}, \tilde{n})$ of $\mathbf{T}_0 \triangleq \mathbf{T}(\mathbf{C}_0)$ (6.9) can be expressed as (see (4.123))

$$T_0[\tilde{k}, \tilde{n}] = \frac{x_0}{\sqrt{MN}} \exp\Big(-j2\pi\Big(p_0 \frac{\tilde{k}}{M} - q_0 \frac{\tilde{n}}{N}\Big)\Big). \tag{6.10}$$

From the last equation, it is inferred that an estimate $\hat{\mathbf{h}}_{\mathrm{c}} \triangleq [\hat{h}_{\mathrm{c}}[\tilde{k}, \tilde{n}]]$ of $\mathbf{h}$ can be evaluated on the basis of $\mathbf{r}_0$ as (see (6.6))

$$\hat{\mathbf{h}}_{\mathrm{c}} = \mathbf{K}_0 \odot \mathbf{r}_0, \tag{6.11}$$

where $\mathbf{K}_0 \triangleq [K_0[\tilde{k}, \tilde{n}]]$ is an $M \times N$ matrix with $K_0[\tilde{k}, \tilde{n}] \triangleq 1/T_0[\tilde{k}, \tilde{n}]$ for any $\tilde{k}$ and $\tilde{n}$. Note that, according to (6.7), the matrix $\hat{\mathbf{h}}_{\mathrm{c}}$ (6.11) can be seen as the noisy superposition of L 2D complex exponentials, whose parameters (namely, their complex amplitude and normalized frequencies) fully describe the inner structure communication channel. The procedure we propose for the *channel estimation* consists of the three steps described

below (the ith step is denoted **Si**); such steps are sequentially executed and involve the OTFS pilot symbol only (i.e., $\mathbf{C}_0$).

S1) *Extraction of the full CSI* – In this step, $\hat{\mathbf{h}}_{\rm c}$ is evaluated according to (6.11).

S2) *Channel parameter estimation* – The matrix $\hat{\mathbf{h}}_{\rm c}$ is processed by an algorithm for MHR[6], that produces the estimates $\{(\hat{A}_l, \hat{F}_{\tau_l}, \hat{F}_{\nu_l}); l = 0, 1, ..., \hat{L}-1\}$ and $\hat{L}$ of $\{(A_l, F_{\tau_l}, F_{\nu_l}); l = 0, 1, ..., L-1\}$ and L, respectively.

S3) *Channel reconstruction* – An estimate $\hat{\mathbf{h}} \triangleq [\hat{h}[\tilde{k}, \tilde{n}]]$ of the channel matrix $\mathbf{h}$ is evaluated using (6.7) for $\tilde{k} = 0, 1, ..., M-1$ and $\tilde{n} = 0, 1, ..., N-1$ ($F_{\tau_l} = \hat{F}_{\tau_l}$, $F_{\nu_l} = \hat{F}_{\nu_l}$, $A_l = \hat{A}_l$, and $L = \hat{L}$ are assumed in this case).

The estimate $\hat{\mathbf{h}}$, made available at the end of **S3**, can be employed for *channel equalization* in the following $(D-1)$ OTFS symbols (i.e., $\{\mathbf{C}_d; d = 1, 2, ..., D-1\}$); this task requires sequentially accomplishing the two steps described below (the ith step is denoted **Ei**).

E1) *Evaluation of the equalizer gain* – The MMSE gain $\mathbf{G}_{\rm mmse} \triangleq [G_{\rm mmse}[\tilde{k}, \tilde{n}]]$ is evaluated; here,

$$G_{\rm mmse}[\tilde{k}, \tilde{n}] = \hat{h}^*[\tilde{k}, \tilde{n}] \left(\hat{h}[\tilde{k}, \tilde{n}] \hat{h}^*[\tilde{k}, \tilde{n}] + \hat{\sigma}^2 \right)^{-1}, \tag{6.12}$$

with $\tilde{k} = 0, 1, ..., M-1$ and $\tilde{n} = 0, 1, ..., N-1$, and $\hat{\sigma}^2$ represents an estimate of the noise variance σ^2.

E2) *Channel equalization* – The estimate (see (6.6))

$$\hat{\mathbf{T}}_d = \mathbf{r}_d \odot \mathbf{G}_{\rm mmse}, \tag{6.13}$$

of $\mathbf{T}(\mathbf{C})$ (6.9) is computed for $d = 1, 2, ..., D-1$. The matrix $\hat{\mathbf{T}}_d$ undergoes an order (M, N) DSFT; this produces

$$\hat{\mathbf{\Lambda}}_d = {\rm DSFT}_{M,N}[\hat{\mathbf{T}}_d] \triangleq \mathbf{\Xi}_M^H \hat{\mathbf{T}}_d \mathbf{\Xi}_N, \tag{6.14}$$

with $d = 1, 2, ..., D-1$. Finally, all the elements of the matrix $\hat{\mathbf{\Lambda}}_d$ associated with the suppressed channel symbols are discarded, whereas the remaining elements undergo data detection. This produces the estimate $\hat{c}_{m,n}^{(d)}$ of $c_{m,n}^{(d)}$ for any useful value of (m, n) and for $d = 1, 2, ..., D-1$.

The channel estimation & equalization procedure described above deserves the following comments:

1) The computational costs for both channel estimation and equalization are linear in both M and N. Channel estimation, performed solely for the OTFS pilot symbol, requires $\mathcal{O}(N_{\rm ce})$ flops, where $N_{\rm ce} = N_{\rm S1} + N_{\rm S2} + N_{\rm S3}$; here, $N_{\rm S1} = MN$, $N_{\rm S2}$ and $N_{\rm S3} = MN$ are the costs required to perform steps **S1**, **S2**, and **S3**, respectively. The cost $N_{\rm S2}$ represents the most relevant term and depends on the adopted MHR algorithm; the expression of this term is provided in Table 6.1 for the three MHR algorithms considered in Section 6.5.

[6]Since step **S2** has a significant impact on the effectiveness of the subsequent steps, we have opted for the CSFDEC algorithm described in Chapter 1; in fact, this algorithm has been shown to be accurate and reliable, even in the presence of closely spaced tones.

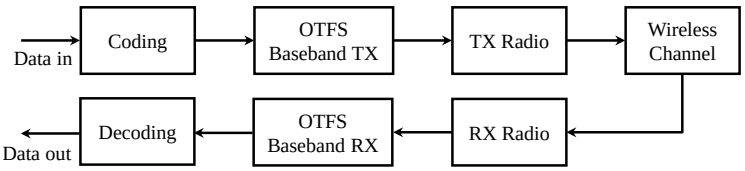

FIGURE 6.2: High level model of the proposed proof-of-concept.

Finally, the computational cost of equalization is approximately of order $\mathcal{O}(MN)$ for each OTFS symbol.

2) The matrix $\hat{\mathbf{h}}_{\mathrm{c}}$ (6.11) computed in **S1** can be used in place of $\hat{\mathbf{h}}$ in the equalization process (see (6.12)). If this choice is made, steps **S2** and **S3** are not executed; this case is referred to as *simplified channel estimation* (SCE) in the following. Note, however, that this choice results in noisier channel estimates and, consequently, in worse equalization performance at low SNR values, as evidenced by the obtained numerical results.

3) The pilot-aided estimates of the parameters (i.e., of the complex amplitude and normalized frequencies) describing the structure of the communication channel computed in **S2** can be employed not only for channel estimation at the RX side, but also for target detection and estimation at the TX side in a wireless system accomplishing JCAS.

The overall method for channel estimation & equalization described above is dubbed *joint channel estimation & equalization* (JCEE) in the following.

6.4 Implementation of a real communication system with USRPs

In this section, we briefly analyze the implementation of the communication system on USRP SDRs, featuring a single transmitter and receiver. A high-level overview is shown in Fig. 6.2. The system operates as follows: at the TX side, a binary data sequence is processed by the *coding* block, that performs scrambling, (optional) channel coding and Gray coding. The resulting encoded binary sequence feeds the baseband part of the transmitter; this generates the OTFS-DCP samples to be sent to the RF portion of the transmitter; this performs frequency up-conversion and radiates the modulated signal. The RX chain consists of a radio receiver, that accomplishes frequency downconversion and sampling, and whose output samples feed the OTFS-DCP baseband RX chain. Finally, the data emerging from this block are decoded; the processing tasks accomplished by this part follow a reverse order with respect to that of the encoding stages. Some relevant technical details about the OTFS baseband TX and RX blocks are provided below; in both cases, we refer to Fig. 6.1.

Transmitter – In the following, a list of tasks accomplished by the baseband part of the transmitter is provided, and various details about each task are illustrated.

Generation of the sequence of OTFS symbols – As described in the previous section, a stream of coded data bits is mapped into symbols from an M_{c}ary constellation. These

symbols are grouped into ordered sets of $MN_{\rm u}$ elements each (the lth set is denoted $\mathcal{S}_l$ in Fig. 6.1). Each set $\mathcal{S}_l$ is then mapped to an $M \times N$ matrix $\mathbf{C}_l$ with $M(N - N_{\rm u})$ null elements added by the SC insertion block.

Frame generation – Each element of the matrix sequence $\{\mathbf{C}_l\}$ undergoes IDSFT processing, followed by DCP insertion. The resulting matrix sequence is partitioned into blocks, each consisting of $(D-1)$ elements; note that each element is a $\bar{M} \times \bar{N}$ matrix. Then, each block is enriched with an OTFS pilot symbol (an $\bar{M} \times \bar{N}$ matrix), which is added at its beginning. Note that each pilot symbol conveys a single non-zero channel symbol known to the receiver and the pilot rate is $1/D$. Finally, the elements of each block are concatenated to generate the $\bar{M} \times (\bar{N}D)$ matrix[7] $\bar{\mathbf{X}}$ and the (fixed) $\bar{M}$-dimensional preamble $\bar{\mathbf{U}}$, exploited at the RX side for frame synchronization, is concatenated with the last matrix to generate the $\bar{M} \times (\bar{N}D+1)$ matrix $\bar{\mathbf{X}}_{\rm p} \triangleq [\bar{\mathbf{U}}, \bar{\mathbf{X}}]$. The generation of the vector $\bar{\mathbf{U}}$ involves the following two steps: 1) the order M DFT of a Barker code sequence of length $L_{\rm B}$ is computed; 2) the DFT output is cyclically extended, thus producing a vector of size $\bar{M}$. The second step is accomplished by adding a CP and a CPO to the output of the first one; the rules employed for generating the cyclic extension are the same as those adopted for OTFS symbols in the FD.

Generation of the transmitted signal – The vector $\bar{\mathbf{X}}_{\rm p}$ undergoes factor $N_{\rm c}$ TD upsampling; this is performed on each row of $\bar{\mathbf{X}}_{\rm p}$, thus generating the $\bar{M} \times (\bar{N}D+1)N_{\rm c}$ dimensional matrix $\bar{\mathbf{X}}_{\rm p}^{(\rm U)} \triangleq [\bar{x}_{\rm p}^{(\rm U)}[k,l]]$. This matrix is applied to a digital filter bank, which consists of $\bar{M}$ filters running in parallel and produces a sequence of equally spaced samples of the complex envelope of the modulated signal. Sample generation is based on a discrete time version of (6.2)-(6.3). Therefore, the nth sample is computed as (see (6.2)-(6.4))

$$s[n] = \sum_{k=-(M/2+N_{cp}^{(\rm FD)})}^{M/2+N_{cpo}^{(\rm FD)}-1} \bar{x}_{\rm p}^{(\rm U)}[k,n] * \bar{\phi}_k[n] \tag{6.15}$$

for $n = 0, 1, ..., N^{(\rm tx)} - 1$; here, $N^{(\rm tx)} \triangleq (\bar{N}D + N_{\rm p} + 1)N_{\rm c}$ is the overall number of samples after filtering,

$$\bar{\phi}_k[\tilde{n}] = p(\tilde{n}/N_{\rm c}) \exp\big(j2\pi k\tilde{n}/N_{\rm c}\big), \tag{6.16}$$

for $\tilde{n} = -\lfloor N_{\rm p}/2 \rfloor N_{\rm c}, ..., -1, 0, 1, ..., \lfloor N_{\rm p}/2 \rfloor N_{\rm c} - 1$ ($\bar{\phi}_k[\tilde{n}] = 0$ anywhere else) and $N_{\rm p}$ represents the duration (in symbol intervals) of the truncated version of $p(t)$. Finally, the sequence $\{s[n]\}$ is sent[8] to the TX radio block, which performs frequency up-conversion, signal amplification and radio transmission.

Receiver – Similarly to the transmitter, in the following we list the tasks executed by the baseband part of the receiver and provide various technical details about each of them. In the description, we focus on the processing accomplished on a single snapshot of the received signal; such a snapshot is long enough to capture at least a single frame.

[7] The time index is omitted hereafter in order to ease notation.

[8] Appropriate *data quantization* must be applied to the sequence $\{s[n]\}$ to ensure compatibility with the data format required by the SDR [113]. Typically, *float64* data types should be converted to the *int16* format.

Receive filtering – The down-converted baseband samples available at the output of the RX radio block are first processed by a filter bank, consisting of M distinct matched filters. Here, the filter bank input is the sample sequence $\{r[n]; n = 0, 1, ..., N^{(\mathrm{rx})} - 1\}$, with $N^{(\mathrm{rx})} > N^{(\mathrm{tx})}$. The samples available at the filter bank output are collected in the $M \times (N^{(\mathrm{rx})} + N_{\mathrm{c}}N_{\mathrm{p}})$ matrix $\mathbf{Y} \triangleq [Y[\tilde{k}, \tilde{n}]]$; here,

$$Y[\tilde{k}, \tilde{n}] = r[\tilde{n}] * \bar{\phi}_{\tilde{k}}[\tilde{n}] \tag{6.17}$$

represents the $\tilde{n}$th sample[9] (with $\tilde{n} = 0, 1, ..., N^{(\mathrm{rx})} + N_{\mathrm{c}}N_{\mathrm{p}} - 1$) available at the output of the $\tilde{k}$th filter (see (6.16)).

Frame synchronization and sample selection – The identification of the start of each frame and the selection of the associated samples is achieved by:

1) Computing the V-dimensional cross-correlation vector $\mathbf{q} \triangleq [q[0], q[1], ..., q[V-1]]^T$ between the $(MN^{(\mathrm{rx})})$-dimensional vector $\mathbf{y}$ and $\mathbf{U}$; here, $V \triangleq MN^{(\mathrm{rx})} + M - 1$, $\mathbf{y} \triangleq [y[0], y[1], ..., y[MN^{(\mathrm{rx})} - 1]]^T$ results from the ordered concatenation of the columns of the matrix $\mathbf{Y}$, $\mathbf{U} \triangleq [u[0], u[1], ..., u[M-1]]^T$ is an M-dimensional vector obtained from $\bar{\mathbf{U}}$ by discarding its first $N_{cp}^{(\mathrm{FD})}$ elements and its last $N_{cpo}^{(\mathrm{FD})}$ elements. Moreover, $q[v] \triangleq y[v] * u^*[v]$ (with $v = 0, 1, ..., V-1$).

2) Evaluating $\hat{v} = \arg\max_v |q(v)|$.

3) Retaining the $M(\bar{N}D + 1)N_{\mathrm{c}}$ consecutive elements of $\mathbf{y}$, whose index starts from $\hat{v}$. Such elements are re-organized in an $M \times (\bar{N}D + 1)N_{\mathrm{c}}$ dimensional matrix $\bar{\mathbf{Y}}$.

Downsampling, partitioning and TD CP removal – First of all, the matrix $\bar{\mathbf{Y}}$ undergoes *downsampling* along its columns by a factor N_{c}. Then, the first column of the resulting down-sampled matrix is removed in order to eliminate the samples associated with the transmitted preamble $\mathbf{U}$ and the resulting matrix is partitioned into D matrices $\{\bar{\mathbf{R}}_l; l = 0, 1, ..., D-1\}$, each having size $M \times \bar{N}$. Finally, the contribution of the TD CP is removed by dropping the first $N_{cp}^{(\mathrm{TD})}$ columns; this produces set $\{\mathbf{R}_l; l = 0, 1, ..., D-1\}$, that collects D matrices, all having size $M \times N$. Each of the matrices $\{\mathbf{R}_l\}$ is processed to detect a single OTFS symbol.

Channel estimation and equalization – The JCEE algorithm is executed over the detected frame. For this reason, the matrix $\mathbf{R}_0$, being associated with the OTFS pilot symbol (which has been inserted at the beginning of the considered frame), is processed to estimate the CSI over the detected frame. The estimated channel is exploited for accomplishing MMSE equalization over the remaining $(D-1)$ OTFS symbols; this generates the set $\{\hat{\mathbf{T}}_l; l = 1, 2, ..., D-1\}$, that collects $(D-1)$ matrices, all having a size $M \times N$.

5) *Fourier processing and SC removal* – Each of the matrices $\{\hat{\mathbf{T}}_l\}$ undergoes an order (M, N) DSFT, followed by SC removal and minimum Euclidean distance data detection. Finally, the detected data are sent to the decoding block.

It is important to underline that, in the proposed system, no specific algorithm for the estimation of the residual CFO and TO is employed. However, the JCEE algorithm compensates for these effects by utilizing the estimated CSI in its equalization step.

[9]Note that $\bar{\phi}_{\tilde{k}}[\tilde{n}] = \bar{\phi}^*_{\tilde{k}}[-\tilde{n}]$ for any $\tilde{n}$.

6.5 Numerical Results

Computer simulations have been run to assess the performance of the JCEE method and to compare it with the algorithms devised by *Raviteja et. al* [83] and by *Gaudio et al.* [88]; these are referred to as Alg-R and Alg-G, respectively, in the following. The JCEE algorithm, Alg-R, and Alg-G operate in a similar fashion for channel estimation (see steps **S1**–**S3**) and equalization (see steps **E1**–**E2**), the only difference being represented by the MHR procedure employed in step **S2**; this ensures a fair comparison.

TABLE 6.1: Complexity orders of the considered MHR techniques.

Technique	N_{S2}
Alg-R	$LM_0N_0\log_2(M_0N_0)$
CSFDEC	$13M_0N_0\log_2(M_0N_0)+13L^2N_{\mathrm{it}}N_{\mathrm{ref}}I_{\mathrm{m}}I_{\mathrm{n}}$
Alg-G	$LM_0N_0\log_2(M_0N_0)+LN_{\mathrm{it}}N_{\tilde{\tau}}N_{\tilde{\nu}}M^2N^2$

Therefore, the computational complexity of the considered techniques differs for that of step **S2** only; the complexity of this step is provided in Table 6.1 for each of the considered options. The complexity orders listed in that table deserve the following comments: 1) $M_0 \triangleq N_{\mathrm{m}}M$ and $N_0 \triangleq N_{\mathrm{n}}N$, where N_{m} and N_{n} are the *oversampling* factors in the 2D spectrum evaluation by Alg-R, and by the initialization steps of the CSFDEC algorithm and Alg-G, respectively; 2) N_{it} represents the number of iterations carried out in each refinement step of the CSFDEC algorithm and Alg-G; 3) I_{m} and I_{n} are the interpolation orders for the 2D interpolation[10] procedure accomplished by the CSFDEC algorithm; 4) N_{ref} is the number of re-estimations carried out by the CSFDEC algorithm; 5) $N_{\tilde{\tau}}$ and $N_{\tilde{\nu}}$ are the overall number of trial values for the 2D grid deployed by Alg-G for the refinement of delay and Doppler, respectively.

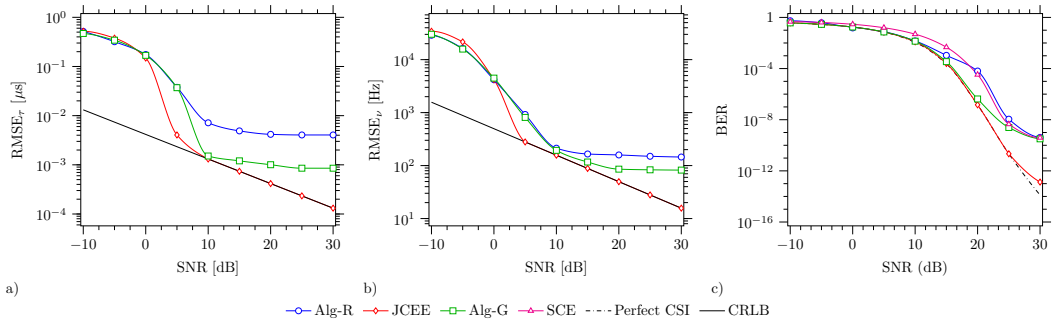

FIGURE 6.3: Root mean square error performance achieved by Alg-R, the JCEE algorithm and Alg-G in a) delay and b) Doppler shift estimation; the CRLBs are also shown. c) Bit error rate performance achieved by the considered methods; the equalization only and perfect CSI are also shown.

In the simulations, we generated an OTFS frame with $D = 10$ OTFS symbols. The channel model was derived using GQR [104] to approximate a doubly selective channel with a truncated exponential power delay profile (maximum delay $\tau_{\max} = 2$ µs) and Jake's

[10]The MatblabR2023b *spline* interpolation has been adopted.

power spectrum for the Doppler effect (maximum Doppler shift $\nu_{\max} = 2.9$ kHz). This has resulted in a channel model characterized by $L = 6$ channel paths, whose complex amplitudes are represented as the superposition of six complex exponentials.

The following parameters have been selected for the OTFS-DCP modulation format: 1) $M = 64$ and $N = 32$ for the generation of the data matrix $\mathbf{C}$; 2) frequency spacing $\Delta_f = 250$ kHz; 3) TD CP size $N_{cp}^{(\mathrm{TD})} = N/4$; 4) FD CP and CPO sizes $N_{cp}^{(\mathrm{FD})} = N_{cpo}^{(\mathrm{FD})} = M/16$; 5) carrier frequency $f_{\mathrm{c}} = 24$ GHz; 6) roll-off factor for the RRC pulse $\alpha = 0.25$; 7) cardinality of the PSK modulation $M_{\mathrm{c}} = 4$ (Gray coding is used in symbol mapping).

The performances of the considered methods have been compared in terms of: 1) the RMSE achieved for delay (RMSE_τ) and Doppler shift (RMSE_ν) estimation (see Fig. 6.3-a) and Fig. 6.3-b)) by Alg-R, Alg-G and the JCEE algorithm;

2) the BER achieved by the OTFS-DCP based communication system (see Fig. 6.3-c)). In generating the numerical results, the following choices have been made for all the considered algorithms: 1) the oversampling factors $N_{\mathrm{m}} = N_{\mathrm{n}} = 4$ (consequently $M_0 = N_0 = 2048$) have been adopted for all the algorithms; 2) the overall number of paths (L) and the noise variance (σ^2) have been assumed to be known at the RX side; 3) in the CSFDEC algorithm, $N_{\mathrm{it}} = 10$, $I_{\mathrm{m}} = I_{\mathrm{n}} = 7$ and $N_{\mathrm{ref}} = 2$ have been selected; 4) in Alg-G, $N_{\tilde{\tau}} = N_{\tilde{\nu}} = 21$ and $N_{\mathrm{it}} = 3$ have been selected.

Some results about RMSE_τ and RMSE_ν are shown in Fig. 6.3-a) and Fig. 6.3-b), respectively, for an SNR $\in [-10, 30]$ dB; the CRLB is also provided as a reference. The BER performance achievable in the same SNR range through the use of all the considered methods is shown in Fig. 6.3-c); moreover, the BER curves referring to the SCE case and to the case in which the CSI is completely known at the RX side (*perfect CSI*) are also shown for comparison.

The results in Fig. 6.3 a)-c) lead to the following conclusions:

1) A SNR *threshold* can be easily identified in all the RMSE curves; this threshold is approximately equal to 5 dB for the JCEE algorithm, and 10 dB for both Alg-R and Alg-G.

2) Both Alg-R and Alg-G exhibit a RMSE *floor* at high SNRs. On the one hand, Alg-R restricts the peak search to the 2D spectrum of $\hat{\mathbf{h}}_{\mathrm{c}}$ (6.11) without including a refinement step. On the other hand, although Alg-G employs a refinement step based on an on-grid approximate ML technique, its accuracy is limited by the grid size. Increasing the grid size can improve estimation accuracy at the price of a significant increase in computational complexity (see Table 6.1).

3) The JCEE algorithm achieves superior estimation accuracy (close to the CRLB) in terms of both RMSE_τ and RMSE_ν while maintaining manageable complexity; this is mainly due to the fact that the CSFDEC algorithm employed in step **S2** operates in an off-grid fashion.

4) Alg-R and the JCEE algorithm provide the worst and the best BER performance, respectively. However, Alg-R achieves better performance than that referring to the SCE case up to a SNR $\simeq 17$ dB. This is due to the fact that, as already mentioned in the

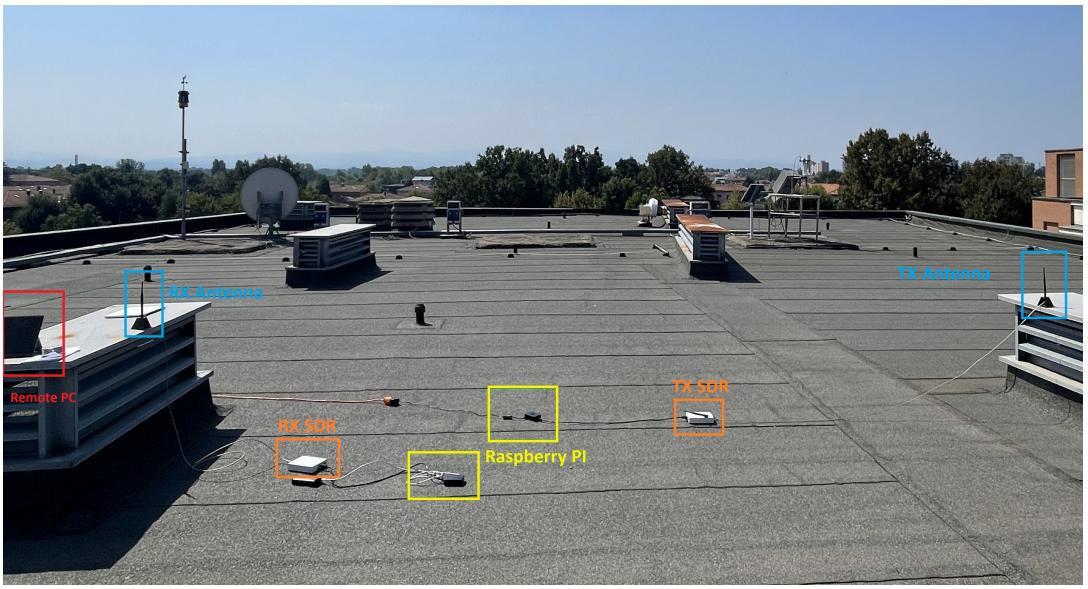

FIGURE 6.4: Experimental setup adopted in our measurement campaign. Both transmitter and receiver are composed of: 1) a RPI5 device, 2) a NI-2901 SDR; 3) a single antenna element.

previous section, Alg-R provides a more accurate CSI (thanks to steps **S2** and **S3**) than that evaluated through step **S1** only if low SNRs are considered.

6.6 Experimental results

A measurement campaign has been carried out on the terrace of the MO-26 building at the Department of Engineering "Enzo Ferrari" (University of Modena and Reggio Emilia, Italy) in order to assess the performance of the OTFS-DCP based communication system under various propagation conditions.

The experimental setup, shown in Fig. 6.4, included two USRP NI-2901 devices, one for transmission, the other one for reception, each equipped with a single antenna. Both devices have been connected via Universal Serial Bus (USB) 3.0 to dedicated Raspberry Pi 5 (RPI5) computers. A separate PC, linked to each RPI5, was used to initiate data communication. Two options were available for signal processing at the RX side: the received signal samples could be processed directly by a RPI5, or could be stored on it (in the latter case, they have been processed by a PC in our laboratory); a flexible baseband processing framework, compatible with both Matlab and Python, has been developed for this purpose.

In the experiments, the following parameters have been selected for the OTFS-DCP modulation: 1) $M = 64$ and $N = 64$ for each OTFS symbol; 2) TD CP size $N_{cp}^{(\mathrm{TD})} = 25$; 3) FD CP & CPO sizes $N_{cp}^{(\mathrm{FD})} = N_{cpo}^{(\mathrm{FD})} = 2$; 4) roll-off factor $\alpha = 0.25$, length $N_{\mathrm{p}} = 17$ and

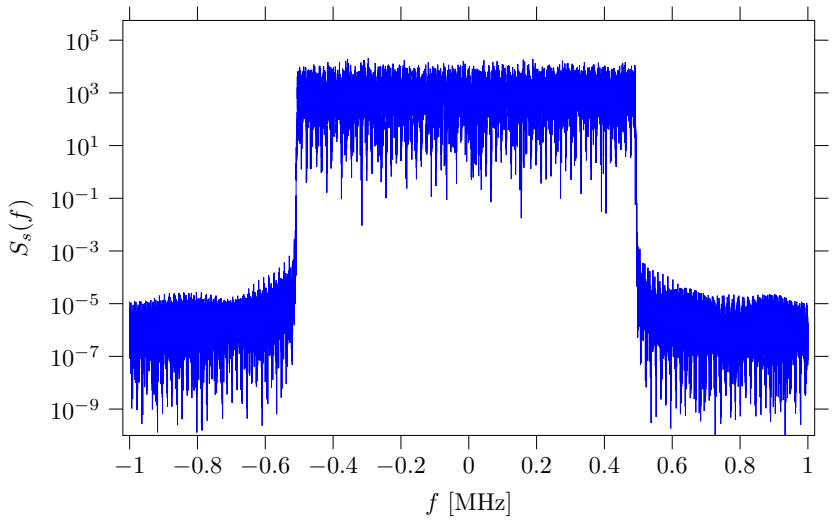

FIGURE 6.5: Power spectral density of the complex envelope of the considered OTFS-DCP modulation.

oversampling factor $N_{\rm c} = \bar{M} = 68$ for the TX pulse $p(t)$; 5) $M_{\rm c} = 4$ for the constellation size (a QPSK constellation was used); 6) carrier frequency $f_c = 2.4$ GHz; 7) symbol interval $T_s = 68$ µs; 8) Barker code sequence length $L_{\rm B} = 13$.

The choice of these parameters entails that: 1) the overall number of useful channel symbols conveyed by each OFDM signal is $N_{\rm u} = 48$; 2) the bandwidth of the radiated signal is $B = 1$ MHz; 3) the normalized resolutions for the delay and Doppler frequency are $\bar{F}_\tau = 1/N = 0.016$ and $\bar{F}_\nu = 1/M = 0.016$, respectively; 4) the maximum absolute value of the normalized Doppler shift not entailing a data loss is $|F_\nu| = 2$ (thanks to the insertion of the FD CP & CPO). Note also that: a) the normalized TX and RX gains have been set to 0.78 and 0.66, respectively; b) in all the experiments the same image has been transmitted (converted into a binary sequence before undergoing scrambling and Gray coding in the coding block of Fig. 6.2); c) no channel coding has been used.

The PSD, $S_s(f)$, of the complex envelope of the considered OTFS-DCP modulation is illustrated in Fig. 6.5. The PSD shape is in agreement, up to a scale factor, with the theoretical one (see Fig. 5.4) and with the value of bandwidth given above (1 MHz). Note also that 6% of the spectrum is occupied by the contributions of the FD CP & CPO.

In our measurement campaign, we considered two scenarios. In the first scenario (denoted **SC1**), the following choices have been made: 1) The distance between TX and RX antennas, $d_{\rm TR}$, has been set to 5, 15, 25, 35, 45, and 55 m; 2) the frame length D has been set to 4; 3) a single-tap channel with fixed Doppler has been simulated at the transmitter to mimic a relative radial velocity v between TX and RX. The last result was achieved by introducing an extra phase rotation $\exp(j2\pi F_\nu \tilde{n}/N_{\rm c})$ in the RHS of (6.16). In particular, the values 0, 150, 300 and 600 km/h have been assigned to v (the corresponding values of normalized Doppler frequency F_ν are 0, 0.05, 0.09 and 0.18, respectively; see (6.8)).

In the second scenario (denoted **SC2**), a Doppler shift has been introduced in the same way as in **SC1**, but a constant velocity $v = 250$ km/h ($F_\nu = 0.075$) and a fixed distance

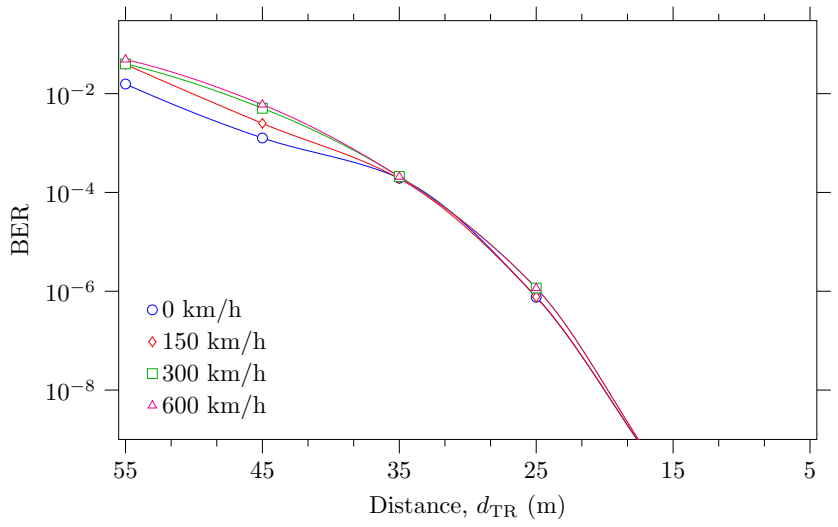

FIGURE 6.6: Bit error rate performance versus the distance d_{TR} in **SC1**; four different velocities are considered.

$d_{\mathrm{TR}} = 15$ m have been selected. However, measurements were taken for different sizes of the OTFS-DCP frame, specifically for $D \in \{3, 5, 7, 9, 12, 15\}$.

The choice of the two experimental scenarios is motivated as follows. **SC1** has allowed us to analyze the dependence of error performance on SNR and velocity, while **SC2** has unveiled the impact of frame length on error performance and, in particular, has shown the effect of using the same CSI estimate, based on the single pilot available at the beginning of each frame, for channel equalization over all the data symbols within the frame itself. Some numerical results referring to **SC1** are illustrated in Fig. 6.6, where the dependence of the BER[11] on the distance d_{TR} is represented for $v = 0$, 150, 300 and 600 km/h. These results deserve the following comments:

1) In this scenario, the velocity does not have a significant impact on BER performance. This confirms that the proposed OTFS-DCP based system is able to reliably operate at high speeds.

2) As the distance between the TX and RX antennas decreases, the BER curves referring to different velocities tend to converge, since the SNR gets larger.

3) The effects of residual (i.e., fractional) TO and CFO[12] are mitigated by the JCEE algorithm.

Some results referring to **SC2** are illustrated in Fig. 6.7 and in Fig. 6.8, and are listed in Table 6.2. Specifically, Fig. 6.7 shows how BER[13] varies with frame length D. Note that

[11] BER values have been computed based on data estimates obtained in the transmission of $40 \cdot 10^6$ bits for each combination of distance and velocity.

[12] According to the NI2901 reference manual [113], the frequency accuracy relative to the carrier frequency f_c is 2.5 parts per million (ppm). This implies that the maximum normalized CFO, at $f_c = 2.4$ GHz, is 0.006.

[13] The BER estimates obtained in **SC2** are based on the data acquired in the transmission of 500 frames for each D value considered.

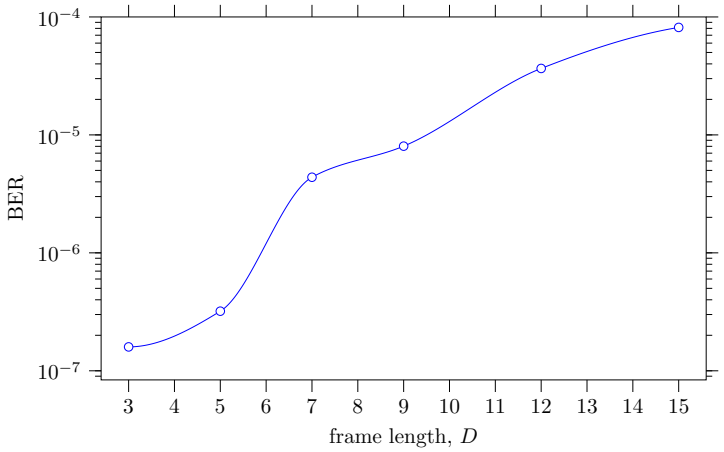

FIGURE 6.7: Bit error rate performance versus the frame length D in **SC2** ($v = 250$ km/h and $d_{\mathrm{TR}} = 15$ m).

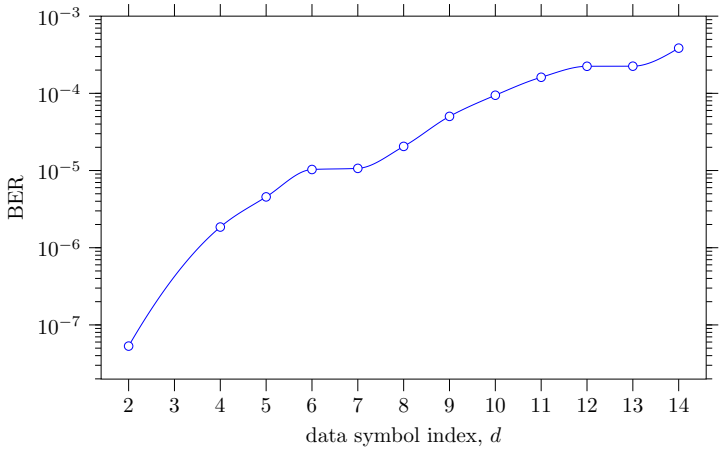

FIGURE 6.8: Bit error rate performance versus the data symbol index d in **SC2** ($v = 250$ km/h and $d_{\mathrm{TR}} = 15$ m).

TABLE 6.2: Maximum number of consecutive bit errors detected in the first OTFS symbol and in the last one of the same frame in **SC2**; six different values of D are considered.

D	3	5	7	9	12	15
$N_{\mathrm{E}}^{(\max)}(1)$	0	0	0	0	0	0
$N_{\mathrm{E}}^{(\max)}(D-1)$	1	2	7	15	24	33

BER worsens as D increases. This is due to the fact that no CSI tracking is accomplished over each OTFS frame and, consequently, the average quality of channel equalization becomes poorer for longer data frames. This consideration is also supported by Fig. 6.8, that shows the BER dependence on OTFS symbol index d for $D = 15$ (so d ranges from 2 to 14, since $d = 0$ corresponds to the pilot symbol and no errors were detected for $d = 1$). These results reveal that, at high speed, error rate is dominated by the contribution due to OTFS symbols farther from the pilot symbol; for this reason, long frames should be avoided without reliable CSI tracking. Table 6.2 further explores this issue by listing the maximum number of consecutive bit errors, $N_{\mathrm{E}}(d)$, for $d = 1$ and $d = D - 1$ (i.e., for the first information symbol and the last one, respectively). The results show the presence of a steady increase in consecutive errors as D grows, with the longest error events usually occurring in the last symbol of the frame. Therefore, if long frames are employed and no channel tracking is adopted, a powerful error correction code is required to guarantee reliable communications in the presence of strong Doppler.

6.7 Conclusions

In this chapter, a novel algorithm, dubbed JCEE, has been devised for channel estimation and equalization in OTFS-DCP systems. The obtained numerical results demonstrate that the JCEE algorithm offers superior accuracy in channel parameter estimation compared to alternative methods, while maintaining manageable complexity, making it a promising solution for OTFS-based JCAS systems requiring channel estimation for sensing at their TX side and for equalization at their RX side.

Additionally, the implementation of an OTFS-DCP based communication system on USRP SDRs has been illustrated. The description has focused on the overall system architecture and on some specific technical details that have been deemed useful to any reader interested in developing a similar project. The experimental results have shown that: 1) the system is able to operate reliably in the presence of strong Doppler effects if the JCEE algorithm is employed for channel estimation and equalization; 2) the error rate tends to appreciably increase with the distance from pilot symbols if no channel tracking is used. The use of channel coding schemes and the development of new synchronization and channel estimation techniques represent important topics for future research activities.

7 Conclusions

This dissertation has explored multi-carrier modulation schemes, specifically OFDM and OTFS, within the context of JCAS systems. These modulation formats have been examined from two distinct perspectives. While numerous studies in the literature have focused on OFDM from a communication standpoint, this thesis has concentrated on utilizing OFDM as a waveform for sensing purposes. Conversely, OTFS, being a more recent modulation format, has primarily been investigated for communication applications. The relationship between the two modulation formats is that OFDM served as a foundational guide to understand the principles necessary for developing OTFS. This understanding has enabled the creation of an OTFS modulation format that is robust against doubly selective channels, incorporating a double cyclic prefix; one in the time domain and the other in the frequency domain.

The dissertation has also explored key technical aspects of JCAS systems. First, we derived, analyzed, and compared radar parameter estimation techniques based on maximum likelihood principles, examining the trade-off between computational complexity and estimation accuracy. These analyses were conducted for both SISO and MIMO systems employing OFDM and operating at millimeter-wave frequencies, addressing the additional challenges and limitations that arise in these scenarios.

A detailed analysis of channel estimation for both modulation schemes was conducted. For OFDM, this analysis has focused on *colocated* radar systems, where data payloads are known to the receiver. In contrast, for OTFS, the analysis encompassed the placement of pilot symbols, the development and complexity analysis of estimation algorithms, and the evaluation of performance losses due to the inclusion of guard symbols. Regarding OTFS, the deployment of the novel modulation format, which includes a double cyclic prefix, has been proposed and successfully implemented in SDR devices. This achievement not only bridges the gap between theoretical concepts and practical applications but also offers valuable guidelines for future implementations. By demonstrating the feasibility and effectiveness of OTFS-DCP in real-world scenarios, this work significantly contributes to the advancement of communication systems and sets a solid foundation for further research and development in this field.

While this dissertation has laid a solid foundation for understanding and developing JCAS systems based on multi-carrier modulation formats, several avenues for future research remain open.

Future research could explore novel algorithms that jointly optimize radar sensing and communication tasks in increasingly complex scenarios, such as multi-user environments or dense vehicular networks. In this context, an important extension involves distributed radar systems, where multiple interconnected radar nodes collaborate to achieve enhanced environmental sensing. The target parameter estimation algorithms developed in this dissertation could serve as a foundation for such systems, enabling improved accuracy and

efficiency. Key research challenges in this area include synchronization across distributed nodes, efficient resource allocation, and the development of robust communication strategies to maximize both sensing and communication performance.

The proposed OTFS modulation with a double cyclic prefix has shown promising results. However, its extension to MIMO has not been investigated yet. This could be helpful in investigating the scalability of OTFS-based JCAS systems to massive MIMO architectures, including hybrid beamforming techniques and their impact on both sensing and communication performance in high mobility environments.

As JCAS systems are likely to play a central role in next-generation communication networks, their integration with emerging 6G technologies, such as terahertz communication and AI-driven network management, represents an interesting direction for future research.

Nevertheless, to further enhance spectral efficiency in JCAS applications, future work could consider non-orthogonal multi-carrier modulations. These schemes, such as Spectrally Efficient Frequency Division Multiplexing (SEFDM) or Generalized Frequency Division Multiplexing (GFDM), relax orthogonality constraints, thereby increasing the utilization of available spectrum. Investigating their application in JCAS systems, along with their impact on radar sensing capabilities and computational complexity, represents a valuable research opportunity.

In conclusion, this dissertation has provided a comprehensive analysis and set of methodologies for leveraging OFDM and OTFS in JCAS systems, highlighting their potential to revolutionize radar and communication technologies. The findings and insights presented herein offer a robust foundation for further innovation in this rapidly evolving field.

A

Appendix

A.1 Appendices of Chapter 1

A.1.1 Spectral Cancellation of a Two-Dimensional Complex Tone

In this paragraph, the derivation of the expression of the vector $\bar{\mathbf{C}}_{0,0}(\cdot,\cdot,\cdot)$ appearing in the RHS of (1.58) is sketched. This vector is evaluated to cancel the contribution of the sequence

$$s_{m,n}\left(\bar{F}_\nu, \bar{F}_r, \bar{A}\right) = \bar{A}\,\bar{w}_\nu^m\,\bar{w}_r^n \tag{A.1}$$

to the vector $\bar{\mathbf{Y}}_{0,0}$ (1.26) (the adopted cancellation procedure is expressed by (1.57) and (1.58)); here, $\bar{w}_\nu \triangleq \exp(j2\pi\bar{F}_\nu)$ and $\bar{w}_r \triangleq \exp(-j2\pi\bar{F}_r)$. Since $\bar{\mathbf{Y}}_{0,0}$ is the order (M_0, N_0) DSFT of the zero-padded version $\hat{\mathbf{H}}_{0,0}^{(ZP)}$ 1.27 of the matrix $\hat{\mathbf{H}}_{0,0} = [\hat{H}_{m,n}]$, it is easy to show that

$$\bar{\mathbf{C}}_{0,0}\left(\bar{A}, \bar{F}_\nu, \bar{F}_r\right) = \bar{A}\,\bar{\mathbf{W}}_0, \tag{A.2}$$

where $\bar{\mathbf{W}}_0$ denotes the order (M_0, N_0) DSFT of the $M_0 \times N_0$ matrix

$$\bar{\mathbf{w}}_0 \triangleq \begin{bmatrix} \bar{\mathbf{w}} & \mathbf{0}_{M,N_0-N} \\ \mathbf{0}_{M_0-M,N} & \mathbf{0}_{M_0-M,N_0-N} \end{bmatrix}, \tag{A.3}$$

$\bar{\mathbf{w}} \triangleq [w_{m,n}]$ is an $M \times N$ matrix such that $w_{m,n} \triangleq \bar{w}^{m-n}$, with $m = 0, 1, ..., M-1$ and $n = 0, 1, ..., N-1$, and $\bar{w} \triangleq \bar{w}_\nu\,\bar{w}_r$. Then, the (m,n)th element of the matrix $\bar{\mathbf{W}}_0$ is given by

$$\begin{aligned} \bar{W}_0[m,n] &= \frac{1}{M_0}\sum_{l=0}^{M-1} \bar{w}_\nu^l \exp\left(-j2\pi\frac{m}{M_0}l\right) \frac{1}{N_0}\sum_{p=0}^{N-1} \bar{w}_r^p \exp\left(j2\pi\frac{n}{N_0}p\right) \\ &= \frac{1}{M_0}\sum_{l=0}^{M-1} \left(\hat{q}_\nu\,[m]\right)^l \frac{1}{N_0}\sum_{p=0}^{N-1} \left(\hat{q}_r\,[n]\right)^p, \end{aligned} \tag{A.4}$$

where $\hat{q}_\nu[m] \triangleq \exp(j2\pi(\hat{F}_\nu - m/M_0))$ and $\hat{q}_r[m] \triangleq \exp(-j2\pi(\hat{F}_r - n/N_0))$. Finally, it is useful to note that the identity

$$\sum_{n=0}^{N-1} q^n = \frac{q^N - 1}{q - 1}, \tag{A.5}$$

holding for any $q \in \mathbb{C}$, can be exploited for an efficient computation of the two sums appearing in the RHS of (A.4).

A.1.2 Cancellation of Two-Dimensional Spectral Leakage

In this paragraph, the expression of the quantity $\bar{Y}_{k_1,k_2}(\cdot\,,\cdot;\cdot,\cdot,\cdot)$ appearing in the RHS of (1.60) and (1.62) is derived. This quantity is computed by the CSFDEC algorithm to cancel the contribution of the sequence $\{s_{m,n}(\bar{F}_{\nu_k},\bar{F}_{r_k},\bar{A}_k)\}$ (see (A.1)) to $\bar{Y}^{(i)}_{k_1,k_2}(\rho^{(i)}_{\nu},\rho^{(i)}_{r})$ (1.61) for $k_1,k_2=0,1,2,3$. It is not difficult to show that

$$\bar{Y}_{k_1,k_2}\left(\hat{F}^{(i)}_{\nu,c_i}\,,\hat{F}^{(i)}_{r,c_i};\hat{A}^{(i-1)}_{k},\hat{F}^{(i-1)}_{\nu_k},\hat{F}^{(i-1)}_{r_k}\right)=\bar{A}^{(i-1)}_{k}\,\bar{W}^{(k)}_{k_1k_2}\left(\hat{F}^{(i)}_{\nu,c_i}\,,\hat{F}^{(i)}_{r,c_i};\hat{F}^{(i-1)}_{\nu_k},\hat{F}^{(i-1)}_{r_k}\right), \tag{A.6}$$

where

$$\bar{W}^{(k)}_{k_1k_2}\left(\hat{F}^{(i)}_{\nu,c_i}\,,\hat{F}^{(i)}_{r,c_i};\hat{F}^{(i-1)}_{\nu_k},\hat{F}^{(i-1)}_{r_k}\right)=\frac{1}{M_0}\sum_{m=0}^{M-1}m^{k_1}\left(\bar{q}_{\nu}\left(\hat{F}^{(i)}_{\nu,c_i},\hat{F}^{(i-1)}_{\nu_k}\right)\right)^{m}$$
$$\cdot\,\frac{1}{N_0}\sum_{n=0}^{N-1}n^{k_2}\left(\bar{q}_{r}\left(\hat{F}^{(i)}_{r,c_i},\hat{F}^{(i-1)}_{r_k}\right)\right)^{n}, \tag{A.7}$$

with $\bar{q}_{\nu}(\hat{F}^{(i)}_{\nu,c_i},\hat{F}^{(i-1)}_{\nu_k})\triangleq\exp(j2\pi(\hat{F}^{(i-1)}_{\nu_k}-\hat{F}^{(i)}_{\nu,c_i}))$, $\bar{q}_{r}(\hat{F}^{(i)}_{r,c_i},\hat{F}^{(i-1)}_{r_k})\triangleq\exp(-j2\pi(\hat{F}^{(i-1)}_{r_k}-\hat{F}^{(i)}_{r,c_i}))$; here $\hat{F}^{(i-1)}_{\nu_k}$ and $\hat{F}^{(i-1)}_{r_k}$ are the *fine estimates* of the normalized Doppler frequency and normalized delay, respectively, computed at the $(i-1)$th iteration for the kth target.

Note that the identities (A.5),

$$(q-1)^2\sum_{n=0}^{N-1}n\,q^n=(N-1)\,q^{N+1}-N\,q^N+q, \tag{A.8}$$

$$(q-1)^3\sum_{n=0}^{N-1}n^2\,q^n=(N-1)^2\,q^{N+2}+N^2\,q^N-q^2-q-\left(2\,N^2-2\,N-1\right)\,q^{N+1} \tag{A.9}$$

and

$$(q-1)^4\sum_{n=0}^{N-1}n^3\,q^n=q+4q^2+q^3-N^3q^N+\left(3N^3-3N^2-3N-1\right)q^{N+1}$$
$$+\left(-3N^3+6N^2-4N\right)q^{N+2}+(N-1)^3q^{N+3} \tag{A.10}$$

holding for any $q\in\mathbb{C}$, can be exploited for an efficient computation of all the factors appearing in the RHS of (1.60) and (1.61) (with $k_1,k_2=0,1,2,3$).

A.1.3 Computational Complexity of the CSFDE Algorithm

In this Appendix, the derivation of the approximation (1.64) of $\mathcal{C}_{\mathrm{CSFDE}}$ is sketched. The evaluation of $\mathcal{C}_{\mathrm{CSFDE}}$ requires that of the computational costs $\mathcal{C}_0(\mathrm{CSFDE})$ and $\mathcal{C}_i(\mathrm{CSFDE})$ appearing in the RHS of (1.64). The cost $\mathcal{C}_0(\mathrm{CSFDE})$ can be easily estimated as

$$\mathcal{C}_0(\mathrm{CSFDE})=\mathcal{C}_{\hat{l},\hat{p}}+\mathcal{C}_{\bar{\mathbf{Y}}_{k_1,k_2}}+\mathcal{C}_{\hat{\Omega}}+\mathcal{C}_{\hat{\Delta}}, \tag{A.11}$$

where:

1) the cost $\mathcal{C}_{\hat{l},\hat{p}}$ is the cost of evaluating (1.50) and thus is equal to $5M_0N_0 + 2$;

2) the cost[1] $\mathcal{C}_{\bar{\mathbf{Y}}_{k_1,k_2}}$ is the contribution due to the computation of the matrices $\{\bar{\mathbf{Y}}_{k_1,k_2}\}$ (1.39) and is equal to $16\,M_0\,N_0\log_2(M_0\,N_0)$ ($13M_0N_0\log_2(M_0N_0)$) if 16 (13) DSFT of order (M_0, N_0) are evaluated, i.e., if (1.41)((1.46)) is employed in the evaluation of $\hat{\Omega}$ and $\hat{\Delta}$;

3) both $\mathcal{C}_{\hat{\Omega}}$ and $\mathcal{C}_{\hat{\Delta}}$ are negligible, being equal to 134 (102) FLOPs if (1.41) ((1.46)) is employed in the evaluation of $\hat{\Omega}$ and $\hat{\Delta}$. Substituting these results in the RHS of (A.11) and keeping the dominant terms only leads to the conclusion that

$$\mathcal{C}_0(\text{CSFDE}) \approx 16M_0N_0\log_2(M_0N_0). \tag{A.12}$$

Similarly, the cost $\mathcal{C}_i(\text{CSFDE})$ can be easily estimated as

$$\mathcal{C}_i(\text{CSFDE}) = \mathcal{C}_{\bar{Y}} + \mathcal{C}_{\hat{\rho}_\nu} + \mathcal{C}_{\hat{\rho}_r} + \mathcal{C}_{\hat{A}} + \mathcal{C}_{\bar{Y}_{k_1,k_2}} + \mathcal{C}_{\hat{\Omega}} + \mathcal{C}_{\hat{\Delta}}. \tag{A.13}$$

Here,

1) the cost $\mathcal{C}_{\bar{Y}}$ refers to the evaluation of (1.23). This cost is in the order of $25MN$ if the evaluation of $\bar{Y}(\hat{F}_\nu, \hat{F}_r)$ is based on the exact computation through (1.23). Conversely, this cost becomes $I_\nu I_r$ if it is based on the interpolation of multiple elements of the matrix $\bar{\mathbf{Y}}_s$ (1.34). In this last case, I_ν and I_r represent the interpolation orders adopted in the Doppler and range domains for the evaluation of (1.23);

2) the cost $\mathcal{C}_{\bar{Y}_{k_1,k_2}}$ is equal to $15\,\mathcal{C}_{\bar{Y}}$ ($12\,\mathcal{C}_{\bar{Y}}$) if (1.41) ((1.46)) is adopted in the evaluation of $\hat{\Omega}$ and $\hat{\Delta}$;

3) the costs $\mathcal{C}_{\hat{A}}$, $\mathcal{C}_{\hat{\Omega}}$ and $\mathcal{C}_{\hat{\Delta}}$ refer to the evaluation of $\hat{A}$ (1.33), $\hat{\Omega}$ and $\hat{\Delta}$ (1.42), respectively, and can be safely neglected. The last results lead easily to the conclusion that

$$\mathcal{C}_i\,(\text{CSFDE}) \approx 16\,I_\nu I_r, \tag{A.14}$$

if (1.41) is employed and 2D interpolation is employed in the evaluation of $\bar{Y}_{k_1,k_2}(\hat{\rho}_\nu^{(i-1)}, \hat{\rho}_r^{(i-1)})$ (1.61). Finally, substituting the RHSs of (A.12) and (A.14) in that of (1.63) yields (1.64).

A.1.4 Cramer-Rao Lower Bounds for 2D Frequency Estimators

CRLBs for OFDM-based radar systems have already been derived in [8, Sec V-A, eq. (46)-(47)] and [114, Sec IV-B, eq. (18)-(19)], but refer to Doppler and range only. In this dissertation, CRLBs have been derived for the ML estimation problem (1.16) investigated in Chapter 1. The procedure we followed is conceptually the same as that adopted in [54].

[1]Note that this cost includes the computation of the spectrum $\bar{\mathbf{Y}}_{0,0}$ (see (1.26)).

For this reason, the inverse of the Fisher Information Matrix (FIM)

$$\mathrm{E}\left\{\frac{\partial L\left(\hat{\mathbf{H}}_{0,0}\,|\theta\right)}{\partial\theta}\left(\frac{\partial L\left(\hat{\mathbf{H}}_{0,0}\,|\theta\right)}{\partial\theta}\right)^{H}\right\}, \tag{A.15}$$

has been evaluated; here, $\theta \triangleq [F_\nu, F_r\,, a, \phi]^T$ is the vector collecting the parameters to be estimated ($a = |A|$ and ϕ denote the magnitude and the phase, respectively, of the complex amplitude A of the 2D-tone (see (1.15)), $\hat{\mathbf{H}}_{0,0}$ is the $M \times N$ matrix defined by (1.28) (its element $\hat{H}_{m,n}$ is expressed by (1.15)), $L(\cdot\,|\cdot)$ is the *log-likelihood* function

$$L\big(\hat{\mathbf{H}}_{0,0}|\tilde{\theta}\big) = K_L - MN\ln\sigma_W^2 - \frac{1}{\sigma_W^2}\sum_{m=0}^{M-1}\sum_{n=0}^{N-1}\varepsilon_{m,n}\Big(\tilde{F}_\nu, \tilde{F}_r, \tilde{a}\exp\big(j\tilde{\phi}\big)\Big), \tag{A.16}$$

here, $\tilde{\theta} \triangleq [\tilde{F}_\nu, \tilde{F}_r\,, \tilde{a}, \tilde{\phi}]^T$, K_L is a constant, σ_W^2 is the variance of the noise samples $\{\bar{W}_m(n)\}$ (see (1.12)) and $\varepsilon_{m,n}(\cdot,\cdot,\cdot)$ is defined by (1.18); note that the last quantity depends on the measurements $\{\hat{H}_{m,n}\}$.

The CRLBs derived for the estimation of F_ν, F_r, a and ϕ are thus

$$\mathrm{CRLB}_{F_\nu}\,(M, N, \mathrm{SNR}) = \frac{3}{2\pi^2\mathrm{SNR}\,M\;(M^{\,2}-1)\;N}, \tag{A.17}$$

$$\mathrm{CRLB}_{F_r}\,(M, N, \mathrm{SNR}) = \frac{3}{2\pi^2\mathrm{SNR}\,MN\;(N^{\,2}-1)}, \tag{A.18}$$

$$\mathrm{CRLB}_{a}\left(M, N, \sigma_W^2\right) = \frac{\sigma_W^2}{2\,M\,N} \tag{A.19}$$

and

$$\mathrm{CRLB}_{\phi}\,(M, N, \mathrm{SNR}) = \frac{7\,M\,N\,+M\,+N-5}{2\,\mathrm{SNR}\,M\;(M+1)\;N\;(N+1)}, \tag{A.20}$$

respectively, where $\mathrm{SNR} \triangleq a^2/\sigma_W^2$ is the SNR referring to the signal model (1.15).

Finally, it is worth pointing out that: 1) the bounds (A.17), (A.18) and (A.20) are inversely proportional to the SNR, whereas the bound (A.19) is directly proportional to the noise variance σ_W^2, but independent of the amplitude a; 2) the bounds (A.17) and (A.18) are identical to those provided in [8, Sec V-A] and [114, Sec IV-B], even if the expressions illustrated in the first reference refer to $\omega_\nu = 2\pi F_\nu$ and $\omega_\tau = 2\pi F_r$, whereas those provided in the second one refer to target speed and range (see [8, Sec. V-A; eqs. (46)-(47)] and [114, Sec. IV-B; eqs. (18)-(19)], respectively).

A.2 Appendices of Chapter 3

A.2.1 Cramer-Rao Lower Bounds for 4D Frequency Estimation

Cramer-Rao lower bounds for OFDM-based radar systems have been already derived in [23] and [8], but refer to the estimation of Doppler and range only. In this Appendix, the procedure we followed in the evaluation of the CRLBs for Doppler, range, azimuth and elevation is sketched.

First of all, let us consider the signal model (3.40), that refers to K distinct targets; the parameters of these targets are collected in the vectors[2]

$$\mathbf{\Gamma} \triangleq [\gamma_0, \gamma_1, ..., \gamma_{K-1}]^T, \tag{A.21}$$

$$\mathbf{F}_\nu = [F_{\nu_0}, F_{\nu_1}, ..., F_{\nu_{K-1}}]^T, \tag{A.22}$$

$$\mathbf{F}_\rho = [F_{\rho_0}, F_{\rho_1}, ..., F_{\rho_{K-1}}]^T, \tag{A.23}$$

$$\mathbf{F}_V = [F_{V_0}, F_{V_1}, ..., F_{V_{K-1}}]^T \tag{A.24}$$

and

$$\mathbf{F}_H = [F_{H_0}, F_{H_1}, ..., F_{H_{K-1}}]^T. \tag{A.25}$$

We also define: 1) the trial vectors $\tilde{\mathbf{\Gamma}}$, $\tilde{\mathbf{F}}_\nu$, $\tilde{\mathbf{F}}_\rho$, $\tilde{\mathbf{F}}_V$ and $\tilde{\mathbf{F}}_H$ in a similar way as $\mathbf{\Gamma}$, $\mathbf{F}_\nu$, $\mathbf{F}_\rho$, $\mathbf{F}_V$ and $\mathbf{F}_H$, respectively (see (A.21)-(A.25)); 2) the vectors $\hat{\mathbf{\Gamma}}$, $\hat{\mathbf{F}}_\nu$, $\hat{\mathbf{F}}_\rho$, $\hat{\mathbf{F}}_V$ and $\hat{\mathbf{F}}_H$, structured like $\mathbf{\Gamma}$, $\mathbf{F}_\nu$, $\mathbf{F}_\rho$, $\mathbf{F}_V$ and $\mathbf{F}_H$, respectively, but collecting the ML estimates of all the considered parameters.

The CRLBs we are interested in refer to the ML estimation problem

$$\big(\hat{\mathbf{F}}_\nu, \hat{\mathbf{F}}_\rho, \hat{\mathbf{F}}_V, \hat{\mathbf{F}}_H, \hat{\mathbf{\Gamma}}\big) \triangleq \underset{\tilde{\mathbf{F}}_\nu, \tilde{\mathbf{F}}_\rho, \tilde{\mathbf{F}}_V, \tilde{\mathbf{F}}_H, \tilde{\mathbf{\Gamma}}}{\arg\min} \varepsilon(\tilde{\mathbf{a}}); \tag{A.26}$$

here,

$$\varepsilon(\tilde{\mathbf{a}}) \triangleq \frac{(\mathbf{x} - \tilde{\mathbf{x}})(\mathbf{x} - \tilde{\mathbf{x}})^H}{MNN_{\mathrm{T}}N_{\mathrm{R}}} \tag{A.27}$$

is a MSE referring to the $(M\,N\,N_{\mathrm{T}}\,N_{\mathrm{R}})$-dimensional column vector

$$\mathbf{x} \triangleq \mathbf{\Gamma}^T \mathbf{\Psi}\big(\mathbf{F}_\nu,\, \mathbf{F}_\rho,\, \mathbf{F}_V, \mathbf{F}_H\big) + \mathbf{w} \tag{A.28}$$

and its useful component

$$\tilde{\mathbf{x}} = \mathbf{x}(\tilde{\mathbf{a}}) = \tilde{\mathbf{\Gamma}}^T \tilde{\mathbf{\Psi}}. \tag{A.29}$$

In the last two formulas,

$$\tilde{\mathbf{a}} \triangleq \big[\tilde{\mathbf{F}}_\nu^T,\, \tilde{\mathbf{F}}_\rho^T,\, \tilde{\mathbf{F}}_V^T,\, \tilde{\mathbf{F}}_H^T,\, \tilde{\mathbf{\Gamma}}^T\big]^T \tag{A.30}$$

[2] The kth element of the vector $\mathbf{\Gamma}$ represents the complex amplitude of the kth target and coincides with the parameter A_k defined in Section 3.6.

is a $(5K)$-dimensional column vector collecting the trial values of the target parameters, $\mathbf{w}$ is a $(M\,N\,N_{\rm T}\,N_{\rm R})$-dimensional noise vector, $\tilde{\mathbf{\Psi}} = \mathbf{\Psi}(\tilde{\mathbf{F}}_\nu,\, \tilde{\mathbf{F}}_\rho,\, \tilde{\mathbf{F}}_V,\, \tilde{\mathbf{F}}_H)$,

$$\mathbf{\Psi}(\mathbf{F}_\nu,\, \mathbf{F}_\rho,\, \mathbf{F}_V,\, \mathbf{F}_H) \triangleq \mathbf{A}(\mathbf{F}_\nu) \star \mathbf{B}(\mathbf{F}_\rho) \star \mathbf{C}(\mathbf{F}_V) \star \mathbf{D}(\mathbf{F}_H) \tag{A.31}$$

is a $(M\,N\,N_{\rm T}\,N_{\rm R}) \times K$ steering matrix, and $\mathbf{A}(\mathbf{F}_\nu)$, $\mathbf{B}(\mathbf{F}_\rho)$, $\mathbf{C}(\mathbf{F}_V)$ and $\mathbf{D}(\mathbf{F}_H)$ are $M \times K$, $N \times K$, $N_{\rm R} \times K$ and $N_{\rm T} \times K$ matrices, respectively; the kth column (with $k = 0, 1, ...K-1$) of the last four matrices is defined as

$$\mathbf{A}(F_{\nu_k}) \triangleq [a_0(F_{\nu_k}), a_1(F_{\nu_k}), ..., a_m(F_{\nu_k}), ..., a_{M-1}(F_{\nu_k})]^T, \tag{A.32}$$

$$\mathbf{B}(F_{\rho_k}) \triangleq [a_0(-F_{\rho_k}), a_1(-F_{\rho_k}), ..., a_n(-F_{\rho_k}), ..., a_{N-1}(-F_{\rho_k})]^T, \tag{A.33}$$

$$\mathbf{C}(F_{V_k}) \triangleq [a_0(-F_{V_k}), a_1(-F_{V_k}), ..., a_q(-F_{V_k}), ..., a_{N_{\rm R}-1}(-F_{V_k})]^T, \tag{A.34}$$

and

$$\mathbf{D}(F_{H_k}) \triangleq [a_0(-F_{H_k}), a_1(-F_{H_k}), ..., a_p(-F_{H_k}), ..., a_{N_{\rm T}-1}(-F_{H_k})]^T, \tag{A.35}$$

respectively ($a_z(F_X)$ is defined by (3.32), with $z = m$, n, q or p, and $X = \nu$, ρ, V or H if $z = m$, n, q or p, respectively).

If we assume that the elements of the noise vector $\mathbf{w}$ are Gaussian, mutually independent and have zero mean and variance σ_W^2, the CRLBs of all the parameters of interest are represented by the diagonal elements of the matrix

$$\mathbf{V} = \sigma_W^2 \mathbf{F}^{-1}, \tag{A.36}$$

where

$$\mathbf{F} \triangleq 2\Re\left\{ \frac{\partial \tilde{\mathbf{x}}}{\partial \tilde{\mathbf{a}}} \left(\frac{\partial \tilde{\mathbf{x}}}{\partial \tilde{\mathbf{a}}} \right)^H \right\} \tag{A.37}$$

is the $(5K \times 5K)$-dimensional FIM computed for the vector $\tilde{\mathbf{x}}$,

$$\frac{\partial \tilde{\mathbf{x}}}{\partial \tilde{\mathbf{a}}} = \left[\bar{\mathbf{A}}, \bar{\mathbf{B}}, \bar{\mathbf{C}}, \bar{\mathbf{D}}, \tilde{\mathbf{\Psi}} \right]^T, \tag{A.38}$$

$\bar{\mathbf{A}} \triangleq [\bar{\mathbf{A}}_0, \bar{\mathbf{A}}_1, ..., \bar{\mathbf{A}}_{K-1}]$, $\bar{\mathbf{B}} \triangleq [\bar{\mathbf{B}}_0, \bar{\mathbf{B}}_1, ..., \bar{\mathbf{B}}_{K-1}]$, $\bar{\mathbf{C}} \triangleq [\bar{\mathbf{C}}_0, \bar{\mathbf{C}}_1, ..., \bar{\mathbf{C}}_{K-1}]$, $\bar{\mathbf{D}} \triangleq [\bar{\mathbf{D}}_0, \bar{\mathbf{D}}_1, ..., \bar{\mathbf{D}}_{K-1}]$,

$$\bar{\mathbf{A}}_k \triangleq -\tilde{\gamma}_k \left(\mathbf{\Upsilon}_M \odot \mathbf{A}(\tilde{F}_{\nu_k}) \right) \star \mathbf{B}(\tilde{F}_{\rho_k}) \star \mathbf{C}(\tilde{F}_{V_k}) \star \mathbf{D}(\tilde{F}_{H_k}), \tag{A.39}$$

$$\bar{\mathbf{B}}_k \triangleq \tilde{\gamma}_k\, \mathbf{A}(\tilde{F}_{\nu_k}) \star \left(\mathbf{\Upsilon}_N \odot \mathbf{B}(\tilde{F}_{\rho_k}) \right) \star \mathbf{C}(\tilde{F}_{V_k}) \star \mathbf{D}(\tilde{F}_{H_k}), \tag{A.40}$$

$$\bar{\mathbf{C}}_k \triangleq \tilde{\gamma}_k\, \mathbf{A}(\tilde{F}_{\nu_k}) \star \mathbf{B}(\tilde{F}_{\rho_k}) \star \left(\mathbf{\Upsilon}_{N_{\rm R}} \odot \mathbf{C}(\tilde{F}_{V_k}) \right) \star \mathbf{D}(\tilde{F}_{H_k}), \tag{A.41}$$

$$\bar{\mathbf{D}}_k \triangleq \tilde{\gamma}_k\, \mathbf{A}(\tilde{F}_{\nu_k}) \star \mathbf{B}(\tilde{F}_{\rho_k}) \star \mathbf{C}(\tilde{F}_{V_k}) \star \left(\mathbf{\Upsilon}_{N_{\rm T}} \odot \mathbf{D}(\tilde{F}_{H_k}) \right), \tag{A.42}$$

and

$$\mathbf{\Upsilon}_X \triangleq [0, -j2\pi, ..., -j2\pi(X-1)]^T. \tag{A.43}$$

for any integer X.

In our work, all the above-mentioned CRLBs have been evaluated numerically on the basis of (A.36)-(A.43); in particular, in the computation of $\bar{\mathbf{A}}_k$, $\bar{\mathbf{B}}_k$, $\bar{\mathbf{C}}_k$ and $\bar{\mathbf{D}}_k$, the following choices have been made for any k: 1) the complex gain $\tilde{\gamma}_k$ (corresponding to A_k

in Section 3.6) has been set to unity in all the considered scenarios; 2) the noise variance σ_W^2 has been derived from (3.131), since the SNR and the amplitudes of the target echoes are known in all the considered scenarios. Moreover, as far as the normalized frequencies $\tilde{F}_{\nu_k}$, $\tilde{F}_{\rho_k}$, $\tilde{F}_{V_k}$ and $\tilde{F}_{H_k}$ are concerned, the following rules have been followed:

a) $\tilde{F}_{X_0}$ has been set to the expected value $\bar{F}_{X_0}$ of the normalized frequency of the first target (with $X = \nu$, ρ, V or H). This choice is motivated by the fact that, in all the considered scenarios, the four normalized frequencies characterizing the first target are uniformly distributed random variables; therefore, $\bar{F}_{X_0} = (F_{X_{\max}} - F_{X_{\min}})/2$ (the values of $F_{X_{\max}}$ and $F_{X_{\min}}$ are provided in Section 3.6).

b) The other $(K-1)$ frequencies $\{\tilde{F}_{X_k}; k = 1, 2, ..., K-1\}$ have been set to $\bar{F}_{X_0} + k\, F_{X_{\text{bin}}}\, F_{X_{\text{res}}}$ for any k; here, $F_{X_{\text{bin}}} = X_{\text{bin}}$ represents the normalized bin spacing between adjacent targets adopted in the considered scenario and $F_{X_{\text{res}}} = 1/Q$, where $Q = M$, N, N_{R} or N_{T} if $X = \nu$, ρ, V or H, respectively.

A.3 Appendices of Chapter 4

A.3.1 Derivation of the Fourier coefficients of the transmitted OTFS signal

In this appendix, the expression (4.69) of the coefficients $S_{k,q}^{(\mathrm{TD})}(\mathbf{C})$ is derived. To begin, we substitute the RHS (4.64) in that of (4.68); this produces

$$S_{k,q}^{(\mathrm{TD})}(\mathbf{C}) \triangleq \frac{1}{T}\sum_{l=-\infty}^{+\infty} x_{k,l}\int_0^T p(t-lT_\mathrm{s})\exp\big(j2\pi k\Delta_f(t-lT_\mathrm{s})\big)\exp\left(-j2\pi q\frac{t}{T}\right)dt. \quad \text{(A.44)}$$

The last formula can be rewritten as

$$S_{k,q}^{(\mathrm{TD})}(\mathbf{C}) \triangleq \frac{1}{T}\sum_{n=0}^{N-1} x_{k,n}\sum_{l'=-\infty}^{+\infty}\int_0^T p(t-(n+l'N)T_\mathrm{s})\exp\big(j2\pi k\Delta_f t\big)\exp\left(-j2\pi q\frac{t}{T}\right)dt, \quad \text{(A.45)}$$

where $l = n + l'N$, $n = 0, 1, ..., N-1$, and l' is an arbitrary integer; moreover, $T_\mathrm{s} = 1/\Delta_f$. Replacing the variable t with $t' \triangleq t - (n + l'N)T_\mathrm{s}$ in the RHS of the last formula yields, after some straightforward manipulation,

$$S_{k,q}^{(\mathrm{TD})}(\mathbf{C}) = \frac{1}{\sqrt{N}T_\mathrm{s}}X_{k,q}\sum_{l'=-\infty}^{+\infty}\int_{-(n+l'N)T_\mathrm{s}}^{-(n+(l'-1)N)T_\mathrm{s}} p(t')\exp\Big(-j2\pi\Big(\frac{q-kN}{T}\Big)t'\Big)\,dt', \quad \text{(A.46)}$$

where $X_{k,q}$ is expressed by (4.70). Since the sum over l' in (A.46) involves the integration interval only, that equation can be rewritten as

$$S_{k,q}^{(\mathrm{TD})}(\mathbf{C}) = \frac{X_{k,q}}{\sqrt{N}T_\mathrm{s}}\int_{-\infty}^{+\infty} p(t)\exp\Big(-j2\pi\Big(\frac{q-kN}{T}\Big)t\Big)\,dt, \quad \text{(A.47)}$$

if the variable t is used in place of t'. The integral in the last formula represents the FCT of $p(t)$ (i.e., $P(f)$; see (4.7)) evaluated at the frequency $f = (q-kN)/T$. Therefore, (4.69) can be easily inferred from (A.47).

A.3.2 Derivation of the received OTFS signal model in the presence of an ideal communication channel

In this appendix, the expression of the OTFS signal model $r[\tilde{k}, \tilde{n}]$ (4.79) is derived. First of all, we substitute the RHS of (4.76) in that of (4.78); this yields

$$r[\tilde{k},\tilde{n}] = \frac{1}{\sqrt{N}}\sum_{q=0}^{N-1}\left[\sum_{k=-\infty}^{+\infty} X_{k,q}\,\hat{G}_{\tilde{k}-k,q}\right]\exp\Big(j2\pi\frac{q}{N}\tilde{n}\Big). \quad \text{(A.48)}$$

In the last formula, the inner sum can be interpreted, for a given q, as the response, at the $\tilde{k}$th instant, of a discrete-time linear filter, having *impulse response* $\{\hat{G}_{k,\cdot}\}$, to the periodic

sequence $\{X_{k,\cdot}\}$ (whose period is equal to M). Therefore, it can be expressed as (e.g., see [115, Sec. 7.6.2, eq. (7.28)])

$$\sum_{k=-\infty}^{+\infty} X_{k,q}\,\hat{G}_{\tilde{k}-k,q} = \frac{1}{\sqrt{M}} \sum_{p=0}^{M-1} \bar{X}_{p,q}\,\bar{g}_{p,q} \exp\Big(-j2\pi \frac{p}{M}\tilde{k}\Big), \tag{A.49}$$

where $\bar{X}_{p,q}$ and $\bar{g}_{p,q}$ are defined in (4.80) and (4.81), respectively. Substituting the RHS of (A.49) in that of (A.48) yields (4.79).

A.3.3 Derivation of the OTFS signal model at the RX side in the presence of a doubly selective fading channel

In this appendix, the expression of the OTFS signal model $r_l[\tilde{k},\tilde{n}]$ (4.105) is derived. To begin, we reformulate (4.100) replacing the index q with $\tilde{q} \triangleq q - \tilde{k}N$; this produces

$$r_{k,l}[\tilde{k},\tilde{n}] = \frac{A_l}{\sqrt{N}} \exp\Big(-j2\pi\tilde{k}F_{\tau_l}\Big) \exp\Big(j2\pi\tilde{n}F_{\nu_l}\Big) \cdot \sum_{\tilde{q}=-\infty}^{+\infty} X_{k,\tilde{q}}\,G_{\tilde{k}-k,\tilde{q},l} \exp\Big(-j2\pi\frac{\tilde{q}}{N}F_{\tau_l}\Big) \exp\Big(j2\pi\frac{\tilde{q}}{N}\tilde{n}\Big), \tag{A.50}$$

where

$$G_{x,\tilde{q},l} \triangleq \frac{1}{T_\mathrm{s}} P\Big(\frac{\tilde{q}+xN}{T}\Big) P^*\Big(\frac{\tilde{q}+F_{\nu_l}N}{T}\Big). \tag{A.51}$$

Then, we replace the index $\tilde{q}$ with the couple of indices (q,u) such that $\tilde{q} \triangleq q + uN$, with $q = 0, 1, ..., N-1$ and u arbitrary integer; this yields

$$r_{k,l}[\tilde{k},\tilde{n}] = \frac{A_l}{\sqrt{N}} \exp\big(-j2\pi\tilde{k}F_{\tau_l}\big) \exp\big(j2\pi\tilde{n}F_{\nu_l}\big) \sum_{q=0}^{N-1} X_{k,q}\,\hat{G}_{\tilde{k}-k,q}(F_{\tau_l},F_{\nu_l}) \exp\Big(j2\pi\frac{q}{N}\tilde{n}\Big), \tag{A.52}$$

where

$$\hat{G}_{x,q}(F_{\tau_l},F_{\nu_l}) \triangleq \sum_{u=-\infty}^{+\infty} G_{x,q,l} \exp\Big(-j2\pi\frac{q+uN}{N}F_{\tau_l}\Big) = \frac{1}{T_\mathrm{s}} \sum_{u=-\infty}^{+\infty} P\Big(\frac{q+(u+x)N}{T}\Big) \cdot P^*\Big(\frac{q+\big(u+F_{\nu_l}\big)N}{T}\Big) \exp\Big(-j2\pi\frac{(q+uN)}{N}F_{\tau_l}\Big) \tag{A.53}$$

represents the counterpart of the quantity $\hat{G}_{x,q}$ (4.77) defined for the case of an ideal channel; note, however, that, unlike $\hat{G}_{x,q}$, $\hat{G}_{x,q}(F_{\tau_l},F_{\nu_l})$ depends not only on the pulse spectrum $P(f)$, but also on the normalized delay F_{τ_l} and the normalized Doppler frequency F_{ν_l}.

Equation (A.52) describes the contribution given to the output of the $\tilde{k}$th RX filter by the lth path of the communication channel fed by the kth component of $s(t;\mathbf{C})$ (4.63). The contribution of all the components of the last signal can be accounted for by summing

over the index k (see (4.63)); this produces

$$r_l[\tilde{k},\tilde{n}] \triangleq \sum_{k=-(M/2+N_{cp}^{(\mathrm{FD})})}^{M/2-1+N_{cpo}^{(\mathrm{FD})}} r_{k,l}[\tilde{k},\tilde{n}], \tag{A.54}$$

which can be rewritten as

$$r_l[\tilde{k},\tilde{n}] \triangleq \sum_{k=-\infty}^{+\infty} r_{k,l}[\tilde{k},\tilde{n}], \tag{A.55}$$

thanks to the assumptions made on the cyclic structure of the transmitted signal. Then, substituting the RHS of (A.52) in that of the last equation yields

$$r_l[\tilde{k},\tilde{n}] = \frac{A_l}{\sqrt{N}} \exp\bigl(-j2\pi\tilde{k}F_{\tau_l}\bigr) \exp\Bigl(j2\pi\tilde{n}F_{\nu_l}\Bigr) \cdot \sum_{q=0}^{N-1} \left[\sum_{k=-\infty}^{+\infty} X_{k,q}\, \hat{G}_{\tilde{k}-k,q}(F_{\tau_l},F_{\nu_l})\right] \exp\Bigl(j2\pi\frac{q}{N}\tilde{n}\Bigr). \tag{A.56}$$

The last expression contains the convolution

$$\sum_{k=-\infty}^{+\infty} X_{k,q}\, \hat{G}_{\tilde{k}-k,q}(F_{\tau_l},F_{\nu_l}), \tag{A.57}$$

that can be interpreted as the response, at the $\tilde{k}$th instant, of a discrete-time linear filter, having impulse response $\{\hat{G}_{k,\cdot}(F_{\tau_l},F_{\nu_l})\}$, to the periodic sequence $\{X_{k,\cdot}\}$ (whose period is equal to M). Then, following the same line of reasoning as that illustrated for the derivation of (A.49), (A.56) can be easily reformulated as (4.105).

A.3.4 Power spectral density of OTFS modulation

In this appendix, the derivation of (4.126)-(4.127) is sketched. Our mathematical developments rely on the model (4.63), that represents the complex envelope (4.62) of an OTFS signal as the superposition of the signals of the set

$$\mathcal{S}^{(\mathrm{TD})} \triangleq \{s_k^{(\mathrm{TD})}(t;\mathbf{C});\, k=-M/2+N_{cp}^{(\mathrm{FD})}, -M/2+N_{cp}^{(\mathrm{FD})}+1, ..., M/2-1+N_{cpo}^{(\mathrm{FD})}\}, \tag{A.58}$$

with (see (4.64))

$$s_k^{(\mathrm{TD})}(t;\mathbf{C}) \triangleq \sum_{l=-N_{cp}^{(\mathrm{TD})}}^{N-1} x_{k,l}\, p(t-lT_s) \exp\bigl(j2\pi k\Delta_f(t-lT_s)\bigr) \tag{A.59}$$

for any k. Note also that: a) $s_k^{(\mathrm{TD})}(t;\mathbf{C})$ represents the frequency-shifted version of the complex envelope of an OFDM signal (the frequency shift is given by $k\Delta_f$, that also corresponds to the central frequency of that signal); b) the use of the TD CP implies that

the overall bandwidth Δ_f is employed to transmit $N + N_{cp}^{(\mathrm{TD})}$ symbols. In our derivations, we assume that:

1) The useful elements[3] $\{c_{m,n}\}$ of the channel symbol matrix $\mathbf{C}$ have the following properties: a) they belong to an M_{c}ary constellation; b) they are statistically independent and identically distributed (in particular, they have zero mean and variance σ_c^2). The last assumption implies that the channel symbols $\{x_{k,l}\}$ are also statistically independent and identically distributed thanks to the *orthogonality* property of the DSFT transform (see (4.91)).

2) The spectrum $P(f)$ of the pulse $p(t)$ appearing in the RHS of (A.59) is expressed by (4.16).

Based on these assumptions, it can be proved that the *cross-correlation* function

$$R_{k,m} \triangleq \mathrm{E}\Big[s_{k+m}^{(\mathrm{TD})}(t;\mathbf{C})(s_k^{(\mathrm{TD})}(t;\mathbf{C}))^*\Big] \tag{A.60}$$

is equal to zero for any $m \neq 0$, so that all the signals of the set $\mathcal{S}^{(\mathrm{TD})}$ (A.58) are *statistically uncorrelated*. Consequently, the PSD of $s(t;\mathbf{C})$ (4.63) can be expressed as the superposition of the PSD of all the signals of $\mathcal{S}^{(\mathrm{TD})}$, i.e., as in (4.126). Moreover, for any $k \neq 0$, the PSD $S_{s_k}(f)$ of $s_k^{(\mathrm{TD})}(t;\mathbf{C})$ can be obtained from that of $s_0^{(\mathrm{TD})}(t;\mathbf{C})$ by introducing a simple frequency shift. Since $s_0^{(\mathrm{TD})}(t;\mathbf{C})$ represents the complex envelope of an OFDM signal (see (4.64)), its PSD is expressed by [81, Subsect. 3.7.3.3, eq. (3.295)]. These considerations lead easily to (4.127).
□

[3]Do not forget that a portion of the elements of $\mathbf{C}$ is set to zero.

Bibliography

[1] J. A. Zhang *et al.*, "An Overview of Signal Processing Techniques for Joint Communication and Radar Sensing," *IEEE J. Sel. Topics Signal Process.*, vol. 15, pp. 1295–1315, Nov. 2021.

[2] K. V. Mishra, M. Bhavani Shankar, V. Koivunen, B. Ottersten, and S. A. Vorobyov, "Toward Millimeter-Wave Joint Radar Communications: A Signal Processing Perspective," *IEEE Signal Process. Mag.*, vol. 36, pp. 100–114, Sept. 2019.

[3] L. Zheng and X. Wang, "Super-Resolution Delay-Doppler Estimation for OFDM Passive Radar," *IEEE Trans. Signal Process.*, vol. 65, pp. 2197–2210, May 2017.

[4] C. Sturm and W. Wiesbeck, "Waveform Design and Signal Processing Aspects for Fusion of Wireless Communications and Radar Sensing," *Proc. of the IEEE*, vol. 99, pp. 1236–1259, July 2011.

[5] S. Mercier, S. Bidon, D. Roque, and C. Enderli, "Comparison of Correlation-Based OFDM Radar Receivers," *IEEE Trans. Aerosp. Electron. Syst.*, vol. 56, pp. 4796–4813, Dec. 2020.

[6] Y. L. Sit, C. Sturm, and T. Zwick, "Doppler estimation in an OFDM joint radar and communication system," *2011 German Microw. Conf.*, p. 4, Mar. 2011.

[7] S. Mercier, D. Roque, S. Bidon, and C. Enderli, "Correlation-Based Radar Receivers with Pulse-Shaped OFDM Signals," in *2020 IEEE Radar Conf. (RadarConf20)*, pp. 1–6, IEEE, Sept. 2020. Florence, Italy.

[8] R. Xie, D. Hu, K. Luo, and T. Jiang, "Performance Analysis of Joint Range-Velocity Estimator With 2D-MUSIC in OFDM Radar," *IEEE Trans. Signal Process.*, vol. 69, pp. 4787–4800, Sept. 2021.

[9] Y. Liu, G. Liao, Y. Chen, J. Xu, and Y. Yin, "Super-Resolution Range and Velocity Estimations With OFDM Integrated Radar and Communications Waveform," *IEEE Trans. Veh. Technol.*, vol. 69, pp. 11659–11672, Oct. 2020.

[10] F. Zhang, Z. Zhang, and W. Yu, "Joint Range and Doppler Estimation with Amplitude Weighted Linearly Constrained Minimum Variance Method for OFDM-based RadCom Systems," in *2020 IEEE Radar Conf. (RadarConf20)*, RadarConf20, pp. 1–6, IEEE, Sept. 2020. Florence, Italy.

[11] F. Zhang, Z. Zhang, W. Yu, and T.-K. Truong, "Joint Range and Velocity Estimation With Intrapulse and Intersubcarrier Doppler Effects for OFDM-Based RadCom Systems," *IEEE Trans. Signal Process.*, vol. 68, pp. 662–675, Jan. 2020.

[12] U. Singh, R. Mitra, V. Bhatia, and A. Mishra, "Target Range Estimation in OFDM Radar System via Kernel Least Mean Square Technique," in *Int. Conf. on Radar Systems (Radar 2017)*, Institution of Engineering and Technology, Oct. 2017.

[13] A. El Assaad, M. Krug, and G. Fischer, "Distance and vehicle speed estimation in OFDM multipath channels," in *2016 21st Int. Conf. on Microwave, Radar and Wireless Commun. (MIKON)*, pp. 1–5, IEEE, May 2016.

[14] J. Fink, M. Braun, and F. K. Jondral, "Effects of Arbitrarily Spaced Subcarriers on Detection Performance in OFDM Radar," in *2012 IEEE Veh. Technol. Conf (VTC Fall)*, pp. 1–5, IEEE, Sept. 2012.

[15] P. Di Viesti, A. Davoli, G. Guerzoni, and G. M. Vitetta, "Recursive Algorithms for the Estimation of Multiple Superimposed Undamped Tones and Their Application to Radar Systems," *IEEE Trans. Aerosp. Electron. Syst.*, pp. 1–20, Apr. 2023.

[16] I. Ziskind and M. Wax, "Maximum likelihood localization of multiple sources by alternating projection," *IEEE Trans. Acoust., Speech, Signal Process.*, vol. 36, pp. 1553–1560, Oct. 1988.

[17] D. Rife and R. Boorstyn, "Single tone parameter estimation from discrete-time observations," *IEEE Trans. Inf. Theory*, vol. 20, pp. 591–598, Sept. 1974.

[18] E. Isaacson and H. B. Keller, *Analysis of numerical methods*. New York: Dover Publications, 1994.

[19] J.-P. Berrut and L. N. Trefethen, "Barycentric Lagrange Interpolation," *SIAM Rev.*, vol. 46, pp. 501–517, Jan. 2004.

[20] E. Sirignano, A. Davoli, G. M. Vitetta, and F. Viappiani, "A Comparative Analysis of Deterministic Detection and Estimation Techniques for MIMO SFCW Radars," *IEEE Access*, vol. 7, pp. 129848–129861, Sept. 2019.

[21] A. Davoli, E. Sirignano, and G. M. Vitetta, "Three-Dimensional Deterministic Detection and Estimation Algorithms for MIMO SFCW Radars," in *2020 IEEE Radar Conf. (RadarConf20)*, pp. 1–6, IEEE, Sept. 2020. Florence, Italy.

[22] C. R. Berger, B. Demissie, J. Heckenbach, P. Willett, and S. Zhou, "Signal Processing for Passive Radar Using OFDM Waveforms," *IEEE J. Sel. Topics Signal Process.*, vol. 4, pp. 226–238, Feb. 2010.

[23] P. Kumari, J. Choi, N. Gonzalez-Prelcic, and R. W. Heath, "IEEE 802.11ad-Based Radar: An Approach to Joint Vehicular Communication-Radar System," *IEEE Trans. Veh. Technol.*, vol. 67, pp. 3012–3027, Apr. 2018.

[24] G. Duggal, S. Vishwakarma, K. V. Mishra, and S. S. Ram, "Doppler-Resilient 802.11ad-Based Ultrashort Range Automotive Joint Radar-Communications System," *IEEE Trans. Aerosp. Electron. Syst.*, vol. 56, pp. 4035–4048, Oct. 2020.

[25] R. C. Daniels, E. R. Yeh, and R. W. Heath, "Forward Collision Vehicular Radar With IEEE 802.11: Feasibility Demonstration Through Measurements," *IEEE Trans. Veh. Technol.*, vol. 67, pp. 1404–1416, Feb. 2018.

[26] M. L. Rahman, J. A. Zhang, X. Huang, Y. J. Guo, and R. W. Heath, "Framework for a Perceptive Mobile Network Using Joint Communication and Radar Sensing," *IEEE Trans. Aerosp. Electron. Syst.*, vol. 56, pp. 1926–1941, June 2020.

[27] J. A. Zhang, A. Cantoni, X. Huang, Y. J. Guo, and R. W. Heath, "Framework for an Innovative Perceptive Mobile Network Using Joint Communication and Sensing," in *2017 IEEE 85th Vehicular Technology Conference (VTC Spring)*, pp. 1–5, 2017.

[28] J. A. Zhang, X. Huang, Y. J. Guo, and M. L. Rahman, "Signal stripping based sensing parameter estimation in perceptive mobile networks," in *2017 IEEE-APS Topical Conference on Antennas and Propagation in Wireless Communications (APWC)*, pp. 67–70, 2017.

[29] G. Hakobyan and B. Yang, "High-Performance Automotive Radar: A Review of Signal Processing Algorithms and Modulation Schemes," *IEEE Signal Process. Mag.*, vol. 36, pp. 32–44, Sept. 2019.

[30] L. Zheng, M. Lops, Y. C. Eldar, and X. Wang, "Radar and Communication Coexistence: An Overview: A Review of Recent Methods," *IEEE Signal Process. Mag.*, vol. 36, pp. 85–99, Sept. 2019.

[31] A. Hassanien, M. G. Amin, E. Aboutanios, and B. Himed, "Dual-Function Radar Communication Systems: A Solution to the Spectrum Congestion Problem," *IEEE Signal Process. Mag.*, vol. 36, pp. 115–126, Sept. 2019.

[32] F. Liu, C. Masouros, A. P. Petropulu, H. Griffiths, and L. Hanzo, "Joint Radar and Communication Design: Applications, State-of-the-Art, and the Road Ahead," *IEEE Trans. Commun.*, vol. 68, pp. 3834–3862, June 2020.

[33] Z. Feng, Z. Fang, Z. Wei, X. Chen, Z. Quan, and D. Ji, "Joint radar and communication: A survey," *China Commun.*, vol. 17, pp. 1–27, Jan. 2020.

[34] D. Ma, N. Shlezinger, T. Huang, Y. Liu, and Y. C. Eldar, "Joint Radar-Communication Strategies for Autonomous Vehicles: Combining Two Key Automotive Technologies," *IEEE Signal Process. Mag.*, vol. 37, pp. 85–97, July 2020.

[35] T. Wild, V. Braun, and H. Viswanathan, "Joint Design of Communication and Sensing for Beyond 5G and 6G Systems," *IEEE Access*, vol. 9, pp. 30845–30857, Feb. 2021.

[36] L. Giroto de Oliveira, B. Nuss, M. B. Alabd, A. Diewald, M. Pauli, and T. Zwick, "Joint Radar-Communication Systems: Modulation Schemes and System Design," *IEEE Trans. Microw. Theory Techn.*, vol. 70, pp. 1521–1551, Mar. 2022.

[37] J. A. Zhang, M. L. Rahman, K. Wu, X. Huang, Y. J. Guo, S. Chen, and J. Yuan, "Enabling Joint Communication and Radar Sensing in Mobile Networks—A Survey," *IEEE Commun. Surveys Tuts.*, vol. 24, no. 1, pp. 306–345, 2022.

[38] D. Roque and S. Bidon, "Range Migration in Symbol-Based OFDM Radar Receivers," in *2021 IEEE 22nd Int. Workshop on Signal Process. Adv. in Wireless Commun. (SPAWC)*, SPAWC, pp. 496–500, IEEE, 2021.

[39] C. F. Van Loan and G. Golub, "Matrix computations," *Matrix Computations*, vol. 53, 1996.

[40] P. Di Viesti, A. Davoli, G. Guerzoni, and G. M. Vitetta, "Novel Methods for Approximate Maximum Likelihood Estimation of Multiple Superimposed Undamped Tones and Their Application to Radar Systems," *TechRxiv*, Aug. 2021.

[41] X. Liu, T. Zhang, Q. Shi, and L. Kong, "CP-OFDM radar range reconstruction in a chaotic Doppler disturbed scenario," in *2020 IEEE Radar Conference (RadarConf20)*, pp. 1–5, IEEE, Sept. 2020. Florence, Italy.

[42] S. Mercier, D. Roque, and S. Bidon, "Study of the Target Self-Interference in a Low-Complexity OFDM-Based Radar Receiver," *IEEE Trans. Aerosp. Electron. Syst.*, vol. 55, pp. 1200–1212, June 2019.

[43] G. Liu, H. Niu, M. Zheng, D. Bao, J. Cai, G. Qin, B. Wu, P. Li, and N. Liu, "Integration of Communication and SAR Radar Based on OFDM with Channel Estimation in High Speed Scenario," in *IGARSS 2019 - 2019 IEEE Int. Geoscience and Remote Sens. Symp.*, pp. 2519–2522, IEEE, July 2019. Yokohama, Japan.

[44] Y. Zeng, Y. Ma, and S. Sun, "Joint Radar-Communication: Low Complexity Algorithm and Self-Interference Cancellation," in *2018 IEEE Global Commun. Conf. (GLOBECOM)*, pp. 1–7, Dec. 2018. Abu Dhabi, United Arab Emirates.

[45] J. B. Sanson, D. Castanheira, A. Gameiro, and P. P. Monteiro, "Fusion of Radar and Communication Information for Tracking in OFDM Automotive Radar at 24 GHz," in *2020 IEEE/MTT-S International Microwave Symposium (IMS)*, pp. 1153–1156, IEEE, Aug. 2020. Los Angeles, CA, USA.

[46] S. Schieler, C. Schneider, C. Andrich, M. Döbereiner, J. Luo, A. Schwind, R. S. Thomä, and G. Del Galdo, "OFDM waveform for distributed radar sensing in automotive scenarios," *Int. Journal of Microw. and Wireless Technol.*, vol. 12, pp. 716–722, Oct. 2020.

[47] J. Tsao and B. Steinberg, "Reduction of sidelobe and speckle artifacts in microwave imaging: the CLEAN technique," *IEEE Trans. Antennas Propag.*, vol. 36, pp. 543–556, Apr. 1988.

[48] J. Li and P. Stoica, "Efficient mixed-spectrum estimation with applications to target feature extraction," *IEEE Trans. Signal Process.*, vol. 44, pp. 281–295, Feb. 1996.

[49] J. Rissanen, "A universal prior for integers and estimation by minimum description length," *The Annals of statistics*, vol. 11, pp. 416–431, June 1983.

[50] D. H. N. Nguyen and R. W. Heath, "Delay and Doppler processing for multi-target detection with IEEE 802.11 OFDM signaling," in *2017 IEEE Int. Conf. on Acoust., Speech and Signal Process. (ICASSP)*, pp. 3414–3418, Mar. 2017.

[51] A. Jakobsson, A. Swindlehurst, and P. Stoica, "Subspace-based Estimation of Time Delays and Doppler Shifts," *IEEE Trans. Signal Process.*, vol. 46, pp. 2472–2483, Sept. 1998.

[52] U. Singh, V. Bhatia, and A. Mishra, "Delay and Doppler shift estimation for non-constant envelope modulation in OFDM radar system," in *Int. Conf. on Radar Systems (Radar 2017)*, pp. 1–5, 2017.

[53] T. Moon, "The expectation-maximization algorithm," *IEEE Signal Process. Mag.*, vol. 13, pp. 47–60, Nov. 1996.

[54] Ying-Xian Yao and S. Pandit, "Cramer-Rao lower bounds for a damped sinusoidal process," *IEEE Trans. Signal Process.*, vol. 43, pp. 878–885, Apr. 1995.

[55] Y. Zhang, Q. Li, L. Huang, and J. Song, "Waveform design for joint radar-communication system with multi-user based on MIMO radar," in *2017 IEEE Radar Conference (RadarConf)*, pp. 0415–0418, May 2017.

[56] S. H. Dokhanchi, B. S. Mysore, K. V. Mishra, and B. Ottersten, "A mmWave Automotive Joint Radar-Communications System," *IEEE Trans. Aerosp. Electron. Syst.*, vol. 55, pp. 1241–1260, June 2019.

[57] G. L. Stuber, J. R. Barry, S. W. McLaughlin, Y. Li, M. A. Ingram, and T. G. Pratt, "Broadband MIMO-OFDM wireless communications," *Proc. IEEE*, vol. 92, pp. 271–294, Feb. 2004.

[58] M. Jiang and L. Hanzo, "Multiuser MIMO-OFDM for Next-Generation Wireless Systems," *Proc. IEEE*, vol. 95, pp. 1430–1469, July 2007.

[59] C. Knill, B. Schweizer, S. Sparrer, F. Roos, R. F. H. Fischer, and C. Waldschmidt, "High Range and Doppler Resolution by Application of Compressed Sensing Using Low Baseband Bandwidth OFDM Radar," *IEEE Trans. Microw. Theory Techn.*, vol. 66, pp. 3535–3546, July 2018.

[60] J. B. Sanson, P. M. Tomé, D. Castanheira, A. Gameiro, and P. P. Monteiro, "High-Resolution Delay-Doppler Estimation Using Received Communication Signals for OFDM Radar-Communication System," *IEEE Trans. Veh. Technol.*, vol. 69, pp. 13112–13123, Nov. 2020.

[61] D. Werbunat, F. Sgroi, C. Knill, B. Schweizer, B. Meinecke, R. Michev, J. Hasch, and C. Waldschmidt, "Multiplexing of OFDM-Based Radar Networks," in *2021 IEEE Radar Conference (RadarConf21)*, pp. 1–6, May 2021.

[62] Z. Xu and A. Petropulu, "A Bandwidth Efficient Dual-Function Radar Communication System Based on a MIMO Radar Using OFDM Waveforms," *IEEE Trans. Signal Process.*, vol. 71, pp. 401–416, Feb. 2023.

[63] Y.-C. Lin, T.-S. Lee, Y.-H. Pan, and K.-H. Lin, "Low-Complexity High-Resolution Parameter Estimation for Automotive MIMO Radars," *IEEE Access*, vol. 8, pp. 16127–16138, Jan. 2020.

[64] J. Wang, P. Wang, F. Luo, and W. Wu, "Waveform Design and DoA-DoD Estimation of OFDM-LFM Signal Based on SDFnT for MIMO Radar," *IEEE Access*, vol. 11, pp. 1348–1358, Jan. 2023.

[65] S.-F. Chuang, W.-R. Wu, and Y.-T. Liu, "High-Resolution AoA Estimation for Hybrid Antenna Arrays," *IEEE Trans. Antennas Propag.*, vol. 63, pp. 2955–2968, July 2015.

[66] L. Liu and S. Zhang, "A Two-Stage Radar Sensing Approach based on MIMO-OFDM Technology," in *2020 IEEE Globecom Workshops (GC Wkshps)*, pp. 1–6, Dec. 2020.

[67] H. Lee and J. Chun, "Virtual array response vector for angle estimation of MIMO radar with a wide-band interleaved OFDM signal," *IEEE Wireless Commun. Lett.*, vol. 25, pp. 1539–1543, May 2021.

[68] C. Knill, F. Embacher, B. Schweizer, S. Stephany, and C. Waldschmidt, "Coded OFDM Waveforms for MIMO Radars," *IEEE Trans. Veh. Technol.*, vol. 70, pp. 8769–8780, Sept. 2021.

[69] M. F. Keskin, H. Wymeersch, and V. Koivunen, "MIMO-OFDM Joint Radar-Communications: Is ICI Friend or Foe?," *IEEE J. Sel. Topics Signal Process.*, vol. 15, pp. 1393–1408, Nov. 2021.

[70] V. Popović-Bugarin and S. Djukanović, "A Low Complexity Model Order and Frequency Estimation of Multiple 2-D Complex Sinusoids," *Digital Signal Processing*, vol. 104, p. 102794, 2020.

[71] V. Solak, S. Aldirmaz-Colak, and A. Serbes, "Fast and Efficient 2-D and K-D DFT-Based Sinusoidal Frequency Estimation," *IEEE Trans. Signal Process.*, vol. 70, pp. 5087–5101, Nov. 2022.

[72] D. Fan *et al.*, "Angle Domain Channel Estimation in Hybrid Millimeter Wave Massive MIMO Systems," *IEEE Wireless Commun.*, vol. 17, pp. 8165–8179, Dec. 2018.

[73] P. Di Viesti, A. Davoli, G. Guerzoni, and G. M. Vitetta, "Novel Deterministic Detection and Estimation Algorithms for Colocated Multiple-Input Multiple-Output Radars," *IEEE Access*, vol. 10, pp. 2216–2255, 2022.

[74] S. Zhang, Y. Luo, Z. Wang, H. Sun, and X. Wang, "A radar extended target angle estimation method based on effective phase clustering," *The Journal of Engineering*, vol. 2023, p. e12343, Dec. 2023.

[75] D. K. Pin Tan, J. He, Y. Li, A. Bayesteh, Y. Chen, P. Zhu, and W. Tong, "Integrated Sensing and Communication in 6G: Motivations, Use Cases, Requirements, Challenges and Future Directions," in *2021 1st IEEE International Online Symposium on Joint Communications & Sensing (JC&S)*, pp. 1–6, Feb. 2021.

[76] Z. Wei, H. Qu, Y. Wang, X. Yuan, H. Wu, Y. Du, K. Han, N. Zhang, and Z. Feng, "Integrated Sensing and Communication Signals Toward 5G-A and 6G: A Survey," *IEEE Internet Things J.*, vol. 10, pp. 11068–11092, July 2023.

[77] F.-M. Han and X.-D. Zhang, "Wireless multicarrier digital transmission via weyl-heisenberg frames over time-frequency dispersive channels," *IEEE Trans. Commun.*, vol. 57, pp. 1721–1733, June 2009.

[78] A. Bemani, N. Ksairi, and M. Kountouris, "Affine Frequency Division Multiplexing for Next Generation Wireless Communications," *IEEE Trans. Wireless Commun.*, vol. 22, pp. 8214–8229, Nov. 2023.

[79] R. Hadani, S. Rakib, M. Tsatsanis, A. Monk, A. J. Goldsmith, A. F. Molisch, and R. Calderbank, "Orthogonal Time Frequency Space Modulation," in *2017 IEEE Wireless Communications and Networking Conference (WCNC)*, pp. 1–6, Mar. 2017.

[80] R. Hadani and A. Monk, "OTFS: A New Generation of Modulation Addressing the Challenges of 5G," Feb. 2018.

[81] G. M. Vitetta, D. P. Taylor, G. Colavolpe, F. Pancaldi, and P. A. Martin, *Wireless communications: algorithmic techniques*. John Wiley & Sons, 2013.

[82] P. Bello, "Time-frequency duality," *IEEE Trans. Inf. Theory*, vol. 10, pp. 18–33, Jan. 1964.

[83] P. Raviteja, K. T. Phan, and Y. Hong, "Embedded Pilot-Aided Channel Estimation for OTFS in Delay–Doppler Channels," *IEEE Trans. Veh. Technol.*, vol. 68, pp. 4906–4917, May 2019.

[84] P. Raviteja, Y. Hong, E. Viterbo, and E. Biglieri, "Practical Pulse-Shaping Waveforms for Reduced-Cyclic-Prefix OTFS," *IEEE Trans. Veh. Technol.*, vol. 68, pp. 957–961, Jan. 2019.

[85] S. K. Mohammed, "Derivation of OTFS Modulation From First Principles," *IEEE Trans. Veh. Technol.*, vol. 70, pp. 7619–7636, Aug. 2021.

[86] L. Xiao, S. Li, Y. Qian, D. Chen, and T. Jiang, "An Overview of OTFS for Internet of Things: Concepts, Benefits, and Challenges," *IEEE Internet Things J.*, vol. 9, pp. 7596–7618, May 2022.

[87] P. Raviteja, K. T. Phan, Y. Hong, and E. Viterbo, "Interference Cancellation and Iterative Detection for Orthogonal Time Frequency Space Modulation," *IEEE Trans. Wireless Commun.*, vol. 17, pp. 6501–6515, Aug. 2018.

[88] L. Gaudio, M. Kobayashi, G. Caire, and G. Colavolpe, "On the Effectiveness of OTFS for Joint Radar Parameter Estimation and Communication," *IEEE Trans. Wireless Commun.*, vol. 19, pp. 5951–5965, Sept. 2020.

[89] A. Janssen, "The Zak transform: A signal transform for sampled time-continuous signals," *Philips Journal of Research*, vol. 43, Jan. 1988.

[90] P. Singh, S. Tiwari, and R. Budhiraja, "Low-Complexity LMMSE Receiver Design for Practical-Pulse-Shaped MIMO-OTFS Systems," *IEEE Trans. Commun.*, vol. 70, pp. 8383–8399, Dec. 2022.

[91] K. Wu, J. A. Zhang, X. Huang, and Y. J. Guo, "OTFS-Based Joint Communication and Sensing for Future Industrial IoT," *IEEE Internet Things J.*, vol. 10, pp. 1973–1989, Feb. 2023.

[92] X. Wang, X. Shi, J. Wang, and J. Song, "On the Doppler Squint Effect in OTFS Systems Over Doubly-Dispersive Channels: Modeling and Evaluation," *IEEE Trans. Wireless Commun.*, vol. 22, pp. 8781–8796, Dec. 2023.

[93] Z. Ding, R. Schober, P. Fan, and H. Vincent Poor, "OTFS-NOMA: An Efficient Approach for Exploiting Heterogenous User Mobility Profiles," *IEEE Trans. Commun.*, vol. 67, pp. 7950–7965, Nov. 2019.

[94] Y. Ge, Q. Deng, P. C. Ching, and Z. Ding, "Receiver Design for OTFS with a Fractionally Spaced Sampling Approach," *IEEE Trans. Wireless Commun.*, vol. 20, pp. 4072–4086, July 2021.

[95] W. Abu-Al-Saud and G. Stuber, "Efficient wideband channelizer for software radio systems using modulated PR filterbanks," *IEEE Trans. Signal Process.*, vol. 52, pp. 2807–2820, Sept. 2004.

[96] Y. Qiu, Z. Liu, and D. Qu, "Filtered bank based implementation for filtered OFDM," in *2017 7th IEEE International Conference on Electronics Information and Emergency Communication (ICEIEC)*, pp. 15–18, July 2017.

[97] G. D. Surabhi, R. M. Augustine, and A. Chockalingam, "On the Diversity of Uncoded OTFS Modulation in Doubly-Dispersive Channels," *IEEE Trans. Wireless Commun.*, vol. 18, pp. 3049–3063, Apr. 2019.

[98] I. A. Khan and S. K. Mohammed, "A Low-Complexity OTFS Channel Estimation Method for Fractional Delay-Doppler Scenarios," *IEEE Wireless Commun. Lett.*, vol. 12, pp. 1484–1488, Sept. 2023.

[99] G. D. Surabhi and A. Chockalingam, "Low-Complexity Linear Equalization for OTFS Modulation," *IEEE Commun. Lett.*, vol. 24, pp. 330–334, Feb. 2020.

[100] F. Liu, Z. Yuan, Q. Guo, Z. Wang, and P. Sun, "Message Passing-Based Structured Sparse Signal Recovery for Estimation of OTFS Channels With Fractional Doppler Shifts," *IEEE Trans. Wireless Commun.*, vol. 20, pp. 7773–7785, Dec. 2021.

[101] L. Gaudio, G. Colavolpe, and G. Caire, "OTFS vs. OFDM in the Presence of Sparsity: A Fair Comparison," *IEEE Trans. Wireless Commun.*, vol. 21, pp. 4410–4423, June 2022.

[102] M. Kollengode Ramachandran and A. Chockalingam, "MIMO-OTFS in High-Doppler Fading Channels: Signal Detection and Channel Estimation," in *2018 IEEE Global Communications Conference (GLOBECOM)*, pp. 206–212, Dec. 2018.

[103] V. Kumar Singh, M. F. Flanagan, and B. Cardiff, "Maximum Likelihood Channel Path Detection and MMSE Channel Estimation in OTFS Systems," in *2020 IEEE 92nd Vehicular Technology Conference (VTC2020-Fall)*, pp. 1–5, Dec. 2020.

[104] E. Chiavaccini and G. Vitetta, "GQR models for multipath Rayleigh fading channels," *IEEE J. Sel. Areas Commun.*, vol. 19, no. 6, pp. 1009–1018, 2001.

[105] J. G. Proakis, *Digital communications*. McGraw-Hill, Higher Education, 2008.

[106] T. Thaj and E. Viterbo, "OTFS Modem SDR Implementation and Experimental Study of Receiver Impairment Effects," in *2019 IEEE Int. Conf. on Commun. Workshops (ICC Workshops)*, pp. 1–6, 2019.

[107] M. R. N. Rahman, I. W. G. Wiryabawa, and E. Y. Hamid, "Development of OTFS Receiver System Using SDR," in *2023 17th Int. Conf. on Telecommun. Sys., Services, and Applications (TSSA)*, pp. 1–4, 2023.

[108] A. Devices, "Adalm Pluto." `https://www.analog.com/en/resources/evaluation-hardware-and-software/evaluation-boards-kits/adalm-pluto.html#eb-overview`. [Accessed 25-09-2024].

[109] M. Nauman, L. Lopacinski, N. Maletic, M. Scheide, M. Krstic, and E. Grass, "6G and Beyond: Synchronization Challenges and Solutions with OTFS Modulation using SDR," in *2023 31st Telecommunications Forum (TELFOR)*, pp. 1–4, 2023.

[110] Y. X. Yap, N. Bhushan, O. Dizdar, A. Sattarzadeh, D. Redgate, V. Battula, and S. Wang, "A Proof of Concept for OTFS Resilience in Doubly-Selective Channels by GPU-Enabled Real-Time SDR," in *GLOBECOM 2023 - 2023 IEEE Global Commun. Conf.*, pp. 7206–7212, 2023.

[111] P. Karpovich, T. Zielinski, R. Maksymiuk, K. Abratkiewicz, P. Tomikowski, and P. Samczyński, "Experimental Testing of an OTFS-Modulated Waveform in a Joint Radar-Comm System," in *2023 IEEE Radar Conference (RadarConf23)*, pp. 1–6, 2023.

[112] X. Wei, L. Zhang, W. Yuan, F. Liu, S. Li, and Z. Wei, "SDR System Design and Implementation on Delay-Doppler Communications and Sensing," in *2023 IEEE Wireless Commun. and Networking Conf. (WCNC)*, pp. 1–6, 2023.

[113] National Instruments, "NI-2901 reference manual." `https://www.ni.com/docs/en-US/bundle/usrp-2901-specs/page/specs.html?srsltid=AfmBOoq95Z9QFdHRexYpJd2p7fujfClfQb55otlQNUv8hzjNbqJjelU8`. [Accessed 25-09-2024].

[114] M. Braun, C. Sturm, and F. K. Jondral, "On the single-target accuracy of OFDM radar algorithms," in *2011 IEEE 22nd Int. Symp. on Pers., Indoor and Mobile Radio Commun.*, pp. 794–798, IEEE, Sept. 2011.

[115] R. Baraniuk, *Signals and systems*. Rice University, 2015.